Rheinische Friedrich-Wilhelms Universität Bonn

Institut für Physikalische und Theoretische Chemie

Oxidation of Methanol and Carbon Monoxide on Platinum Surfaces. The Influence of Foreign Metals.

Dissertation

zur

Erlangung des Doktorgrades (Dr. rer. nat.)

der

Matematisch-Naturwissenschaftlichen Fakultät

der

Rheinischen Friedrich-Wilhelms-Universität Bonn

vorgelegt von

Barbora Láňová

aus

Zastávka u Brna, Tschechien

Bonn, 2009

Angefertigt mit Genehmigung der Mathematisch-Naturwissenschaftlichen Fakultät der Rheinischen Friedrich-Wilhelms-Universität Bonn

Promotionskommission:

Erstgutachter (Betreuer): Prof. Dr. Helmut Baltruschat

Zweitgutachter: Prof. Dr. Moritz Sokolowski

Fachnahes Mitglied: Prof. Dr. Werner Mader

Fachangrenzendes Mitglied: Prof. Dr. Karl Maier

Tag der Einreichung im Dekanat: 10.02.2009

Tag der mündlichen Prüfung: 18.06.2009

Erscheinungsjahr: 2009

Diese Arbeit wurde als Dissertation im Fachbereich Physikalische Chemie an der Mathematisch-Naturwissenschaftlichen Fakultät der Rheinischen Friedrich-Wilhelms-Universität in Bonn, zur Erlangung des Doktorgrades, im Arbeitskreis von Herrn Prof. Dr. H. Baltruschat, angefertigt.

Die Autorin versichert, dass die vorliegende Arbeit eigenständig verfasst und keine weiteren Hilfsmittel als die angegebenen verwendet zu haben. Alle verwendete Literatur und Informationsquellen sowie weitere Hilfsmittel sind in den Zitaten und Fußnoten gekennzeichnet.

Bonn, 10. Februar 2009

Barbora Láňová

No amount of experimentation can even prove me right; a single experiment can prove me wrong.

Albert Einstein

Contents

Preface

Since 1839, as Sir William Robert Grove demonstrated the Schoenbein´s discovery of the principle of fuel cells on practical scales, these are making headlines across the globe in almost every area of a power production including buildings, cars and portable electronics.

The combustion of fossil fuels releases emissions into the air, especially NO_x, SO_x and a major pollutant carbon dioxide (CO_2), which influence the greenhouse effect, worldwide climate changes as well as the health of people. For the overall benefit of the environment, the use of fossil fuels needs to be reduced and new technologies need to be developed. Fuel cells are considered as a prime candidate for the "green" energy production: clean, quiet and efficient.

Fuel cells are electrochemical devices, where the chemical energy of a fuel (hydrogen, natural gas, methanol, gasoline, etc.) and an oxidant (air or oxygen) is directly converted into the electrical energy with a high efficiency [1]. In principle, the fuel cell operates like a battery. An important difference is that batteries store the chemical energy, while fuel cells can produce the electricity continuously as long as the fuel and the oxidizer are supplied. The basic physical structure or the building block of a fuel cell consists of an electrolyte layer in contact with a porous anode and cathode on either side. A simplified diagram that demonstrates how the fuel cell works is shown in Figure 1.

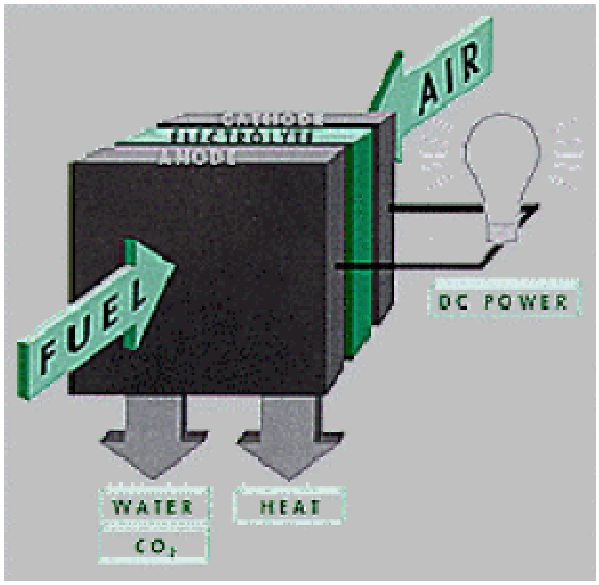

Figure 1 Simplified Fuel Cell Schema (Reprinted from Ref. [2])

The individual fuel cells can be then combined into a fuel cell "stack". The number of fuel cells in the stack determines the total voltage, and the surface area of each cell determines the total current. The total electrical power generated is then given by multiplying the voltage by the current. The different types of fuel cells can be grouped into low and high temperature applications as well as be classified by the electrolyte material used in the cell; see Table 1.

Table 1 The overview of fuel cells giving cell reactions, operating temperatures, applications, and specifications (Reprinted from Ref. [3])

Type	Temperature	Anode reaction	Cathode reaction	Applications	Advantages	Disadvantages
AFC *Alkaline*	*60-90°C*	$H_2+2OH^- \rightarrow 2H_2O + 2e^-$	$½O_2+H_2O+2e^- \rightarrow 2OH^-$	*Space shuttle*	*Simple system design*	*Not CO_2 tolerant*
PEMFC *Polymer-Exchange Membrane*	*80-110°C*	$H_2 \rightarrow 2H^+ + 2e^-$ *or* $CH_3OH+ H_2O \rightarrow CO_2 + 6H^+ + 6e^-$	$½O_2+2H^++2e^- \rightarrow H_2O$ *or* $½O_2+6H^++6e^- \rightarrow 3H_2O$	*Plug power, transport*	*Faster start-up, no leakage of electrolyte, methanol is easier to store*	*Not CO tolerant, water management problem in membranes, methanol crossover*
PAFC *Phosphoric Acid*	*160-200°C*	$H_2 \rightarrow 2H^+ + 2e^-$	$½O_2+2H^++2e^- \rightarrow H_2O$	*Heat and power plant*	*Higher operating temp, reduces CO problem*	*Liquid electrolyte leaks, lower phosphoric acid conductivity*
MCFC *Molten Carbonate*	*600-800°C*	$H_2 + CO_3^{2-} \rightarrow H_2O+ CO_2+2H^+$	$½O_2+CO_2+2e^- \rightarrow CO_3^{2-}$	*Heat and power plant*	*High efficiencies possible, internal reforming possible, CO and CO_2 tolerant*	*Longer start-up, electrolyte creep possible, NiO cathode can creep and cause short circuit*
SOFC *Solid Oxide*	*800-1000°C*	$H_2+ O^{2-} \rightarrow H_2O + 2e^-$	$½O_2+2e^- \rightarrow O^{2-}$	*Heat and power plant*	*No electrolyte creeping, high efficiencies and internal reforming possible, CO and CO_2 tolerant*	*CO and CO_2 tolerant, high operating temperatures, need different materials*

Among the different fuel cell types, the Proton Exchange Membrane Fuel Cells (PEMFC), also known as solid polymer or polymer electrolyte fuel cells, have one of the highest application prospects. The PEMFC contains an electrolyte made of a layer of a solid polymer (usually a sulfonic acid polymer, NafionTM) that allows protons to

be transmitted from one face to the other. Advantages of the PEMFC over the other types of fuel cells are a high power density and relative easy operating conditions.

One type of the PEMFC´s is the Direct Methanol Fuel Cell (DMFC) where a polymer membrane serves as an electrolyte in which methanol is used instead of hydrogen. Here, methanol is applied directly in the fuel cell, in contrast to the indirect methanol fuel cell, where methanol is first reformed to hydrogen. In both fuel cell types, the main product of this reaction is carbon dioxide, although in some cases other oxidation products, such as formaldehyde, formic acid, etc. could be formed as side products which may be short-lived. In some cases, also the intermediate products can be identified, for example by IR spectroscopy or differential electrochemical mass spectrometry. The overall methanol oxidation to carbon dioxide releases six electrons; hence, the specific energy of methanol is close to 0.84 A h g^{-1} [4].

A major problem in DMFC is the contamination of a pure Pt anode catalyst by even trace levels of carbon monoxide (CO), less than 10 ppm from the reformed gas, which leads to reduced performance and damage of catalytic materials within the cell. One possibility to hinder the "so called" poisoning of the anode is to change the properties of platinum by an alloying of the Pt electrode with other metals, so that CO is oxidized directly to CO_2 under the fuel cell operational conditions.

A possible alternative to decrease the poisoning by adsorbed CO is the use of Pt alloyed with elements such as ruthenium (Ru), osmium (Os), tin (Sn), molybdenum (Mo), rhenium (Re), bismuth (Bi), palladium (Pd) and others, which have been found to have a positive effect on the catalytic activity towards methanol oxidation. The utilization of these elements can promote the electrocatalytical oxidation of CO at less positive potentials than on pure platinum, thanks to the formation of OH^- species on the secondary metal at potentials lower than on Pt. The enhanced catalytic activity of such modified surfaces in comparison to pure platinum surfaces is usually ascribed to two effects or their combination:

1) the bifunctional mechanism, where the unique catalytic properties of each of the elements are combined in a synergic fashion to yield a surface which is more active than each of the elements alone [5], and
2) the ligand or the electronic effect, in which one of the elements alters the electronic properties of the other, thus yielding a more active catalytic surface.

Nevertheless, the optimal alloy composition and the mechanistic role of the co-catalysts are still a subject of ongoing research and discussion.

Other factors which influence the catalytic activity of the electrode are the support, the ionomer content in the active layer, the preparation method, and the fuel feed.

It is obvious that the use of carbon supported nanoparticle catalysts in fuel cells is advantageous because of their large surface to volume ratio. However, also the fundamental physical and chemical properties of such nanoparticles are remarkably altered as the particle size changes [6-13].

Amongst other, the main objective of the present work is the characterization of platinum-based nanoparticle electrodes with a low amount of platinum ($10 \mu g_{Pt}\ cm^{-2}$) with respect to its real surface area. The oxidation behavior of CO adsorbed at different platinum based nanoparticle electrodes, polycrystalline platinum and at Pt(665), had been studied by the Differential Electrochemical Mass Spectrometry (DEMS). Furthermore, the effect of the modification of Pt surfaces with Ru ad-atoms is also investigated. The model bimetallic catalyst surfaces were prepared by depositing submonolayers of Ru on platinum nanoparticle electrodes, polycrystalline Pt and Pt(665). In this study, some binary (PtRu) and quarternary (PtRuOsIr) alloyed catalysts are also investigated.

In the case of the methanol oxidation reaction the validity of a parallel path mechanism on different platinum based surfaces is proven. Although formaldehyde and formic acid cannot be directly detected by DEMS, using a dual thin layer flow through cell the formation rate of CO_2 can be quantitatively detected. In addition, the current efficiencies for CO_2 during methanol oxidation, the formation rate of CO_{ad} and maximum coverage of CO_{ad} adsorbed during methanol oxidation at different potentials are investigated on different Pt surfaces.

In addition, the combination of the DEMS and the isotopic labeling with ^{13}C was used to investigate the behavior of methanol and CO adsorbates at different surfaces: (1) monometallic - pure polycrystalline Pt, Pt(665) and Pt nanoparticle electrode (2) bimetallic - Ru modified polycrystalline Pt, Pt(665) and Pt colloidal nanoparticles and (3) trimetallic – Ru and Mo modified Pt nanoparticles.

Furthermore, the temperature dependence of the CO and methanol oxidation presented in this study is also of interest.

Chapter 1 Fundamentals

In this chapter, fundamentals of used electrochemical methods and DEMS, as well as metallic nanoparticles and single crystal surfaces, are described. The carbon monoxide and methanol adsorption/oxidation reactions will be reviewed from the literature.

1.1. CYCLIC VOLTAMMETRY, CHRONOAMPEROMETRY AND CHRONOPOTENTIOMETRY

The voltammetry (advanced by Nobel Prize winner Jaroslav Heyrovsky) is one of many methods in the electrochemistry used for the study of electrode processes, e.g. adsorption, desorption or the rate of the electron transfer. In such experiments the kinetic or mechanistic information are obtained from current or potential measurements. In this study chronoamperometry [14], chronopotentiometry and cyclic voltammetry (CV) [15-18] were used. These methods use a three electrode configuration – reference, counter and working - controlled by a potentiostat. The measuring program is regulated by a function generator.

The chronopotentiometry is a galvanostatic method, in which the current flowing through the cell is stepped instantaneously from zero to a finite value and the potential of the working electrode is monitored as it relaxes towards its new steady state. The chronoamperometry is a potentiostatic experiment analogous to the chronopotentiometry. In this kind of experiments, the response of the current is monitored as the potential of the working electrode is changed.

In contrast, the cyclic voltammetry belongs to the potentiodynamic techniques. Here the potential of the working electrode (in our cases Pt-based electrodes) is changed as a linear function of time from one potential limit to the other and back. Its response (a current flowing through the working electrode) is monitored as a function of the applied potential (so called cyclic voltammogram, CV). The rate of the change of the potential with time is denoted as a scan rate. The overall shape of the curve gives details of the electrode process kinetics. The change in the shape, as the rate of the potential change is altered, gives information on the rates of the involved process.

1.2. DIFFERENTIAL ELECTROCHEMICAL MASS SPECTROMETRY

DEMS is an experimental method, which combines the electrochemical methods with a parallel mass spectrometric *"on-line"* analysis of volatile reaction products and intermediates produced at the working electrode. This technique was initially

developed by Bruckenstein and Gadde in early seventies as Electrochemical Mass Spectroscopy (EMS) [19] and later modified and perfected by Wolter and Heitbaum in 1984 [20]. Using a turbomolecular pump system including two pumping stages, the time response becomes short enough to allow a rapid introduction of volatile electrochemical reaction products into the ionisation chamber. In order to emphasize the method from a product sampling, i.e. integrating approaches, this technique was called Differential Electrochemical Mass Spectroscopy (DEMS).

In DEMS experiments, during the electrochemical experiment (cyclic voltammetry, potential or galvanic step), the ion current corresponding to a given specie of interest is recorded mass spectrometrically in parallel to the faradaic electrode current (or the potential in the case of chronopotentiometry). Our instrument allows the simultaneous detection of up to 30 different masses. These ions are collected with a dwell time τ (~ 10 ms to 5 s). This constant should be small enough, so that for each mass fragment the potential resolution is better than 5 mV (τ depends also on the number of used mass channels).

1.2.1. Construction of DEMS

The whole experimental setup can be divided into two main devices; the electrochemical and the mass-spectrometrical part.

The electrochemical unit consists of an electrochemical cell, a potentiostat and a function generator. The details of the electrochemical cell will be discussed in Chapter 1.2.2. A home build potentiostat, a home build function generator and a home build jump generator (Institute of physical and theoretical Chemistry, University of Bonn) were used for the potentiodynamic experiments in contrast to the potentiostatic and galvanostatic experiments, where a combined potentiostat/galvanostat from EG&G (model 273) was used.

The mass-spectrometrical device is composed of a vacuum system, a quadrupole mass spectrometer (Balzers QMG-422), a pressure control unit as well as an electronic control unit. Figure 1-1 shows the vacuum system used in this study. It consists of two vacuum chambers connected in series and is described in detail in Ref.[21].

The vacuum is generated by a turbomolecular pump (2) TPU 261 (10^{-4} mbar) on the main chamber and by TPU 072 (10^{-5} mbar) on the rod system of the mass spectrometer. Both turbomolecular pumps are pre-evacuated with a common rotary pump (1) DUO 016B. On the first chamber, a valve for connection to

the electrochemical cell (3) and also a calibration leak valve (4) are situated. On the boundary between these two chambers the entrance to the Electron Ionisation (EI) chamber of the mass spectrometer (5) is situated. In our case a crossbeam ion source is used for the ionisation of the analyte. The electron beam (usually 70 eV energy) is produced by filaments (rhenium or tungsten wires) and the emission current is fixed at 0.7 mA (max. 1.5 mA). Here also a direct inlet (8) to the mass spectrometer is situated.

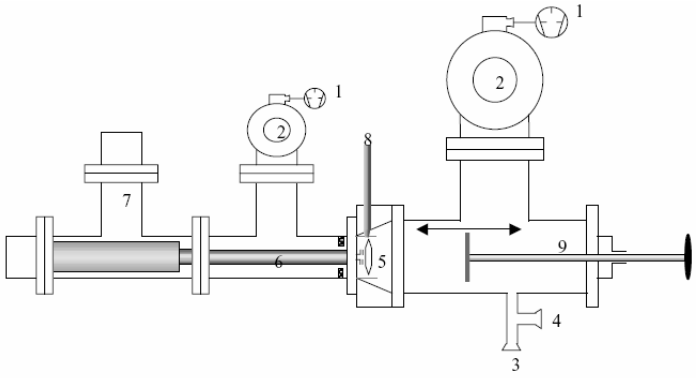

1. *rotary pumps*
2. *turbomolecular pumps;*
3. *convection to the electrochemical cell*
4. *connection to the calibration leak*
5. *ion source*
6. *quadrupol rods*
7. *secondary electron multiplier*
8. *direct inlet*
9. *linear drive*

Figure 1-1 Vacuum system

The second chamber includes quadrupole rods (6) and a detector. A quadrupole mass analyzer is essentially a mass selective filter based on mass-to-charge ratio of sampled ions. In fact, the number of ions leaving the mass analyzer is usually quite small, so that the use of Secondary Electron Multiplier (7) (SEM, Type 217 with Cu-Be dynodes) besides a standard faraday cup is necessary to get a good signal.

1.2.2. DEMS Cell

The electrochemical cell is also a very important part of the whole DEMS setup. In all measurements presented in this work, which were done under continuous electrolyte flow, the so called "dual thin layer flow-through cell", initially designed by Jusys et al. [22], was used. This cell (see Figure 1-2) consists of two separate compartments: an electrochemical compartment with an electrolyte inlet, where the faradaic reactions take place, and a mass spectrometric compartment with an electrolyte outlet.

The species produced in the first compartment are transported through six capillaries (11) to the second compartment, where the volatile ones can evaporate into the mass spectrometer and are measured as an ion current. The electrolyte volume and the geometric surface area (0.283 cm^2) of the working electrode (3) are defined by a thin (ca 100 μm) PTFE ring (4) on the disc shaped working electrode. Due to

the fact that the IR drop in the electrolyte thin layer is large, the use of two counter electrodes is advantageous. One of the counter electrodes is positioned on the input of the inlet capillary together with a reference electrode (here a Reversible Hydrogen Electrode, RHE) and an entrance for a syringe. The syringe serves for an injection of the CO saturated solution into the cell. The second counter electrode is placed on the outlet together with a peristaltic pump, which allows an electrolyte flow at a constant rate.

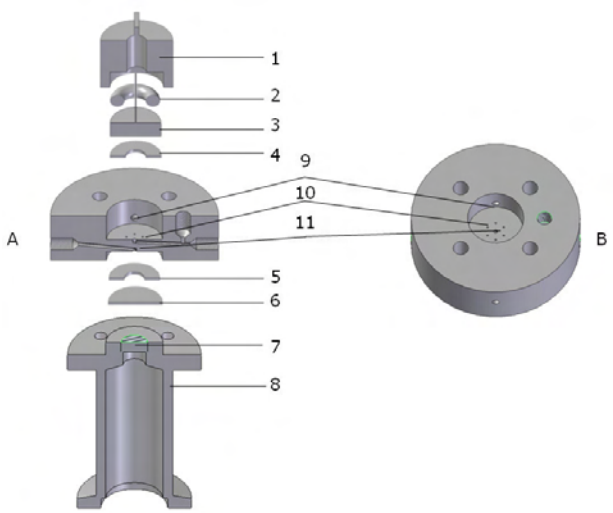

´A) side view of Kel-F body of the cell
´B) top view of the cell
1. *Kel-F holder*
2. *Kalrez gasket*
3. *electrode*
4. *and 5. Teflon spacer*
6. *porous Teflon membrane*
7. *stainless steel frit*
8. *stainless steel connection to the vacuum system and the mass spectrometer*
9. *capillaries for flushing with Ar*
10. *inlet-out-let capillaries*
11. *connecting capillaries*

Figure 1-2 Dual thin layer flow-through cell

A disadvantage of this cell is that, depending on the flow rate, a notable fraction of the product is transported out of the cell volume and lost due to the fact that the convective transport parallel to the electrode/membrane is faster than the diffusive transport perpendicular to the electrode/membrane.

1.2.3. Calibration of DEMS

Not only the qualitative detection of the volatile electrochemical products, but also the determination of the amount of these products or its formation rate, is possible with DEMS. To convert the ion currents determined by DEMS to the amount of species, the mass spectrometer needs to be calibrated under the same experimental conditions.

In general, for the calibration of the mass spectrometer two different methods can be used:

a) a direct calibration using a calibration leak (K^o)

By this external calibration a definite volume of a calibration gas probe is introduced through the calibration leak valve (position 4 in Figure 1-1) directly into the mass spectrometer. The calibration leak is in detail described in Ref. [23].

According to the ideal gas law, from the decrease of the pressure measured in the calibration valve (*dp/dt*, usually 10^{-3} mbar s^{-1}), the flow rate of species entering the mass spectrometer (*dn/dt* ≈ 10^{-9} mol s^{-1}) can be determined.

The mass spectrometrically determined ion current of the corresponding species, I_i, is therefore proportional to the calibration constant K^o and the flow rate of species entering the mass spectrometer:

$$I_i = K^0 \frac{dn_i}{dt} \qquad \text{(Equation 1-1)}$$

The slope of the correlation of the measured ion current with the flow rate of species from the calibration leak volume into the vacuum system gives (according to Equation 1-1) the value of K^o for the measured species. K^o contains all settings of the vacuum system and the mass spectrometer, e.g. emission current, pressure in the vacuum or temperature, and also the ionisation probability of the corresponding species.

This kind of calibration can be used for all gaseous and liquid substances with a vapour pressure above 10 mbar.

b) an indirect calibration using an electrochemical reaction (K^*)

In contrast to the direct calibration using the calibration leak, the indirect calibration is possible when using a known electrochemical reaction with a current efficiency of 100%, e.g. the oxidation of adsorbed carbon monoxide (CO) to carbon dioxide (CO_2) on a platinum surface [20]. In this case, the integrated faradaic oxidation current, Q_f^{total}, and the integrated ion current for CO_2, Q_i^{44}, have to be used for the determination of K^* (Equation 1-2). The faradaic charge for the oxidation of CO on platinum electrodes contains about 20% of a non faradaic charge, mainly caused by the different double layer charge in the region from 350 to 1000 mV with and without CO, and additionally due to the shift of the point of zero charge due to the CO adsorption [24-26], therefore

$$K^* = \frac{Q_i^{44} \cdot z}{Q_f} = \frac{Q_i^{44} \cdot z}{0.8 \cdot Q_f^{total}} \qquad \text{(Equation 1-2)}$$

where Q_i^{44} is the integrated ion current of the corresponding species; Q_f is the effective faradaic charge (i.e., non-faradaic charge is corrected by factor of 0.8); z is the number of electrons transferred during the electrochemical reaction and K^* is the calibration constant.

Contrary to the calibration through the calibration leak, using the internal calibration a part of the produced species doesn´t enter the vacuum system. Therefore the external calibration constant, K^o, and the internal calibration constant, K^*, are different. They are related by the transfer efficiency, N. The transfer efficiency is given by the ratio of the amount of the mass spectrometrically detected species, n_i, and the total amount of species produced electrochemically, n_f:

$$N = \frac{n_i}{n_f} \qquad \text{(Equation 1-3)}$$

and

$$K^0 = \frac{K^* \cdot F}{N} \qquad \text{(Equation 1-4)}$$

where F is the Faraday constant and N is the transfer efficiency of used cell.

When using the one compartment thin layer cell, "under stopped-flow" conditions almost all produced volatile species access the vacuum system, N=1. In this study, the dual thin layer flow-through cell was used all the time. In this case, under the continuous flow, the value of N is dependent on the flow rate of the electrolyte and varies between $0<N<1$ [23, 27].

In order to register possible changes in the sensitivity of the mass spectrometer, the calibration constant K^* should be measured several times during the day.

1.3. PLATINUM SURFACES

In technological applications, platinum is a widely used catalyst material. The platinum surfaces can be used either in a massive form (e.g., single crystal electrodes) or in a finely divided form (e.g., supported metal catalysts). For many electrochemical and electrocatalytical processes the surface structure is crucial.

1.3.1. Single crystal surfaces

Due to the known regular surface geometry, Pt single crystal electrodes are suited model systems for the analysis of the relationship between the surface structure and the surface reactivity.

The crystal itself is composed of regularly repeating structural motives (e.g., atoms). In the ideal case, the space lattice three-dimensional infinite array of atoms is surrounded in an identical way by its neighbours with a periodicity free from defects. The crystal structure itself is obtained by associating with each lattice point into an identical structural motive. The orientation of a surface or a crystal plane is usually defined by considering how the plane (or indeed any parallel plane) intersects the main crystallographic axes of the solid using the Miller Indices, (hkl). Platinum is a metal having the face centred cubic (fcc) structure, where the planes with the lowest indexes are the (111), (110) and (100) faces free of steps (Figure 1-3).

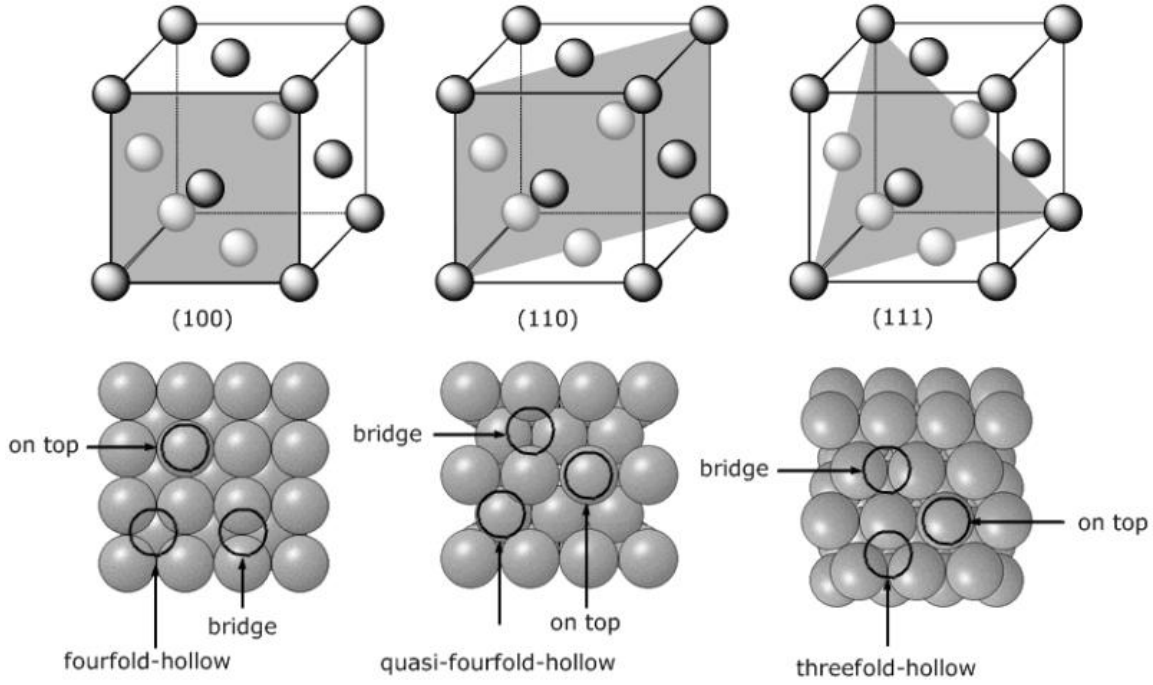

Figure 1-3 Fcc(100), fcc(110) and fcc(111) planes in three dimensions, their Miller indices and the corresponding top views of the surface structures

The atomic structure of the Pt(665) surface, used in this work, is composed of terraces and steps, and belongs to high-index-surfaces (denoted as vicinal stepped surfaces), where the Miller indices are relatively large. Inversely, it is difficult to determine the Miller indices from the atomic surface structures even with known average concentrations of terraces, steps and kinks. Therefore, a new nomenclature, the so called "step notation", has been developed by Lang et al. [28], which directly declare the width and the orientation of the terraces as well as the height and the orientation of the steps. In our case, Pt(665) is denoted as Pt(S)-[12(111)x(111)], which means a terrace width of 12 atoms with (111) orientation of the atoms in this terrace, and a local orientation of the one atom high step with (111) geometry. A model of the Pt(665) surface is shown in Figure 1-4.

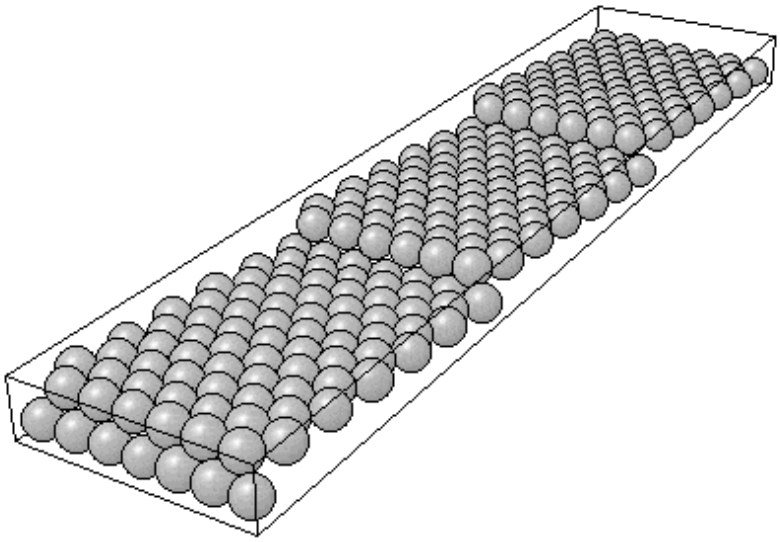

Figure 1-4 Surface structure of Pt (665) stepped single crystal

A such stepped surface contains sites with different physical and chemical properties which can be distinguished, for example electrochemically due to different adsorption of hydrogen on the terraces and on the steps [29].

Generally, the ordered Pt(111) and Pt(100) vicinal surfaces ((111) or (100) terrace separated by one atom height steps) appear to be the stable surface structures of many high-Miller-index surfaces. The preparation of well-ordered and clean sample surfaces was initially obtained only in an ultra-high vacuum (UHV) chamber [30, 31].

A major break-through was achieved in 1980 by Clavilier et al. [32, 33], who demonstrated that also under atmospheric conditions a simple and very convenient flame-annealing and quenching method can be used to prepare well-ordered single crystal surfaces. Immediately after the flame-annealing treatment, the hot crystals were quenched in water and so the danger of a surface contamination was minimized. Later, in order to avoid strains in the crystal structure and surface defects caused due to the rapid cooling [34], an intermediate cooling step [35, 36] was introduced to this method.

Different stepped surfaces were systematically studied by cyclic voltammetry. In particular, through the extensive work of Clavilier et al. [32, 37-39], the different single crystal platinum surfaces were investigated, and the relationship between the hydrogen adsorption-desorption and the Pt single crystal surface structure was quantitatively analyzed. The experimental results have shown that the structure sensitive hydrogen adsorption/desorption varies systematically with changing of the indices, and that such voltammograms can be used as a reference for in situ

surface characterization. Such a general survey of voltammograms for various surfaces of platinum single crystals is depicted in Figure 1-5.

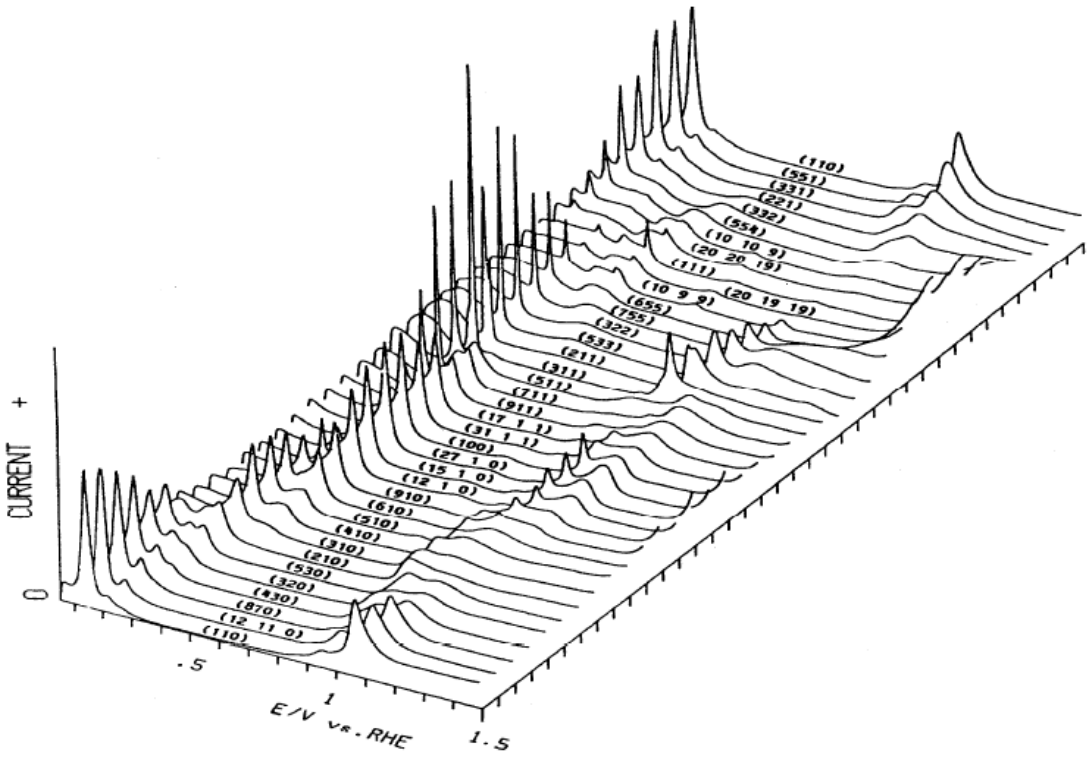

Figure 1-5 Voltammograms of different surfaces consisting of steps and terraces (Reprinted from Ref. [29])

In order to avoid an oxygen adsorption, which has been shown to cause disordering on Pt stepped surfaces, it is important to fix the upper potential limit at/below 900 mV [35, 40].

The opposite of a single crystal structure is a polycrystalline platinum, which is made up of a number of smaller crystals within a certain structure. The polycrystalline surface has a large quantity of different adsorption places, the reactions (a hydrogen adsorption/desorption) take place in parallel and therefore it is not possible to distinguish between them.

1.3.2. Nanoparticle surfaces

In the case of nanoparticle catalysts, there is no simple ideal structure modelling all aspects of nanoparticle catalysts, but some types of highly facetted metallic nanoparticles can be described using well-characterized single crystal surfaces. The equilibrium morphology of a three dimensional (3D) free nanoparticle is determined by the Wulff rule [41]. The shape of the nanoparticle is assumed to be a truncated octahedron (Figure 1-6), having eight hexagonal facets of a (111) orientation and six square facets of a (100) orientation [42] and Ref.[10] in [43].

This facets are bounded by edge atom rows that are similar to the topmost rows in the (110) surface. The regular polyhedron shapes are valid only at 0 K, where the surface energy anisotropy is maximal.

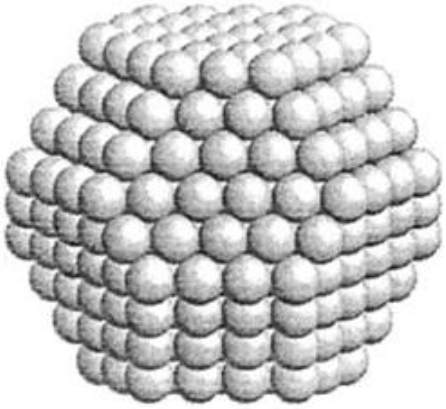

Figure 1-6 Wulff construction for a typical fcc metal, a truncated octahedron (Reprinted from ref. [44])

In practice, the nanoparticles must be supported and the interface with the support needs to be included into the Wulff approach. This problem of the equilibrium shape of supported catalysts was first solved by Kaishew (see [43] and citations therein) and it is known as the Wulff-Kaishew theorem, where the equilibrium shape of such supported metals is defined by the surface energy of the facets and the interaction with the substrate as quantified by the adhesion energy:

$$\frac{\Delta h_s}{h_i} = \frac{E_{adh}}{\gamma_i} \qquad \text{(Equation 1-5)}$$

The Wulff shape (see Figure 1-7) is truncated at the interface by the amount Δh_s. h_i is the central distance to the facet parallel to the interface and γ_i is the corresponding surface energy. The adhesion energy, E_{adh}, (≈ the work of adhesion) is equal to the work necessary to separate the crystal from the support by an infinite distance. When the adhesion energy is two times larger than the surface energy γ_i, $\Delta h_s = 2h_i$, it is like the crystal has sunk into the substrate. In fact, that means that the crystal is a 2D layer on the substrate; it corresponds to a perfect wetting. Detailed studies of the morphology and the equilibrium shape of supported nanocrystals were published by Müller et al. [45-47] and by Henry et al. [43, 48].

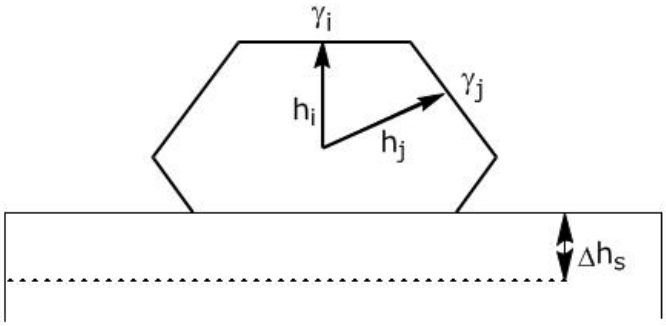

Figure 1-7 Schematic representation of the equilibrium shape of a supported crystal [43]

The preparation methods of metal nanoparticles could be separated into two main classes: (a) the physical deposition and (b) the chemical synthesis.

One of the physical methods is the metal evaporation [49-52], where the metal is heated by a plasma, a resistive heating or an electron bombardment and thereby evaporated. The agglomeration can be avoided by using suited surfactants. Otherwise, laser ablation methods [53-55] are also very often used.

Chemical syntheses are more convenient because the size, the shape and the composition of the produced nanoparticles can be controlled more easily. Common strategies involve the reduction of metal salts in the presence of organic surfactants (e.g., ligands, polymers and tensides). Besides electrochemical methods [56-58] also a hydrazine [59], carboxylates [60], aldehydes [61], solvated electrons [62] and others can be used as the reducing agents.

The carbon supported colloidal nanoparticles used in this work were obtained from the MPI in Mülheim (M. Lopez and M. Reetz) [56, 63]. For the fabrication of these nanoparticles a base induced hydrolysis/condensation of precious metal salts in the presence of suitable surfactants was used. This method, pictured in Figure 1-8, gives rise to the preparation of particles with a high degree of a dispersion and a narrow size distribution [63, 64].

$$M_1L_a + M_2L_b + M_3L_c + M_4L_d + H_2O \xrightarrow{\text{Surfactant}} [M_1M_2M_3M_4Ox]\,[\text{Surfactant}] \quad \text{(Equation 1-6)}$$

metal M: Pt, Ru, Os, Ir, Mo, W, Sn, Fe etc.
surfactant: sulfobetaines, carbobetaines, polyoxyethylenesters, Nafion®

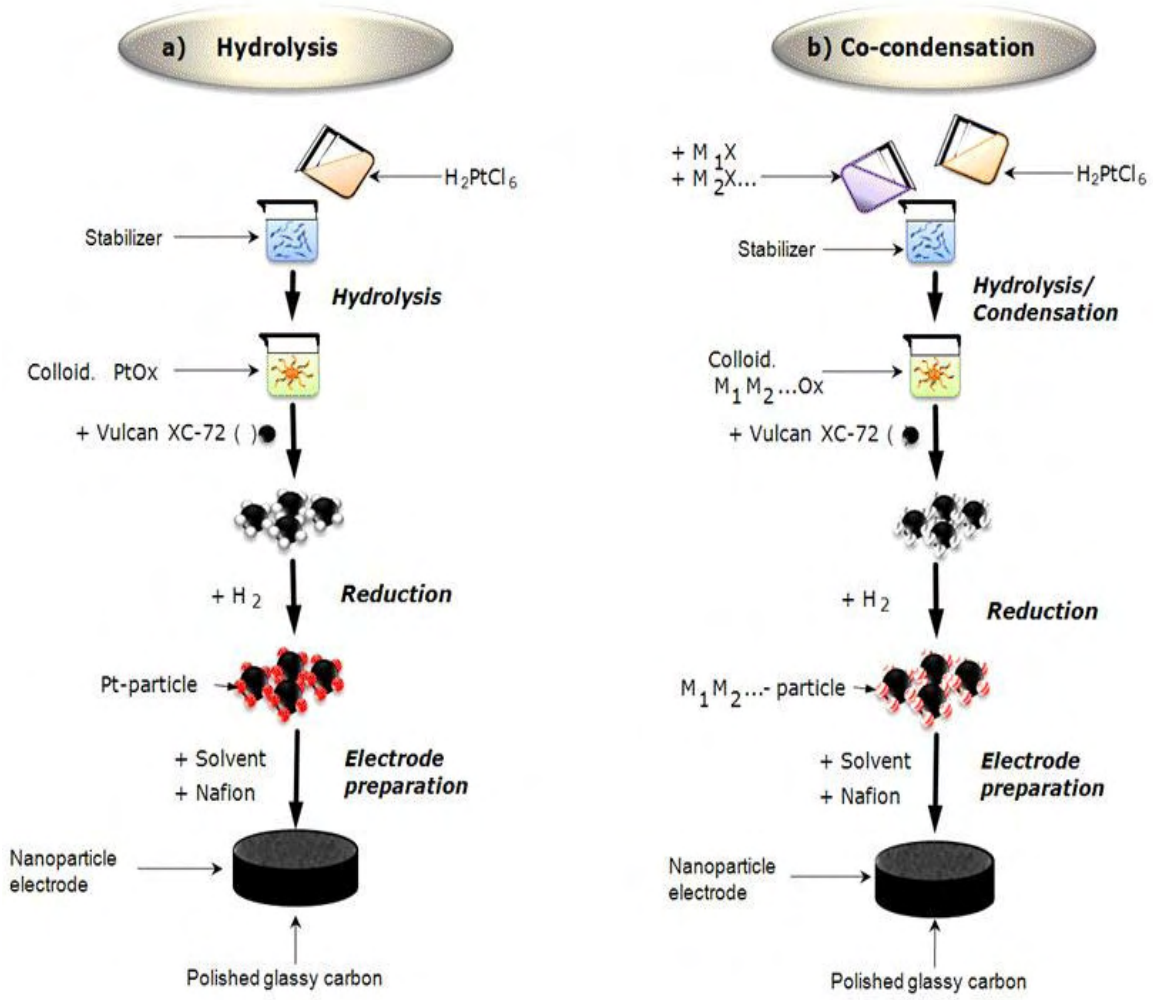

Figure 1-8 Fabrication methods of platinum-based nanoparticles

This concept of the co-condensation can be used for the preparation of very well defined colloidal multi-metallic oxide nanoparticles (Figure 1-9).

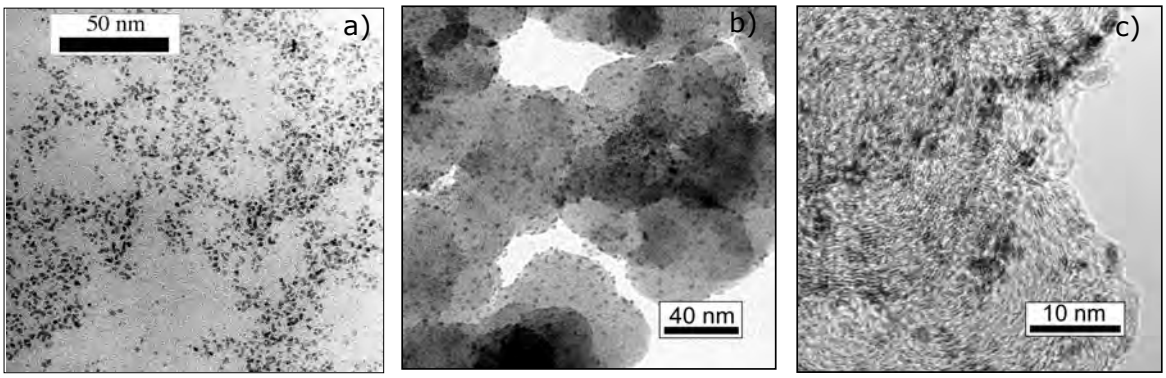

Figure 1-9 TEM- images of some Platinum-based nanoparticles: a) $PtRuOsIrO_x$ (d=1.6 ± 0.3 nm), b) $PtRuO_x$ on Vulcan XC-72(d=1.8 ± 0.4 nm) and c) PtO_x (d=1.6 ± 0.3 nm)

The metal composition of the nanoparticles is controlled by using defined ratios of the metal precursors. In the next step, such pre-catalysts are immobilized on high surface area substrates. All the nanoparticle catalysts used in this work were supported on Vulcan XC-72. An undesired particle agglomeration is not observed, due to the rapid immobilization of the colloids.

The deposition of such platinum-based nanocatalysts onto a glassy carbon substrate will be described in detail in the experimental part (Chapter 2.3.1).

1.4. MODIFICATION OF PLATINUM SURFACES

As mentioned above, the poisoning of the pure Pt catalyst by CO is the substantial problem in DMFC. In order to overcome this effect, the modification of the Pt electrode with submonolayers of foreign metal ad-atoms (e.g., Ru, Mo) and its influence on the catalytic activities have been studied for very long time.

Modified Pt surfaces can be produced by the preparation of alloy nanoparticles (see above) or by methods like a spontaneous deposition [65-77], an electrodeposition [65, 78-81] or a metal vapour deposition [82-85].

1.4.1. Submonolayer deposition of ruthenium

Extensive studies of the potentiostatic deposition of ruthenium on polycrystalline platinum and Pt(111) were performed using X-ray photoelectron spectroscopy (XPS), Scanning Tunnelling Microscopy (STM) and IR spectroscopy by Stimming et al. [78-81]. The chemical modification by the electrochemical deposition of Ru was performed from acidic solutions of $RuCl_3$ over a wide range of deposition potentials. It was found that at potentials below 250 mV a massive nucleation and growth of the Ru metal occur. In the potential range between 300 and 800 mV (vs. RHE) the submonolayer deposition takes place. Such Ru islands have a monoatomic height and a diameter of about 3 nm. At potentials above 900 mV no Ru deposition was observed. The surface coverage as well as the density of islands on the platinum surface depend strongly on the deposition potential; both increase with decreasing potential (see Figure 1-10).

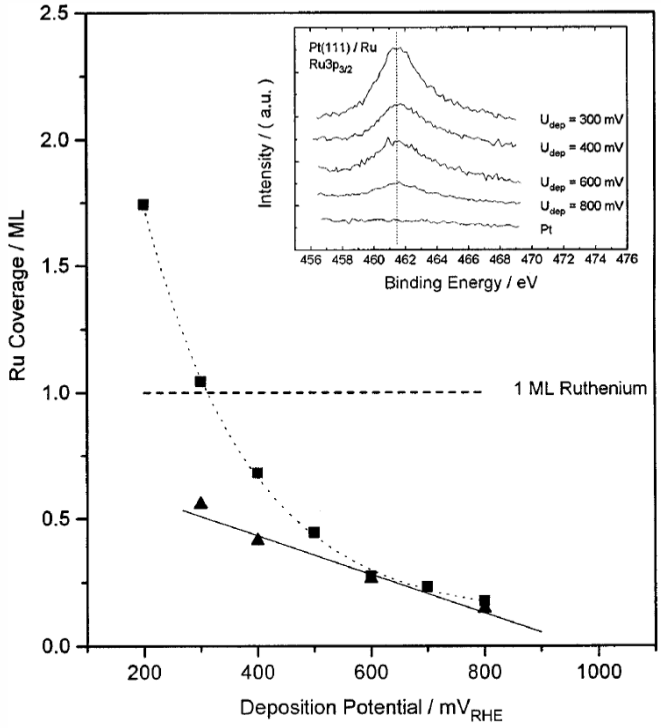

Figure 1-10 Ru coverage determined by XPS as a function of deposition potential for polycrystalline Pt (squares) and Pt (111) (triangles). The insert shows the XPS spectra (Ru 3p3/2 emission) of Ru-modified Pt(111) at various deposition potentials. (Reprinted from ref. [78])

The spontaneous deposition ("open-circuit" conditions) of ruthenium on low-index platinum electrodes was essentially studied by Chrzanowski et al. [67-69, 86]. It was found that the coverage of the spontaneously deposited ruthenium depends strongly on the surface structure. Under these condition, the highest coverage was achieved on Pt(100) whereas the declining coverage order (0.24 > 0.10 > 0.05) is Pt(100) > Pt(111) > Pt(110).

„Ex-situ"-STM experiments also showed that the coverage of Ru on Pt(111) by the spontaneous deposition amounts to 20% [66, 70]. The array of the Ru islands was found to be largely of a monatomic height, but a fraction of the islands, ca. 10% of the total ruthenium deposit, forms a second layer over the inner layer. In further research by Crown et al. [71, 74] the deposition time was varied between 10 and 150 seconds also on Pt(110) and Pt(100) (Figure 1-11). The ruthenium islands were found to be uniformly distributed across the surface, without a preference toward the step edges. At Pt(100) the formed islands were roughly the same size as those found on the Pt(111) surface and the maximum coverage was achieved after 90 s (21%) with 7% of the ruthenium coverage as bi-layer islands. In the case of Pt(110) the ruthenium coverage increased slowly and steadily with the time to its maximum

0.10 ML at 150 s. Formation of the second layer was observed above 90 s of the deposition, comprising only 5% of the total ruthenium coverage.

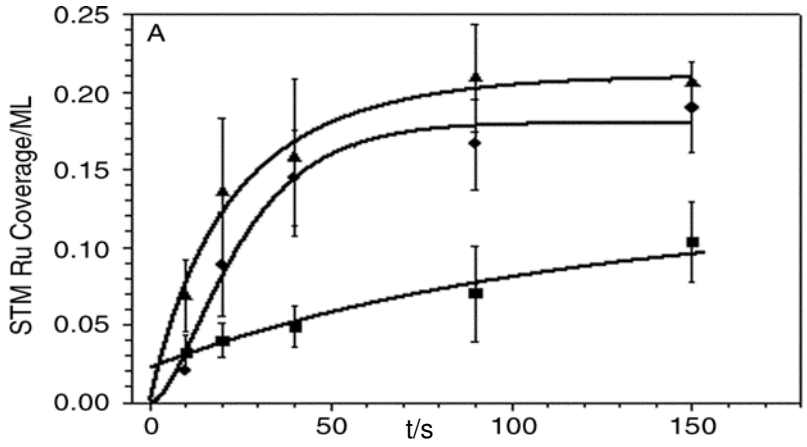

Figure 1-11 Coverage values obtained using STM vs. deposition time for Pt(hkl)/Ru. Pt(100)-triangles, Pt(111)-circles, Pt(110)-squares. Data points represent an average of at least 4 separate images taken on various areas of the crystal. [71]

In the special case of a repeating deposition (4-times) of ruthenium on Pt(111), the surface coverage was slightly increased to 30–35% with 2-12 nm large ruthenium islands of varying heights but still homogeneously distributed over the platinum surface. 65% of the island fraction were of a monolayer height, 25% islands consisted of two layers and about 10% were 3 ML or higher. On Pt(100) and Pt(110), the formation of the 2nd and 3rd layer was much lower.

Samjeske et al. [87, 88] have investigated the Ru deposition on stepped Pt single crystals, especially on Pt(111), Pt(332) and Pt(665). They found that it is possible to deposit Ru at the monoatomic steps of stepped Pt surfaces, which leads to a surface with a known atomic arrangement of constituents. This facilitates the fundamental understanding of electrocatalytic processes on Pt-Ru surfaces.

Both, the spontaneous [65, 73, 89] and the electrochemical deposition of Ru [65, 89, 90] can be also used for decoration of the carbon supported Pt nanoparticles, similarly to the platinum single crystals. Too little is known about the structure of such nanoparticle deposits due to the fact that it is very difficult to carry out STM, LEED, LEIS and AES experiments on such colloidal nanoparticles. Maillard et al. [65] estimated the Ru coverage by cyclic voltammetry. In the case of the spontaneous deposition, saturation coverage of ca. 22%, as opposed to 46% in the case of the electrochemical deposition, was observed.

1.4.2. Submonolayer deposition of molybdenum

Many studies which are engaged in the modification of the platinum surface with molybdenum and its catalytic effect were inspired by the work of Shropshire [91], who, for the first time, used the molybdates as a catalyst for the methanol oxidation just by adding Na_2MoO_4 into the methanol solution. He ascribed the catalysis to the Mo(IV)/Mo(V) couple. Recently, Li et al. [92] reported similar results for different concentrations of acidic media.

Kita et al. [93-95] have studied the electrochemical deposition of molybdenum at platinized platinum electrodes. Using XPS and an extended analysis of voltammograms it was observed that the methanol oxidation is catalyzed by the adsorbed Mo(IV)/Mo(III) redox couple. In contrast to Shropshire´s conclusions, Mo(VI) is found to be catalytically inactive.

Samjeske et al. [88, 96] studied the co-catalytic effect of Mo on the oxidation of adsorbed CO on Pt(111), Pt(332) and porous polycrystalline Pt electrodes. Also here, the Mo surface composition was determined by XPS. The authors estimated a number of approximately six electrons per adsorbed Mo atom on Pt(111). From this it follows that the oxidation state of Mo is zero in the hydrogen adsorption region; Mo is in its metallic state on the surface. Positive of the maximum oxidation peak at 420 mV it is in oxidation state +VI.

1.4.3. Submonolayer deposition of selenium

Also the electrocatalytic action of Se ad-atoms deposited on Pt, Ru or Pt-Ru surfaces has long become the topic of a large body of research [97-103]. Feliu et al. [101-103] showed that Pt(111) can be irreversibly modified by selenium up to a coverage of about 0.5 (UHV conditions). Using the spontaneous deposition by an immersion of Pt electrodes in Se(IV) containing solution, it was possible to get different coverages. At a coverage of about 0.33 the hydrogen adsorption was completely inhibited (the whole surface was blocked by Se). In the case of Pt(111), the formation of Se^0 ad-layers, which undergo a surface redox process involving 4 electrons per Se ad-atom, was found. It is suggested that each Se ad-atom blocks three substrate adsorption sites. The voltammetric profiles of Pt(332) = [6(111)x(111)] and Pt(755) = [6(111)x(100)] partially covered with Se, show that the Se does not preferentially adsorb on the Pt(110) step sites. This was also confirmed on Pt(110) and Pt(100) electrode surfaces where SeO_2 ad-layers were dissolved without any evidence of $Se(IV)_{ads}$ stabilization. It is assumed that the simultaneous oxidation of platinum substrate may be responsible for the faster formation of soluble Se(IV)

species in relation to the well ordered Pt(111), where the oxide formation does not occurs so easily.

Kiskinova et al. [104] determined the structure of the Se ad-layers on Pt(111) surfaces. The LEED patterns showed formation of a p(2x2) structure at low Se coverages, while with the increasing coverage a ($\sqrt{3}$x$\sqrt{3}$)R30° structure was formed and at the maximum coverage of 0.5, an ordered (4x4) pattern was also observed.

1.5. ELECTROCATALYTIC OXIDATION OF CARBON MONOXIDE

The electrooxidation of carbon monoxide on platinum in aqueous acidic electrolytes is one of the most extensively studied electrochemical reactions over the past decades. The main interest is centred on two practical problems pertaining to the application of platinum based catalysts; (i) the search for catalysts for DMFC´s and (ii) the development of CO-tolerant anodes for the H_2/O_2 acid fuel cells. For both types of fuel cells, it is essential to oxidize and remove CO from the platinum surface at lower overpotentials.

1.5.1. Mechanism of the oxidation of carbon monoxide

It is generally accepted that under chemical as well as electrochemical conditions, the electrooxidation of adsorbed CO occurs *via* a Langmuir-Hinshelwood mechanism, where the adsorbed CO reacts with oxygen containing species present on the surface. According to the present understanding, the overall reaction mechanism on pure platinum can be represented by equations:

$$H_2O + *Pt \Leftrightarrow OH_{ads,Pt} + H^+ + e^- \qquad \text{(Equation 1-7)}$$

$$CO_{ads,Pt} + OH_{ads,Pt} \Rightarrow CO_2 + H^+ + e^- + 2\ *Pt \qquad \text{(Equation 1-8)}$$

where the formation of adsorbed (denoted by "$_{ads}$") hydroxyl in the first step (Equation 1-7) involves the adsorption to a free site (denoted by "*"). This site becomes free again in the second step (Equation 1-8). May the second step occur, adsorbed CO as well as adsorbed hydroxyl must be adsorbed at adjanced sites, which implies the mobility of at least one of these two adsorbates. One molecule of CO_2, two protons, two electrons as well as two free adsorption sites are formed according to the Langmuir-Hinshelwood mechanism.

1.5.2. Oxidation of carbon monoxide on pure platinum surfaces

The electrooxidation of CO adsorbed on different platinum surfaces was extensively investigated by many groups, for example [105-110]. Therefore, only a short

overview for the CO-oxidation in CO-free sulfuric acid will be given in the following part.

1.5.2.1. Massive electrodes

The mechanism of the CO adsorption/oxidation on polyoriented platinum was intensively investigated by different techniques for more than half a century [111-115]. Due to the adsorption of CO on the platinum surface, the hydrogen adsorption sites can be completely blocked (depending on the adsorption potential) [116, 117]. CO is then oxidized during a potential sweep to CO_2 in a well defined small peak below 600 mV, so called "pre-peak", and a main oxidation peak at about 700 mV [106].

The potential dependence of the saturation coverage of carbon monoxide on Pt(pc), Pt(111) and Pt(100) was systematically studied using stripping voltammetry and FT-IR spectroscopy by Cuesta et al. [118-120]. For all these electrodes, a decrease of the CO coverage with increasing adsorption potential was found, see Figure 1-12.

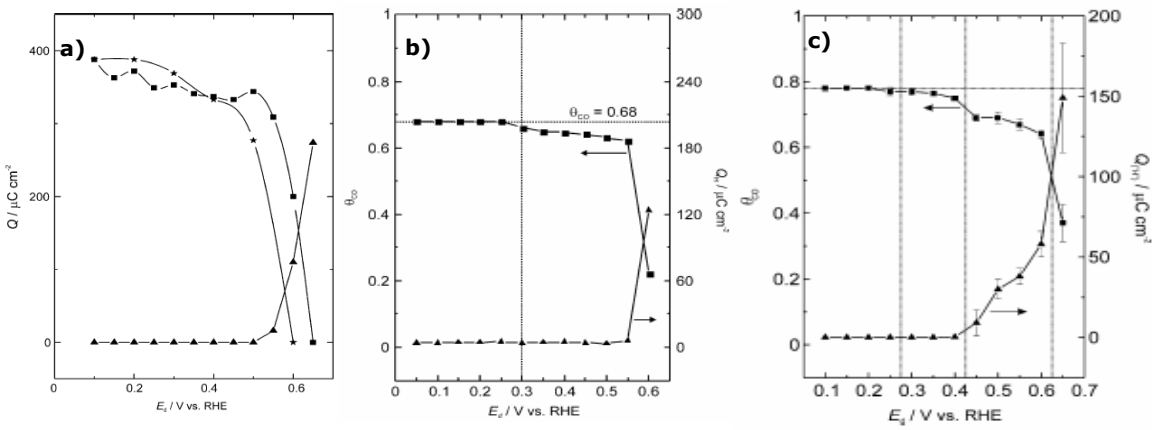

Figure 1-12 Plot of the CO-coverage on the a) Pt(pc) b) Pt(111) and c) Pt(100) electrode in CO-free 0.1M H_2SO_4 as a function of the dosing potential, obtained from CO-stripping voltammograms (squares) and from the integration of the CO_2 band in FT–IR spectra (stars). The total charge, without double layer correction, in the hydrogen adsorption region of the cyclic voltammogram (triangles) is also included in the figure. [118-120]

In the case of flame-annealed and quenched polyoriented platinum [118], a formation of two different kinds of adsorbed CO ad-layers was found. At adsorption potentials below 300 mV, the CO ad-layers are characterized by a well defined pre-peak and a split main peak. For an adsorption potential (E_{ad}) in the range of 300-500 mV, the pre-peak is completely absent and a main peak with a small shoulder at its low potential side is observed. The two contributions in the main peak were assigned to the oxidation of CO adsorbed on different surface sites. The highest CO coverage was found at a dosing potential of 100 mV which corresponds to the stripping charge density of 388 μC cm^{-2} (1.21 10^{15} molecules cm^{-2}). Subsaturated

CO ad-layers (i.e. with some free adsorption sites) are formed at a dosing potential of 550 and 600 mV. Above the adsorption potential of 650 mV no CO remains on the surface.

On Pt(100) electrodes [119], the maximum coverage (ϑ_{CO})[1] of 0.78 can be found at adsorption potentials below 250 mV (vs. RHE). On this surface, four different kinds of CO ad-layer were detected. The complete blocking of the hydrogen adsorption occurs at dosing potentials below 400 mV. When the dosing potential is below 250 mV, the CO ad-layer is characterized by a pre-peak and a main stripping peak at 550 mV. In the adsorption potential range of 300-400 mV, a main peak at 840 mV preceded by a very small hump is observed. A third kind of the CO ad-layer was found at dosing potentials 450-600 mV, where the CO stripping curve is split in two peaks, showing some irreproducibility. The fourth, non-equilibrium CO ad-layer is formed at E_{ad} = 650 mV, where only a single peak at 750 mV is formed.

In the case of Pt(111) [120], the saturation coverages were found when the adsorption potential was more negative than 300 mV, with the maximum coverage of 0.68, which very likely corresponds to the (√19x√19)R23.4°-13CO ad-layer structure firstly reported by Villegas and Weaver [121]. Based on these results, it was concluded, that the pre-peak in the CO-stripping voltammograms corresponds to the oxidation of the CO molecules adsorbed at the steps, and of a small amount of CO molecules adsorbed on the terraces and diffusing to the steps, and that the main peak appears due to the fast oxidation of the remaining terrace CO when the nucleation of oxygenated species on the terraces starts. This assumption implies that the diffusion of chemisorbed CO molecules from terraces to steps is slow and supports the hypothesis already noted by Markovic and Ross [122].

The adsorption isotherm of CO on Pt(111) in an electrochemical environment was for the first time determined by Cuesta et al. [123]. It was established that to increase ϑ_{CO} on Pt(111) above 0.68 the minimum CO concentration of 0.1% (CO concentration in gas phase) is necessary, and that above the CO partial pressure of 0.6%, ϑ_{CO} reaches the maximum possible value of 0.75.

For more experimental data for the CO oxidation on low-platinum-index surfaces see for example [113, 124-136].

[1] There are two common definitions of the surface coverage:
The surface coverage of the adsorbate (N) is related to
a) the maximum reachable surface coverage (N_{max}): $\Theta_{CO}=N/N_{max}$
b) the number of substrate atoms (N_{subs}): $\vartheta_{CO}=N/N_{subs}$

The mechanism and kinetics of the CO ad-layers on Pt(111) in the sulfuric acid was studied by Lebedeva et al. [137] using chronoamperometry. For the oxidation of a saturated CO ad-layer the oxidation was initiated by an apparently zeroth-order process followed by the main oxidation process, which is shown to be a Langmuir-Hinshelwood type. In the initiation process, 2-3% of the initial coverage was oxidized. This process was assigned to the Langmuir-Hinshelwood mechanism in which no effective freeing of sites for the adsorption of oxygen containing species occurs as the first few CO molecules are oxidized. In the case of sub-saturated CO coverages, depending on the initial CO coverage, two different types of current transients were observed. At coverages below 0.3 ML the transients were also in quantitative agreement with those expected from the Langmuir-Hinshelwood mechanism, but the transients observed for coverages between 0.3 and 0.6 ML were found to be more complex.

The effect of the density of steps on the electrooxidation of CO adsorbed on Pt[n(111)xPt(111)] surfaces in sulfuric acid was studied using cyclic voltammetry [138]. The CO was preferentially adsorbed on the steps, blocking the electrochemical hydrogen adsorption there and the overpotential for the oxidation of CO saturated ad-layers increases with the decreasing step density, i.e. in the sequence Pt(553)<Pt(554)<Pt(111). At low CO coverages the peak potential of the CO oxidation increases linearly with the CO coverage in the case of Pt(111), while it does not depend on the CO coverage for Pt(553) and Pt(554). The authors explain the catalytic effect of steps in terms of the enhanced formation of oxygen-containing species, needed for the CO oxidation, at surfaces with a higher step density. In further experiments [139] the kinetics of the electrochemical oxidation of a CO ad-layer on Pt[n(111)x(111)] electrodes in 0.5 M H_2SO_4 has been studied using chronoamperometry. The objective of these experiments was to elucidate quantitatively the effect of steps on the reaction kinetics and the mechanism. Two processes were distinguished in the current transients during the oxidation of a saturated CO ad-layer, similarly to the case of Pt(111) [137], see above. Using the mean-field approximation for the Langmuir-Hinshelwood mechanism, the reaction kinetics in the main peak region was modelled. The surface diffusion coefficient of CO was estimated to be higher than 10^{-11} cm^2 s^{-1}. The authors concluded that the reaction preferably takes place at the steps (at least in the potential region studied), while the terraces merely supply CO through a fast surface diffusion. Significantly, the reaction would not take place on an ideal atomically flat Pt(111) surface in the potential region studied. The role of steps is thus to preferentially adsorb the oxygen-containing species with which CO reacts. The intrinsic catalytic

activity of the steps on the Pt[*n*(111)x(111)] surfaces with $n > 5$ is here shown to be independent of the step density.

1.5.2.2. Nanoparticle electrodes

Savinova et al. [9, 140-142] studied the reactivity of the carbon monoxide monolayer oxidation on Pt nanoparticles supported on a glassy carbon using stripping voltammetry, chronoamperometry and also modelling. In the particle size interval from ca. 1 to 4 nm significant size effects on the reaction kinetic were observed, i.e. the positive shift of the CO stripping peak with the decreasing particle size and a pronounced asymmetry of the current transients at a constant potential. Based on neither mean field nor nucleation & growth models, they suggested a restricted CO_{ads} mobility at Pt nanoparticles below ca. 2 nm size, with the diffusion coefficient strongly dependent on the particle size (~10^{-16} cm^2 s^{-1} and >10^{-13} cm^2 s^{-1} for ca. 2 nm and 3 nm), and indicated a transition towards fast diffusion when the particle size exceeds ca. 3 nm. Similarly to the low-index-surfaces, the electrocatalytic activity of Pt in the CO monolayer oxidation was found to be strongly structure sensitive also at the platinum nanoparticle surfaces. The lowest reaction overpotential (and thus the highest catalytic activity) was found for Pt agglomerates, which are more reactive compared to either smooth polycrystalline Pt foil or isolated nm-sized particles. This phenomenon was explained by a high defect density on the surfaces of these structures. The CO oxidation at Pt nanoparticles takes place at potentials close to or higher than that typical for polycrystalline Pt. Nanoparticles with the particle size below 3 nm showed a "negative" size effect, which manifested itself by an increase in the reaction overpotential with the decrease in the particle size. At larger particle sizes the dependence levels off, the catalytic activity of Pt particles with diameters above 3 nm approaches that of polycrystalline Pt. In these experiments some splitting of the CO oxidation peak was observed for model Pt/GC electrodes. This reproduces very closely the behaviour of commercial carbon-supported fuel cell electrocatalysts at high metal contents. However, using FTIR spectroscopy and CO stripping voltammetry, it was demonstrated that the peak splitting is a consequence of inter-particle heterogeneity [143].

Later, Mayrhofer et al. [10, 144] reported conflicting data. The onset potential of the CO oxidation was found to be almost independent of the particle size in the range from 1 to 5 nm. On the other hand, it was claimed that the CO_2 production rate is strongly dependent on the particle size. They suggested that the oxidative removal of CO is mainly controlled by the number of "defects", which may serve as an active centre for OH adsorption.

The discrepancies in the literature were reconciled by exploring the influence of the experimental conditions on the stripping voltammetry and chronoamperometry [13]. Here, the strong particle size effects were confirmed in the size range from 1.8 to 5 nm and attributed to the size-dependent CO_{ads} + OH_{ads} interaction as well as to the size-dependent CO_{ads} surface diffusion coefficient. In addition, the peak position in the stripping voltammograms and the current transients were regarded as a fingerprint of the particle size and structure, and therefore they can be used as a diagnostic tool to determine the presence of coalesced particles, particles with bimodal size distribution, etc.

The mechanism of the CO electrocatalytic oxidation on a carbon-supported Pt electrocatalyst was also studied using Nuclear Magnetic Resonance (NMR) spectroscopy in conjunction with voltammetry [145]. In this study, the states of adsorbed CO, the conditions which give rise to them, and their oxidation pathways were investigated as a function of CO_{ads} coverage and the electrode potential of the adsorption. Three distinct forms of CO_{ads} were identified on the Pt electrocatalyst: a linear carbonyl, a bridged carbonyl, and a reduced carbonyl (-CHO) form. The relative populations of these three species were found to be strongly dependent on E_{ads} and substantially independent of the coverage. Different oxidation behaviours were observed for different populations of the three CO_{ads} species, suggesting that different oxidation reaction pathways are associated with the three CO_{ads} states.

1.5.3. Catalytical effects

In the case of the modified platinum surfaces, the electrooxidation of carbon monoxide (especially in the case of the methanol oxidation reaction) can be enhanced by the bifunctional mechanism, sterical effects (geometric or "ensemble" effect) and the electronic effect (ligand effect), respectively (Figure 1-13).

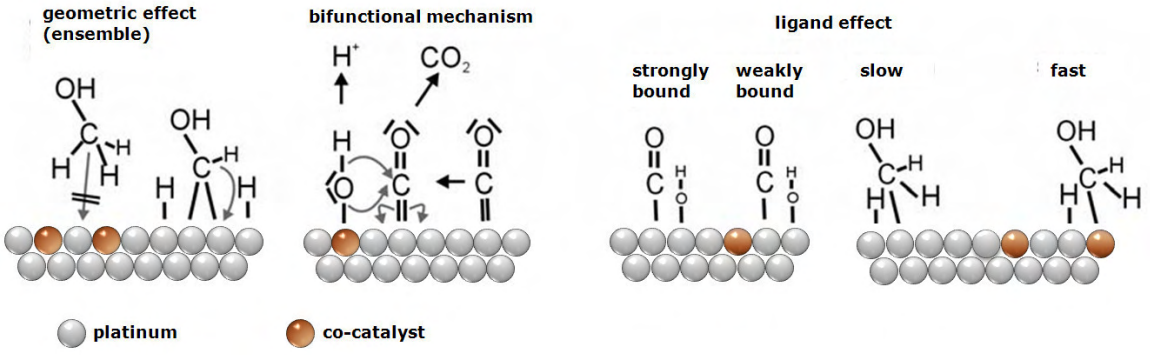

Figure 1-13 Action of co-catalysts on carbon monoxide and methanol adsorption/oxidation (Ref. [88])

According to the ***bifunctional mechanism*** [5, 22, 146-151], the water dissociation is activated by the alloying metal at lower overpotentials than by pure Pt, which initiates the electrooxidation of CO adsorbed on the neighbouring Pt site (Eg.1-11). The concept of this model is most likely:

$$H_2O + *Pt \Leftrightarrow OH_{ads,Pt} + H^+ + e^- \quad \text{(Equation 1-7)}$$

$$H_2O + *Ru \Leftrightarrow OH_{ads,Ru} + H^+ + e^- \quad \text{(Equation 1-9)}$$

$$CO_{ads,Ru} + OH_{ads,Pt} \Rightarrow CO_2 + H^+ + e^- + *Pt + *Ru \quad \text{(Equation 1-10)}$$

$$CO_{ads,Pt} + OH_{ads,Ru} \Rightarrow CO_2 + H^+ + e^- + *Ru + *Pt \quad \text{(Equation 1-11)}$$

In the ***ligand (electronic) effect*** [147, 148, 150, 152, 153], the electronic properties of intermediates are altered by the promoter. This effect describes changes in the chemical properties of the atoms in the surface due to the alloying and is therefore related to the electronic structure of the adsorption site. A good measure of the reactivity is the metal d-band centre.

Finally, the ***ensemble (morphological) effect*** [147, 152, 153] is referred to the changes in the catalytic properties of an ensemble of atoms in the surface when the chemical composition of the ensemble changes. The dilution of the active component with the catalytically inert metal changes the distribution of active sites, thereby opens different reaction pathways.
While most studies of electrocatalysis by Pt alloys reported so far invoke the bifunctional effect, clear information of the corresponding electronic and ensemble effects are more difficult to find.

1.5.4. Influence of foreign metals on the electrooxidation of adsorbed CO

RUTHENIUM

Most of the studies in the CO monolayer electrooxidation on Ru-decorated Pt(111) were performed by Friedrich et al. [79, 81, 134] and Wieckowski et al. [67-69].

Friedrich et al. [81] observed a single CO stripping peak for the surfaces with Ru coverage higher than 0.3 with a maximum shifted negatively compared to the position of the CO electrooxidation on pure Pt(111). A small shoulder in the current peak was found for surfaces with the Ru coverage of 0.3. This shoulder has been detected as a second peak by Massong et al. [154] and then confirmed by Lu et al. [75, 155] and Davies et al. [83]. The split of the CO oxidation peak was

observed also for Ru-decorated Pt nanoparticles by Bergens et al. [156, 157], Wieckowski et al. [76, 158, 159] and secondly also at a series of ruthenium modified Pt nanoparticles prepared by a surface organometallic chemistry (SOMC) [160].

The combined application of solid-state electrochemical NMR (EC NMR), cyclic voltammetry (CV), and potentiostatic current on the CO oxidation over Ru modified Pt nanoparticles [159] gave evidence for two types of CO (CO on pure Pt and CO on Pt/Ru sites), but showed no NMR evidence for a rapid exchange between the two CO populations. It was found that CO molecules on the primarily Pt domains behave much like CO on pure Pt, with there being little effect of Ru. In contrast, CO´s on Pt/Ru sites had highly shifted ^{13}C-NMR resonances, and they undergo thermally activated surface diffusion at higher temperatures. For CO on Pt, the correlation observed between the 2∂* Fermi level local density of states and the steady-state current suggest a role for Ru in weakening the Pt-CO bond, thereby increasing the CO oxidation rate (current).

Two distinct CO species were identified on Ru-decorated Pt(111) electrodes [79, 155] and Ru-decorated Pt nanoparticle electrodes [76, 159]: CO adsorbed on the Pt substrate and CO adsorbed on the ruthenium islands. This is in contrast to the studies on PtRu alloys, where only one CO species could be detected [114, 161, 162] and confirms that the Ru islands are formed on the Pt surface, as known from the STM studies [66, 70, 71, 74, 78, 81, 87].

The shape of the CO oxidation peak is also influenced by the ruthenium coverage. At moderately low coverages two overlapping current peaks with comparable charges are visible. With increasing ruthenium coverage, the peak at the more positive potential disappears, whereas either a single peak or a peak followed by a tailing or a shoulder is observed. A further increase in the Ru coverage does not lead to more changes. Note also that the onset of the CO electrooxidation is similar for all Ru-decorated Pt nanoparticles and depends on the Ru coverage.

Using double-potential step chronoamperometry [75] it was confirmed that at low potentials, the oxidation of CO chemisorbed on Pt(111)/Ru occurs *via* the Langmuir-Hinshelwood mechanism. This shows that a diffusion of CO on ruthenium to the Ru edge is not needed for a complete stripping of CO from such islands. In contrast, CO chemisorbed on Pt sites not occupied by Ru is oxidized at the Pt(111)/Ru edge, and there may be a surface diffusion contribution to the complete removal of CO from the surface. However, the part of the CO ad-layer

oxidation in the second voltammetric peak area occurs with no participation of a surface diffusion, according to the pseudo-first order surface reaction kinetics.

Similarly, at vicinal Pt(111) surfaces in which Ru is predominantly deposited below step edges, two CO stripping peaks were observed for a surface with terraces twelve atoms wide, but the peak at a higher potential was barely present on a surface with terraces six atoms wide [87, 88], pointing to the effect of the size of Pt domains in determining whether a high-potential CO stripping peak will be observed.

MOLYBDENUM

The co-catalytic effect of Mo on the oxidation of adsorbed CO on Pt(111), Pt(332), smooth and porous polycrystalline Pt electrodes was studied by Baltruschat and co-workers [96, 154]. From the linear relationship between the oxidation charge of Mo and the suppression of the CO adsorption when varying the Mo coverage it was shown that CO does not adsorb on Mo. The action of Mo shifts the usual pre-peak to lower potentials, whereas the main oxidation peak is hardly affected. The charge under the pre-peak was independent of the Mo coverage. The effect of Mo was then explained by an oxygen spillover effect, which is only working for CO in the weakly adsorbed state. With a sequential step decoration on Pt(332) by Ru and Mo, it was shown that a synergetic effect of both co-catalysts could be obtained.

SELENIUM

In early study of Kiskinova et al. [104] the CO adsorption on Pt(111) with a p(2x2)Se overlayer had been studied by TPD, LEED and digital ESDIAD. The presence of the p(2x2) chalcogene overlayer effects amongst others a reduction of the CO adsorption rate, the CO maximum coverage and the adsorption binding energy.
Later Herrero et al. [102] confirmed that the Se hinders the CO oxidation when the CO molecule is completely surrounded by the ad-atoms and that the presence of Se ad-atoms on the surface modifies the distribution of the CO populations, favouring the presence of linearly bounded CO against multi-bonded CO.

OSMIUM

The catalytic activity of Pt(111)/Os surfaces towards CO was studied by Wieckowski and co-workers [163] using various methods of surface analysis (e.g., STM, XPS and electroanalytical methods). The electrooxidation of adsorbed CO on Pt(111)/Os showed a two peak pattern. This is quite similar to Pt(111)/Ru, where similar onset potentials for CO electrooxidation were found. It was shown that the onset potential for the CO stripping is lowered from 530 to 450 mV when the Os coverage is increased from 0.2 to 0.7 ML.

These results were explained by the bifunctional mechanism similar to that of Pt(111)/Ru, only with a different optimal balance of Pt and Os sites compared to Pt and Ru sites.

1.6. ELECTROCATALYTIC OXIDATION OF METHANOL

Among many different electrode metals tested for this reaction, platinum-based materials display a sufficiently high stability and activity when used as an anode material (see in ref. [164, 165] and references therein). The overall reaction mechanism for the methanol electrooxidation is a $6e^-$ oxidation forming CO_2 as given by Equation 1-13:

$$CH_3OH + H_2O \rightarrow CO_2 + 6H^+ + 6e^- \qquad \text{(Equation 1-13)}$$

It is assumed that the adsorption of methanol on platinum-based surfaces proceeds through a sequence of steps shown in Figure 1-14 [166].

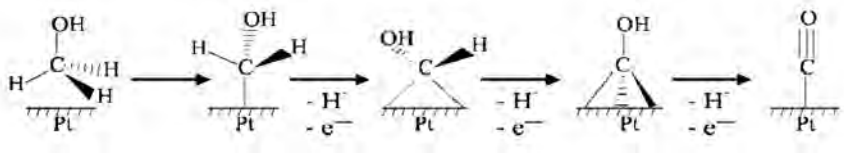

Figure 1-14 Surface electroadsorption of methanol on platinum and subsequent oxidation by consecutive stripping of protons and electrons [3]

In this scheme the electrosorption of methanol on the platinum surface occurs with a sequential proton and an electron stripping, giving the main catalyst poison, carbon monoxide. Subsequent reactions are believed to involve an oxygen transfer to the Pt-CO species to produce carbon dioxide.

As early suggested by Breiter [167], the total oxidation process of methanol probably consists of parallel reactions: one *via* surface bonded CO, which is a major product and second *via* dissolved intermediates (formaldehyde and formic acid) [168, 169], whose yield is dependent on the experimental conditions, e.g. surface roughness, concentration. This process , so called "dual path mechanism" [164, 170-173], can in principal be formulated as follows:

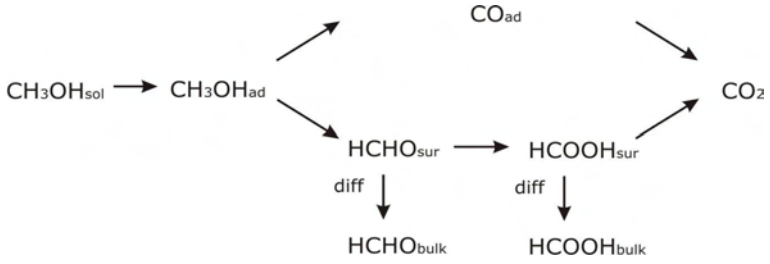

Besides the soluble intermediates mentioned above, methylformate ($HCOOCH_3$) [169, 174, 175] and 1,1-dimethyoxymethane ($H_2C(OCH_3)_2$) [174] have also been detected. The methanol oxidation on smooth polycrystalline Pt proceeds mainly *via* dissolved intermediates, but on highly rough and porous Pt electrodes, these intermediates have a greater chance to remain in a contact with the electrode and are further oxidized to CO_2. However, it is well known that platinum is easily poisoned by strongly adsorbed reaction intermediates, especially carbon monoxide (CO), produced by chemisorption of methanol (as mentioned above), and that such a surface is no longer active [176-178]. Compared to the lowest potential which allows the formation of CO from methanol on Pt, potentials at least 100-200 mV more positive are required to activate water and produce the surface oxides needed to oxidize surface CO to CO_2 [179].

The yields of methanol oxidation products were studied by Belgsir [180] and, more recently, by Korzeniewski [171] and Wang et al. [173, 175]. On a smooth polycrystalline Pt electrode Korzeniewski and Childers reported a formaldehyde yield of 38% at 250 mV vs. Ag/AgCl in 15 mM CH_3OH + 0.1 M $HClO_4$, the yield decreases at higher potentials. On porous Pt electrode, 50% HCHO, 34% HCOOH and only 16% of CO_2 were found by Wang et al. at 650 mV vs. RHE in 0.1 M CH_3OH + 0.5 M H_2SO_4.

It is well-known that also the supporting electrolyte has an effect on the rate of the methanol oxidation [181-184]. The cyclic voltammograms for the methanol oxidation exhibit much higher currents in $HClO_4$ than in H_2SO_4. In sulfuric acid, the adsorption of sulfate ions competes with the dissociative adsorption of methanol, and so the oxidation *via* CO_{ad} is inhibited this way.

Studies of the catalytic decomposition of methanol on low Miller index platinum surfaces [183-194] clearly demonstrate that the methanol oxidation is a surface sensitive reaction.

Using integrated voltammetry and chronoamperometry, Herrero et al. [183] observed that on Pt(111) and Pt(110) surfaces, a C-H bond cleavage and a concerted electron-transfer reaction are involved in the rate determining step. At the Pt(100) surface, the rate determining step is the second C-H bond cleavage, preceded by an electrochemical equilibrium reaction involving the first C-H bond break. The instantaneous currents for methanol (free of methanol self-inhibition effects) showed that the Pt(110) surface is the most active and the Pt(111) surface is the least active in the methanol oxidation. This behaviour was later confirmed by

other groups [165, 185, 195], where the Pt(110) surface was found to be not only the most active plane, but also the most sensitive to the poisoning in relation to Pt(111) and Pt(100) surfaces. The Pt(111) plane appeared to be the least sensitive to the poisoning, even if the current densities are rather weak. The Pt(100) plane remains blocked by the adsorbing species in a large range of potentials and the currents increase sharply after removing the adsorbed blocking species at higher potentials.

Contrary to these results, Housmans et al. [190] reported that the reactivity for the methanol oxidation reaction increases in the order Pt(111) < Pt(110) < Pt(100). While, in sulfuric acid, the oxidation of methanol on Pt(111) seems to show a preference for the direct oxidation pathway (through soluble intermediates), in perchloric acid, the indirect pathway *via* adsorbed CO appears to be favoured. In the absence of specifically adsorbed anions, steps of (110) orientation were suggested to catalyze the formation of soluble intermediates. In sulfuric acid, introducing steps on the (111) terraces leads to an increase in the relative rate of the indirect oxidation pathway, presumably as a result of a disruption of the anion ad-layer. Since the activity of the well-ordered Pt(110) is lower than that of the stepped surfaces Pt(554) and Pt(553), methanol appears to decompose preferably at step sites which are directly neighboured by a (111) terrace site. This combination, that is, a step plus terrace site, seems to be a particularly favourable "ensemble site" for the methanol decomposition.

On the Pt[*n*(111)x(110)] stepped surfaces, the reactivity of the methanol oxidation is strongly catalyzed by the presence of step and defect sites [196] and the overall oxidation rate increases with an increasing density of steps. Furthermore, the defect or step sites on such surfaces are more affected by the presence of methanol than the terraces. This shows that either the decomposition products of methanol or the methanol itself preferably occupies the steps. According to the chronoamperometric measurements, it could be suggested that the methanol decomposition into the CO poisoning species takes place preferentially at or near to the steps. In contrast, at Pt[*n*(111)x(100)] surfaces a decrease in the activity with the increase of the step density was observed [197].

In the recent study of Tripkovic [198], it was shown that the activity of Pt nanoparticles (Pt/C) can be correlated with the activities of the sites dominating in Pt nanoparticles as the electrocatalytic activity for the methanol oxidation of the Pt/C catalyst is between the activity of Pt(111) and Pt(110) surfaces.

Under conditions of a forced convection, CO_2 is only produced in the reaction path *via* adsorbed CO, whereas dissolved intermediates, which arise in the 2nd reaction path, are only oxidized to CO_2 in the absence of any convection or at rough, porous electrodes [173, 175, 199]. Furthermore, the rate of the methanol oxidation *via* dissolved intermediates increases with the methanol concentration, whereas the rate of oxidation *via* CO_{ad} is found to be independent on the methanol concentration [173].

As already mentioned before; the use of nanocolloidal particles as catalysts in fuel cells is especially advantageous because of their large surface to volume ratio. However, the fundamental physical and chemical properties of such nanoparticles are remarkably altered as the particle size and/or the shape or the morphology changes. The influence of the particle size and/or the loading on the methanol oxidation reaction has been investigated by numerous groups [6, 8, 12, 199-203]. However, there is no common view on the effect of the particle size on the activity.

For example, Takasu et al. [201, 204] studied the size effects of ultrafine platinum particles, prepared by a vacuum evaporation of platinum onto the glassy carbon, on the electrocatalytic oxidation of methanol in aqueous solutions of perchloric acid and sulfuric acid. The specific activity for the electrochemical oxidation of methanol was found to decrease with decreasing size of the platinum particles. Furthermore, the ratio of the exposed (110) plane decreased with the decrease in the particle size, whereas that of the (100) plane increased. In addition, no strong effect of anions (ClO_4^- and SO_4^-) on the electrochemical oxidation of methanol has been observed.

Also Frelink et al. [8] reported on a decrease in the methanol oxidation activity with decrease in the particle size in the range 4.5-1.2 nm; whereas for nanoparticles larger than ca. 4.5 nm the methanol oxidation activity remains almost constant. The particle size effect could be explained in terms of either the increased coverage of adsorbed hydroxyl species, which inhibit the methanol oxidation, or the reduction in the number of methanol adsorption sites with the decreasing particle size.

In a recent study, Bergamaski et al. [12] have shown that for catalysts presenting only small particles (less than 10 nm), there is an optimum in the particle size range for an efficient electrooxidation of methanol to CO_2 between 3 and 10 nm. Loss in the efficiency was observed for either too small or too large particles leading mainly to the partial oxidation of methanol to formaldehyde. In the case of overly small particles, the loss in the efficiency was accounted to morphological changes, whereas in the case of overly large particles (>10 nm) the more facile formaldehyde desorption to the solution becomes critical.

The influence of the catalyst loading was investigated by Jusys et al. [199] on the basis of DEMS experiments under continuous flow conditions. The electrochemical efficiencies, the product distribution, and the Turnover Frequencies (TOF) of partial reactions (methanol oxidation to formaldehyde, formic acid, and CO_2), and, accordingly, the number of electrons per CO_2 molecule formed during the methanol oxidation reaction (MOR) showed a pronounced dependence on the catalyst loading: firstly, the current efficiency for methanol oxidation to formaldehyde decayed significantly (from 40% to almost 0%), while that for the complete oxidation to CO_2 increased from 50% to 80% with the increasing Pt loading. The variation in the current efficiency for the methanol oxidation to formic acid was small (ca. 10%). Secondly, the product distribution varied accordingly: Low formic acid yields (5-20%) were accompanied by a decaying formaldehyde yield (60% to zero) and increasing CO_2 yield (30-80%) with an increasing catalyst loading. Thirdly, the apparent Faradaic TOF values calculated by assuming a complete methanol oxidation were significantly lower than those determined from the TOF numbers for the individual reaction pathways and products at low catalyst loadings, while at high loadings, where the complete oxidation of methanol (to CO_2) is preferred, they agree satisfactorily. The pronounced variations in product distribution/TOF values with the catalyst loading could be attributed to increasing re-adsorption and subsequent complete oxidation of desorbed reaction intermediates (formaldehyde and formic acid) at higher catalyst loadings, while at low loadings or on smooth electrodes these intermediates are more likely to survive.

1.6.1. Influence of foreign metals on the electrooxidation of methanol

To solve the problem of the surface poisoning and to improve the electrocatalytic activity of platinum, a modification of the catalyst surface by the addition of other metal to platinum is widely studied.

RUTHENIUM

Already in the early 1960s, the combination of Pt and Ru was recognized as an effective methanol catalyst which not only acts by lowering the oxidation potential of the adsorbed molecules [173, 205, 206], but also by increasing the current transient [73, 82, 207, 208]. The catalytic effect has been observed in different forms of PtRu materials, such as alloys [82, 205, 207, 209-213], electrodeposits of Pt and Ru [206], Ru adsorbed on Pt [68, 69, 82, 86, 207, 213], etc.. Although all these materials exhibit catalytic properties towards the methanol oxidation, they do not show the same activity.

Systematic studies on the catalytic activity of methanol on ruthenium spontaneously deposited on Pt(*hkl*) surfaces were made by the group of Wieckowski [68, 69, 86]. They estimated that at the optimal Ru coverage the activity for the methanol oxidation increases in the order Pt(100)/Ru < Pt(110)/Ru < Pt(111)/Ru. Especially, a maximum in the activity of the methanol oxidation was found for the Pt(111) surface covered with 0.2 ML of Ru, while a broad maximum in the range of 0.15 to 0.5 ML was reported by Hoster et al. [207, 211]. Hoster et al. also showed that the reaction rate of methanol on Ru modified Pt(111) depends on the method of preparation, hence the surface structure and the Pt:Ru distribution, and so the most probable rate-determining step is the reaction between the adsorbed CO with Ru oxide.

Wang et al. [173, 214] reported that on Ru-modified Pt(*hkl*) electrodes ($\vartheta_{Ru}\approx$0.25-0.35), the current efficiency of CO_2 is higher than that on pure platinum electrodes. The omitted average current efficiency for CO_2 reached 39% on Pt(pc)/Ru, 61% on Pt(111)/Ru and 46% on Pt(332)/Ru in one cycle of the potential sweep. The ratio of the average amount of CO_2 to methylformate was approximately 46, 80 and 71 for Pt(pc)/Ru, Pt(111)/Ru and Pt(332)/Ru respectively. At the maximum of the Faradaic current peak in the anodic scan, the current efficiency for CO_2 was only 34% (Pt(pc)/Ru), 35% (Pt(111)/Ru) and 37% (Pt(332)/Ru). It was suggested that the methanol oxidation *via* CO_{ad} to form CO_2 mainly takes place near Ru islands, while the methanol oxidation *via* soluble intermediates occurs at the steps or defects. At potentials > 650 mV, Ru ad-atoms lose their co-catalytic activity toward the methanol oxidation possibly due to the formation of an inactive anhydrous Ru oxide, as indicated by the same current efficiency for CO_2 as on pure Pt.

The optimum activity for the methanol oxidation at room temperature on Pt/Ru alloys had been reported by Gasteiger et al. [210, 215] at a surface composition of about 10 at.% Ru. Such a surface showed a relatively weak dependence on the methanol concentration, whereas on alloy surfaces with 50 at. % the rates were concentration dependent. This effect was explained by the limiting rate of the methanol adsorption on Ru-rich surfaces, whereas the rate determining step on pure Pt surfaces is the oxidative removal of methanol dehydrogenation fragments.

Also Maillard et al. [65] observed a maximum in the electrocatalytic activity towards the methanol oxidation at a Ru coverage ~ 10% in the case of the spontaneous deposition and at a Ru coverage ~ 20% for the electrodeposition. However, for the electrodeposited Ru the higher current densities for the methanol oxidation were

obtained, as compared to the spontaneous deposit. This signifies that depending on the deposition process, Ru ad-layers with a different chemical composition (oxidation states) could be formed.

In addition, it was shown by Frelink et al. [150] that on PtRu the methanol adsorption already occurs at potentials in the hydrogen region, while on Pt methanol is adsorbed only after virtually all adsorbed hydrogen has been removed from the surface. This may suggest an electronic effect of the Pt/Ru electrode. It was also reported that the onset potential of the oxidation is lowered with increasing amounts of Ru ad-atoms.

Also other groups [159, 206] proposed that in addition to the bifunctional effect, some electronic interactions may play role in the methanol oxidation reaction.

MOLYBDENUM

Additionally, few ternary and higher PtRu-based alloys have also been intensively studied. It was shown, that the behaviour towards the methanol oxidation can be modified due to the addition of a third metal to the binary Pt-Ru catalyst.

Lamy et al. [216] observed that PtRuMo ternary catalysts showed a higher catalytic activity toward the methanol oxidation at low potentials (typically under 500 mV vs RHE) under stationary conditions than PtRu binary catalysts prepared in the same way. The current densities measured on PtRuMo during the methanol electrooxidation were up to 10 times higher than those observed on PtRu.

Similarly, an enhanced specific surface activity of PtRuMo catalyst toward MOR at 60^{o}C, normalized to the current per square centimeter of a noble metal surface area, was reported by Jusys and co-workers [217] in comparison to the PtRu catalyst. In contrast, Song et al. [218] found a decrease in the activity for the methanol oxidation for PtRu electrodes modified by Mo oxide.

OSMIUM/IRIDIUM

The simultaneous addition of Ru and Os to Pt was also investigated [219-221]. It was clearly shown, that the minimum in the anodic wave is shifted to progressively negative potentials, going from Pt to PtRu to PtRuOs.

The surprising result was that the addition of small amounts of Ir to the PtRuOs ternary catalysts significantly improved their performance [220, 222, 223]. The role of Ir appears to be different from that of Ru and Os, since Ir forms relatively strong

bonds to C but not to O. The role of Ir is to accelerate the activation of the C-H bonds in methanol [222, 223].

1.7. EFFECT OF TEMPERATURE

At elevated temperatures, the methanol oxidation reaction at platinum and platinum based electrodes have been studied extensively [224-229], while there are only few reports on the oxidation of carbon monoxide [226, 230-233].

Generally, on pure Pt electrodes the peak of CO stripping shifts towards more negative potentials with increasing temperature independent of the surface. However, the peak shape and its current density do not change significantly with the temperature, thus indicating that the CO oxidation mechanism is not affected by the temperature.

The activation energy found for a Pt wire [116] is ~137 kJ mol^{-1}, which is slightly higher than that of 132 kJ mol^{-1} reported for the electrooxidation of CO adsorbed on Pt(111) [230]. It should be noticed that while at Pt(111) the peak potential for the CO stripping varied linearly with the temperature up to 40°C (at higher temperatures the CO coverage was decreased from 0.68 to 0.53), in the case of a smooth Pt wire no such effects were noticed. This can be explained by the disordered character of the CO chemisorbed on polycrystalline Pt, while on Pt(111) the ordered $(\sqrt{19}x\sqrt{19})R23.40^{\circ}$-$\Theta_{CO}$ structure of CO is expected to be more sensitive to temperature changes. The activation energy for the Pt wire [116] was 20% smaller than that calculated for platinized Pt [234] and about 18% larger than for carbon supported Pt nanoparticles [232].

On carbon supported PtRu catalyst, Kawaguchi et al. [232] reported that the oxidation potential of CO_{ad} decreases with an increasing temperature only up to 40°C and then becomes constant, while Dinh et al. [226] observed a decrease of the onset potential in the whole range of the temperature (25-100°C) on unsupported PtRu catalysts.

For the MOR on PtRu catalysts it was shown that increasing the temperature to 60°C the most active composition was shifted to the higher Ru composition from ~10% (25°C) to ~30% and the onset potential was shifted more negatively. Also the current efficiency for CO_2 was increased at higher temperatures, but the highest instantaneous current efficiency was found on pure Pt surface [209, 224]. Gasteiger et al. [209] attributed the shift in optimum composition with temperature to the shift in the rate-determining step from the methanol adsorption/dehydrogenation at a low temperature to the surface reaction between the dehydrogenated intermediate and surface OH species at the high temperature. The same rate determining step at

higher temperatures was proposed also by other groups [225-227], whereas a slow methanol adsorption was reported by Schmidt et al. [228] and Meli et al. [229] at 60°C, or between 25 and 75°C, respectively.
A wide range of experimental activation energies (E_a) for the MOR can be found in the literature from 16 kJ mol^{-1} to 95 kJ mol^{-1} for a number of Pt and PtRu surfaces [86, 209, 229, 233, 235-238].

1.8. ISOTOPE EXCHANGE

In the early study of Iwasita et al. [239] the interaction of methanol and carbon monoxide with its adsorbed species was studied on polycrystalline porous platinum in an acidic media by on-line mass spectrometry and isotopic labelling. It was found that when methanol is adsorbed on the surface, bulk methanol molecules cannot fully displace the adsorbed particles, but they can be partially displaced by CO from the solution (15-30%). In the case of CO adsorbed on platinum surface, an extensive exchange between adsorbed CO with the bulk CO has been observed.

Later, using radioactive tracer techniques, the CO_{ad} displacement by bulk CO was studied at Pt and PtRu nanoparticle electrodes, monitoring in situ the desorption/exchange process [240]. ^{14}CO pre-adsorbed from a methanol solution was exposed to non-radiolabeled CO bubbled through the supporting electrolyte. Within 100 minutes this $^{14}CO_{ad}$ was completely exchanged by the CO solution, leaving an ad-layer of non-radiolabeled CO on the surface.

Recently, the CO_{ad} desorption/exchange kinetics on platinum film electrode were studied by Heinen et al. [241] using combined in situ IR spectrometry and online mass spectrometry under controlled electrolyte flow conditions. They showed that the pre-adsorbed $^{13}CO_{ad}$ is rapidly exchanged by the ^{12}CO from the solution and the time required for the complete exchange depends strongly on the concentration of the ^{12}CO in the electrolyte. Under the given conditions such an exchange took about 10 minutes using a saturated ^{12}CO solution, whereas it exceeds 30 minutes if only 1% ^{12}CO in Argon was used. This behaviour was attributed to the decrease in the desorption barrier, which is mainly due to a combination of two effects; Firstly, an increase in the total CO_{ad} coverage with increasing CO concentration in the solution, secondly a pronounced decay of the CO adsorption energy with the CO_{ad} coverage.

Chapter 2 Experimental

2.1. CHEMICALS AND CLEANLINESS

CHEMICALS

All solutions were prepared using ultrapure water (Millipore, 18.2 MΩ cm, < 3 ppb TOC) and deaerated by high purity Ar prior to each measurement. As a base electrolyte a 0.5 M sulfuric acid was used. Chemicals used for preparation of electrolytes and cleaning baths are given in the Table 2-1.

Table 2-1 List of the used chemicals

reagent	Formula	purity	company
Argon	Ar	5.0	Air Products
Carbon monoxide ^{12}C	CO_2	4.7	Messer Griesheim
Carbon monoxide ^{13}C	$^{13}CO_2$	4.7 20%, Ar 5.0 80%	Linde
Chrome(VI)-Oxide	CrO_3	- / puriss. p. a.	Merck
Ethylene glycol	$C_2H_4(OH)_2$	- / puriss. p. a.	Merck
Hydrofluoric acid	HF	40% / p.a.	Merck
Hydrogen peroxide	H_2O_2	35% / med. reinst.	Merck
Methanol	CH_3OH	- / puriss. p. a.	Merck
Nafion	$C_7HF_{13}O_5S$. C_2F_4	n.s.	Aldrich
Natriummolybdate	Na_2MoO_4 x H_2O	- / puriss. p. a.	Fluka
Nitric acid	HNO_3		Merck
Potassium hydroxide	KOH	Semiconductor grade	Aldrich
Ruthenium-III-chloride	$RuCl_3$	p.a.	Merck
Sulfuric Acid	H_2SO_4	95-97% /suprapure	Merck
Water	H_2O	100%-3ppb	Millipore system

CLEANLINESS

The electrochemical measurements on platinum surfaces (especially on the single crystal surfaces) are very sensitive towards impurities, especially organic compounds or strong adsorbing anions which can be easily adsorbed on platinum. Therefore, all glassware including volumetric flasks, as well as Teflon- or PTFE-components and tubings were first carefully cleaned over night in a 5 M KOH solution in order to remove possible anions and/or organic contaminations. To remove possible cationic compounds and/or metal residues a bath of chromic acid solution (640 ml H_2SO_4, 360 ml H_2O and 21.4 mg CrO_3) was used (overnight). Afterwards, all cleaned parts were rinsed with Millipore-water.

The cleanliness of the system was controlled by a simple adsorption test (a blind experiment). Here, during the potential scan in the base electrolyte, the potential was stopped in the double layer region (approx. 350 mV) in the anodic direction for 5 minutes. Afterwards, a new cyclic voltammogram is recorded together with the ion current of the mass *m/z* = 44 till no changes in the cyclic voltammogram are visible and the detected amount of carbon dioxide is zero or maximal 5% of one monolayer.

2.2. DATA COLLECTION

For the data collection, computers with integrated A/D convertor boards were used. For detection of the faradaic current by potentiodynamic measurements, a computer (486 DX2-66) with a DASH 1602 measuring board (Keithley) together with software for the data collection developed in our department (Potmadash) were used. For potentiostatic and also galvanostatic experiments a notebook (Toshiba Satellite 210 CS) with a measuring board from National Instruments (PC dash 1200) and software LabView (National Instruments) were used. Parallel to the faradaic current, data from the mass spectrometer were registered with special software Quadstar (Pfeiffer Vacuum) which makes it possible to detect the ion current for each *m/z* separately. The data were evaluated with Origin (Originlabs).

2.3. ELECTRODES

The reversible hydrogen electrode (RHE) was used as a reference electrode in this study. The connection to the cell (see Chapter 1.2.2.) consists of a PTFE capillary filled with the base electrolyte (0.5 M H_2SO_4) attached to the inlet of the cell. Both counter electrodes are made of a platinum wire. A summary of working electrodes used in this work is given in Table 2-2.

Table 2-2 Working electrodes

electrode	description		
	orientation / particle size	Weight % metal	company
Pt(665)	± 0,5°	-	Metal Crystals & Oxides LTD.
Pt(pc)	none	-	
PtO_x^E/C	∅2.0nm	10% Pt	E-TEK, Inc; Lot#3193702NR
$PtRu^E$/C	∅2.0nm	13.3% Pt; 6.8% Ru	E-TEK, Inc; Lot#3028401
PtO_x^M/C	∅1.9nm	13.2% Pt	MPI Mülheim; LOP-LB625
$PtRuO_x^M$/C	∅1.8nm	8.3% Pt; 3.8% Ru	MPI Mülheim; LOP-LB677
$PtRuOsIrO_x^M$/C	∅1.6nm	13.4%Pt; 9.1%Ru; 1.4%Os; 1.0%Ir	MPI Mülheim; LOP-LB764
$PtRuMo^M$/C	n.a.	13.4%Pt; 2.1%Ru; 1.6%Mo	MPI Mülheim; LOP-LB675

C, Vulcan XC-72 ; ^{E}, nanoparticles from E-TEK, Inc. ; ^{M}, nanoparticles from MPI Mülheim

2.3.1. Preparation of nanoparticle electrodes

Glassy carbon disc electrodes (Sigradur G, HTW GmbH) with a diameter of 10 mm, polished to a mirror finish (0.1 µm Al_2O_3), were used as a substrate for the carbon supported catalysts [242]. For the electrode preparation, a defined volume (in the range of 20 to 30 µL) of an ultrasonically dispersed catalyst in ethylene glycol was pipetted onto the glassy carbon substrate, creating a catalyst film with a platinum loading of 10 $\mu g_{Pt}\, cm^{-2}$ (suspensions in ethylene glycol resulted in smoother deposits than suspensions in water). After evaporating the solvent at 80-100°C, the deposited Pt catalysts were covered with 82 µl of Nafion solution in water at a concentration of ca. 1.44 mg mL^{-1}, and dried at an ambient temperature. The aqueous solution of Nafion was prepared by diluting the commercial solution (isopropanol 5 wt. %, Aldrich) with water and subsequent evaporation of the isopropanol. The resulting Nafion film with a thickness of about 1 µm was of sufficient strength to permanently attach the catalyst particles to the glassy carbon electrode [242].

Before the measurements, the colloidal catalysts based on platinum oxides were reduced to the metallic platinum at a potential of approximately 300 mV. Then the potential was stepped in a cathodic direction to 50 mV and kept there, till constant currents were recorded.

Because of a small contamination from Nafion solution, the platinum nanoparticle electrode was cycled several times in the potential range of 50-1000 mV till the CV

was stable. The upper limit of the potential scans was set to 800 mV for all Ru containing catalysts in order to avoid dissolution of Ru.

2.3.2. The preparation of the single crystal electrode Pt(665)

In this thesis, also a disc shaped single crystal with a diameter of 1 cm and the orientation Pt(665) (= [12(111) x (111)]) was used. Prior to each experiment, the single crystal surface was prepared by a flame annealing according to the method of Clavilier [32]. The electrode was first cleaned for 10 minutes in concentrated nitric acid and afterwards also by the cyclic voltammetry between 50-1500 mV in the supporting electrolyte. Then the electrode was uniformly annealed in the oxidative flame of a propane/butane gas burner for approximately 30 seconds (orange glow). Then the crystal was cooled down in an argon atmosphere for four minutes. Finally, the electrode surface was contacted (hanging meniscus) to the supporting electrolyte at a potential of 50 mV, and a CV was recorded in a potential range of 50-800 mV to test the quality of the preparation [37, 38, 88] (at potentials > 1000 mV, the Pt surface becomes rough due to the adsorption of oxygen).

To protect the treated Pt(665) against possible contaminations during the transfer of the single crystal into the DEMS cell, the single crystal face was covered with one drop of the base solution saturated with argon.

Clavilier reported [37] a theoretical charge of 21 μC cm^{-2} for the peak at 125 mV due to the hydrogen adsorption at the steps of local 110 geometry, and the total theoretical charge of 302 μC cm^{-2} between 50-750 mV.

2.3.3. Determination of the active surface area

The active surface area of the polycrystalline Pt electrode can be determined by underpotential deposition of hydrogen (H_{UPD}) assuming 210 μC cm^{-2} for the total charge in the hydrogen adsorption region (70-350 mV) after the subtraction of the double layer charging current [21, 243].

$$A_{sur,H} = \frac{Q(H_{ad})^{\exp}}{210\,\frac{\mu C}{cm^2}} \qquad \text{(Equation 2-1)}$$

where $Q(H_{ad})^{exp}$ is the experimental total charge in the hydrogen adsorption region. Using $Q(H_{ad})^{exp}$ and the hydrogen adsorption charge for the corresponding single crystal surface, $Q(H_{ad})^{theo}$, the surface area of any single crystal electrode can be calculated:

$$A_{sur,H} = \frac{Q(H_{ad})^{\exp}}{Q(H_{ad})^{theo}}$$ (Equation 2-2)

For Pt(665) the $Q(H_{ad})^{theo}$ is 195 µC cm^{-2} for the potential region of 50-350 mV according to Clavilier et al. [37-39].

This method is not well suited for Pt nanoparticles, because of the low H_{UPD} charge as compared to the double layer charging of the carbon support. Therefore, the electrochemically active surface area, A_{sur}, of different catalysts was determined by CO stripping voltammetry:

$$A_{sur,CO} = \frac{Q_f^{max}}{0.7 \cdot 2 \cdot 210 \frac{\mu C}{cm^2}}$$ (Equation 2-3)

where 2 is the number of electrons and 0.7 is the maximum coverage (CO molecules per number of Pt surface atoms). This is an average value often observed on Pt electrodes. Since it also corresponds to the coverage of 1.45 nmol cm^{-2} observed on different smooth and stepped Pt single crystal electrodes [244], it is assumed that it also holds for Pt nanoparticles.

The faradaic charge of the CO_2 formation from the CO adsorbate cannot be easily obtained from the measured current through the electrochemical cell due to the unknown contribution of the double layer charging. Instead, the true faradaic charge corresponding to the formation of CO_2 *via* a 2 e$^-$, $Q_{f,true}^{max}$, is determined with the help of the integrated ion current for CO_2, Q_i^{max}, using the calibration constant, K^*. The calibration constant was determined from a calibration experiment involving CO oxidation on polycrystalline Pt, as described in [24]:

$$Q_{f,true}^{max} = \frac{2 \cdot Q_i^{max}}{K^*}$$ (Equation 2-4)

From the integrated ion current of CO_2, Q_i^{max}, and of the methanol adsorbate, Q_i, the relative coverage of the methanol adsorbate, Θ_{CO}, can be determined according to:

$$\Theta_{CO} = \frac{\Gamma_{CO}}{\Gamma_{CO}^{max}} = \frac{Q_i}{Q_i^{max}}$$ (Equation 2-5)

where Γ_{CO} is the surface coverage of the CO adsorption from methanol, Γ_{CO}^{max} is the maximum of adsorbed CO from the CO saturated electrolyte.

This characterization of the different electrodes by the adsorption of CO from dissolved CO was repeated at the end of all experiments, to make sure that the surface has not changed.

An alternative method for determination of the active surface area of Pt, Ru and PtRu surfaces which is based on UPD of copper (Cu_{UPD}) was presented by Green and Kucernak [245]. They demonstrated that the stripping of the Cu_{UPD}-deposit can be used for the estimation of the electrochemically active surface areas of such electrodes. In addition, the coverage of bare ruthenium sites on the electrode surface can be also estimated due to the resolved peaks into their constituent components for Cu on either Pt or Ru in alloyed Pt-Ru. The corresponding surface areas are then calculated assuming a charge density of 420 μC cm^{-2}:

$$A_{sur,Cu} = \frac{Q(Cu_{upd})^{exp}}{420\,\frac{\mu C}{cm^2}} \qquad \text{(Equation 2-6)}$$

where $Q(Cu_{upd})^{exp}$ is the experimental charge for the Cu_{UPD} desorption peak determined by integration of the CV between 300 and 700 mV corrected for the background current in sulfuric acid free of copper.

In the case of deposited multilayers of Ru, Bogolowski et al. [246] found, that the specific charge for Cu_{UPD} on Ru is different from that on Pt. The real surface area can be than determined by:

$$A_{sur,Cu} = \frac{Q(Cu_{upd})^{exp}}{520\,\frac{\mu C}{cm^2}} \qquad \text{(Equation 2-7)}$$

Baltruschat and coworkers [247] also have shown that the amount of Cu deposited in the UPD-range decreases with the surface concentration of Se.

The theoretical surface area, A_{theor}, of the nanoparticulate electrode can be estimated from the real loading:

$$A_{theor} = N_{Pt} \cdot S \qquad \text{(Equation 2-8)}$$

where N_{Pt} is number of the colloid clusters and S is the area of one colloid cluster. Assuming a narrow distribution and a spherical shape of the colloid particles, then:

$$S = 4 \cdot \pi \cdot r^2 \qquad \text{(Equation 2-9)}$$

and

$$N_{Pt} = \frac{V_{Pt}}{\frac{4}{3} \cdot \pi \cdot r^3} \qquad \text{(Equation 2-10)}$$

where r is the radius of one cluster and V_{Pt} is a volumetric sum of all clusters and can be calculated using:

$$V_{Pt} = \frac{m_{Pt}}{\rho_{Pt}} \qquad \text{(Equation 2-11)}$$

where m_{Pt} is the amount of platinum used for the loading and ρ_{Pt} is the specific mass of platinum (21.45 g cm^{-3}).

It follows:

$$A_{theor} = \frac{m_{Pt} \cdot 4 \cdot \pi \cdot r^2}{\rho_{Pt} \cdot \frac{4}{3} \cdot \pi \cdot r^3} = \frac{3 \cdot m_{Pt}}{\rho_{Pt} \cdot r} \qquad \text{(Equation 2-12)}$$

2.4. Ru, Mo, AND Se DEPOSITION

Ru DEPOSITION

The spontaneous deposition of Ru was carried out directly in the DEMS-cell at open circuit in a $5 \cdot 10^{-3}$ M $RuCl_3$ + 0.5 M H_2SO_4 solution for 2 minutes. After the deposition, the Ru solution was replaced by the base electrolyte. According to [65, 78] this leads to a Ru coverage of about 0.2 monolayer.

The electrochemical deposition of Ru on Pt electrodes was performed potentiostatically according to Geyzers [78, 81] from a $5 \cdot 10^{-3}$ M $RuCl_3$ + 0.5 M H_2SO_4 solution. Varying of the immersion potentials between 300 and 800 mV (5 minutes), (sub-) monolayers of Ru were deposited on Pt surfaces. The step decoration of Pt(665) was achieved at a potential of ca. 600 mV for 5 minutes [87, 88], this should lead to a Ru coverage of around 20% [78]. Multilayers of Ru on Pt were reached when the deposition potential was kept for 10 minutes at 50 mV.

Mo DEPOSITION

The Mo deposition on Pt nanoparticles was performed through a potentiostatic deposition for 3 minutes at 100 mV in a 1 10^{-4} M Na_2MoO_4 + 0.5 M H_2SO_4 solution. After the deposition, the Mo solution was replaced by a 0.5 M H_2SO_4 solution under the potential control (100 mV) and cyclic sweeps were performed between 50 and 600 mV until two successive cycles with no obvious difference were obtained.

Se DEPOSITION

The Se was deposited by a gradual deposition in the thin layer flow through cell during several potential cycles (50 mV s^{-1}) between 50 and 800 mV in 5 10^{-7} M H_2SeO_3 in 0.5 M H_2SO_4. Different Se coverages were observed by varying of

the number of cycles [247]. Then, also under a potential control, the solution was replaced by the base electrolyte and cyclic sweeps were performed until stable CV´s with no obvious difference were observed.

The relative Se coverage, Θ_{Se}^{CO}, was determined by CO stripping experiments. Due to the fact that Se hinders the adsorption of CO on Pt [102] or Ru, the CO oxidation charge on surfaces partially covered by Se corresponds to the free Pt or Ru sites. For submonolayers of Se deposited on Pt or Ru, the real surface area does not change. Thus, it is that found for the catalysts before Se deposition, and $\Theta_{Se} + \Theta_{CO} = 1$,

$$\Theta_{Se}^{CO} = 1 - \frac{Q_{MSe}^{CO}}{Q_{M}^{CO}} = \frac{Q_{M}^{CO} - Q_{MSe}^{CO}}{Q_{M}^{CO}} \qquad \text{(Equation 2-12)}$$

where Q_{MSe}^{CO} is the CO oxidation charge on Se modified surface and Q_{M}^{CO} is the CO oxidation charge on Se free surface. All these charges are recalculated from the mass spectrometric signal for the CO oxidation (see Chapter 2.3.3.). In this way, the double-layer charging effects do not interfere.

For Ru containing surfaces, this method is more reliable for the calculation of the surface coverage, because on Ru the hydrogen adsorption is largely paralleled by an anion and oxygen desorption. In addition, especially for carbon supported electrodes, the hydrogen adsorption region is not well defined, as mentioned above.

2.5. ADSORPTION OF CARBON MONOXIDE

CO was adsorbed at a constant electrode potential of 50 mV by replacing the base electrolyte (0.5 M H_2SO_4) with a 0.5 M H_2SO_4 solution saturated with CO (ca. 10^{-3} mol L^{-1}). After the formation of a CO monolayer, the solution was exchanged for a pure 0.5 M H_2SO_4 solution under potential control (E = 50 mV), in order to have a solution free of CO. Then, the adsorbed CO was oxidized to CO_2 during the positive potential sweep.

2.6. ADSORPTION OF METHANOL

For the oxidation of the methanol adsorbate, the potential was first held at 50 mV (E_0, the potential at which methanol does not yet adsorb) in the base electrolyte, which was then replaced by a 0.1 M CH_3OH + 0.5 M H_2SO_4 solution under potential control. Afterwards, the potential was stepped to more positive potential, E_{ads}, at which methanol could adsorb, for a definite time, t_2. Then the potential was stepped back to 50 mV, E_0. After replacing the solution with the base solution, which lasted

around 5 minutes, t_3, the potential was swept in the anodic direction, t_4. A scheme of the potential program is shown in Figure 2-1.

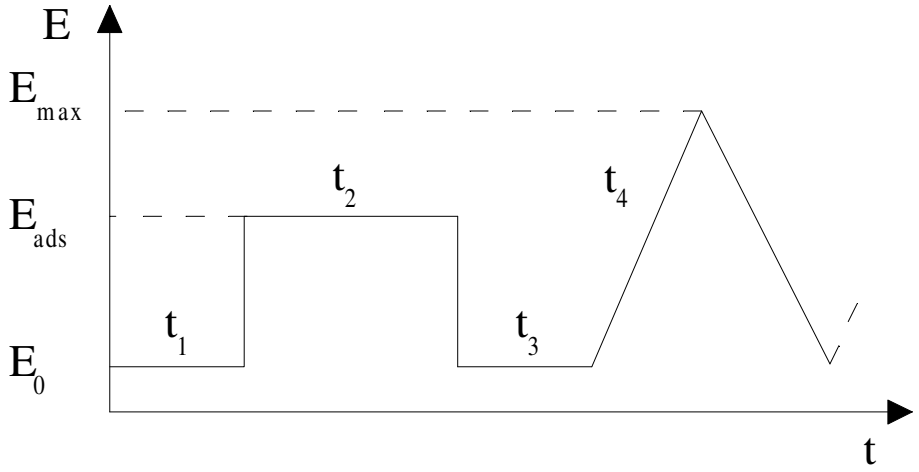

Figure 2-1 Potential program for the methanol adsorption experiments. *E_0 - potential where methanol isn't adsorbed; E_{ads} - potential of adsorption of methanol; E_{max} - upper potential limit of CV; t_1 - time of electrolyte exchange for methanol solution; t_2 - time of methanol adsorption; t_3 - time of electrolyte exchange for base solution; t_4 - cyclic voltammetry*

Bulk oxidation measurements were performed in 0.1 M CH_3OH + 0.5 M H_2SO_4 solutions with a flow rate of 5 µL s^{-1}.

The current efficiency for CO_2 was determined from the faradaic current, I_f, and the ion current, I_i, in the following way:

$$I_f^* = \frac{6 \cdot I_i(44)}{K^*(44)} \qquad \text{(Equation 2-13)}$$

$$A_i = \frac{I_f^*}{I_f} \qquad \text{(Equation 2-14)}$$

where I_f^* is the faradaic current corresponding to the formation of CO_2, K^* is the calibration constant and A_i is the current efficiency for CO_2.

Similarly, the average current efficiency for CO_2, A_q, can also be calculated from the faradaic charge, Q_f, and the integrated ion current.

$$Q_f^* = \frac{6 \cdot Q_i(44)}{K^*(44)} \qquad \text{(Equation 2-15)}$$

$$A_q = \frac{Q_f^*}{Q_f} \qquad \text{(Equation 2-16)}$$

2.7. UNDERPOTENTIAL DEPOSITION OF COPPER

The Cu_{UPD} was performed according to Baltruschat and co-workers [247]. The electrode was cycled with 50 mV s^{-1} in a 10^{-3}M $CuSO_4$ + 0.5 M H_2SO_4 solution down to 50 mV, followed by an anodic cycling up to 300 mV with the scan rate of 5 mV s^{-1}. At this point the potential was stopped for 3 minutes. Then the desorption of UPD deposited Cu was achieved by sweeping up to the upper potential limit [245] and the real surface area was determined according to Chapter 2.3.3..

2.8. GALVANOSTATIC AND POTENTIOSTATIC MEASUREMENTS

In the potentiostatic experiments, after the adsorption of CO or the methanol adsorbate, the potential was stepped into the oxidation regime of CO or methanol, respectively. This potential was applied till the faradaic and the ion current did not change with time. In the galvanostatic measurements, adsorption of CO and adsorption of the methanol adsorbate was also performed under potential control at the above mentioned conditions; then the potentiostat/galvanostat was switched to the galvanostatic operation-mode. The selected current was applied until the potential reached 1000 mV. Then the operation mode was set back to the potentiodynamic conditions. Before and after each galvanostatic experiment a cyclic voltammogram (CV) was recorded to control the state of the surface.

Chapter 3 Electrocatalytic activity of nanoparticles for CO oxidation and their characterisation

First; the activity of the catalysts was tested by the oxidative stripping of a pre-adsorbed CO monolayer on nanoparticle electrodes. This also allows a determination of the real surface area (see Chapter 2.3.3.) and a characterization of the electrocatalytic behaviour with respect to CO oxidation by the onset of CO_{ads} oxidation and the stripping peak potential. In addition, the determination of the surface area using oxidation of a CU_{UPD} layer is shown.

3.1. PLATINUM AND ALLOYED NANOPARTICLES

3.1.1. Platinum nanoparticles

Figure 3-1 shows the oxidative stripping of pre-adsorbed CO on electrochemically reduced PtO_x nanoparticles supported on Vulcan XC-72. The samples were obtained from (a) E-TEK, Inc (PtO_x/C^E) and from (b) MPI Mülheim (PtO_x/C^M). The oxidation behaviour of the pre-adsorbed CO monolayer on both Pt catalysts supported on carbon is in good agreement with the CO-stripping experiments on different Pt nanoparticles already reported in literature (see e.g., [9, 140, 141, 143, 232, 248]).

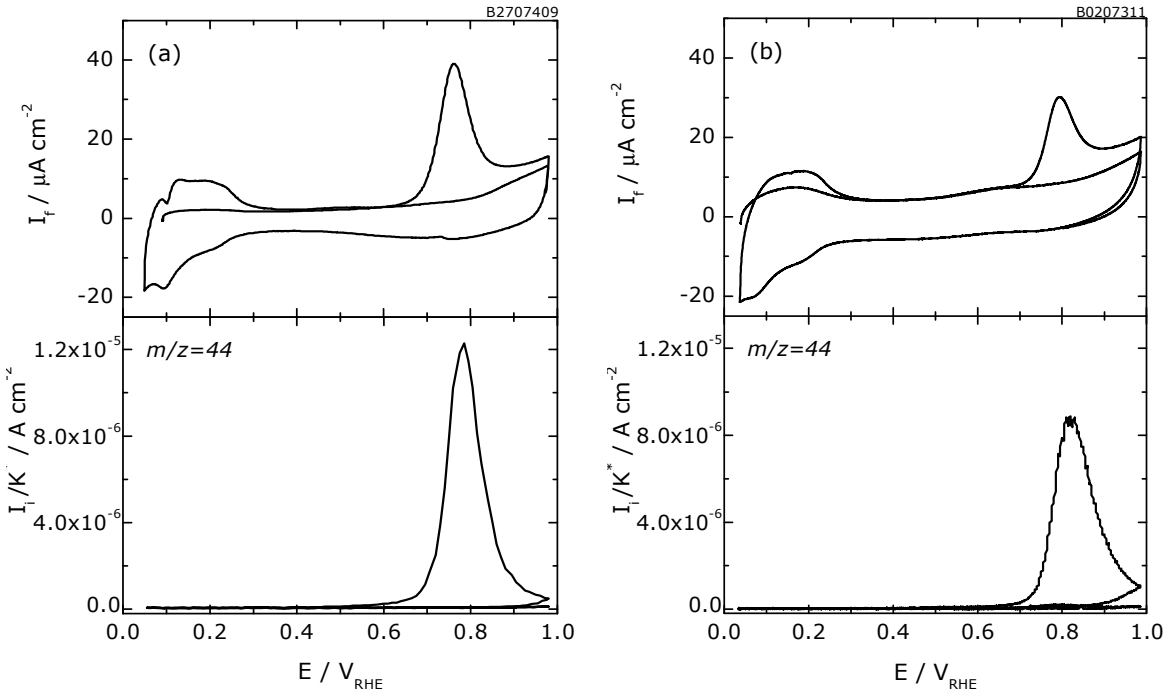

Figure 3-1 Simultaneously recorded faradaic and corresponding ion currents of CO_2, m/z=44, during the oxidation of CO adsorbed on (a) PtO_x^E/C and (b) PtO_x^M/C in 0.5 M H_2SO_4. Scan rate: 10 mV s^{-1}. Electrolyte flow rate: 5 µL s^{-1}. Catalyst loading: 10 μg_{Pt} cm^{-2}. The current is referred to $A_{sur,CO}$.

From the amount of CO_2 formed at this surface during the CO oxidation an active area of 4.4 cm^2 for PtO_x^E/C, and 5.5 cm^2 for PtO_x^M/C are calculated. The theoretical real surface area of 3.9 cm^2, respectively 4.2 cm^2 is calculated. This shows that at

least most of the particles are accessible to CO. The higher experimental value is due to an inhomogeneous distribution of the particles on the glassy carbon surface: Probably, the density and the thickness are larger than the average at the central part of the electrode, which is exposed to the electrolyte, whereas it is smaller at the edge, which in the DEMS cell is covered by a spacer.

The CO_{ad} oxidation on platinum nanoparticles obtained from E-TEK (PtO_x^E/C) starts at about 500 mV, as can be seen in the Mass Spectrometric Cyclic Voltammetry (MSCV) of m/z=44. The maximum current density is reached at 790 mV which is about 30 mV more negative than in the case of nanoparticles obtained from MPI Mülheim (PtO_x^M/C).

3.1.2. Platinum-Ruthenium alloy nanoparticles

As already mentioned in the previous chapter, ruthenium can be added to platinum in order to obtain oxidation potentials much more compatible with a working anode in a direct methanol fuel cell.

Figure 3-2 compares CO stripping voltammograms for two different PtRu alloy nanoparticle electrodes in H_2SO_4.

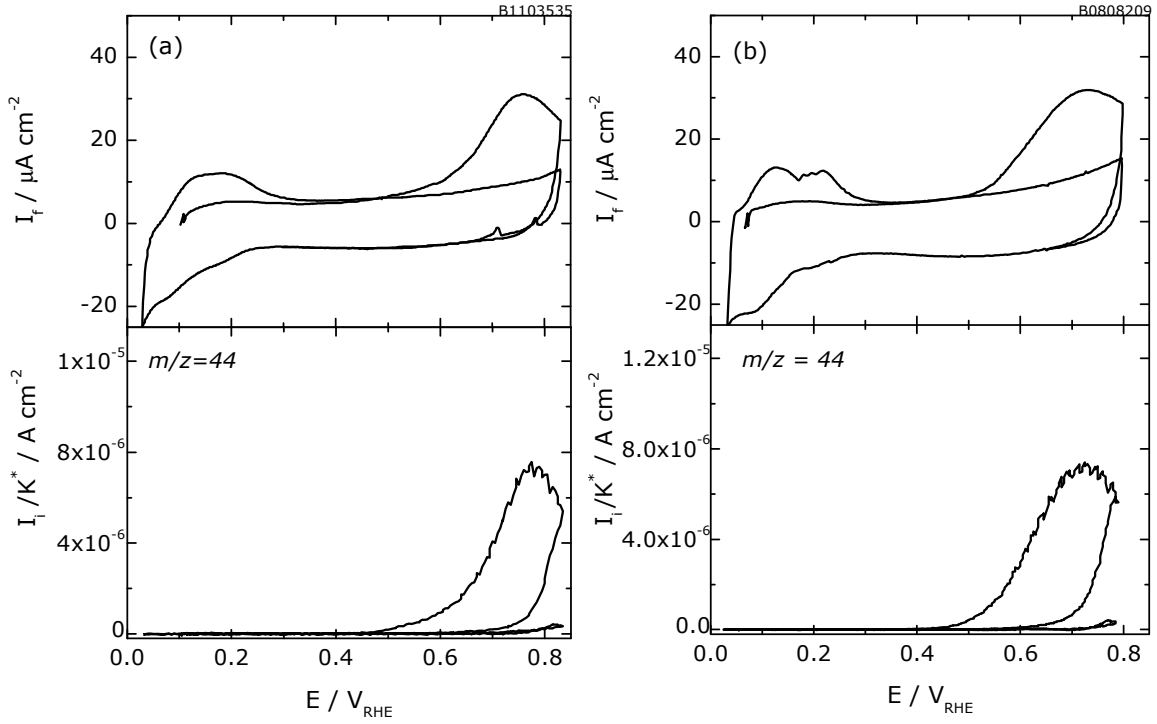

Figure 3-2 Simultaneously recorded faradaic currents and corresponding ion currents of CO_2, m/z=44, during the oxidation of CO adsorbed on Pt-Ru alloy nanoparticles (a) $PtRu^E/C$ and (b) $PtRuO_x^M/C$ in 0.5 M H_2SO_4. Scan rate: 10 mV s^{-1}. Electrolyte flow rate: 5 µL s^{-1}. Catalyst loading: 10 µg$_{Pt}$ cm^{-2}. The current is referred to $A_{sur,CO}$.

In Figure 3-2a the Pt-Ru alloy nanoparticle electrode from E-TEK, Inc. is presented ($PtRu^{E}/C$). The active surface area of 6.0 cm^2 established from the amount of CO_2 formed during the CO oxidation at $PtRu^{E}/C$ is lower than the calculated theoretical surface area (7.5 cm^2). Also in the case of PtRu alloyed catalyst obtained from MPI Mülheim ($PtRuO_x^{M}/C$), the active area determined by the stripping of CO_{ad} (7.2 cm^2) is below that expected from the calculation (7.9 cm^2).

In both cases, the CO_{ad} oxidation starts already at lower potential and the main peak is broader than on the pure platinum nanoparticle electrodes. The oxidation on the $PtRu^{E}/C$ catalyst starts at 450 mV and the maximum current density is observed at 775 mV. Even lower values for the onset potential (400 mV) and the potential of the maximum current density (730 mV) are found during the oxidation of adsorbed CO at $PtRuO_x^{M}/C$.

3.1.3. Platinum-Ruthenium-Osmium-Iridium alloy nanoparticles

In the case of the oxidation of pre-adsorbed CO on the electrochemically reduced $PtRuOsIrO_x^{M}/C$ nanoparticle catalyst some kind of "pre-peak" (onset at 400 mV) is found (Figure 3-3; solid line).

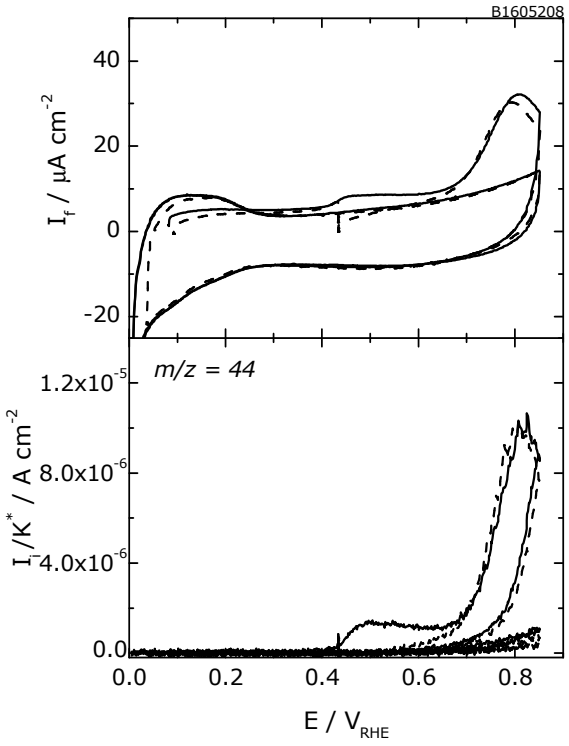

Figure 3-3 Simultaneously recorded faradaic currents and ion currents of CO_2, m/z=44, during the oxidation of CO adsorbed on $PtRuOsIrO_x^{M}/C$ alloy nanoparticles in 0.5 M H_2SO_4. Scan rate: 10 mV s^{1}. Electrolyte flow rate: 5 µL s^{-1}. Dashed line: after holding the potential at 430 mV for 2 min. Catalyst loading: 10 μg_{Pt} cm^{-2}. The current is referred to $A_{sur,CO}$.

This "pre-peak" (32.1 μC cm^{-2}) shows no clear maximum and can be selectively oxidized by holding the potential on the onset of this shoulder (430 mV) for two minutes (dashed line), whereas the position and the charge under the main peak does not change (186.2 μC cm^{-2}).

The narrow main peak is observed at around 810 mV which is close to the position of the peak observed on the pure platinum nanoparticles obtained from the research group in Mülheim.

3.2. MODIFIED PLATINUM NANOPARTICLES

3.2.1. Platinum nanoparticles modified with Ru

In this part, two different methods of Ru deposition (see chapter 2.4.) on PtO_x^E/C will be compared. The catalyst will be characterized by means of the oxidation of pre-adsorbed carbon monoxide and the Cu_{UPD}.

The CO_{ad} oxidation on PtO_x^E/C nanoparticles modified *via* the spontaneous deposition under different conditions is compared in Figure 3-4a. The concentration of the Ru solution (2-10 mM $RuCl_3$ in 0.5 M H_2SO_4) as well as the deposition time (1-3 min) is varied. It is clearly seen that at low concentrations ($2 \cdot 10^{-3}$ M $RuCl_3$) and short deposition times the Ru precipitation is low.

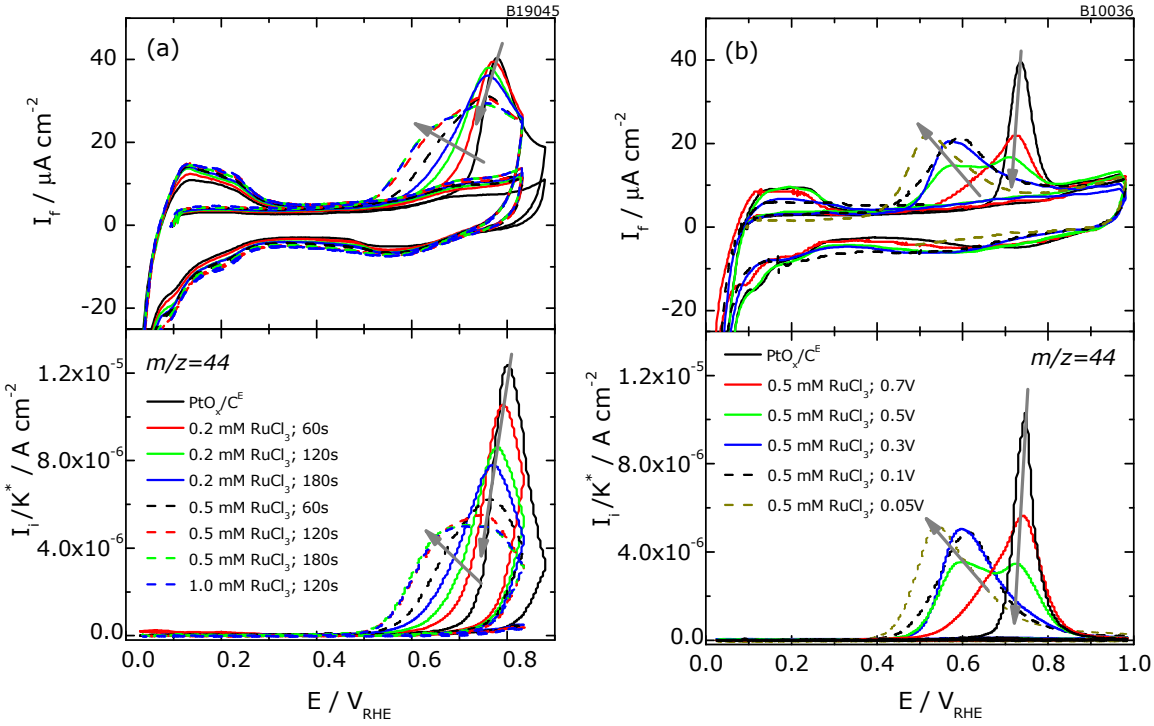

Figure 3-4 Simultaneously recorded faradaic and corresponding ion currents of CO_2, m/z=44, during oxidation of CO adsorbed on Ru modified PtO_x^E/C nanoparticles in 0.5 M H_2SO_4. (a) OCP-deposition of Ru. (b) Electrochemical deposition of Ru for 5 minutes from 0.5 mM $RuCl_3$ at given potential. Scan rate: 10 mV s^{-1}. Electrolyte flow rate: 5 μL s^{-1}. Catalyst loading: 10 μg_{Pt} cm^{-2}. The current is referred to $A_{sur,CO}$.

The maximum achievable coverage (0.2 ML according to [65]) using spontaneous deposition is reached after 2 minutes from a $5 \cdot 10^{-3}$ M $RuCl_3$ solution. This coverage does not change even at longer period of Ru deposition and higher concentration of the Ru solution. With increasing Ru content, the onset of the CO stripping is shifted to lower potential and the maximum gets broader.

In the case of the electrochemical deposition (t_{dep}=5 minutes) not only a Ru coverage higher than 0.2 ML but also Ru-multilayers can be achieved (Figure 3-4b). On the basis of the CO stripping voltammograms, the effect of Ru is clearly seen. Please note that the Ru coverage is roughly estimated according to [81][249] and will be discussed below in detail (Table 3-2). With increasing Ru coverage up to 0.5 ML (E_{ad}=500 mV) the onset of the CO oxidation is strongly shifted to lower potential. This is consistent with literature [114, 250] where it was found that the most active surface for the oxidation of adsorbed CO was an alloy with a Ru surface composition of ≈ 50 at.%. At a higher coverage of ca 0.75 ML (E_{ad}=300 mV) no further shift is observed. At about 0.5 ML of Ru a second peak at more negative potentials appears. As the Ru coverage further increases this peak becomes more pronounced and the peak at higher potentials is diminished.

Voltammograms of Cu_{UPD} stripping on pure and Ru modified PtO_x^E/C substrate are shown in Figure 3-5. Please note that these electrodes are the same as used in the previous experiment in Figure 3-4.

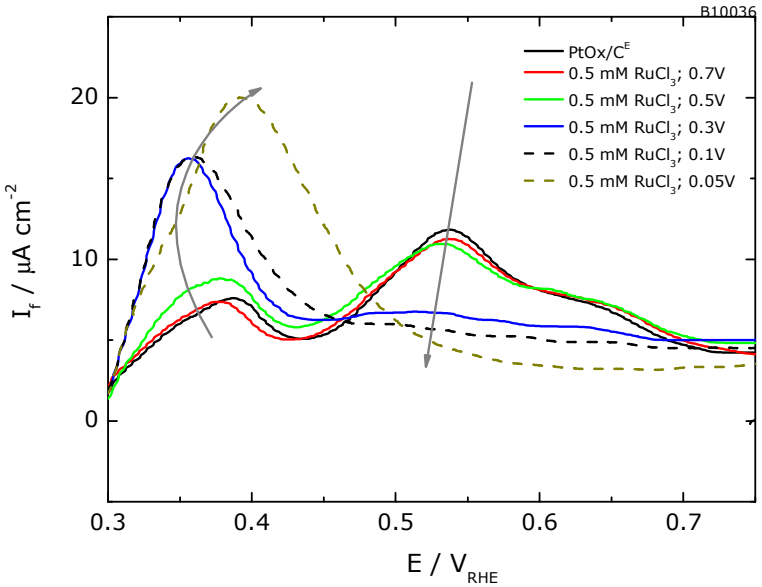

Figure 3-5 Recorded faradaic currents of Cu-desorption from PtO_x^E/C nanoparticles modified by electrochemical deposition of Ru (from 5 mM $RuCl_3$ for 5 minutes) in 0.5 M H_2SO_4. Scan rate: 10 mV s^{-1}. Electrolyte flow rate: 5 µL s^{-1}. Catalyst loading: 10 μg_{Pt} cm^{-2}. The current is referred to $A_{sur,CO}$.

The peaks observed on the pure PtO_x^E/C show similar behaviour to that observed for polycrystalline platinum [245] and nanoparticulate Pt electrodes [245, 251]; differences might be due to differences in crystal facets and the nanoparticulate nature of Pt used in this work.
On Ru modified PtO_x^E/C, the peak for Cu at 380 mV shifts to lower potentials, whereas the broader peak at higher potentials starts to diminish when the Ru content is close one monolayer. On Ru-multilayers, only a single peak at the negative potential is observed. These findings are in good agreement with those of Green and Kucernak [245, 251]. In their study it was already shown that the first peak is caused by the removal of copper deposited on Ru sites alone and the broader feature at higher potential is the removal from the Pt sites.

The Cu_{UPD} charge is determined by the integration of the current between 300 and 700 mV. The surface areas calculated using Equations 2-6 and in the case of Ru-multilayers using Equation 2-7, are summarized in Table 3-2.

Table 3-2 Summary of the features in COad stripping and calculated surface areas on Ru modified PtOxE/C nanoparticulate surfaces

Θ_{Ru}	A_{exp} / cm^2				Θ_{Ru}^{Cu}	CO oxidation (5 mV s^{-1})	
	$A_{sur,CO}$	$A_{sur,Cu,Pt+Ru}$	$A_{sur,Cu,Pt}$	$A_{sur,Cu,Ru}$		E^{onset} / mV	E^{max} / mV
0	2.24	2.62	2.62	0	0	450	770
0.25	2.09	2.42	2.85	0.57	0.24	390	750
0.45	1.97	2.21	1.29	0.92	0.42	385	595/730
0.75	1.87	2.16	0.58	1.58	0.73	380	595
≈ 1	2.25	2.64	0.16	2.48	0.94	375	600
> 1	2.62	3.12	<1	3.12	>0.99	350	540

Θ_{Ru}, Ru coverage according to [249]; Θ_{Ru}^{Cu}, Ru coverage determined by Cu_{UPD}; $A_{sur,CO}$, surface area determined by CO oxidation; $A_{sur,Cu}$, surface area determined by Cu_{UPD} oxidation; E^{onset}, potential of onset ion current; E^{max}, potential of maximum ion current

Additionally to the overall surface area, also the surface area corresponding to Pt and Ru sites can be determined from the Cu_{UPD} oxidation charge under the first (ca 300-450 mV) and second peak (450-700 mV).
The Ru-coverage on the surface can be than determined as follows:

$$\Theta_{Ru}^{Cu} = \frac{Q(Cu_{upd})_{Ru}}{Q(Cu_{upd})_{Pt+Ru}} \qquad \text{(Equation 3-1)}$$

where $Q(Cu_{upd})_{Ru}$ is the oxidation charge under the first peak (300-450 mV) and the $Q(Cu_{upd})_{Pt+Ru}$ is the oxidation charge over the whole potential region (300-700 mV). The Ru coverage calculated from the Cu_{UPD} oxidation, Θ_{Ru}, is consistent with the pre-estimated coverage, Θ_{Ru}.

The overall surface areas calculated from the Cu desorption agrees to within 20% with the surface area calculated from the amount of CO_2 detected during the CO stripping experiment. The non-faradaic contributions to the Cu desorption charge are assumed to be small. Since Ru is covered by anionic species at 300 mV, it can be concluded that, on the Cu, nearly the same amount of anions are adsorbed as on the bare Ru. It is also possible that 10-20% Cu atoms can be adsorbed at the edge sites in addition to the full coverage corresponding to a Pt:Cu ration of 100%. However, these should not be strongly bound and desorb at potentials close to the bulk Cu dissolution and so, they are probably not included in our integration.

3.2.2. Platinum nanoparticles modified with Se

The CO stripping experiments on a PtO_x^E/C surface modified with sub-monolayers of Se are shown in Figure 3-6.

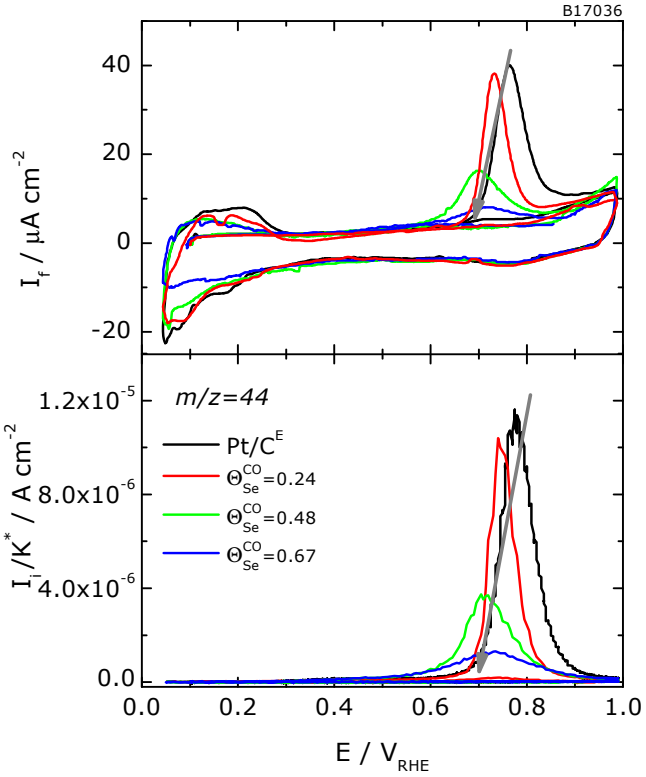

Figure 3-6 Simultaneously recorded faradaic currents and corresponding ion currents of CO_2, m/z=44, during the oxidation of CO adsorbed on selenium modified PtO_x^E/C nanoparticles in 0.5 M H_2SO_4. Scan rate: 10 mV s^{-1}. Electrolyte flow rate: 5 µL s^{-1}. Catalyst loading: 10 μg_{Pt} cm^{-2}. The current is referred to $A_{sur,CO}$.

The CO oxidation peak shifts slightly, by about 60 mV, to more negative potentials and the CO oxidation peak becomes broader as the selenium content increases. The high potential, which is still needed for complete CO oxidation, points at the existence of an inhibition effect on the CO oxidation caused by the high surface concentration of the Se ad-atoms. Also the decrease of the amount of adsorbed and oxidized CO with increase in the Se coverage is observed. At full Se coverage, the CO adsorption is totally suppressed (not shown here); which is consistent with literature [102, 104].

From these experiments also the relative surface coverage is calculated using Equation 2-12. For comparison, the coverage with Se is determined also by the charge of hydrogen adsorption in the range of 50- 350 mV:

$$\Theta_{Se}^{H} = 1 - \frac{Q_{MSe}^{H}}{Q_{M}^{H}} \qquad \text{(Equation 3-2)}$$

where Q^{H}_{MSe} is the H_{UPD} charge on Se modified surface and Q^{H}_{M} is the H_{UPD} charge on Se free surface. Both are determined without any subtraction of a double layer charge. The results are summarized in Table 3-3. It is clearly seen, that at least in the case of Se modified PtO_x^E/C nanoparticle electrodes, both methods for the determination of the Se coverage give similar results.

In Figure 3-7, the CV´s of these electrodes in Cu-containing sulfuric acid are shown. The peak for the CU-UPD dissolution appears at about 360 mV for Se on platinum and increases strongly for high Se coverages, as observed for Se modified polycrystalline Pt [100, 247].

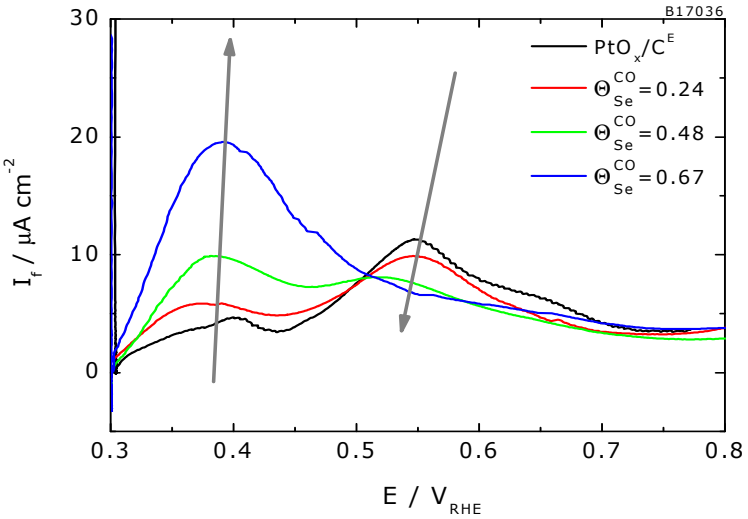

Figure 3-7 Recorded faradaic currents of Cu-desorption from PtO_x^E/C nanoparticles modified by selenium in 0.5 M H_2SO_4. Scan rate: 10 mV s^{-1}. Electrolyte flow rate: 5 µL s^{-1}. Catalyst loading: 10 μg_{Pt} cm^{-2}. The current is referred to $A_{sur,CO}$.

The faradaic charge for the removal of Cu_{UPD} does not change with the Se coverage up to ca 0.5ML, but it is increased at the Se coverage of 0.67 ML. Nagel et al. [246, 247] showed that at polycrystalline platinum and Pt(111) for coverages of Se higher than 0.6 the Cu charge increases possibly due to the formation of Cu_xSe [252].

Table 3-3 Summary of the features in CO_{ad} stripping and calculated surface areas at Se modified nanopartilulate PtO_x^E/C electrodes

Θ_{Se}		A_{exp} / cm^2		CO oxidation (5 mV s^{-1})	
CO	H	$A_{sur,CO}$	$A_{sur,Cu}$	E^{onset} / mV	E^{max} / mV
0	0	2.82	3.21	450	775
0.24	0.21	2.13	2.86	445	750
0.48	0.42	1.45	3.02	445	710
0.67	0.63	0.92	3.95	445	715

Θ_{Se}, Se coverage ; E^{onset}, potential of onset ion current; E^{max}, potential of maximum ion current

The mass spectrometrically determined amount of CO_2 formed gives a more reliable measure for the surface area, provided that the maximum coverages are constant and independent of the particular surface. From the MSCV during the CO oxidation, it is clearly seen that CO does not adsorb on Pt saturated by Se. For surfaces partially covered by Se, a comparison of the charge measured by cyclic voltammetry in the hydrogen region with the mass spectrometrically determined amount of CO_2 suggests that the latter can be used for a determination of the area not covered by Se. Cu upd, on the other hand, also takes place on surfaces completely covered by Se; the Cu desorption charge is independent of the Se coverage on Pt as long as it does not exceed 70% of full coverage [247].

3.2.3. Platinum nanoparticles modified with Ru and Se

Oxidation of CO adsorbed on PtO_x/C^E nanoparticles modified by 0.25 ML of Ru (electrodeposited from 0.5 mM $RuCl_2$ at 700 mV for 5 min), denoted as $Ru_{0.25}$, and different Se coverages is shown in Figure 3-8.

As shown in chapter 3.2.2 for PtO_x^E/C the amount of adsorbed CO decreases with increasing Se coverage. On platinum surfaces partially covered with Ru, the CO oxidation peak slightly shifts by about 20 mV to higher potentials with increasing Se content and the shoulder found on PtO_x^E/C modified by 0.25 ML Ru is diminished. Selenium obviously overcompensates the catalytic effect of Ru.

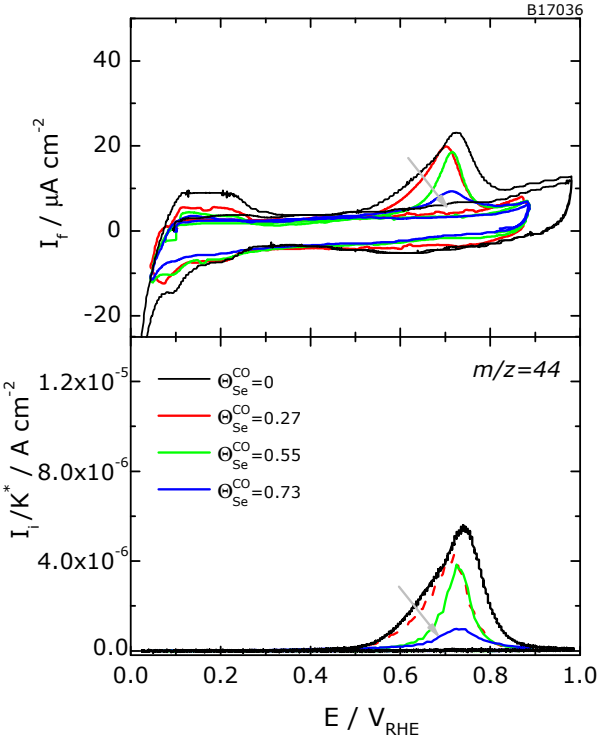

Figure 3-8 Simultaneously recorded faradaic currents and corresponding ion currents of CO_2, m/z=44, during the oxidation of CO adsorbed on $Ru_{0.25}$ and Se modified PtO_x^E/C nanoparticles in 0.5 M H_2SO_4. Scan rate: 10 mV s^{-1}. Electrolyte flow rate: 5 µL s^{-1}. Catalyst loading: 10 μg_{Pt} cm^{-2}. The current is referred to $A_{sur,CO}$.

Also for these surfaces, the relative Se coverage is determined according to the previous chapter and the calculated values are collected together with the important peak features for the CO oxidation in Table 3-4.

The copper desorption from the $Ru_{0.25}$ and Se modified PtO_x^E/C is shown in Figure 3-9.

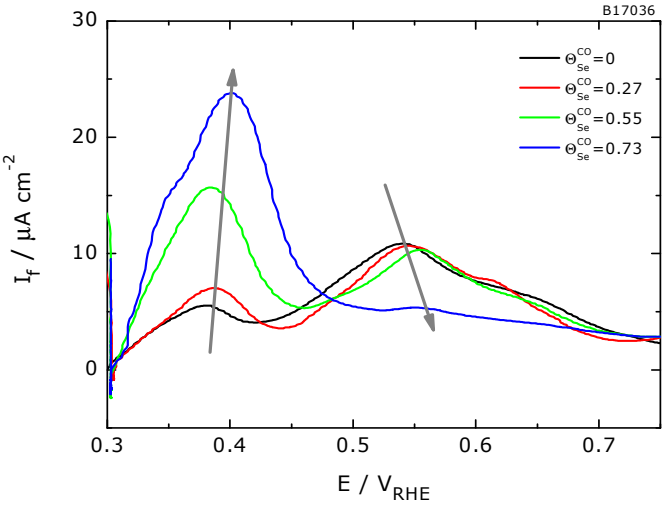

Figure 3-9 Recorded faradaic currents of Cu-desorption from PtO_x^E/C nanoparticles modified by $Ru_{0.25}$ and Se in 0.5 M H_2SO_4. Scan rate: 10 mV s^{-1}. Electrolyte flow rate: 5 µL s^{-1}. Catalyst loading: 10 μg_{Pt} cm^{-2}. The current is referred $A_{sur,CO}$.

The broader feature at higher potentials caused by removal of Cu from the Pt sites (550 mV) slightly decreases as the Se content increases; similarly as observed for PtO_x^E/C/Se system. In contrast, the first peak (380 mV) caused by removal of copper deposited on Ru sites alone increases.

As mentioned before, also here the Cu_{UPD} charge was determined by integration between 300 and 900 mV and the surface areas calculated using Equations 2-6 are summarized in Table 3-4.

Table 3-4 Summary of the features in CO_{ad} stripping and calculated surface areas at Se modified PtO_x^E/C electrodes with Ru ($\vartheta_{Ru}\approx0.25$)

Θ_{Se}		A_{exp} / cm^2		CO oxidation (5 mV s^{-1})	
CO	H	$A_{sur,CO}$	$A_{sur,Cu}$	E^{onset} / mV	E^{max} / mV
0	0	2.82	3.21	390	750
0.27	0.24	2.07	2.76	390	720
0.55	0.52	1.19	2.90	390	730
0.73	0.73	0.57	4.61	390	735

Θ_{Se}, Se coverage; E^{onset}, potential of onset ion current; E^{max}, potential of maximum ion current

3.3. POTENTIOSTATIC AND GALVANOSTATIC OXIDATION OF ADSORBED CO

To examine the mechanism of the CO ad-layer oxidation in more detail, potential step and galvanostatic experiments are carried out on polycrystalline Pt and PtO_x^E/C nanoparticles. Also in these experiments, CO is first adsorbed and then the electrolyte is exchanged for a CO-free solution.

3.3.1. Chronoamperometry

First, preliminary experiments are done without any convection of the electrolyte using a simple H-cell (A_{geo}=0.785 cm^2). Figure 3-10 represents current-time transients recorded during CO monolayer oxidation after stepping the potential from 50 mV (RHE) to the potential located on the onset of the CO oxidation peak found in cyclic voltammetry.

The current transients on both, Pt(pc) and PtO_x^E/C nanoparticle electrodes, exhibit a fast rise after the potential step is applied, then the current decays and a current maximum (or shoulder) is developed. This fast arise in the current is caused by capacitive contributions (double layer charging). This is very similar to the previous observations on polycrystalline Pt [110], Pt single crystals [137, 139] and Pt nanoparticles [9, 13, 140-142].

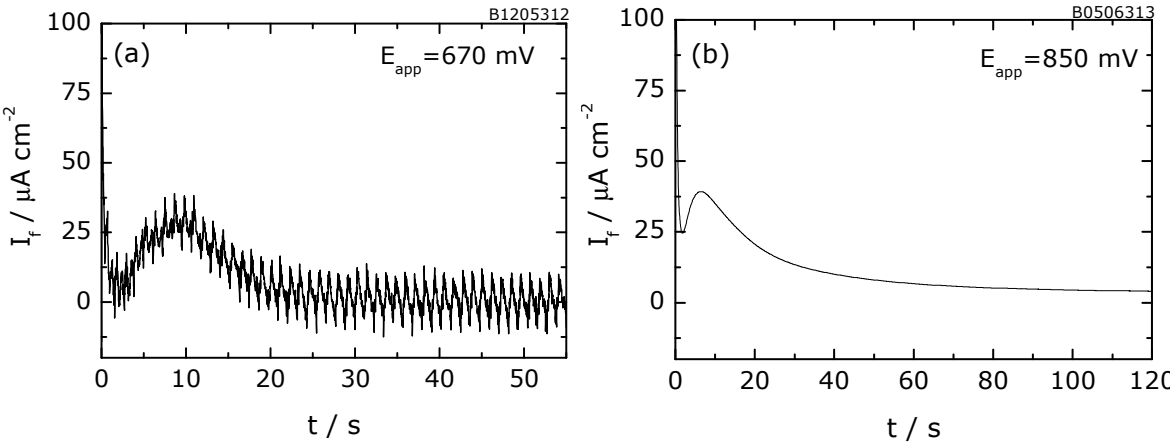

Figure 3-10 H-cell experiment: Potentiostatic electrooxidation of adsorbed CO from saturated CO solution on (a) Pt(pc) at E_{app}=670 mV and (b) nanoparticle electrode (PtO_x^E/C) at E_{app}=850 mV in 0.5 M H_2SO_4. Catalyst loading: 10 μg_{Pt} cm^{-2}. The current is referred to $A_{sur,CO}$.

Moreover, from the current transient of the mass spectrometric signal for CO_2, it is clear that the exponential decaying current in Figure 3-11a is due to the oxidation of weakly adsorbed CO (the "pre-peak" in CV) and cannot result from the double layer charging.

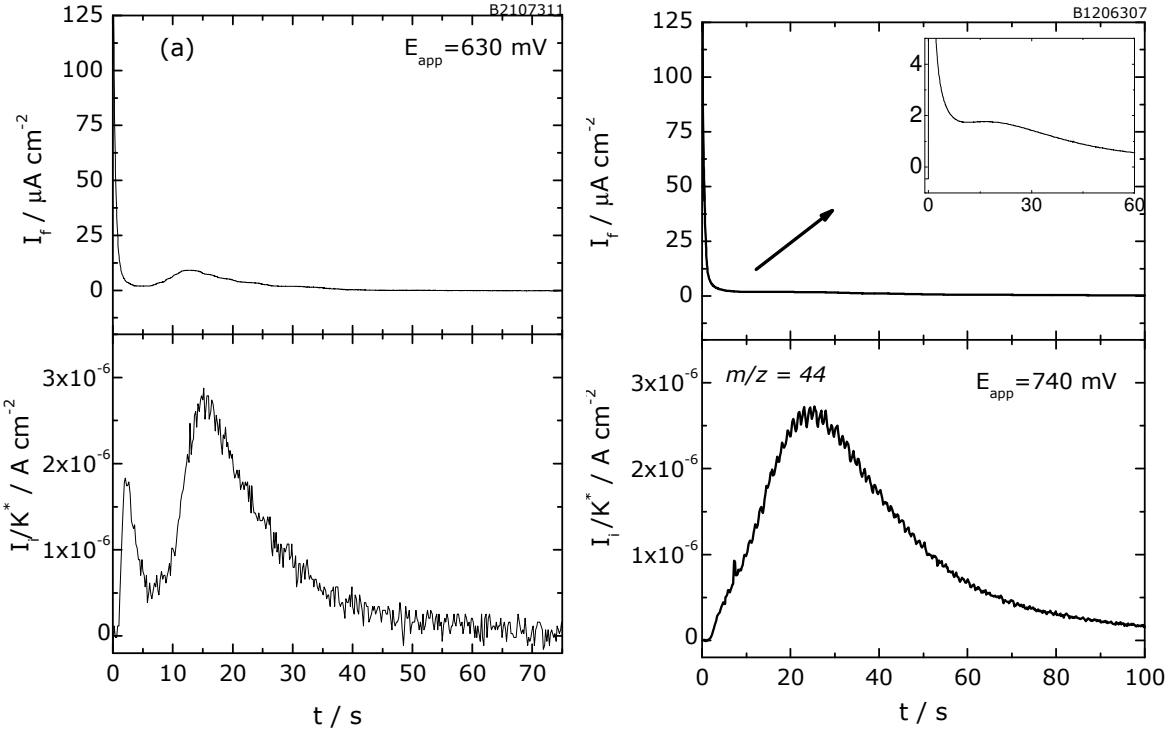

Figure 3-11 DEMS experiment: Potentiostatic electrooxidation of adsorbed CO from saturated CO solution on (a) Pt(pc) at E_{app}=630 mV and (b) PtO_x^E/C electrode at E_{app}=740 mV in 0.5 M H_2SO_4. Electrolyte flow rate: 5 µL s^{-1}. Catalyst loading: 10 μg_{Pt} cm^{-2}. The current is referred to $A_{sur,CO}$.

The current transient for the adsorbed CO on the PtO_x^E/C nanoparticle electrode (Figure 3-11b) showed the typical current maximum [9]. Gustavsson et al. [253] found the same behaviour on Pt/C model catalysts as in our case of polycrystalline Pt. Nevertheless the PtO_x/C^E catalyst used in this study showed also some kind of a "pre-peak" at low potentials together with a split in the maximal current peak in the cyclic voltammetry. The asymmetric shape of the ion current transients points at an instantaneous nucleation of OH and the onset of CO oxidation immediately after the potential step [254].

Note that the ionic charge under the transients corresponds within ±10% to the charge observed under the CO oxidation peak in the cyclic voltammetry.

3.3.2. Chronopotentiometry

The chronoamperometric results were corroborated by galvanostatic oxidation experiments. Chronopotentiometry allows a faster discrimination of the catalytic characteristics of the surface.

As already described by Massong et al. [154], such measurements are much better suited, than the cyclic voltammetry, for fast discrimination between reaction mechanisms, e.g. Langmuir-Hinshelwood or Eley-Rideal types. At the beginning of the oxidation reaction, since the surface is completely covered with CO, the nucleation/growth mechanism (corresponding to a Langmuir-Hinshelwood mechanism with slow or no diffusion [254, 255]) is expected. This means that the nucleation has to proceed to create some free adsorption sites for oxygen. In the case of processes involving nucleation, galvanostatic experiments also offer the advantage that the growth can be monitored at low rates (given by the preset current value), whereas in the potentiostatic or potentiodynamic experiments, the growth process occurs at a much larger rate than the initial nucleation.

The rate, *r*, for the Eley-Rideal mechanism, where one of the reactants from the solution phase reacts with one that is adsorbed on the surface without itself adsorbing on the surface (in our case, adsorbed CO) prior to reaction, is given by

$$r = \frac{\mathrm{d}\Theta}{\mathrm{d}t} = k_{ox}(E) \cdot \Theta \qquad \text{(Equation 3-2)}$$

where $k_{ox}(E) = k^0 \cdot exp\left(\frac{\alpha \cdot n \cdot F \cdot E}{R \cdot T}\right)$.

In the case of the galvanostatic experiments, where the current, *i*, and thus, the rate, *r*, are kept constant, the potential obeys a logarithmic characteristic related to the linear decrease of the coverage with the time.

However, in the Langmuir-Hinshelwood mechanism, where it is assumed that before the rate determining step all reactants are adsorbed on the surface, the rate constant, *r*, is given by

$$r = \frac{\mathrm{d}\Theta}{\mathrm{d}t} = k_{ox}(E) \cdot \Theta \cdot (1 - \Theta) \qquad \text{(Equation 3-3)}$$

Since *r* is kept constant and $\Theta(1-\Theta)$ has a maximum for $\Theta=0.5$, the potential reaches a minimum at this coverage.

Preliminary experiments, without any convection of the electrolyte, were also performed in the H-cell (A_{geo}=0.785 cm^2). The potential transient observed during the oxidation of adsorbed CO on polycrystalline Pt (Figure 3-12a) shows a potential maximum which corresponds to a nucleation overpotential, but can also be explained by a "simple" Langmuir-Hinshelwood mechanism [87, 256]. The potential maximum observed during galvanostatic oxidation on the PtO_x^E/C nanoparticles (Figure 3-12b) is less defined than that observed on the Pt(pc). In both cases, the value of the potential maximum corresponds to the onset potentials of the main peak in cyclic voltammetry. In the case of polycrystalline platinum, the slow increase of potential at the beginning of the oxidation is believed to be due to the transition from the compressed CO ad-layer to the decompressed ad-layer and corresponds to the pre-peak.

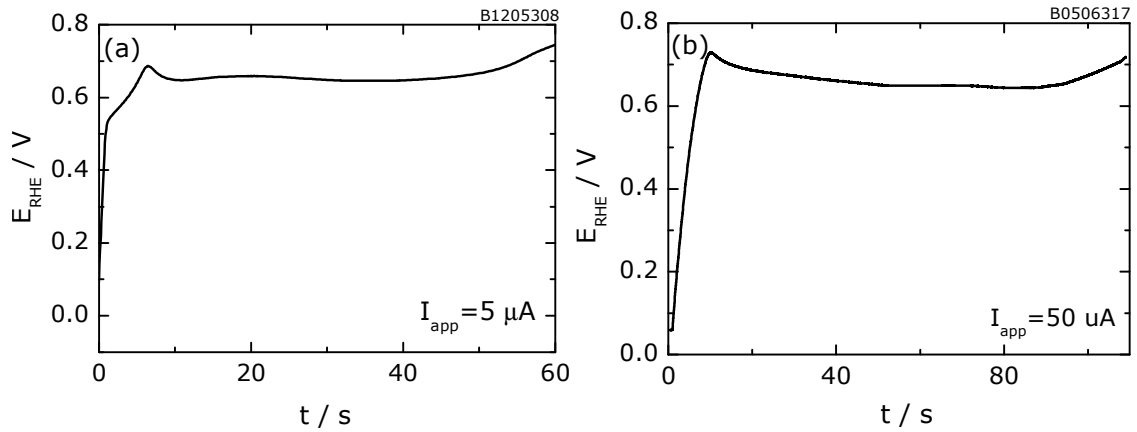

Figure 3-12 H-cell experiment: Galvanostatic electrooxidation of adsorbed CO from saturated CO solution on (a) Pt(pc) at I_{app}=5 µA and (b) PtO_x^E/C nanoparticle electrode at I_{app}=50 µA in 0.5 M H_2SO_4. Catalyst loading: 10 μg_{Pt} cm^{-2}. The current is referred to $A_{sur,CO}$.

This was confirmed by DEMS measurements (Figure 3-13a), where a small amount of CO_2 is found to be produced in a separate peak at the same time, when this small potential plateau is observed in the potential transients. This is then absent in the case of the galvanostatic oxidation of pre-adsorbed CO at PtO_x^E/C, as shown in Figure 3-13b.

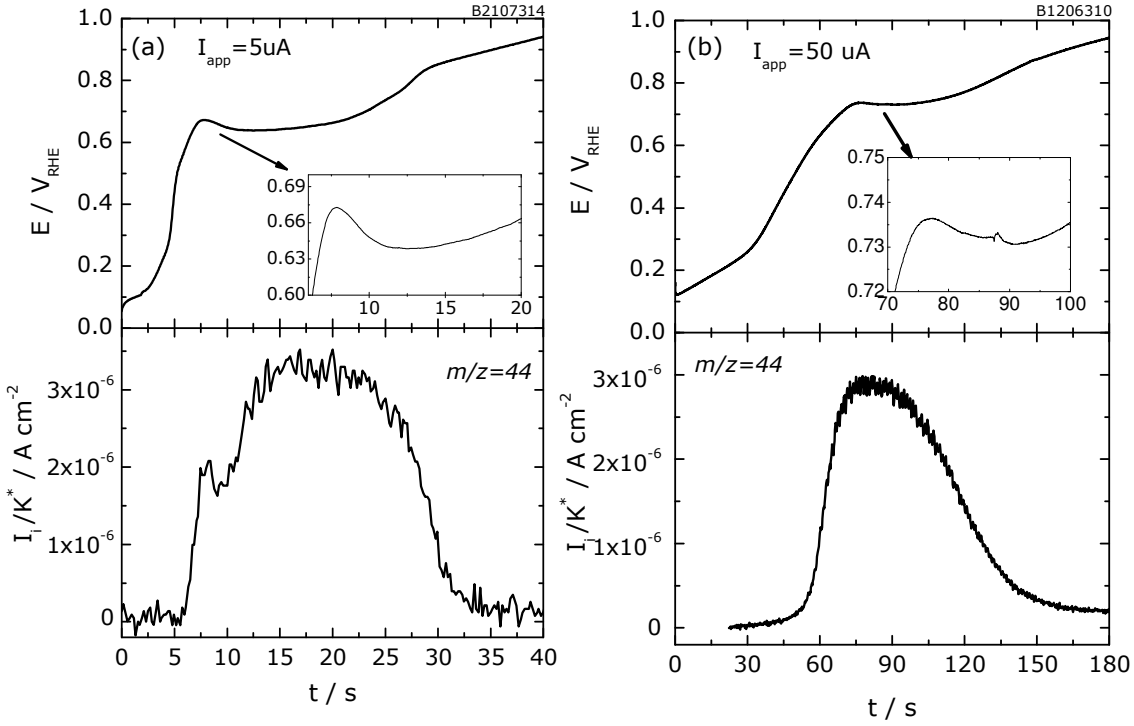

Figure 3-13 DEMS experiment: Galvanostatic electrooxidation of adsorbed CO from saturated CO solution on (a) Pt(pc) at I_{app}=5 μA and (b) PtO_x^E/C nanoparticle electrode at I_{app}=50 μA in 0.5 M H_2SO_4. Electrolyte flow rate: 5 μL s^{-1}. Catalyst loading: 10 μg_{Pt} cm^{-2}. Current is referred to $A_{sur,CO}$.

3.4. DISCUSSION AND REMARKS

In this chapter the catalytic activity of the studied surfaces for the CO oxidation reaction and the determination of the real surface area using the stripping of pre-adsorbed CO and the Cu underpotential deposition are discussed.

The main features of the CO stripping curves are collected in Table 3-5. Within a factor of two, the real surface area, calculated from the CO stripping, agrees with that determined from the particle size assuming a narrow distribution and a spherical shape for the colloid particles (theoretical surface area, A_{theor}), showing that the catalyst is completely active. Interestingly, at $PtRuOsIrO_x^M$/C, the real surface area determined by the CO oxidation is much smaller than the theoretical one. Ir probably has a high affinity to oxygen and thus IrO_2 is segregating to the surface. Such dioxides then block the surface against the adsorption of CO.

On pure PtO_x^E/C, the determination of the active surface area by H_{UPD} (taking the CV of the CO covered electrode as the background, cf. [9]) leads to a surface area of only 2.8 cm^2. This might suggest, that the CO coverage is close to one, as assumed in [9, Friedrich, 2000 #2017] instead of 0.7, as assumed in the calculations. On the other hand, since CO ad-layers often correspond to close packed layers independent of the crystallographic orientation, whereas the charge in the hydrogen region is very sensitive to the crystallographic orientation and anion effects, we believe that the H-coverage is smaller on Pt/C nanoparticles. The experiments involving Cu_{UPD} on the Pt/C nanoparticles produced charges which agree very well with the area determined from CO adsorption (assuming coverage of 0.7).

Table 3-5 Summary of the features in CO_{ad} stripping and calculated surface areas on different nanoparticulate electrodes

surface	∅ / nm	$A_{sur,CO}$ / cm^2	A_{theor} / cm^2	CO oxidation	
				$E^{10\%}$ / mV	E^{max} / mV
PtO_x^E/C	2	4.4	3.9	700	790
PtO_x^M/C	1.9	5.5	4.2	720	820
$PtRu^E/C$	2	6.0	7.5	570	775
$PtRuO_x^M/C$	1.8	7.2	7.9	500	730
$PtRuOsIrO_x^M/C$	1.6	3.6	11.6	420	810

∅, particle size*; A_{exp} E^{max} ,* potential of ion current maximum; *$E^{10\%}$,* potential at which the ion current reaches 10% of the ion current maxima.

The agreement of the area determined by the CO and Cu_{UPD} stripping indicates that the assumption of a maximum coverage 0.7 ML also holds for the modified nanoparticle surfaces. The surface areas calculated from the Cu desorption charges agree to within 20% with the surface area calculated from the amount of CO_2 detected during the CO stripping experiment.

The oxidation process for a saturated layer of CO on $Ru_{0.25}$-modified Pt nanoparticles is found to change significantly as the coverage of Ru changes. Contrary to the PtRu/C alloys, it is clearly seen that the oxidation of the CO takes place in two overlapping peaks, which may be attributed to the different surface phases. A similar, although more pronounced effect was reported in the literature for the Ru decorated Pt(111) [75, 83, 87, 154]. Especially, Wieckowski et al. [75] focused on the reactivity in the potential range of the second voltammetric peak at Pt(111)/Ru surface. Using double potential step chronoamperometric data, two components encoded into the current/time decay were found. The first exponential decay was ascribed to the oxidation of CO chemisorbed at the Pt sites neighbouring the Pt/Ru sites. The second

decay could be either attributed to a surface reaction between rapidly diffusing CO with the Pt/OH site at the Pt/Ru edge, or a diffusional tailing.

The peak splitting observed also at the $Ru_{0.25}$-decorated PtO_x^E/C nanoparticles was already reported by Tong et al. [159]. On the other hand, the stripping of CO_{ad} at the $PtRu^E$/C alloy is found to occur in a single peak, similarly to that found by Gasteiger et al. [250] on well-characterized Pt-Ru alloys. Thus, the presence of Pt and Ru domains on the surface seems to be a prerequisite of the peak splitting. One of the explanations suggests the peak splitting to the slow surface diffusion of CO_{ads} [81] or OH_{ads} [83] between Ru and Pt sites. The second one takes a low reactivity at the Ru/Pt edge [75] into account.

The increase of the Ru coverage leads to a slight shift of both oxidation peaks to lower potentials and to some decrease in the charge under the upper oxidation peak. This is in conflict with reports by Lee [157] and also Frelink [257] who observed no further reduction in the peak potential of CO oxidation after increasing the Ru beyond 15%. But so far, it is consistent with many other studies [146, 258-260]. It also indicates that such surfaces have a higher activity for the CO_{ad} oxidation than pure Pt surfaces.

On Ru-modified Pt nanoparticle surfaces, it is conceivable that the more negative peak corresponds to the CO oxidation on the Ru islands on Pt. In fact the charge under this peak is too large to refer solely to CO oxidation on the Ru islands; it should be assumed that the additional charge originates from the CO present on Pt-Ru edges (Pt sites adjacent to the Ru islands). According to the bifunctional mechanism, these sites are nucleation centres for oxygen-containing species at low electrode potentials and, thus, lower the onset potential of the CO oxidation. The more positive oxidation peak is then associated with the oxidation of CO on the remaining sites far away from ruthenium sites.

Additionally, it is shown that the presence of Se ad-atoms on the PtO_x^E/C and $Ru_{0.25}$-modified PtO_x^E/C surface not only modifies the distribution of the CO population on the surface, but also hinders the adsorption of CO on these sites. This clearly demonstrates that the calculation of the Se surface coverage using CO stripping experiments is possible.

The comparison of the faradaic current transients with the mass spectrometric transients after the potential step shows that these are largely identical at longer times, but that in the faradaic current signal, the initial phase is caused mostly by the double layer charging. In the mass spectrometric signal on polycrystalline platinum,

an initial sharp peak is clearly resolved, which, in this case, must be due to CO_2 formation and cannot result from double layer charging, followed by an exponential decay to the background level. Such pre-peak is not found for the nanoparticulate surface. The initial current increase and the decay developed before the onset of the maximum have been reported not only for single crystals [134, 261] and supported Pt nanoparticles [9, 13, 140, 141, 253], although some authors observed only a current maxima [254, 262]. It is obvious that the current transients progression strongly depends on the origin of the Pt nanostructure, particle size and particle distribution.

Let´s assume that the CO oxidation rate is directly and specifically reflected by the mass spectrometric signal of CO_2 (m/z=44). The relative CO_{ad} coverage transient during the potential step could be easily calculated by integration of the ion current transient and normalization with that of the saturation ad-layer (Figure 3-14).
The different behaviour in the relative coverage during the potential step on Pt(pc) and PtO_x^E/C is clearly seen. On polycrystalline Pt (Figure 3-14a), the CO coverage directly after the potential step decreases rapidly by 5-10%, which reflects the oxidation in the initial current spike. A kind of plateau appears when the reaction rate passes through a minimum at a relative coverage of about 0.9, and then decreases exponentially with time. The maximum reaction rate is reached at a relative coverage of 0.65. In the case of PtO_x^E/C (Figure 3-14b) only a slight decrease in the relative coverage is obtained promptly after the potential step for period about 15 seconds, and then exponentially declines. On the PtO_x^E/C, the maximum of the ion current is reached at a relative coverage of 0.68. It should be pointed out that in contrast to the essentially symmetric transient found at the Pt(pc) electrode, the transient observed at PtO_x^E/C is rather asymmetric.

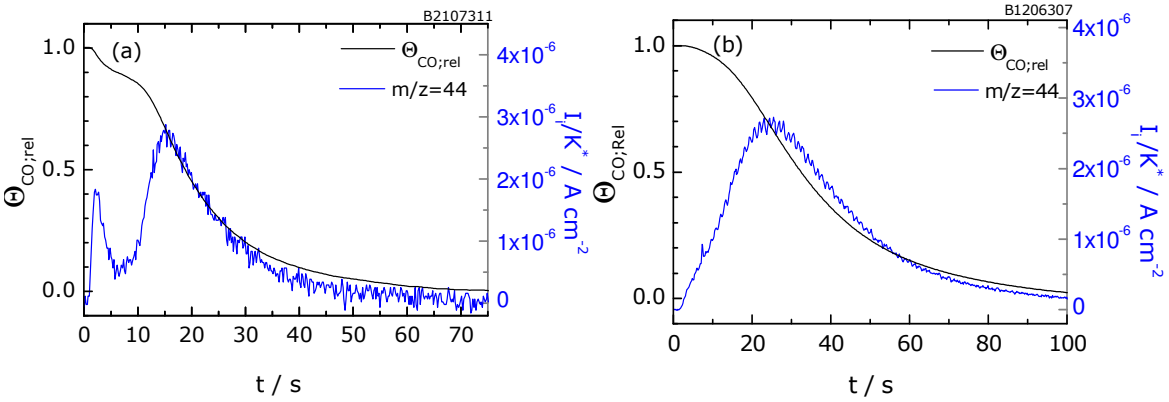

Figure 3-14 The relative CO coverage (black line) obtained by integration of the ion current signal (blue line) during chronoamperometry on (a) Pt(pc) at E_{app}= 630 mV and (b) PtO_x^E/C at E_{app}=740 mV in 0.5 M H_2SO_4. Electrolyte flow: 5 µL s^{-1}. Catalyst loading: 10 μg_{Pt} cm^{-2}. The current is referred to $A_{sur,CO}$.

The relative coverage can be converted to the absolute coverage by using the maximum achievable coverage 0.77 (CO molecules per number of Pt surface atoms) in the conversion. On both studied surfaces, the maximum reaction rate occurs at an absolute coverage close to that of 0.5 ML, which will be expected in the case of "simple" Langmuir-Hinshelwood reaction between adsorbed CO and oxygen containing (OH) species.

In order to quantitatively depict the CO monolayer oxidation at Pt surfaces a couple of models have been proposed. Generally, depending on the CO mobility on the surface, three limiting cases can be distinguished:

/1/ The first limiting case, the so called "mean-field" approximation, is based on an effective intermixing between CO_{ad} and OH_{ad} species, assuming fast diffusion of the reactants [134, 254]. This approach forecasts symmetric current transients with a maximum when half of the CO monolayer is converted to CO_2. This model describes the CO_{ad} oxidation at stepped single crystal electrodes very well [137, 139].

/2/ The second concept is based on the assumption that the OH_{ad} islands are nucleating at the free sites of the CO-covered platinum surface and growing *via* a consumption of immobile CO_{ad} at the rims of islands. This approach, named "nucleation-and-growth" model, results also in symmetric shapes of transients and gives an excellent correlation with the current transients of polycrystalline Pt [110].

/3/ The third – "active sites" model [9, 255]- assumes fast surface diffusion of adsorbed CO as in the case of the "mean-field" approximation, but also presumes that the reaction is taking place only at specific surface sites, e.g. at nanoparticle edges or corners.

Analogous to the chronoamperometric experiment, also the relative CO_{ad} coverage during the chronopotentiometric experiment can be calculated by integrating the ion current transient and normalized to that of the saturation ad-layer (Figure 3-15).

In the case of current controlled experiments, the reaction kinetics according to a "simple" Langmuir-Hinshelwood mechanism (a fast diffusion) leads to a potential minimum at a coverage of Θ=0.5. At the beginning of the potential transient, a potential maximum appears. As already mentioned above, this maximum corresponds to a nucleation overpotential, but could be also explained by the "simple" Langmuir-Hinshelwood mechanism: Due to the $\Theta(1-\Theta)$ term in the rate equation (Equation 3-3), at a constant rate the overpotential has to be high at high and low coverages, but low at medium coverages (Θ=0.5) [88].

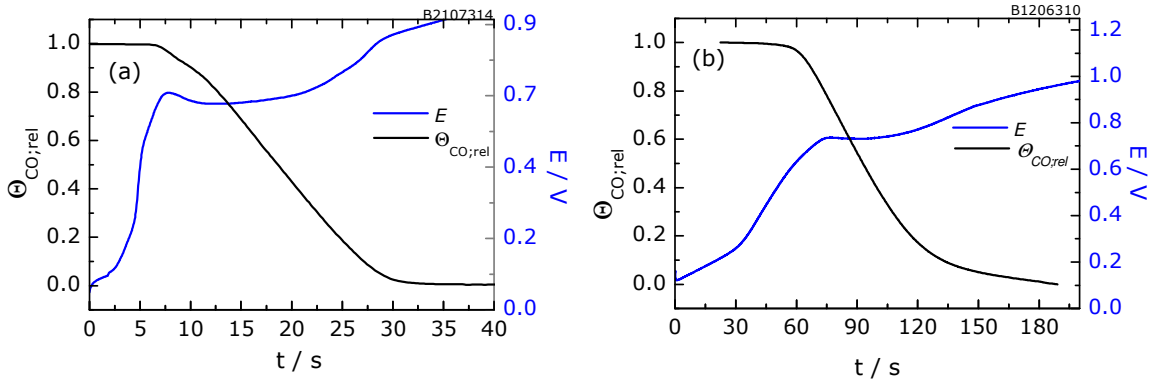

Figure 3-15 Relative CO coverage (black line) obtained by integration of the ion current signal (blue line) on (a) Pt(pc) at I_{app}=5 µA and (b) PtO_x^E/C nanoparticle electrode at I_{app}=50 µA in 0.5 M H_2SO_4 (DEMS). Electrolyte flow rate: 5 µL s^{-1}. Catalyst loading: 10 μg_{Pt} cm^{-2}.

On both surfaces, the transients pass through a clear minimum at intermediate coverages. Interestingly, the position of the minimum is observed at a coverage about 0.75 on the polycrystalline Pt (Figure 3-15a) and at 0.58 on PtO_x^E/C (Figure 3-15b), respectively. This is an argument against a pure Langmuir-Hinshelwood mechanism. Therefore, for a full description of the oxidation rate, a rate limiting surface diffusion and adsorption isotherms including repulsive terms have to be taken into account.

Similar behaviour was observed for stepped single crystals by Samjeske et al. [87], where the role of the steps for the continuous oxidation is demonstrated. On stepped surfaces with (110) steps orientation a minimum was found at coverages close to 0.5 or higher. It could be assumed that the steps act as nucleation centres due to their high catalytic activity. Whereas the (100) sites do not or less effectively act as nucleation sites due to their lower catalytic activity, the potential minimum is then expected before Θ=0.5 is reached.

Chapter 4 Measurements with isotopically modified CO

In this chapter, an interchange of methanol and carbon monoxide with its adsorbed species on Pt and platinum based electrodes in an acidic media is studied using isotopic labelling in combination with differential electrochemical mass spectroscopy (DEMS). In this manner, the contribution of species from methanol and CO during the electrooxidation of the co-adsorbate can be distinguished using isotopic labelled ^{13}CO.

4.1. Pt(665)

First of all, the measurements on Pt(665) surface with a defined structure are introduced. These experiments should provide a closer insight into the process of the electrocatalytic oxidation of CO and methanol, where, the effect of monoatomic steps and the catalytic effect of Ru on the electrooxidation reaction are of particular interest.

The profile of the cyclic voltammogram of the prepared Pt(665) – base CV- in 0.5 M H_2SO_4 (Figure 4-1), in the H-cell, is in good agreement with the data published in literature [37], confirming the surface crystalline order of the electrode and cleanliness of the system. The sharp peak at 110 mV originates from hydrogen adsorption on (110) steps and that at 420 mV corresponds to the order-disorder phase transition in the sulfate ad-layer [263]. Only few defects of (100) orientation can be seen at 248 mV.

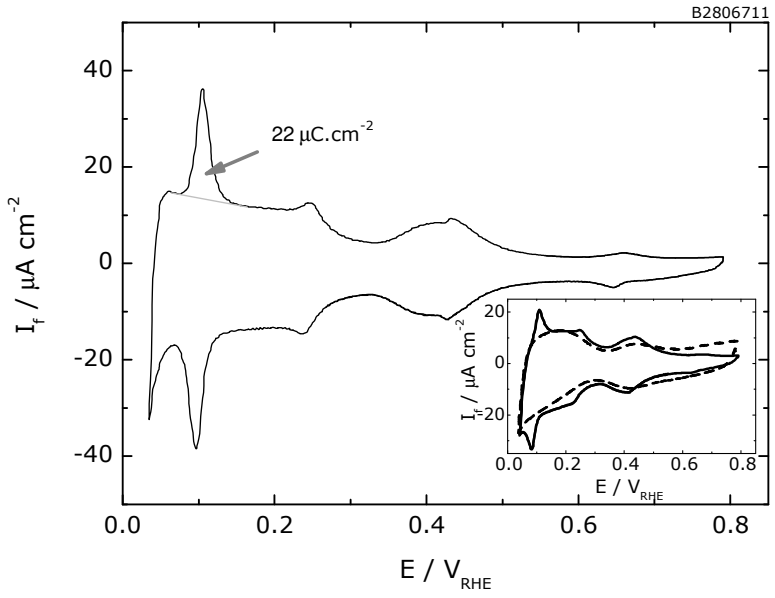

Figure 4-1 Basic CV of Pt(665) in H-cell after preparation in 0.5 M H_2SO_4. Scan rate: 20 mV s^{-1}. Inset: Basic CV in DEMS-Cell. Dashed line: $Ru_{0.2}$ decorated Pt(665) (Θ_{Ru}=0.2). Scan rate: 10 mV s^{-1}. The current is referred to $A_{sur,CO}$.

Experimental charges for the peaks, which corresponds to the hydrogen adsorption on step sites, are close to those expected theoretically [37]; the charge under the (110) adsorption peak is 22 $\mu C\ cm^{-2}$, as compared to a theoretical value of 21 $\mu C\ cm^{-2}$. Also the total charge between 50 and 750 mV of 285 $\mu C\ cm^{-2}$ is close to the value of 292 $\mu C\ cm^{-2}$ reported by Clavilier [37].

For comparison, the base CV´s of pure Pt(665) and also $Ru_{0.2}$-decorated Pt(665) in 0.5 M H_2SO_4, recorded in the DEMS-cell, are shown in the inset of Figure 4-1. It is clearly seen that the hydrogen adsorption on (110) is blocked due to the step decoration with Ru. The current increase above 600 mV in the anodic direction is caused by an adsorption of oxygen, which on Ru starts at considerably lower potentials than on pure Pt. A sole step decoration would correspond to approximately 10% Ru. The experimental conditions are selected in such a manner that, similarly to Pt(pc), the ϑ_{Ru}=0.2. Please note, the exact Ru coverage is not known.

4.1.1. Oxidation of CO-adsorbate

The voltammetric profile of the oxidation of adsorbed CO on the Ru-free surface starts around 440 mV with a symmetric narrow peak at 725 mV (Figure 4-2; dashed line). The small shoulder at the beginning (clearly seen in MSCV) corresponds to the transition from a compressed CO ad-layer to a decompressed adsorbate as mentioned in the previous Chapter.

This pre-peak is missing on $Ru_{0.2}$-decorated Pt(665) and the potential of the main peak is shifted downward to 515 mV. The increase of this peak is much sharper and narrower than that on pure Pt surface and an additional peak is observed at ca. 610 mV. These findings are in very good agreement with data published in literature [87, 88].

The peak at 515 mV originates from the oxidation of the less stable CO adsorbate chemisorbed on Ru and Ru adjacent sites. This CO adsorbate can be selectively oxidized by holding the potential at 370 mV, as shown in Figure 4-2 (green line), where only the remaining CO on terraces is present in the cyclic voltammetry. The current transients of CO_2 production during the electrooxidation of the less stable CO adsorbate on the steps at 370 mV (insets in Figure 4-2) reveal that about 38% of the total amount of adsorbed CO is oxidized (see Table 4-1). This confirms the assumption that under our conditions only the steps are decorated with Ru. The shape of this current transient points to Langmuir-Hinshelwood type of reaction mechanism.

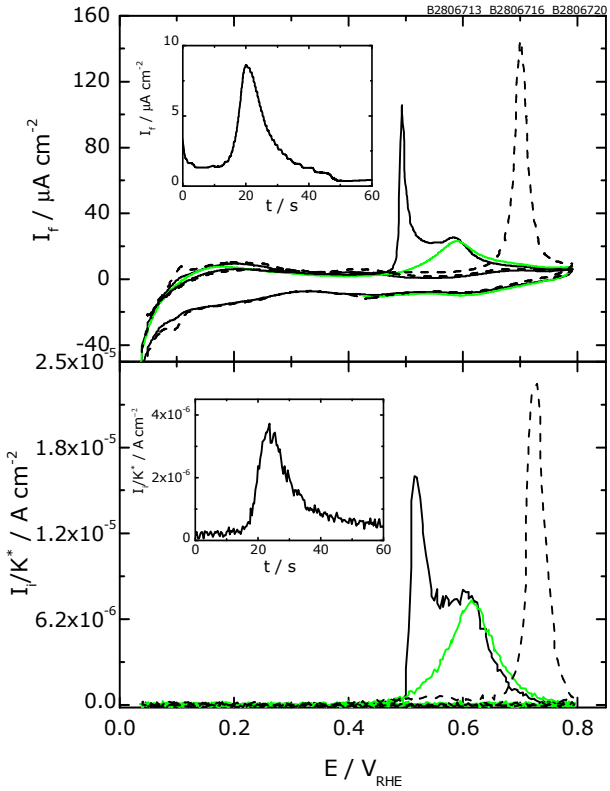

Figure 4-2 Simultaneously recorded faradaic currents and corresponding ion currents of $^{12}CO_2$, m/z=44, during oxidation of ^{12}CO adsorbed on $Ru_{0.2}$-decorated Pt(665) in 0.5 M H_2SO_4. Scan rate: 10 mV s^{-1}. Electrolyte flow rate: 5 µL s^{-1}. Green line: after oxidation of the "first peak" at 370 mV for 5 minutes, than going back to 50 mV. Dashed line: for comparison; oxidation of ^{12}CO adsorbed on pure Pt(665). Inset: Current transients during oxidation of "first peak" at 370 mV. Current is referred to $A_{sur,CO}$.

The values of the oxidation charges determined under the curves presented in Figure 4-2 are collected in Table 4-2. The charge found under the 2nd oxidation peak (after the oxidation of the 1st peak) is lower than expected from the overall charge. This indicates that about 10% of the CO adsorbate is lost during the back-sweep to 50 mV after the CO oxidation at 370 mV.

Table 4-1 Summary of the CO oxidation charge pictured in Figure 4-2

Surface	$Q_{f,true}$ / µC cm^{-2}
Pt(665)	255
Pt(665)/$Ru_{0.2}$	266
"1st peak" on Pt(665)/$Ru_{0.2}$	101
"2nd peak" on Pt(665)/$Ru_{0.2}$	140

$Q_{f,true}$, CO oxidation charge calculated using Equation 2-4. Where $K^* = 7.4 \times 10^{-6}$

Simultaneously a small $^{13}CO_2$ signal response is measured (not shown here). The small quantities (≈ 1-2%) of mass 45 ($^{13}CO_2$) are ascribed to the natural abundance of ^{13}C, which is also present in the ^{12}CO-solution [264].

The charge flow during the CO oxidation at stepped surfaces partially covered by Ru is usually found to be much larger than that on Ru-free surfaces [88]. It was shown that a Pt:Ru alloy electrode is covered by an anionic species even at 100 mV [22]. This species is displaced upon the adsorption of carbon monoxide and re-adsorbed during the CO oxidation. This leads to an additional charge for oxidation even after the background substraction. We therefore calculated the amount of adsorbed CO from the mass spectrometric ion currents. Using this method no differences between the amounts at adsorbed CO on Ru-free and $Ru_{0.2}$-decorated Pt(665) is found.

4.1.2. Oxidation of methanol adsorbate

In following experiments, methanol is adsorbed at a constant potential of 400 mV for 2 min from methanol containing electrolyte (0.1 M CH_3OH + 0.5 M H_2SO_4) at Pt(665) and $Ru_{0.2}$-decorated Pt(665). The faradaic and corresponding ion current transients on Pt(665) and $Ru_{0.2}$-decorated Pt(665) recorded during the adsorption of methanol are shown in Figure 4-3a. Such current transients are recorded for all methanol adsorption experiments. These will be evaluated in more detail in Chapter 7.

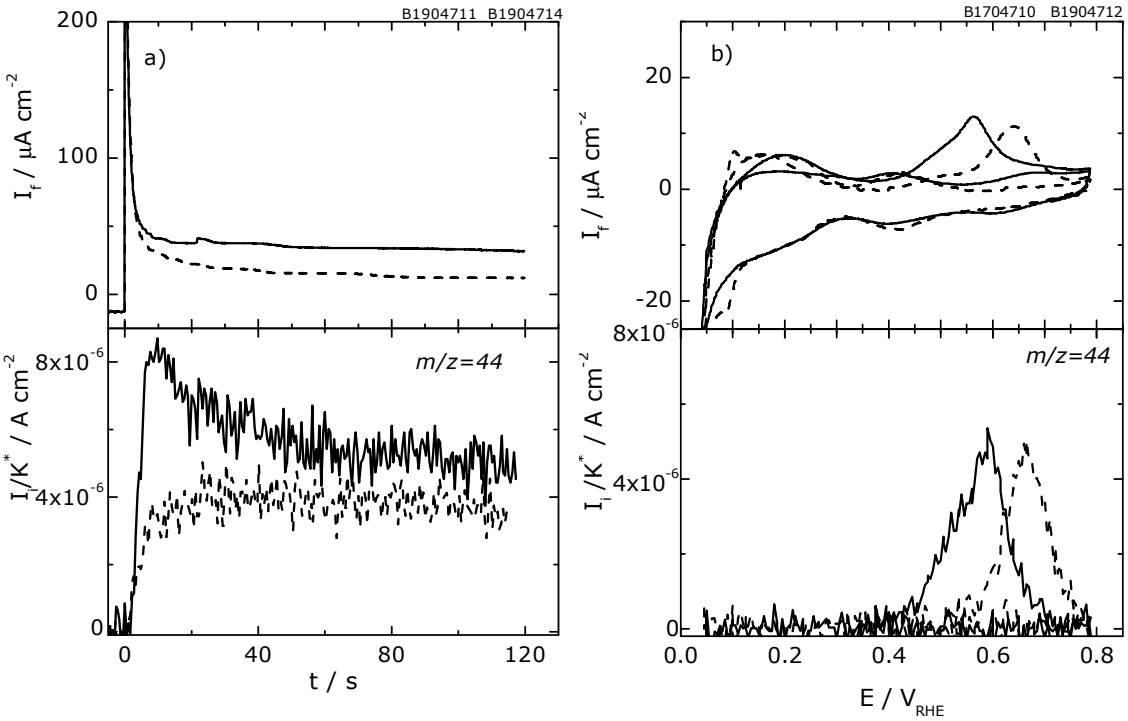

Figure 4-3 a) Simultaneously recorded faradaic and ion (m/z=44) current transients during methanol adsorption at 400 mV for 2 minutes on $Ru_{0.2}$-decorated Pt(665) in 0.5 M H_2SO_4 (solid line). b) Simultaneously recorded faradaic and corresponding ion currents of $^{12}CO_2$, m/z = 44, during oxidation of methanol adsorbed (E_{ad} = 400 mV, t_{ad} = 2min) on $Ru_{0.2}$-decorated Pt(665) in 0.5 M H_2SO_4 (solid line). Dashed line: on pure Pt(665). Scan rate: 10 mV s^{-1}. Electrolyte flow rate: 5 µL s^{-1}. The current is referred to $A_{sur,CO}$.

The onset of oxidation of the methanol adsorption product (hereafter called "methanol adsorbate") on Ru-free Pt(665) is found at 480 mV followed by

a maximum at 665 mV, whereas on the $Ru_{0.2}$-decorated electrode the electrooxidation of the methanol adsorbate starts already at 410 mV; additionally the maximum is shifted to lower oxidation potential of about 590 mV (Figure 4-3b). The oxidation peak on the $Ru_{0.2}$-decorated surface exhibits a small shoulder at low potentials. This shoulder can be attributed to the electronic destabilisation of CO species adsorbed in the vicinity of the steps, i.e. Ru.

4.1.3. Co-adsorption of carbon monoxide and methanol

In an exchange experiment on $Ru_{0.2}$-decorated Pt(665) a full monolayer of ^{13}CO is adsorbed first and then the $^{13}CO_{ad}$ corresponding to the first oxidation peak is oxidized at 370 mV for 5 minutes. Then the potential is set to 50 mV and the solution is exchanged under potential control with 0.1 M methanol (12-C) in 0.5 M sulfuric acid. The potential is then stepped to 400 mV where methanol is co-adsorbed. After switching back to 50 mV, the methanol solution in the cell is changed to the base electrolyte. The carbon dioxide formation is followed by monitoring m/z = 44 (12-C) and m/z = 45 (13-C).

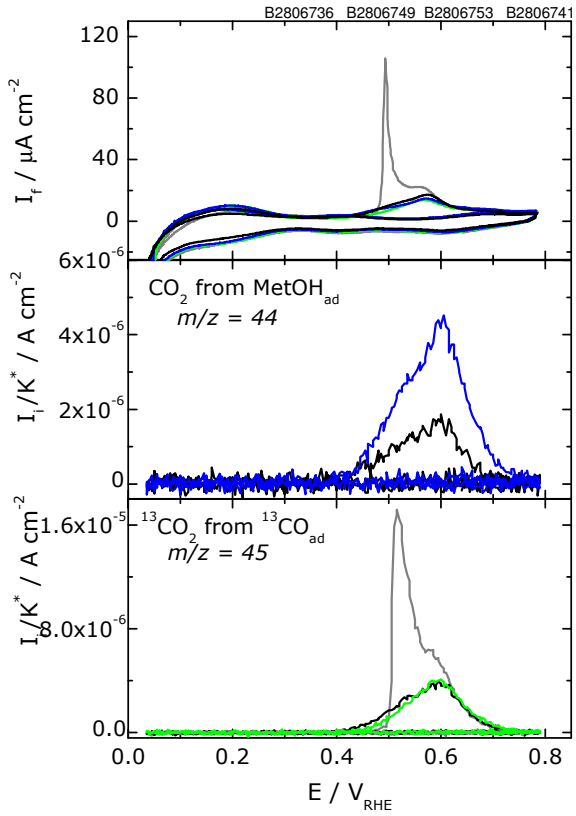

Figure 4-4 Simultaneously measured faradaic currents and corresponding ion currents of $^{12}CO_2$, m/z=44, during oxidation of methanol adsorbed at 400 mV for 2 minutes after adsorption of ^{13}CO and potential stop at 370 mV for 5 minutes on $Ru_{0.2}$-decorated Pt(665) in 0.5 M H_2SO_4 (black line). Scan rate: 10 mV s^{-1}. Electrolyte flow rate: 5 µL s^{-1}. Additionally, $^{13}CO_{ad}$ oxidation without potential stop (grey line), and after potential stop at 370 mV for 5 minutes (green line) are shown. Blue line: oxidation of methanol adsorbed at 400 mV for 2 min. The current is referred to $A_{sur,CO}$.

Figure 4-4 shows, that if only stable adsorption state is occupied by CO, then the interaction between adsorbed CO and bulk methanol results in some additional adsorption of methanol. It is also clearly seen that, in this experiment, methanol is preferentially adsorbed at the stable adsorption states; i.e. far away from Ru. For comparison, the oxidation of ^{13}CO-adsorbate (grey line) and the methanol adsorbate (blue line) are shown.

Similar experiments with a full coverage of carbon monoxide showed that no CO is displaced by the methanol adsorbate (not shown).

On the other hand the interactions between adsorbed and bulk CO is fairly fast not only on $Ru_{0.2}$-decorated but also on Ru-free Pt(665). The adsorbed CO is fully exchanged by bulk CO within 10 minutes (not shown here).

The effect of the potential used for the oxidation of the first peak at Pt(665) is also studied. The mass spectrometric current transients observed during the oxidation of adsorbed CO at four different potentials for 5 minutes are shown in Figure 4-5.

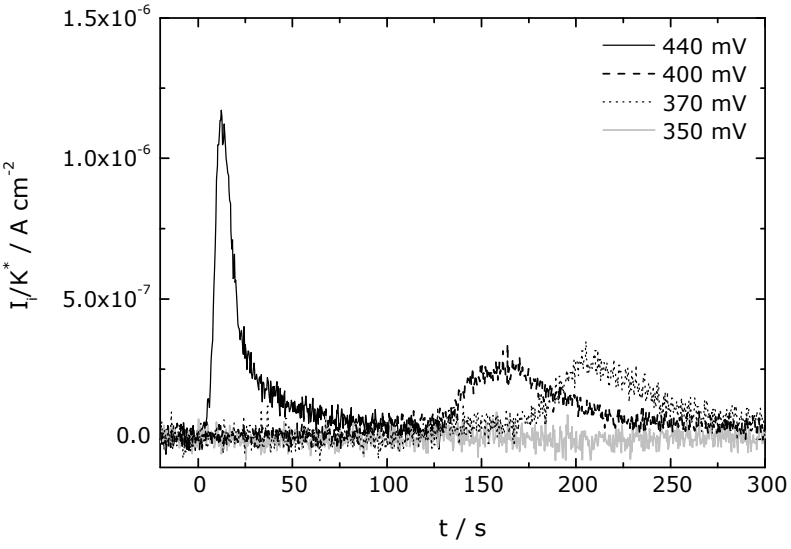

Figure 4-5 Ion current transients of $^{13}CO_2$, m/z=45, during oxidation of adsorbed ^{13}CO at different oxidation potentials for 5 minutes on $Ru_{0.2}$-decorated Pt(665) in 0.5 M H_2SO_4. Electrolyte flow rate: 5 μL s^{-1}. The current is referred to $A_{sur,CO}$.

It is clearly seen that the oxidation of the first peak starts already at potentials lower than that observed directly from the "simple" cyclic voltammetry. However, the delay between the potential stop and the increase in the oxidation current gets larger as the oxidation potential decreases, whereas the ion charge does not change significantly (Table 4-2). At oxidation potential of 350 mV no oxidation occurs within 5 minutes of waiting at this potential.

Table 4-2 Summary of the CO pre-oxidation at different potentials at Pt(665)

E_{ox} / mV	t_{ox} / s	$Q_i(45)$ / A
440	0	1.84×10^{-10}
400	62	1.82×10^{-10}
370	102	1.79×10^{-10}

***E_{ox}*, oxidation potential; *t_{ox}*, delay between the potential stop and the onset of CO oxidation current; *$Q_I(45)$*, ^{13}CO oxidation charge**

4.2. POLYCRYSTALLINE PLATINUM AND PT NANOPARTICLES

Similar to the previous part, the exchange experiments were performed also on polycrystalline platinum and platinum nanoparticles. Additionally, ruthenium and molybdenum is deposited on these surfaces.

4.2.1. CO and methanol adsorbate oxidation

Due to the unknown exact structure of these surfaces, the CO stripping and oxidation of adsorbed methanol are performed ahead of the proper experiments.

4.2.1.1. Oxidation of adsorbed carbon monoxide

Figure 4-6 shows the characteristic faradaic and corresponding mass spectrometric currents for oxidation of ^{12}CO adsorbate on ruthenium modified (a) polycrystalline platinum and (b) PtO_x^E/C nanoparticle electrode and on (c) ruthenium and molybdenum modified PtO_x^E/C electrode.

Two CO stripping peaks (Figure 4-6a (solid line)) are observed for the CO oxidation on $Ru_{0.2}$-modified polycrystalline platinum. The peak at ca. 500 mV originates from the stripping of CO chemisorbed on sites at or near to Ru and can be selectively oxidized by holding the potential at 400 mV (dashed line). The peak at 600 mV occurs from CO chemisorbed on the Pt sites away from the Ru [75]. For comparison the oxidation of carbon monoxide on pure polycrystalline platinum is shown (dotted line), where at high degrees of CO_{ad} coverage, in addition to the main oxidation peak at ca 650 mV, a small pre-peak at 450 mV is observed. In the literature, this peak has been assigned to weakly chemisorbed CO [65, 75, 107, 265].

In Figure 4-6b (solid line) it is visible, that two different oxidation states may also be present on $Ru_{0.2}$-modified PtO_x^E/C nanoparticles. As in the case of $Ru_{0.2}$-modified polycrystalline platinum electrode, the less stable CO adsorbate can be oxidized in the "first peak", separately from the more stable CO adsorbate oxidized in the second

peak by holding the potential just at the onset of the first peak (here 470 mV) for several minutes (Figure 4-6b (dashed line). At the pure Pt nanoparticle electrode (dotted line) only one main peak at 740 mV is observed.

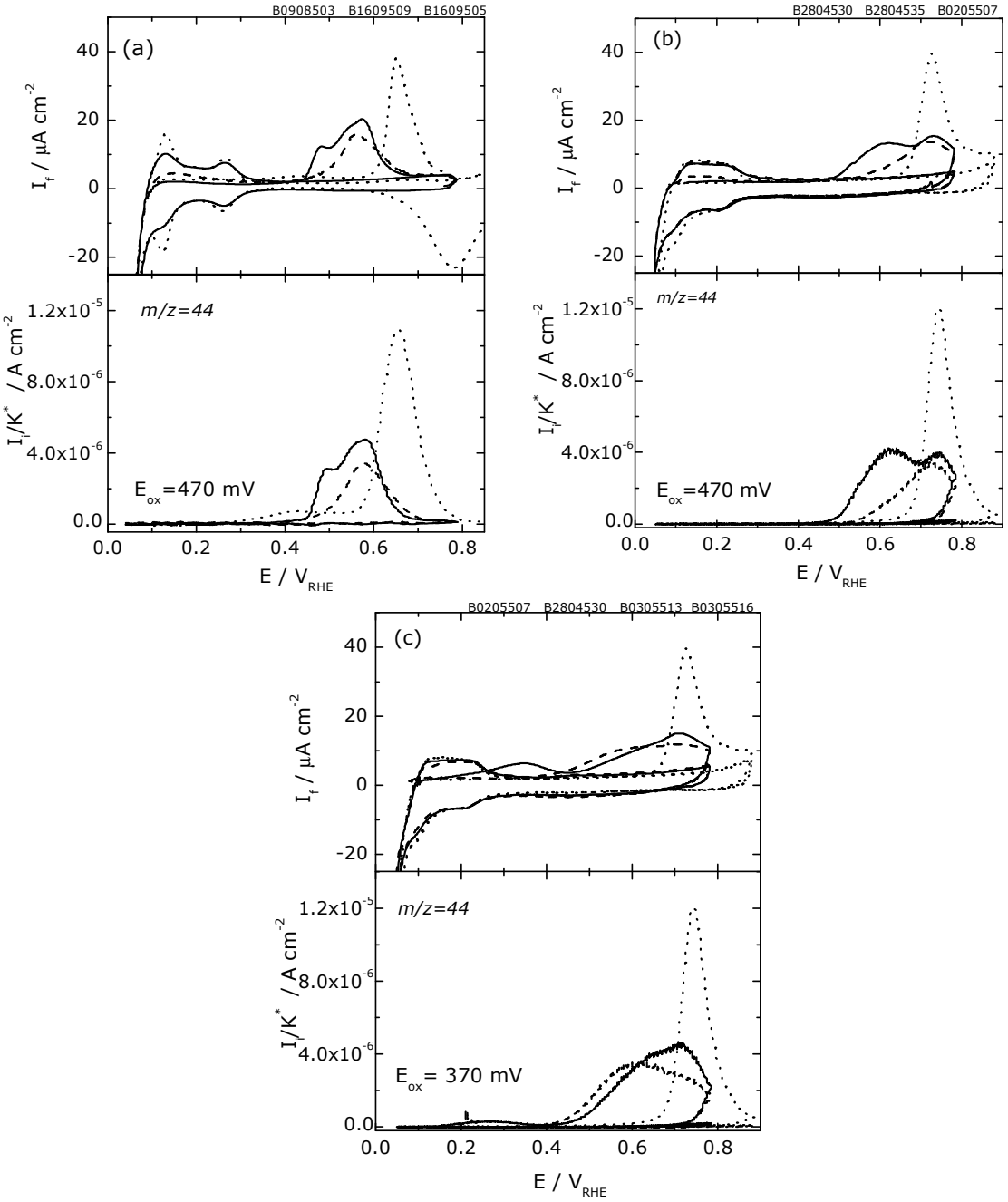

Figure 4-6 Simultaneously recorded faradaic currents and corresponding ion currents of $^{12}CO_2$, m/z=44, during oxidation of ^{12}CO adsorbed on $Ru_{0.2}$-modified (a) Pt(pc) and (b) PtO_x^E/C and (c) $Ru_{0.2}$ and Mo modified PtO_x^E/C nanoparticles in 0.5 M H_2SO_4. Scan rate: 5 mV s^{-1}. Electrolyte flow rate: 5 µL s^{-1}. Dashed line: after oxidation of the "first peak" at E_{ox} over 5 minutes, than going back to the 100 mV Dotted line: oxidation of $^{12}CO_{ad}$ on pure Pt. Catalyst loading: 10 μg_{Pt} cm^{-2}. Current is referred to $A_{sur,CO}$.

The oxidation behaviour of carbon monoxide may be further improved by addition of a third metal. A promising candidate is Mo, which, when used as co-catalyst on Pt, allows to oxidize CO even at potentials below 200 mV [96]. The main peak of CO

adsorbate oxidation, however, is hardly influenced. For a Ru modified Pt (332) single crystal, it was already shown that additional deposition of small amounts of Mo has two effects: (1) it combines the effect of an extremely low oxidation potential of the weakly adsorbed CO induced by Mo with the shift of the main oxidation peak to lower potentials due to Ru, and (2) a synergetic effect, which leads to an further down-shift of the main oxidation peak potential by more than 50 mV [154]. A similar effect, albeit not as significant, is observed at nanoparticle electrodes: For the experiment of Figure 4-6c (solid line), the PtO_x^E/C electrode was first modified by deposition of 20% Ru, and then by Mo. In addition to the pre-peak, which starts at 150 mV, the main, broad oxidation peak is shifted by 50 mV to lower potentials with respect to the electrode, which was modified only by Ru (Figure 4-6b (dotted line)).

In addition to the above experiments, also the oxidation of $^{13}CO_{ad}$ (after adsorption from 20% ^{13}CO in Ar) and the effect of a potential stop in the region of the "pre-peak" were investigated on pure polycrystalline Pt (not shown here). As expected, no differences between adsorption/oxidation of ^{12}CO and ^{13}CO were found in spite of the lower concentration of ^{13}CO. After holding the potential at 350 mV (beginning of the pre-peak) for 5 minutes, the charge for the oxidation of weakly adsorbed CO diminishes to zero while the charge under the main CO_{ad} peak remains constant. This effect indicates a partial desorption of weakly adsorbed CO, which can be separately oxidized at lower potentials.

4.2.1.2. Oxidation of adsorbed methanol

In the following experiments methanol is adsorbed on polycrystalline platinum (Figure 4-7a (solid line)) and at PtO_x^E/C (Figure 4-7b (solid line)) by a special potential step procedure. On both pure Pt-based electrodes, the oxidation of the methanol adsorbate starts at 450 mV and the peak maximum is observed at about 650 mV.

The oxidation of the methanol adsorption product on $Ru_{0.2}$-modified electrodes is shown in Figures 4-7a and b (dashed line). On these electrodes and the nanoparticle electrode modified with Mo additionally to Ru (Figure 4-7b (dotted line)), the electrooxidation of the methanol adsorbate starts already at 350 mV and also the maximum is shifted to lower oxidation potential of about 550 mV. No additional peaks are observed. Since the position of the oxidation peak is well below that observed for pure Pt, a small coverage of Ru seems to promote the oxidation of methanol adsorbed on Pt according to the bifunctional mechanism.

The peak splitting observed for the CO stripping experiments, on the other hand,

shows that CO species adsorbed in the vicinity of Ru are, in addition, subject to an electronic destabilisation. Therefore it is assumed that also on $Ru_{0.2}$-modified polycrystalline Pt and PtO_x^E/C; the different adsorption sites have different adsorption energies. Only at high coverages, the sites in close vicinity to Ru are also occupied and oxidized first upon the anodic stripping. For further details see Ref. [266].

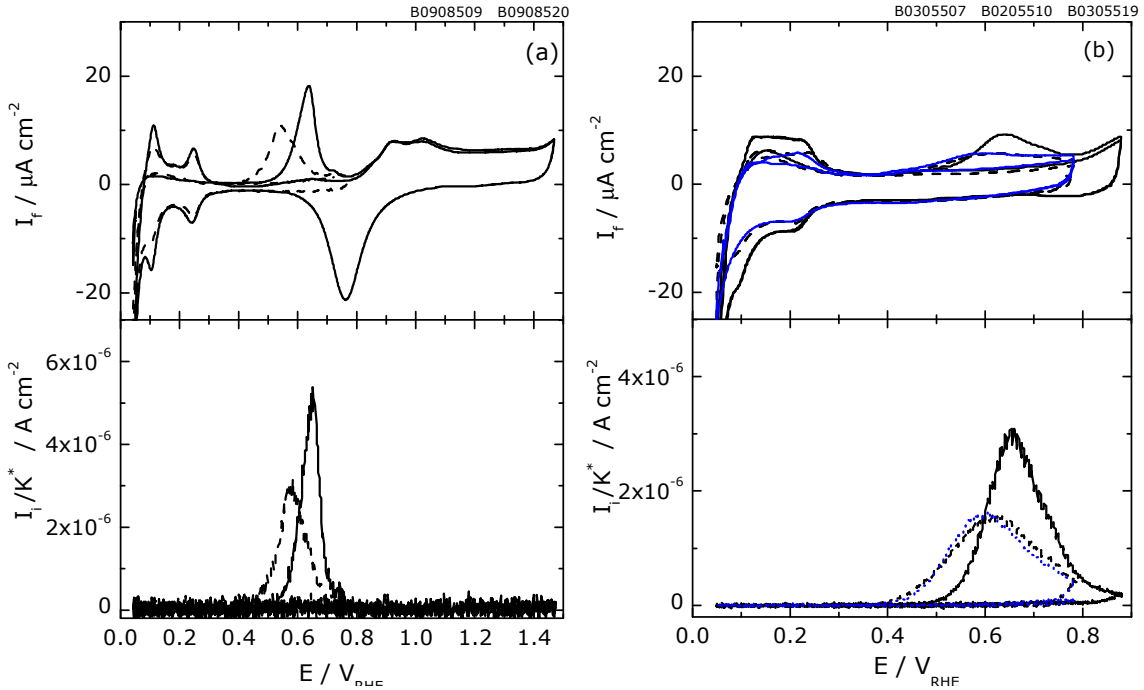

Figure 4-7 Simultaneously recorded faradaic and corresponding ion currents of $^{12}CO_2$, m/z = 44, during oxidation of methanol adsorbed on pure (solid line), $Ru_{0.2}$ modified (dashed line) and $Ru_{0.2}$ and Mo modified (blue line) - (a) Pt(pc) and (b) PtO_x^E/C in 0.5 M H_2SO_4. Scan rate: 5 mV s^{-1}. Electrolyte flow rate: 5 µL s^{-1}. Catalyst loading: 10 μg_{Pt} cm^{-2}. The current is referred to $A_{sur,CO}$.

In Figure 4-7b (dotted line) it is clearly seen, that in the oxidation of adsorbed methanol the co-catalytic effect of Ru and Mo is not as significant as in the case of the CO adsorbate.

Using DEMS, the activity of different ternary $PtRuMeO_x$ (Me = W, Mo, V) catalysts towards methanol oxidation at constant electrode potential at elevated temperature of 60°C was already studied by Jusys et al. [217]. The potentiostatic experiments on catalysts with catalyst loading of 35 µg cm^{-2} were performed in 0.5 M sulfuric acid solution containing 1 M methanol. Under these conditions, the specific surface activity was found to decrease in the order $PtRuVO_x$ > $PtRuMoO_x$ > PtRu > $PtRuWO_x$. This is different from the data showed in the Figure 4-7b, where the activity of Ru and Mo modified electrodes is more or less comparable with that observed at $Ru_{0.2}$-modified surface.

4.2.2. Co-adsorption of CO and methanol

In this series of experiments, 12-C methanol is adsorbed in the way as described above. Then the solution is exchanged with a solution saturated with ^{13}CO (20% in Ar) under potential control (100 mV) and the ^{13}CO is co-adsorbed. After elimination of bulk ^{13}CO with base electrolyte the potential is swept in anodic direction and carbon dioxide formation is followed by monitoring m/z = 44 (12-C) and m/z = 45 (13-C).

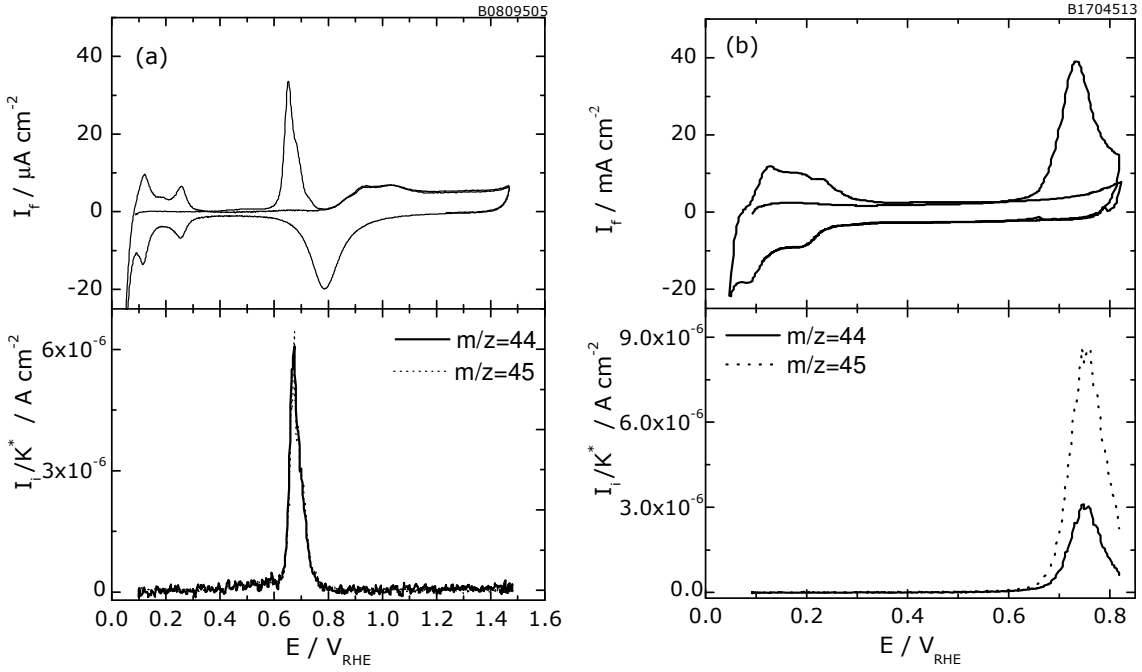

Figure 4-8 Simultaneously recorded faradaic currents and corresponding ion currents of $^{12}CO_2$, m/z = 44, and of $^{13}CO_2$, m/z = 45, during oxidation of methanol co-adsorbed with ^{13}CO on (a) Pt(pc) and (b) PtO_x^E/C in 0.5 M H_2SO_4. Scan rate: 5 mV s^{-1}. Electrolyte flow rate: 5 µL s^{-1}. Catalyst loading: 10 μg_{Pt} cm^{-2}. The current is referred to $A_{sur,CO}$.

A comparison of the result in Figure 4-8a with those for the oxidation of CO_{ad} (Figure 4-6a (dotted line)) and the methanol oxidation (Figure 4-7a (solid line)) shows that interaction between methanol adsorbate and bulk CO on the polycrystalline Pt results in a diminution (20-30%) of m/z=44 (methanol adsorbate) parallel to a partial shift of the latter to the state of weakly chemisorbed CO. The main peak for both 13-C and 12-C species is found at 650 mV, which corresponds to the position for the oxidation of the CO adsorbate.

Also in the case of co-adsorption of methanol together with ^{13}CO at PtO_x^E/C electrode only one main peak at 750 mV for both masses is detected, and some displacement of CO_{ad} formed from methanol by ^{13}C-isotope is observed.

Figures 4-9a-c shows the behaviour of these two co-adsorbates at Ru and Ru-Mo

modified electrodes. In the case of $Ru_{0.2}$-modified polycrystalline platinum (Figure 4-9a) a main peak at 610 mV with a shoulder at about 520 mV is observed for both, m/z=44 and m/z=45, for m/z=45 this shoulder is more pronounced. At the $Ru_{0.2}$-modified PtO_x^E/C (Figure 4-9b) two well distinguished peaks at 630 mV and 740 mV are observed for both masses.

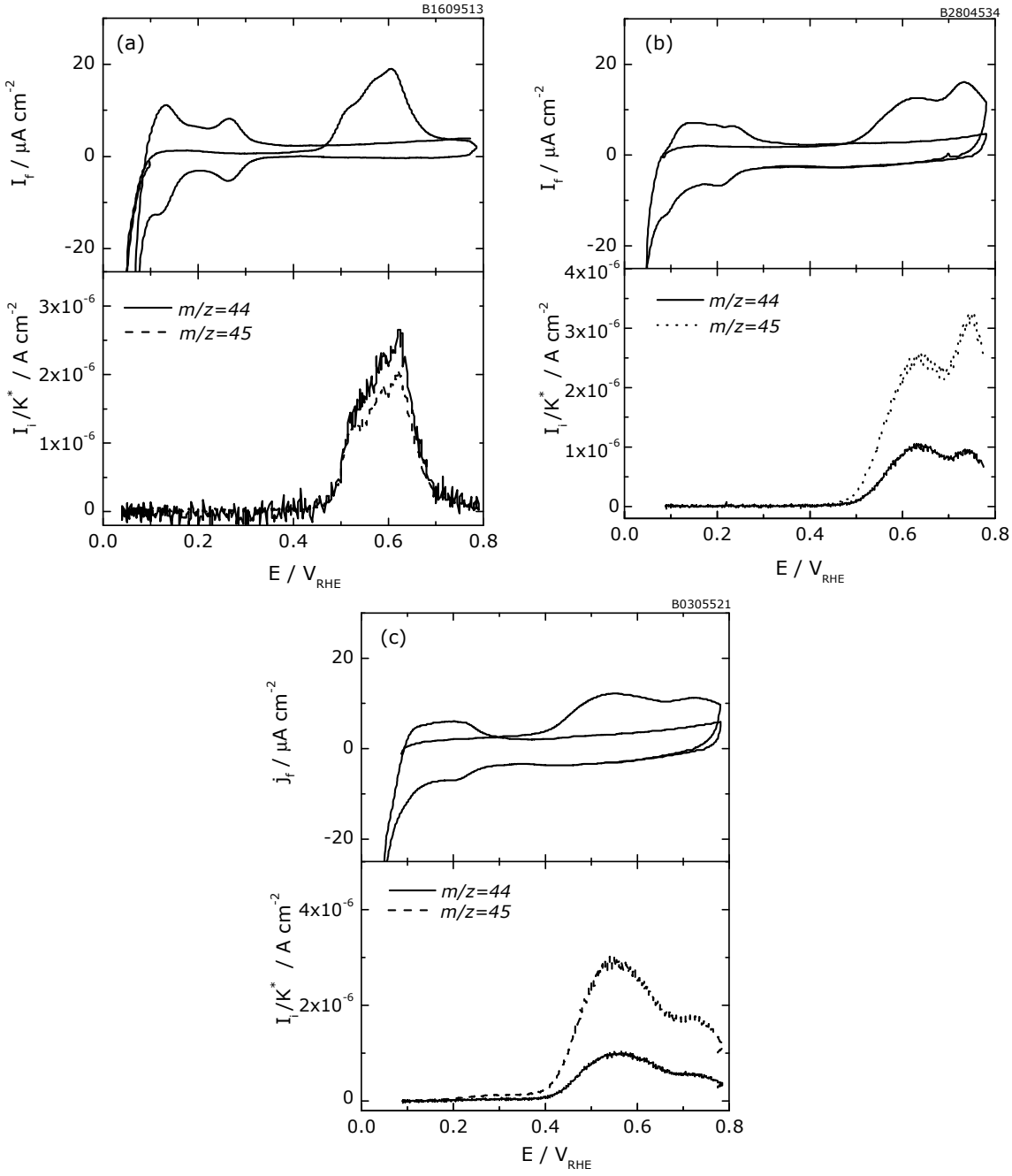

Figure 4-9 Simultaneously recorded faradaic currents and corresponding ion currents of $^{12}CO_2$, m/z=44, during oxidation of methanol co-adsorbed with ^{13}CO (20% in Ar) on modified Pt surfaces (a) Pt(pc)+ $Ru_{0.2}$, (b) PtO_x^E/C+ $Ru_{0.2}$ and (c) PtO_x^E/C+ $Ru_{0.2}$+Mo in 0.5 M H_2SO_4. Scan rate: 5 mV s^{-1}. Electrolyte flow rate: 5 µL s^{-1}. Catalyst loading: 10 μg_{Pt} cm^{-2}. The current is referred to $A_{sur,CO}$.

A similar effect is found also at the Pt electrodes modified with the third metal, Mo

(Figure 4-9c). The different CO adsorbates can be formed and oxidized selectively. Also at such modified electrodes a diminution of 20-30% of m/z=44 (methanol adsorbate) combined with a displacement of a fraction of CO_{ad} formed from methanol by ^{13}CO is observed.

The same procedure is employed to study the interactions between bulk and adsorbed CO. After an adsorption of full coverage of ^{12}CO, the base electrolyte is exchanged to a ^{13}CO containing electrolyte. After 10 min of interaction the electrolyte is then exchanged for the base electrolyte. The adsorbate is oxidized during a potential sweep (Figure 4-10).

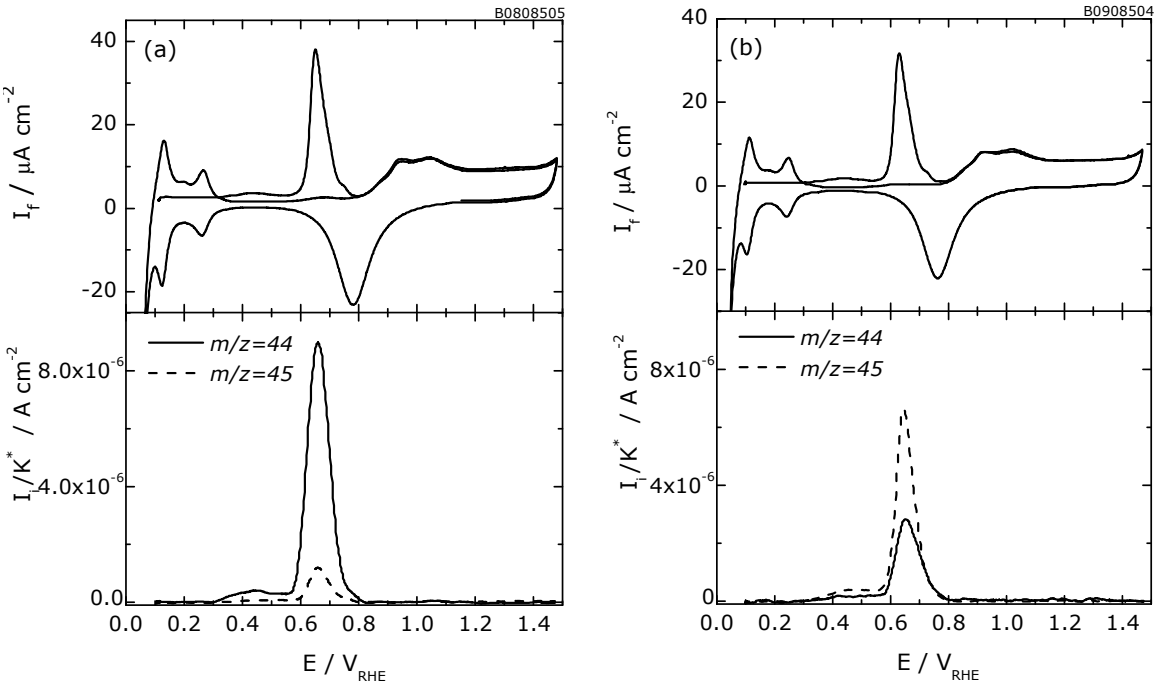

Figure 4-10 Simultaneously recorded faradaic currents and corresponding ion currents of $^{12}CO_2$, m/z=44, of $^{13}CO_2$, m/z=45, during oxidation of CO adsorbate after interaction with CO in solution on Pt(pc) in 0.5 M H_2SO_4. Scan rate: 5 mV s^{-1}. Electrolyte flow rate: 5 µL s^{-1}. (a) ^{13}CO co-adsorbed (b) ^{12}CO co-adsorbed. The current is referred to $A_{sur,CO}$.

A comparison of the charges under the curves for m/z=44 in Figures 4-6a and 4-10a indicates an exchange of ca 20% between adsorbed and bulk CO after 10 min of interaction. This is in agreement with results observed for porous polycrystalline platinum [239]. This is observed also at platinum nanoparticles and the $Ru_{0.2}$-modified electrodes (not shown here). Since the concentration of ^{13}CO solution is below saturation, this should have an influence on the rate of exchange. Therefore, experiments with ^{13}CO pre-adsorbed on the surface and adsorption of ^{12}CO from the solution saturated with ^{12}CO are done. In these experiments (Figure 4-10b) higher exchange rates of about 40%, are observed within 10 minutes.

Figures 4-11a and b show the electrodes modified with $Ru_{0.2}$, where after the adsorption of ^{12}CO and holding the potential at 470 mV, the potential is swept to 100 mV, and the "empty" CO states are refilled by ^{13}CO. The following oxidation sweep shows, that in the first oxidation peak mainly ^{13}CO is oxidized (m/z=45), whereas in the second peak most of the initially adsorbed CO is desorbed. Some mixing, however, occurs. It has been shown that, when an isotopically labelled CO is offered to a fully covered Pt surface, the time constant for mixing is in the range of several minutes [267].

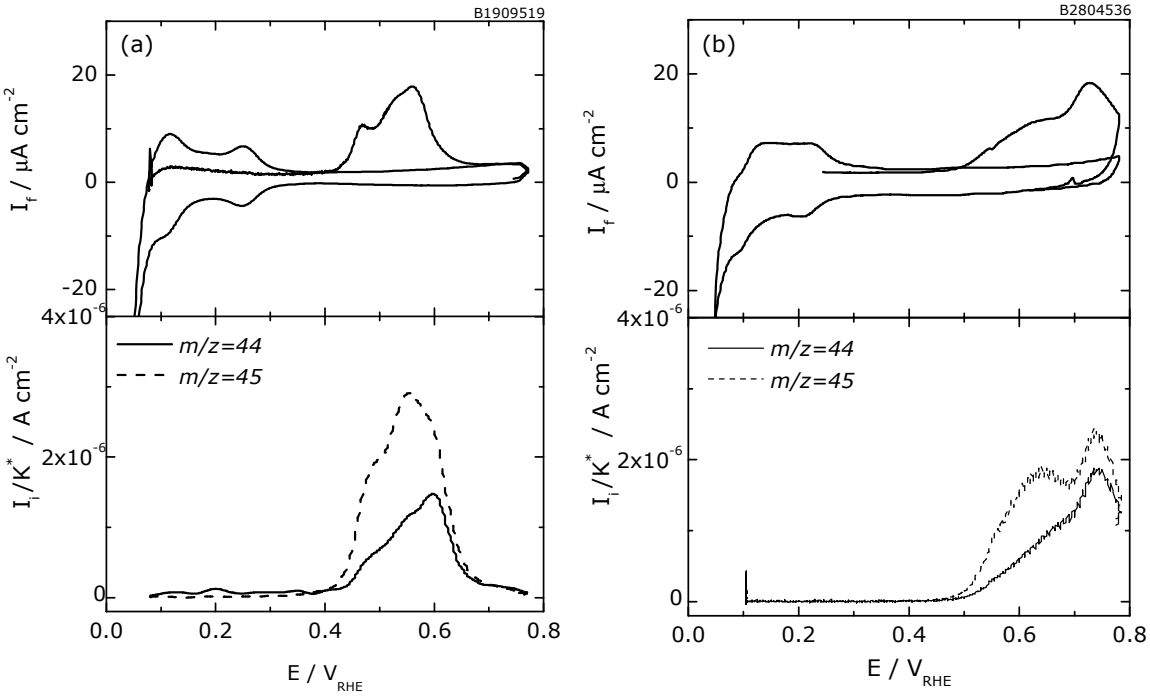

Figure 4-11 Simultaneously recorded faradaic and corresponding ion currents of $^{12}CO_2$, m/z=44, of $^{13}CO_2$, m/z=45, during oxidation of ^{12}CO adsorbate after interaction with ^{13}CO (the weakly adsorbed ^{12}CO in the "first peak" is oxidized) in solution on $Ru_{0.2}$ modified (a) Pt(pc) and (b) PtO_x^E/C in 0.5 M H_2SO_4. Scan rate: 5 mV s^{-1}. Electrolyte flow rate: 5 µL s^{-1}. Catalyst loading: 10 μg_{Pt} cm^{-2}. Current is referred to $A_{sur,CO}$.

4.3. DISCUSSION AND REMARKS

The CO stripping experiments on $Ru_{0.2}$-decorated Pt(665), where the first peak is selectively oxidized, show that the amount of CO oxidized at the low potential is approximately 40%. This amount is higher than one would expect from the number of CO molecules adsorbed directly on or adjacent to Ru sites. These findings are in very good agreement with galvanostatic experiments published by Samjeske et al. [87]. This effect can be explained by means of Figure 4-12 [88]: The electronic effect of Ru leads to an increase in the adsorption enthalpy in the close proximity of Ru (two atomic rows in both directions). This means that the absolute value of the adsorption enthalpy is decreased and CO is therefore oxidized at lower potentials

than that adsorbed farther away from Ru. In contrast, the main activation barrier for oxidation is decreased due to the spillover effect of OH adsorbed on Ru according to the bifunctional mechanism. As a result those CO molecules adsorbed at sites not influenced by Ru are oxidized at somewhat lower potentials than at Ru-free electrodes.

It is assumed that also on $Ru_{0.2}$-modified polycrystalline Pt and PtO_x^E/C, the different adsorption sites have different adsorption energies. The sites in close vicinity to Ru are occupied only at high coverage, and are oxidized first upon anodic stripping.

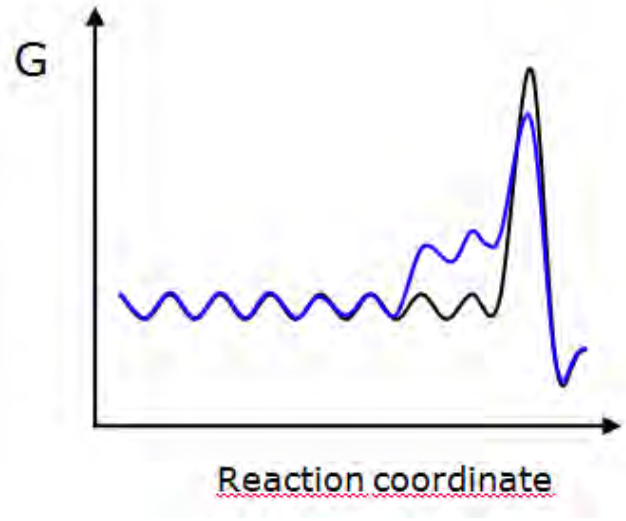

Figure 4-12 Influence of Ru step decoration on adsorption enthalpy of CO_{ad} with respect to the reaction coordinate (schematically). (blu line) Ru-decorated step; (black line) Ru-free surface (Ref. [88]).

It is also shown that using DEMS in combination with isotopic labelled ^{13}CO it is possible to distinguish between the different components of the adsorbate. The result of the isotopic exchange of methanol adsorbates with bulk CO seems to indicate that only one fraction of methanol adsorbate (20-30%) present as weakly adsorbed CO can be desorbed and replaced by bulk CO under our experimental conditions. Also the isotopic exchange between adsorbed and bulk CO takes place on these electrodes. The exchange rate can be influenced by the concentration of the CO in solution. In the case of Pt(665) a very fast exchange is observed.

Modification of the platinum surface by Ru leads to heterogeneous adsorption sites, so that two types of CO species can been identified; the CO adsorbed on/near to Ru sites and CO adsorbed on Pt far away from the Ru sites. The different CO adsorbates can be formed and selectively oxidized. More important, from a practical point of view, is the fact that the co-catalytic effects of Ru and Mo can be combined in a synergetic sense also at nanoparticles; note that both catalysts act in different ways

[154]. Mo only, but most effectively, helps in the oxidation of the weakly adsorbed CO, whereas Ru shifts the main oxidation peak to low potentials. In the case of methanol oxidation, no significant improvement was found at Mo modified Pt/Ru electrodes. These findings correspond to the results already published for similar systems in Ref. [96, 218].

For comparison to the measurements on Ru and Mo modified PtO_x^E/C (Figure 4-6c), the oxidation of carbon monoxide on $PtRuMo^M$/C catalyst (without oxygen content) obtained from MPI Mülheim is shown in Figure 4-13[2]. It is clearly seen that, similarly to $Ru_{0.2}$ and Mo modified PtO_x^E/C, the CO_{ad} oxidation on $PtRuMo^M$/C alloy proceeds in a main oxidation peak (here at 750 mV) with an evident shoulder at lower potentials. Interestingly a clear pre-peak at low potentials (ca 150 mV), which is observed in addition to the main oxidation peak on the $Ru_{0.2}$ and Mo modified PtO_x^E/C (see Figure 4-6c), is missing on $PtRuMo^M$/C. Here, a direct comparison of the onset and the position of the oxidation maxima is not possible due to the different scan rate.

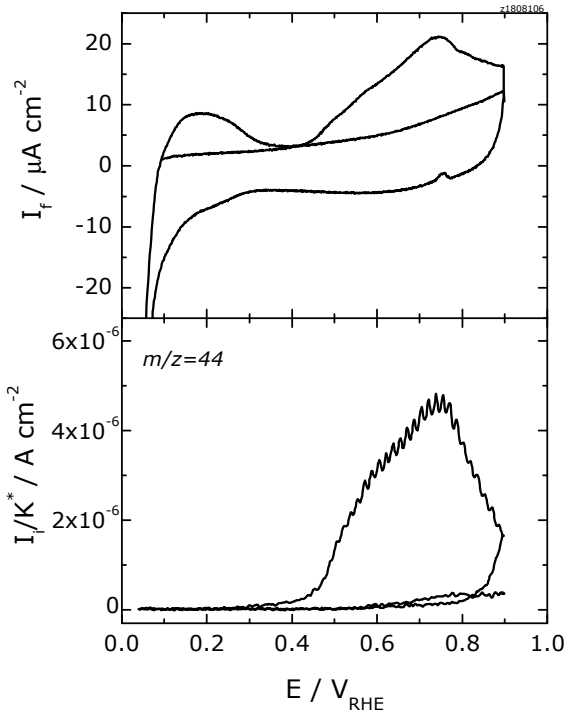

Figure 4-13 Simultaneously recorded faradaic and corresponding ion currents of m/z=44 during the oxidation of CO pre-adsorbed on $PtRuMo^M$/C colloid catalyst in 0.5 M H_2SO_4. Scan rate: 10 mV s^{-1}. Electrolyte flow rate: 5 µL s^{-1}. Current is referred to $A_{sur,CO}$.

On $Ru_{0.2}$-decorated Pt(665), the interaction experiments between CO adsorbed on sites far away from Ru and bulk methanol shows that methanol preferentially adsorbs at these stable sites.

[2] These measurements were performed by Zigmas Ezerskis.

Chapter 5 Electrocatalytic oxidation of methanol adsorbate

The experiments presented in the following section, are performed to study the methanol adsorbate formation in dependence on the adsorption potential and on time, respectively. Supplementary, the kinetic characteristics are also investigated.

5.1. DEPENDENCE OF THE SATURATION COVERAGE OF METHANOL ADSORBATE ON THE ADSORPTION POTENTIAL

First, the influence of the adsorption potential on the methanol adsorbate and its potentiodynamic oxidation on a variety of surfaces is studied. These experiments should provide an insight into the process of the electrocatalytic oxidation of the methanol adsorbate. The effects of different platinum surfaces as well as the catalytical influence of foreign metals on the formation/oxidation of the methanol adsorbate are of particular interest.

5.1.1. Polycrystalline platinum surface

The oxidative stripping of the adsorbate, formed from the adsorption of methanol at different potentials, is shown in Figure 5-1a for a smooth polycrystalline Pt (for clarity, only three adsorption potentials are shown). Interestingly, for the polycrystalline electrode, all curves overlap in the rising part, which suggests that the oxidation rate is of zeroth order with respect to coverage. As a result, the peak potential shifts in the negative direction with decreasing coverage. Therefore, the shift in the peak potential on polycrystalline Pt is not caused by the different adsorption potential, but by the differences in coverage. This is already visible from the oxidation peaks of the methanol adsorbate formed at E_{ad}=300 mV and 700 mV, which deviate in a similar way from that for the methanol adsorbate formed at E_{ad}=500 mV.

The situation on the Ru modified electrodes is quite different: Due to the fact that the electrooxidation of methanol adsorbate on $Ru_{0.2}$-modified polycrystalline Pt is performed in connection with previous series of experiments presented in Chapter 4.1., only the oxidation of methanol adsorbed at 500 mV is shown in Figure 5-1b. However, it was already shown by H. Wang [268] (inset of Figure 5-1b) that during the oxidative stripping at polycrystalline Pt modified with Ru, both the onset potential and the peak potential shift in the anodic direction with decreasing CO (i.e., methanol adsorbate) coverage. This can hardly be explained by a reaction order exceeding 1. Firstly, the shift of the onset potential is too large, and secondly, it is hard to imagine a reason for a high reaction order.

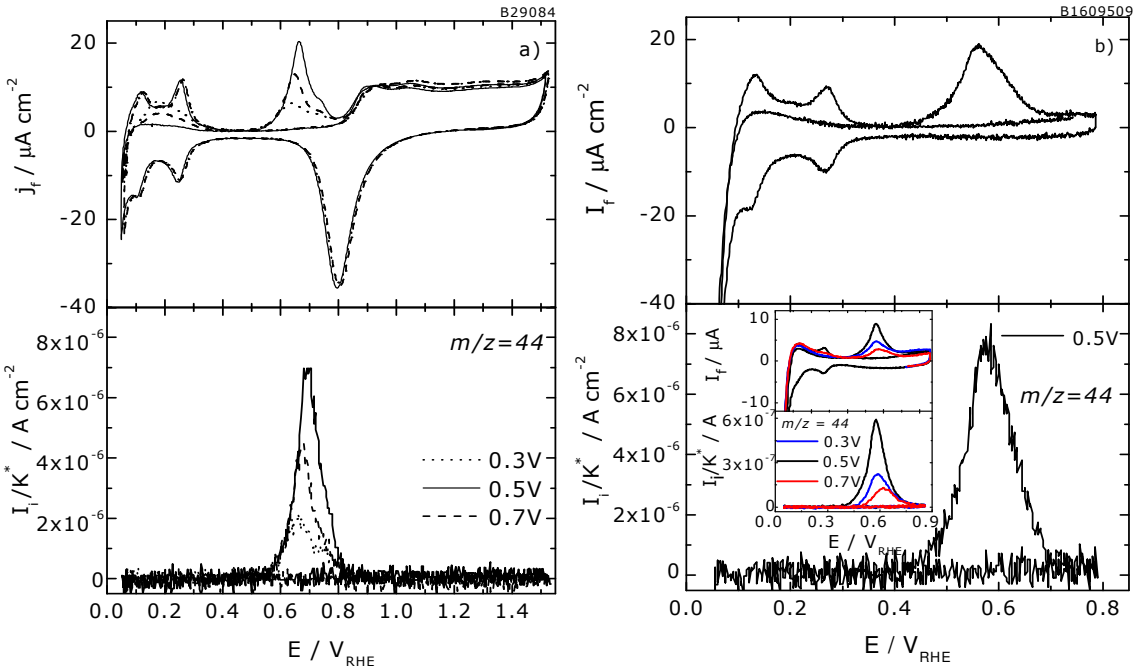

Figure 5-1 Simultaneously recorded faradaic and corresponding ion current of CO_2, m/z=44, during the oxidation of methanol adsorbate on (a) Pt(pc) and (b) $Ru_{0.2}$ modified Pt(pc) in 0.5 M H_2SO_4 solution. Scan rate: 10mV s^{-1}. Flow rate of electrolyte: 5 µL s^{-1}. Methanol adsorption for 2 minutes at potential: 500 mV (solid line), 300 mV (dotted line) and 700 mV (dashed line). Inset: Experiments performed by H. Wang [268]. The current is referred to $A_{sur,CO}$.

Similarly to the interpretation suggested by previous results for CO oxidation on $Ru_{0.2}$-modified Pt electrodes (see Chapter 4), it is assumed that on $Ru_{0.2}$-modified polycrystalline Pt, the different adsorption sites also have different adsorption energies. The sites in close vicinity to Ru are occupied only at high coverage, and are oxidized first upon anodic stripping.

The potential dependence of the maximum CO coverage formed from methanol is depicted in Figure 5-2.

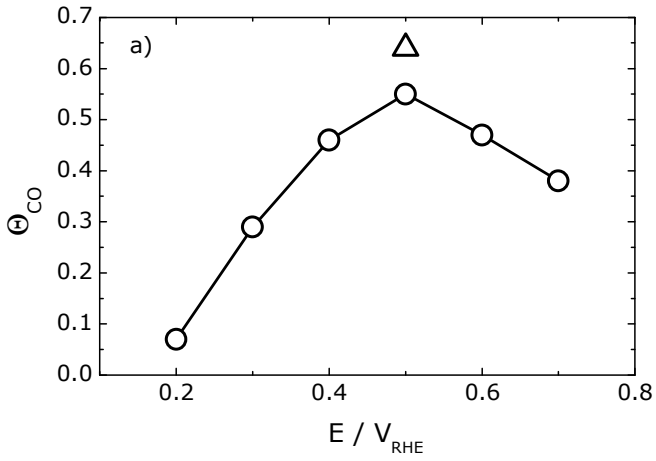

Figure 5-2 Influence of adsorption potential on the relative coverage of methanol (Equation 2-5), Θ_{co}, on Pt(pc) (circles) and $Ru_{0.2}$-modified Pt(pc) (triangle) at room temperature. Adsorption of methanol was carried out in 0.1 M CH_3OH + 0.5 M H_2SO_4 solution for 2 minutes.

At low potentials, the saturation coverage of the methanol adsorbate increases with increasing adsorption potentials, and at high potentials (above 500 mV) it decreases again, due to the oxidation of methanol adsorbate. Therefore, the coverage obtained at 500 mV is the steady state coverage during the methanol oxidation.

The saturation coverage at 500 mV on $Ru_{0.2}$-modified Pt(pc) is slightly higher than that found at pure polycrystalline Pt under the same conditions. The maximum saturation coverage of adsorbed methanol on $Ru_{0.2}$-modified Pt(pc) is found to occur at ca 400 mV [269].

5.1.2. Commercial noble metal catalysts from E-Tek Inc.

The oxidation of the methanol adsorption product formed on nanoparticle electrodes at different adsorption potentials is shown in Figure 5-3a. Differently from polycrystalline Pt, on PtO_x^E/C, the peak potential and the shape of the oxidation curve is independent of the coverage, therefore the reaction is first order with respect to the coverage.

It should be noted that in the CV`s in Figure 5-3, the currents at the positive limit of the first and subsequent sweeps do not overlap. This is not due to a residual CO oxidation, since no CO_2 is formed. Control experiments using the Vulcan XC-72 carbon without Pt catalyst, involving a potential stop in the hydrogen region in the absence of CO or methanol, resulted in the same difference between the first and subsequent sweeps. Therefore, the surface of the carbon is slowly reduced in the hydrogen region and re-oxidized in the subsequent sweep. The corresponding charge is negligible in the case of a full CO layer, and in the case of the methanol adsorbate, where it amounts to 5–10% of the oxidation charge; it was subsequently subtracted in all experiments.

Figures 5-3b and 5-3c clearly demonstrate that at $Ru_{0.2}$-modified PtO_x^E/C electrodes as well as at $PtRu^E$/C alloys, the behaviour is very similar to $Ru_{0.2}$-modified polycrystalline Platinum: In the oxidative stripping not only the onset potential but also the peak potential shifts in the anodic direction with decreasing CO (i.e., methanol adsorbate) coverage. Also on these surfaces it can be assumed that the different adsorption sites have different adsorption energies and that the sites in close vicinity to Ru are occupied only at high coverage, and so oxidized first upon the anodic stripping.

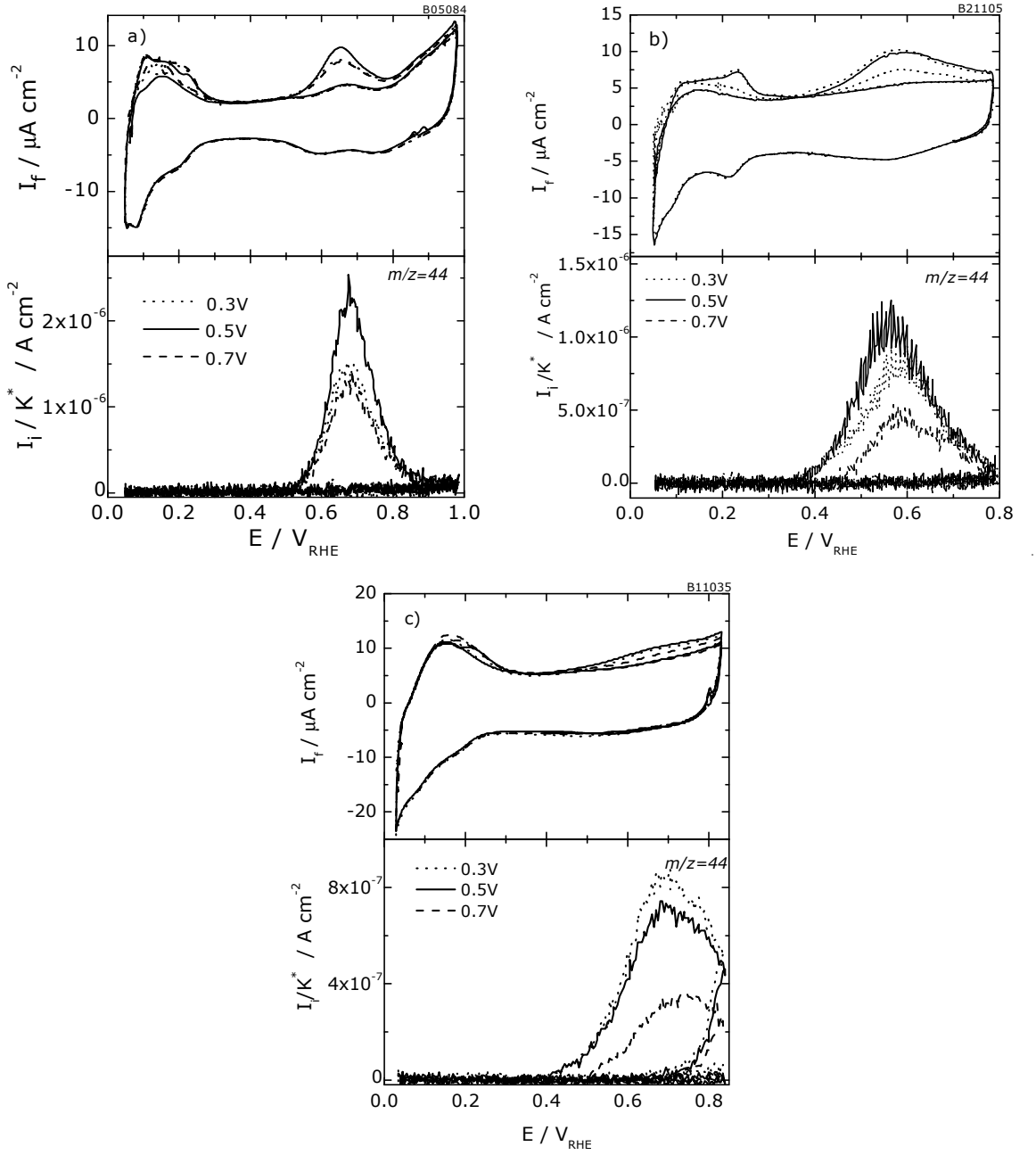

Figure 5-3 Simultaneously recorded faradaic current and corresponding ion current of CO_2, m/z=44, during oxidation of methanol adsorbate on (a) PtO_x^E/C, (b) $Ru_{0.2}$ modified PtO_x^E/C and (c) $PtRu^E$/C in 0.5 H_2SO_4 solution. Scan rate: 10 mV s^{-1}. Flow rate of electrolyte: 5 µL s^{-1}. Methanol adsorption for minutes at potential: 500 mV (solid line), 300 mV (dotted line) and 700 mV (dashed line). Catalyst loading: 10 μg_{Pt} cm^{-2}. The current is referred to $A_{sur,CO.}$

The determined coverage at colloidal nanoparticle electrodes obtained from E-TEK, Inc. (PtO_x^E/C), mentioned above, is summarized in Figure 5-4. The achievable coverage of the adsorbed methanol on PtO_x^E/C is somehow lower than that observed at polycrystalline Pt. The maximum saturation coverage of adsorbed methanol is

[3] The small shoulder in the MSCV of the oxidation of the methanol adsorbate adsorbed at 700 mV on $Ru_{0.2}$ modified PtO_x^E/C is only an artefact.

found at 500 mV, with ca. 56% for polycrystalline Pt and only ca. 28% for PtO_x^E/C nanoparticles, with respect to a full monolayer formed from dissolved CO.

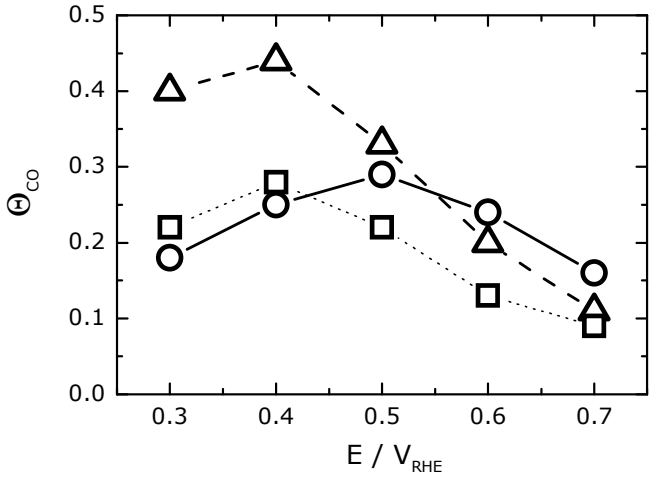

Figure 5-4 The influence of adsorption potential on relative coverage of methanol (Equation 2-5), Θ_{CO}, on PtO_x^E/C (circles), $Ru_{0.2}$-modified PtO_x^E/C (triangles) and $PtRu^E$/C (squares) at room temperature. The adsorption of methanol was carried out in 0.1 M CH_3OH + 0.5 M H_2SO_4 solution for 2 minutes.

The maximum in the surface coverage of adsorbed methanol on $Ru_{0.2}$-modified PtO_x^E/C nanoparticles is obtained at ca. 400 mV. At this and lower potentials the coverage is approximately two-times higher than that on pure platinum. At the potentials above 400 mV it decreases and is getting lower than that on smooth polycrystalline platinum, due to the faster oxidation of the methanol adsorbate. A similar behaviour is obtained also for the $PtRu^E$/C surface; however the coverage at low potentials is only slightly higher than that at the PtO_x^E/C.

The common acceptance of an optimum alloy composition of 50 at.% Ru (bulk) on the methanol electrooxidation was for long time based on the assumption that bulk and surface compositions would be identical. Although it is possible to estimate the initial surface composition of the alloy electrodes, however it is not possible to even approximately quantify the surface composition after the electrode pretreatment, where an uncontrolled dissolution of Ru may occur.

The electrocatalytic activity of methanol on well-defined Pt-Ru alloys was for the first time studied by Gasteiger et al. [215, 270]. In this study the highest catalytic activity toward methanol oxidation was observed at alloy with ≈10 at.% Ru. It is assumed that the adsorption of methanol requires an ensemble of three adjacent Pt atoms. At such optimum surface composition most of the Pt ensembles are adjacent to a Ru atom. The adsorption of methanol is then maximized through a large number of Pt

adsorption sites and the CO is oxidatively removed *via* "hydroxide shuttling" by Ru at low potentials.

Based on the methanol stripping DEMS measurements, the number of electrons released upon oxidation of one adsorbate molecule, *n*, can be calculated. To obtain the corresponding faradaic oxidation charge, Q_f, the procedure for the calibration of the DEMS system described in Chapter 1.2.3. was accepted. The CO coverage formed from methanol and the resulting numbers of electrons per CO_2 product molecule for different adsorption potentials are shown in Table 5-1. The number of electrons per CO_2 product molecule is close to 2 for the highest coverages obtained in the intermediate potential range on both, polycrystalline Pt and on PtO_x^E/C nanoparticles. The calculated values are higher for lower coverages, most likely due to uncertainties in the capacitive contributions to the charge. Thus, at least in the intermediate potential range, but most likely also at potential below and above, the adsorbed molecules are fully dehydrogenated, leaving CO_{ads} as a stable adsorbed species on the surface. For the completeness, the ratio of oxidation charge to the suppressed hydrogen adsorption charge was also calculated, i.e., the classical ′electron per site′ (eps) number. Since the hydrogen charge at the nanoparticles is very small, its partial suppression cannot be determined very reliably. A corresponding systematic error might result in ′eps′ values which are somehow higher at the nanoparticles than that at polycrystalline Pt.

Table 5-1 Comparison of the number of electrons, *n*, per oxidation of one stable adsorbate molecule and CO coverage Θ from methanol adsorbate at different potentials E_{ad} at polycrystalline Pt and PtO_x^E/C.

E_{ads} / V_{RHE}	Θ		*n*		*eps*	
	PtO_x^E/C	Pt(pc)	PtO_x^E/C	Pt(pc)	PtO_x^E/C	Pt(pc)
0.3	0.17	0.29	2.26	2.92	1.13	1.12
0.4	0.21	0.38	1.97	2.30	1.16	0.78
0.5	0.28	0.56	1.84	1.96	1.20	0.91
0.6	0.20	0.38	2.08	2.08	1.17	0.70
0.7	0.13	0.22	2.29	3.23	1.15	0.62

n, number of electrons released upon oxidation of one adsorbate molecule; Θ, CO coverage ($\Theta=\Gamma_{CO}/\Gamma_{CO}^{max}$); *eps*, electrons per site (eps=Q_f/Q_H)

5.1.3. Non-commercial noble metal catalysts from MPI Mülheim

The behaviour on the non-commercial catalyst is pretty similar to that obtained for the commercial ones. Also here, the peak potential for the adsorbate oxidation on the pure PtO_x^M/C (Figure 5-5a) is found to be independent of the coverage, which points out that, with respect to the coverage, the reaction is possibly first order. Interestingly, on these non-commercial nanoparticles the onset of the methanol

adsorbate oxidation starts at an approximately 20 mV lower potential, while the much broader maximum is positioned 25 mV more positive than on the commercial ones. This could be ascribed to broader mean particle size distribution in the case of non-commercial catalysts.

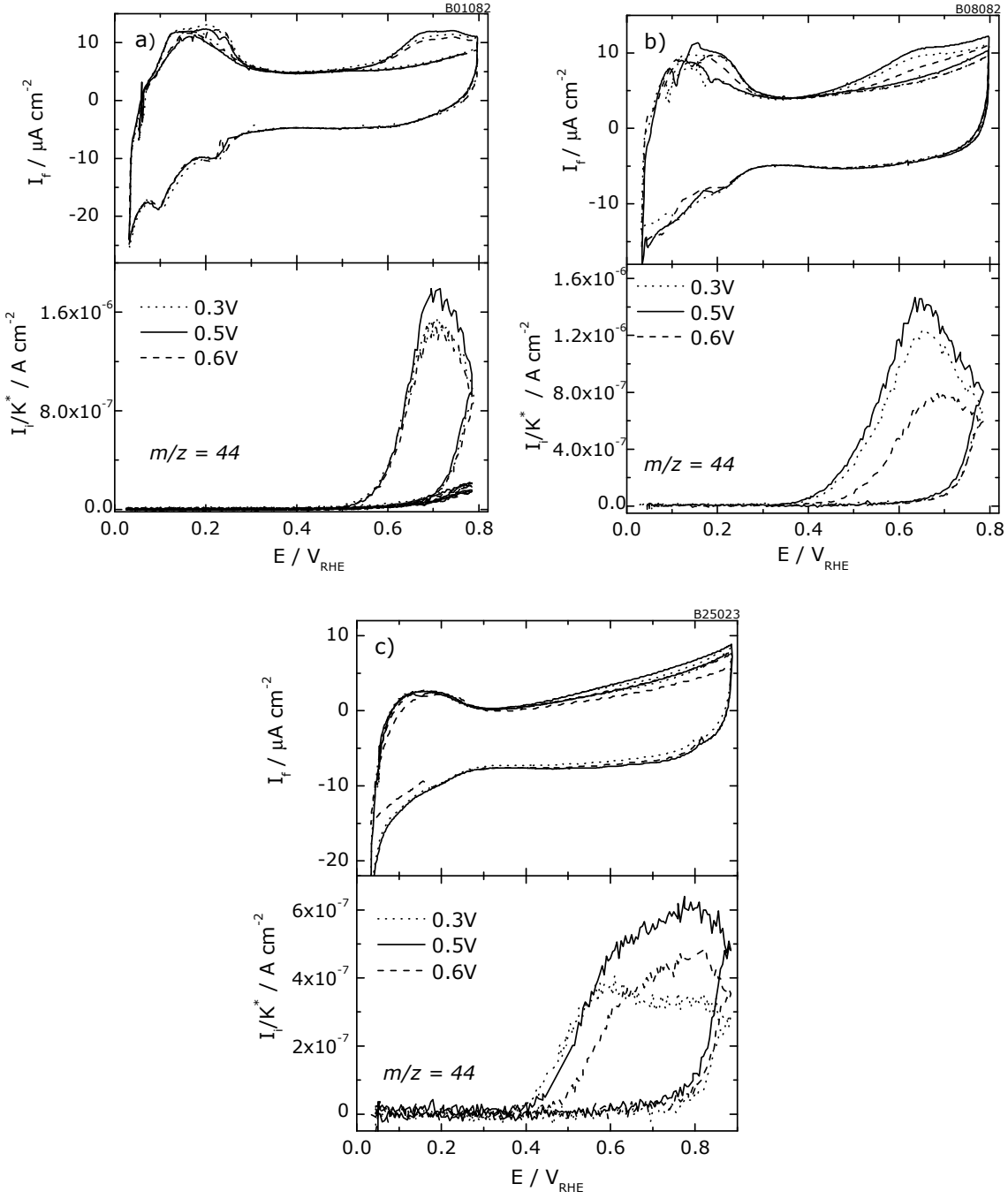

Figure 5-5 Simultaneously recorded faradaic current and corresponding ion current of CO_2, m/z=44, during oxidation of methanol adsorbate on (a) PtO_x^M/C, (b) $PtRuO_x^M$/C and (c) $PtRuOsIrO_x^M$/C in 0.5 M H_2SO_4 solution. Scan rate: 10 mV s^{-1}. Flow rate of electrolyte: 5 µL s^{-1}. Methanol adsorption for 2 minutes at potential: 500 mV (solid line), 300 mV (dotted line) and 600 mV (dashed line). Catalyst loading: 10 μg_{Pt} cm^{-2}. The current is referred to $A_{sur,CO}$.

The oxidation of the methanol adsorbate at the $PtRuO_x^M$/C alloy obtained from MPI Mülheim (Figure 5-5b) is quite conform with that observed for the $PtRu^E$/C catalyst received from E-TEK, Inc. (Figure 5-3c). The only difference is observed in the negative shift of the onset and also of the maximum in the stripping curves. For example, when comparing the oxidation characteristic of adsorbate formed on $PtRuO_x^M$/C at 500 mV both, the onset and the maximum are shifted by approximately 30 mV to lower potentials than that observed on $PtRu^E$/C. During the oxidation of the methanol adsorbate formed at 500 mV at $PtRuOsIrO_x^M$/C catalyst a broad peak with two maxima is observed in the voltammetric curve (Figure 5-5c). These maxima are even more pronounced during the stripping of the adsorbate formed at potentials bellow 400 mV. In the oxidation peak of the methanol adsorbate formed at potentials above 500 mV the more negative peak is largely decreased. Using a higher adsorption potentials (>500 mV) not only the adsorption takes place but also the oxidation of the less stable adsorbate occurs at the same time. The two maxima in the MSCV suggest that two different stable states of the adsorbate are formed on the surface. The maximum observed at 590 mV is close to that observed at $PtRuO_x^M$/C alloy (640 mV). The second maximum, which is observed at 810 mV, is clearly more positive than that detected in the experiments on pure PtO_x^M/C (700 mV), but corresponds to the main peak observed at 810 mV during the CO oxidation (see Chapter 3.1.3.).

In Figure 5-6, the surface coverage against the adsorption potential behaves similar to the commercial surfaces.

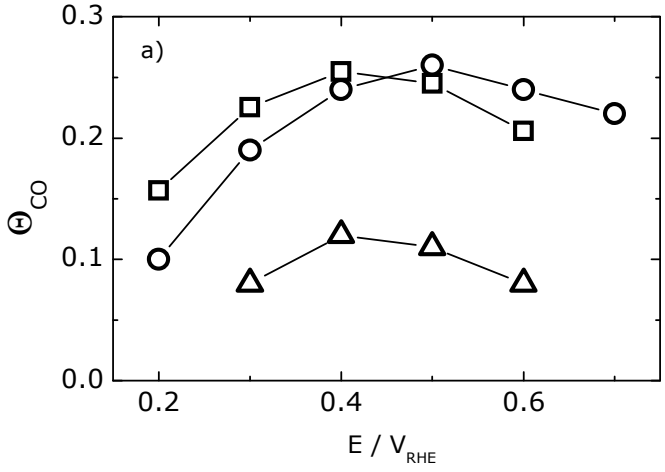

Figure 5-6 Influence of adsorption potential on relative coverage of methanol (Equation 2-5), Θ_{CO}, on PtO_x^M/C (circles), $PtRuO_x^M$/C (squares) and $PtRuOsIrO_x^M$/C (triangles) at room temperature. The adsorption of methanol was carried out in 0.1 M CH_3OH + 0.5 M H_2SO_4 solution for 2 minutes.

The surface coverage of adsorbed methanol on PtO_x^M/C and $PtRuO_x^M$/C nanoparticle electrodes obtained from MPI Mülheim is slightly lower than that observed at similar

catalysts obtained from E-TEK, Inc. All in all, the dependence shows the same characteristics as mentioned with the commercial nanoparticles.

Similarly to $PtRuO_x^M/C$ surface, the maximal coverage is obtained at 400 mV also on the $PtRuOsIrO_x^M/C$ catalyst, which, however, does not exceed 12%. Though this clearly shows that $PtRuOsIrO_x^M/C$ is not active for methanol adsorption, it still seems to be a relatively good catalyst for CO electrooxidation (see Chapter 3.1.3). As already mentioned in Chapter 5.1.2., at least three adjacent Pt atoms are necessary to adsorb one molecule of methanol and these are obviously not present at $PtRuOsIrO_x^M/C$.

5.2. THE RATE OF METHANOL ADSORPTION

The methanol adsorption is also investigated in oxidative stripping experiments by varying the coverage by adsorption of methanol for different adsorption times. In this manner, the adsorption rate of methanol can be determined.

The stripping curves for polycrystalline Pt at a potential of 500 mV for a range of adsorption times, are shown in Figure 5-7.

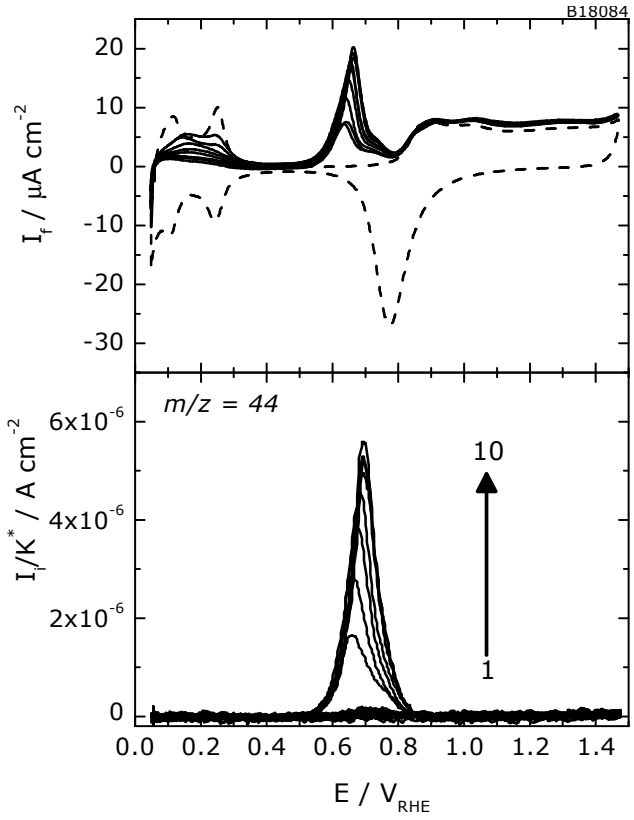

Figure 5-7 Simultaneously recorded faradaic currents and corresponding ion currents of CO_2, m/z=44, during oxidation of methanol adsorbate on Pt(pc) in 0.5 M H_2SO_4. Scan rate: 10 mV s^{-1}. Electrolyte flow rate: 5 μL s^{-1}. Methanol adsorption performed at 500 mV for different times. From 1 to 10: 1, 2, 5, 10, 20, 60, 120, 180, 300 and 600 s from 0.1 M CH_3OH + 0.5 M H_2SO_4 solution. For comparison the CV for an adsorbate free surface is also shown (dashed line). The current is referred to $A_{sur,CO}$.

Here the curves for an adsorption time of 120, 180, 300 and 600 s overlap, confirming that at 120 s the maximum coverage is reached under the present conditions. Varying the coverage of methanol adsorbate by adsorption at a constant potential for different times results in the same dependence of the stripping voltammograms on coverage as varying the coverage by adsorption for a constant time but a different potentials. Hence, the shift in the peak potential at polycrystalline Pt is not due to the different adsorption potential, but due to the different coverages.

Figure 5-8 shows the time dependence of the coverage of methanol adsorbate at adsorption potentials of 300, 500 and 600 mV. It is clearly seen that the adsorption process is very quick at short times, i.e. where the majority of the surface is free. The steepest increase is found at adsorption potential of 600 mV.

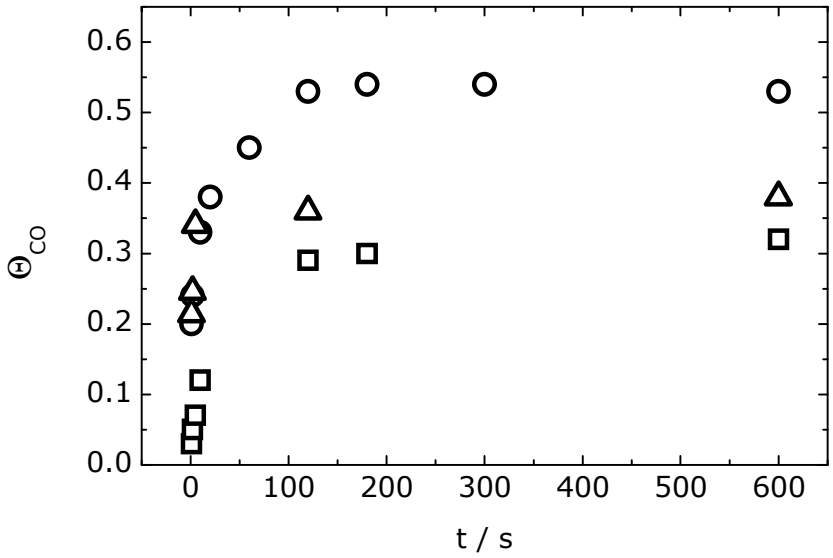

Figure 5-8 Influence of adsorption time on relative coverage of methanol (Equation 2-5), Θ_{CO}, on polycrystalline Pt. Adsorption of methanol was carried out in 0.1 M CH_3OH + 0.5 M H_2SO_4 solution. Methanol adsorption at potential: 500 mV (circles), 300 mV (squares) and 600 mV (triangles).

The same series of experiments is done also for PtO_x^E/C and $PtRu^E$/C colloidal catalysts (Figure 5-9). Similar to the polycrystalline Pt also here, the curves above an adsorption time of 120 s overlap (within error of measurement), what again clearly confirms that at 120 s the maximum coverage is reached.

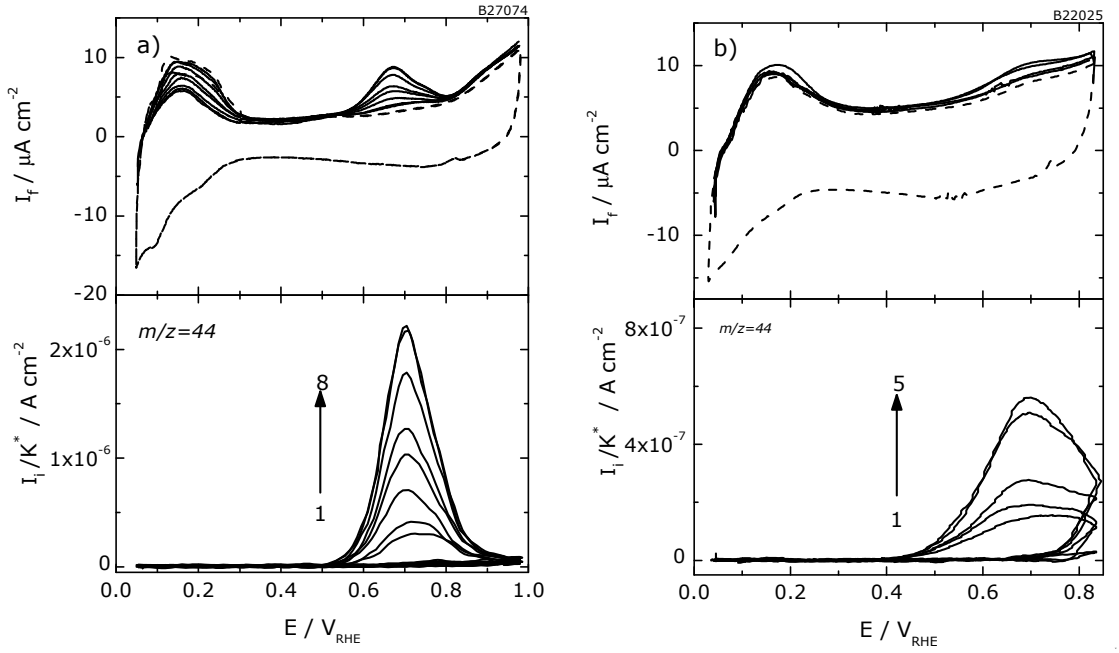

Figure 5-9 Simultaneously recorded faradaic currents and corresponding ion currents of CO_2, *m/z*=44, during oxidation of methanol adsorbate on (a) PtO_x^E/C and (b) $PtRu^E$/C in 0.5 M H_2SO_4. Scan rate: 10 mV s^{-1}. Electrolyte flow rate: 5 µL s^{-1}. Methanol adsorption performed at 500 mV for different times. From (a) 1 to 8: 1, 2, 5, 10, 20, 60, 120, 180 s and (b) 1 to 5: 1, 2, 5, 120 and 600 s from 0.1 M CH_3OH + 0.5 M H_2SO_4 solution . For comparison the CV for adsorbate free surface is also shown (dotted line). Catalyst loading: 10 μg_{Pt} cm^{-2}. The current is referred to $A_{sur,CO}$.

Figure 5-10 demonstrates the time dependent behavior of the methanol adsorbate coverage on PtO_x^E/C and $PtRu^E$/C catalyst, the adsorption potential was 500 mV. In the first approximation, comparing to Figure 5-8 it is clearly visible that the adsorption rate on Pt(pc) is higher than that observed for the colloidal surfaces.

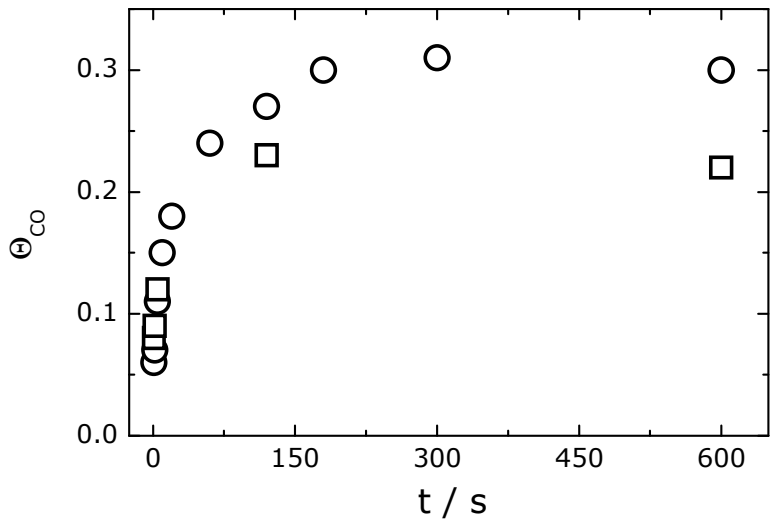

Figure 5-10 Influence of adsorption time on relative coverage of methanol (Equation 2-5), Θ_{CO}, on PtO_x^E/C (circles) and $PtRu^E$/C (squares). Adsorption of methanol carried out in 0.1 M CH_3OH + 0.5 M H_2SO_4 solution at 500 mV.

Corresponding initial rates of methanol adsorption were calculated from the coverage achieved after very short adsorption times (1, 2 and 5 s). The results are shown in Table 5-2.

Table 5-2 Rates of methanol adsorption at polycrystalline Pt and PtO_x^E nanoparticles for different adsorption potentials E_{ad} of methanol.

E_{ad} / V_{RHE}	methanol adsorption rate / ML s^{-1}		
	Pt(pc)	PtO_x^E/C	$PtRu^E$/C
0.3	0.017	0.014	-
0.4	0.038	0.015	-
0.5	0.047	0.021	0.065
0.6	0.056	0.036	-

ML, monolayer of adsorbate

The methanol adsorption rate increases with the adsorption potential. It is faster at polycrystalline Pt than at PtO_x^E colloidal nanoparticles. The adsorption rate determined at adsorption potential of 500 mV on $PtRu^E$/C catalyst is higher than that observed at both pure Pt surfaces. This leads to the conclusion, that even a small content of Ru promotes the adsorption rate of methanol.

5.3. POTENTIOSTATIC AND GALVANOSTATIC OXIDATION OF METHANOL ADSORBATE

The reaction order with respect to the adsorbate coverage is also studied by performing potential step and galvanostatic experiments.

5.3.1. Chronoamperometry

Figure 5-11 compares the oxidation of the methanol adsorbate at polycrystalline platinum (Figure 5-11a) with that at PtO_x^E/C (Figure 5-11b). During oxidation of the methanol adsorbate at polycrystalline Pt both the faradaic current and ion current remain constant over 20 s, as expected for a surface reaction with a reaction order of 0. Similarly, constant oxidation currents have been observed for Cu_{UPD} dissolution on the stepped Pt(332) single crystal, where the rate is given by the length of the steps and therefore is independent of the Cu coverage [271]. For comparison, the oxidation current of the methanol adsorbate on a PtO_x^E/C electrode is exponentially decaying, as expected for a reaction of 1st order.

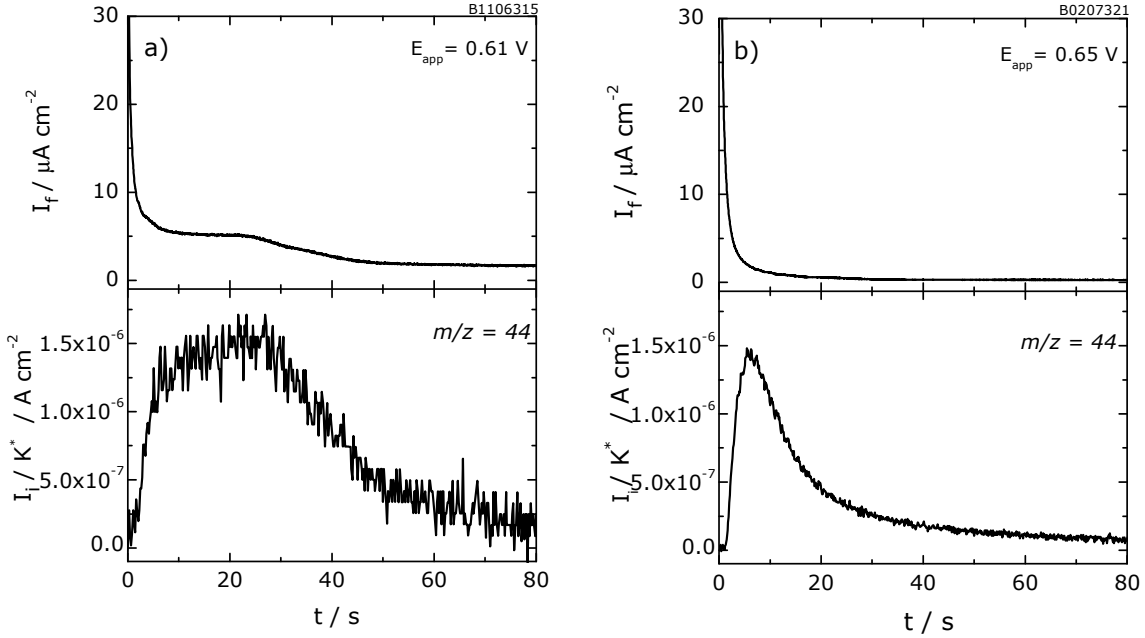

Figure 5-11 Potentiostatic electrooxidation of CO from methanol adsorbed at 500 mV for 2 min on (a) Pt(pc) at E_{app}=610 mV and (b) PtO_x^E/C electrode at E_{app}=650 mV in 0.5 M H_2SO_4. Electrolyte flow rate: 5 µL s^{-1}. Catalyst loading: 10 µg$_{Pt}$ cm^{-2}. Current is referred to $A_{sur,CO}$.

5.3.2. Chronopotentiometry

These results are further confirmed by galvanostatic oxidation experiments: the oxidation of the methanol adsorbate at polycrystalline Pt occurs at a constant potential, as expected for a reaction of zero order (Figure 5-12a), whereas on the PtO_x^E/C nanoparticle electrode the potential monotonically increases (Figure 5-12b).

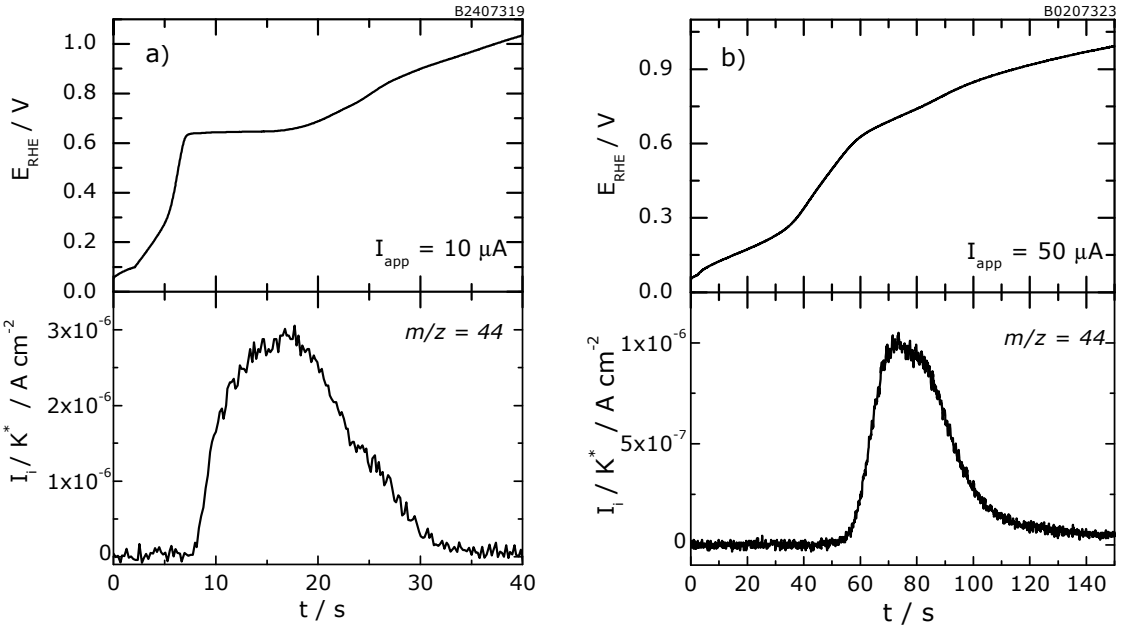

Figure 5-12 Galvanostatic oxidation of CO from adsorbed methanol on (a) Pt(pc) (I_{app}=10 µA) and (b) PtO_x^E/C electrode (I_{app}=50 µA). Electrolyte flow rate: 5 µL s^{-1}. Adsorption of methanol was carried out in 0.1 M CH_3OH + 0.5 M H_2SO_4 solution at 500 mV for 2 min. Catalyst loading: 10 µg$_{Pt}$ cm^{-2}. Current is referred to $A_{sur,CO}$.

A reaction order of nearly zero might be, in part, explained by the Langmuir-Hinshelwood mechanism, according to which the oxidation rate is proportional to $\Theta(1-\Theta)$. This factor is largest at Θ=0.5 and decreases only by 16% for Θ=0.3 or Θ=0.7. However, at a potential slightly below the current maximum of the experiment with the lowest initial coverage (0.3), at which the coverage has decreased by one third of its initial value (i.e., to 0.2), the oxidation rate for the highest initial coverage (0.7) should be proportional to 0.6 (1-0.6)=0.24 as compared to 0.2 (1-0.2)=0.16, i.e., higher by 40%, which is obviously not the case. Modelling of the curves (Figure 5-13) according to the Langmuir-Hinshelwood mechanism gives the same result. Therefore, it has to be assumed that there is another reason for the independence of the oxidation rate on the CO coverage.

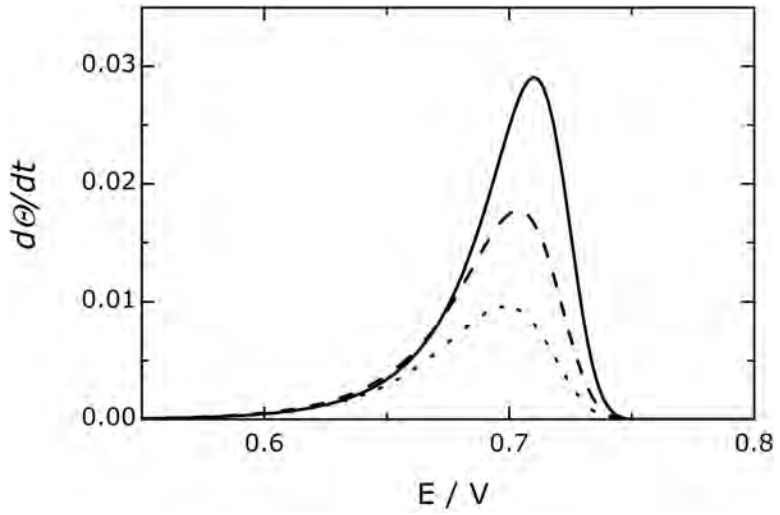

Figure 5-13 Modelling according to the Langmuir-Hinshelwood mechanism: $d\Theta/dt = \Theta.(1-\Theta).k.e^{-\alpha EnF/RT}$, where n = 2, α = 0.5 and k = $9.5 \cdot 10^{-13}$ s^{-1}; for different starting methanol adsorbate coverage - Θ: 0.7 (solid line), 0.5 (dashed line) and 0.3 (dotted line).

Alternatively, the rate determining step might be the adsorption of the oxygen species, whose equilibrium surface concentration is believed to be low. However, this adsorption rate, and therefore, the overall rate would still be proportional to $(1-\Theta_{CO})$, which obviously is not the case. It remains the possibility that either OH adsorption or CO oxidation, are restricted to special, active sites on the surface.

In [173], the authors reported that the reaction order with respect to the methanol concentrations was close to zero for the "direct" reaction path leading to CO_2 *via* adsorbed CO. This can now be understood: the rate limiting step is the oxidation of the adsorbate, which itself of 0^{th} order.

On the PtO_x^E/C nanoparticle electrode, the different nanoparticles cannot communicate with one another. The oxidation can only proceed at active sites of that nanoparticle at which the CO molecules are adsorbed [9, 272]. Both the different

sizes of the nanoparticles and the various kinds of active sites on the different nanoparticles lead to a broad distribution of onset potentials on the single particles, and the width of the oxidation peak, which is larger than on the polycrystalline electrode, is mainly determined by this distribution.

5.4. DISCUSSION AND REMARKS

The methanol adsorption experiments show that methanol adsorption on Pt surfaces is dependent on the potential of the adsorption. The relative coverage of the methanol adsorbate and its adsorption rate increases with the increase of the adsorption potential. In general, the maximum coverage is achieved at the potentials, at which the methanol adsorbate starts to be oxidized. This effect could be explained by several processes on the surface in this potential range. At low adsorption potentials the methanol adsorption is partially inhibited by adsorbed hydrogen, which is displaced by methanol adsorbate at potentials in the so-called double layer region. At higher potentials OH is adsorbed due to the dissociation of water which inhibits again the adsorption of methanol and in addition, the oxidation of adsorbed CO comes into competition with the adsorption.

In addition, the lower surface coverage of methanol adsorbate, as compared to the CO adsorption, at all studied electrode surfaces indicates that methanol adsorption and dissociation to CO needs a surface structure having at least three neighbouring Pt sites.

The reactivity of PtO_x^E/C nanoparticle electrodes with respect to the different reaction steps of methanol oxidation is quite different from that of polycrystalline Pt. As shown in the potential step experiments followed by electrolyte exchange and subsequent adsorbate oxidation, the rate of adsorption of methanol is considerably decreased. A clear decrease in the oxidation rate of the adsorbate, which is observed for CO adsorbed from a saturated CO solution, is not observed for the methanol adsorbate. However, the reaction order with respect to the adsorbate is drastically changed. The order is zero at polycrystalline Pt and closer to one at the PtO_x^E/C nanoparticle electrode. Whereas the latter can be understood from a distribution of PtO_x^E/C nanoparticles with varying coverage and due to the fact that the coverage for methanol is always much lower than 0.5 (assuming a Langmuir isotherm, therefore, the $\Theta(1-\Theta)$ term is monotonically increasing with Θ), to explain the zero reaction order, it has to be assumed that oxidation occurs on a limited number of active sites. Since their number does not vary during the course of the oxidation, one has to conclude, that they are not covered by the methanol adsorbate.

It has been shown before, that adsorbed CO is electronically destabilized in the vicinity of Ru [154]. The present results suggest that this is also true for the methanol adsorbate. When the coverage with CO_{ad} formed from methanol is small, oxidation at a $Ru_{0.2}$-modified and alloyed electrodes occurs at a potential similar to that on pure Pt/C because the adsorbate is adsorbed at the most stable sites, i.e., those least influenced by Ru. At high coverage, the "less stable" sites in close vicinity to Ru or on Ru are also occupied, and the onset of oxidation and the peak potential is shifted to lower values.

When discussing the reason for the catalytic effect of low Ru deposits on Pt surfaces the bifunctional mechanism is often invoked. Methanol is dissociatively adsorbed on Pt sites and water is dissociated on Ru sites giving adsorbed OH. Finally, the adsorbed CO and OH species react together forming CO_2.

While the data obtained with the $PtRu^{E}$/C and $PtRuO_x^{M}$/C alloys are basically similar to those observed with Ru modified PtO_x^{E}/C, the higher adsorbate coverage reached at lower adsorption potentials on the Ru modified catalyst should be noted. This could be explained by the surface morphology of the samples, where at PtRu alloys with a composition of 50:50 (i.e., only 50% Pt) the probability of the existence of Pt_3-places is extremely small.

Methanol adsorption rates are measured. The slower adsorption rates observed in the whole potential region at Pt nanoparticles, in comparison to those found at polycrystalline platinum, can be explained by the lower quantity of steps present on the nanoparticle surface. In fact, it is expected that these differences in the adsorption rates will vary much stronger, if the time of the adsorption is short enough. Unfortunately, the equipment used in this study could not be implemented for adsorption times shorter than 1 s.

Modelling of the kinetic process of the methanol adsorption using a simple rate equation $d\theta/dt = k \cdot (1-\theta)^n$, for n = 3, 4 and 5, is shown in Figure 5-14. The rate constant k used in this modelling is that obtained at E_{ad}=500 mV on Pt(pc). The comparison of these model curves with those experimentally found at E_{ad}=500 mV (Figure 5-8) leads to suggestion that the rate constants are even higher than those experimentally determined. It is obvious that even at these short adsorption times the surface coverage is too high to determine the rate constant exactly. Much smaller surface concentrations are needed to determine the rate constant at the beginning of the methanol adsorption more exactly. For short adsorption times, it seem that a value between n=3 and n=4 describes the adsorption best. For long adsorption times

and large surface concentration of the methanol adsorbate, a large deviation is observed from the behaviour of the curves for n=3 and n=4. This can be explained by assuming a limited surface diffusion of the adsorbate. Every adsorbed methanol adsorbate needs 3 or 4 adsorption places. The free places on the other hand are distributed randomly on the surface, and only for low surface coverages such an assembly of free coordination sites can be easily found by the adsorbate. Therefore the adsorption rate decreases very fast with increasing coverage and approaches zero at coverages well below one, if there is no surface diffusion. This decrease is faster than expected by the simple model applied here, where one would expect an increase even at higher surface coverages.

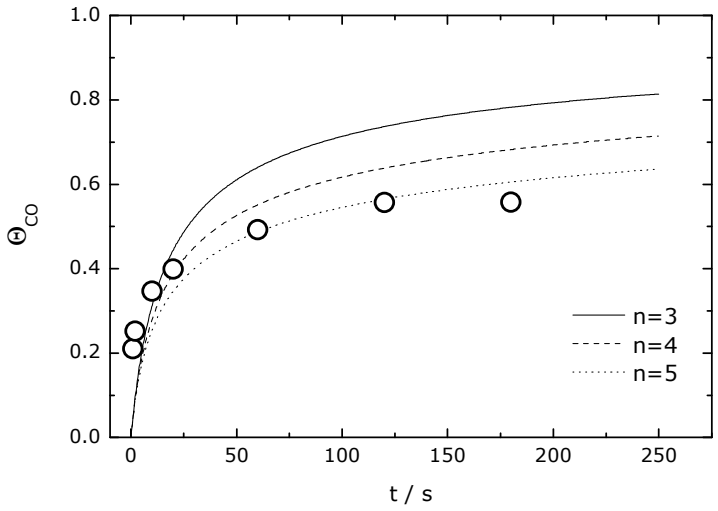

Figure 5-14 Modelling according to the Langmuir-Hinshelwood mechanism: $d\theta/dt = k\cdot(1-\theta)^n$, where $k = 0.056$ ML s^{-1}, determined at Pt(pc) during oxidation of methanol adsorbed at E_{ad}= 500 mV. Circles: for comparison, the experimentally found coverage at different adsorption times for E_{ad} = 500 mV.

As already mentioned above, the maximum coverage is reached at 120 s which is contrary to the kinetic profiles found by Waszczuk et al. [148]. Using radioactive labelling and electrochemistry in so called radio-electrochemical cell, it was found that the methanol adsorption reaction is quite slow and the CO saturation level was not reached until after 2 hours. The reason for such low adsorption rate could be the missing convection in their cell leading to the adsorption of CH_2O which is formed as an intermediate.

Interestingly, the onset of the methanol oxidation at the $PtRuOsIrO_x^M$/C catalyst is partially shifted to lower potentials in the same way as observed for PtRu surfaces. Simultaneously it seems to stabilize a part of the adsorbate on the surface in such way that this could be firstly oxidized at potentials even higher than that on pure Pt surface.

Chapter 6 Electrocatalytic oxidation of bulk methanol

The catalytic activity of platinum and platinum based surfaces toward the electrooxidation of methanol in a sulfuric acid electrolyte at room temperature is studied in this part. Current efficiencies for the formation of CO_2 during methanol oxidation are determined. Also the influence of the surface structure and the effect of co-catalytic metal Ru are studied.

6.1. MASSIVE ELECTRODE SURFACES

Figure 6-1 shows three consecutive positive going sweeps obtained on (a) Ru-free and (b) $Ru_{0.2}$-modified polycrystalline Pt during the potentiodynamic oxidation of methanol. The first sweep on Ru-free surface contains a significant anodic shoulder at low potentials (between 400 and 500 mV) that apparently overlaps with the onset of CH_3OH oxidation. This shoulder can be observed only during the first anodic sweep and is not caused by the formation of CO_2. It is due to the oxidative electrosorption of methanol [205, 206, 273]. The subsequent sweeps do not contain this peak and are appreciably lower in current than the first sweep. This effect, although more significant, is also seen on the $Ru^{0.2}$-modified polycrystalline platinum.

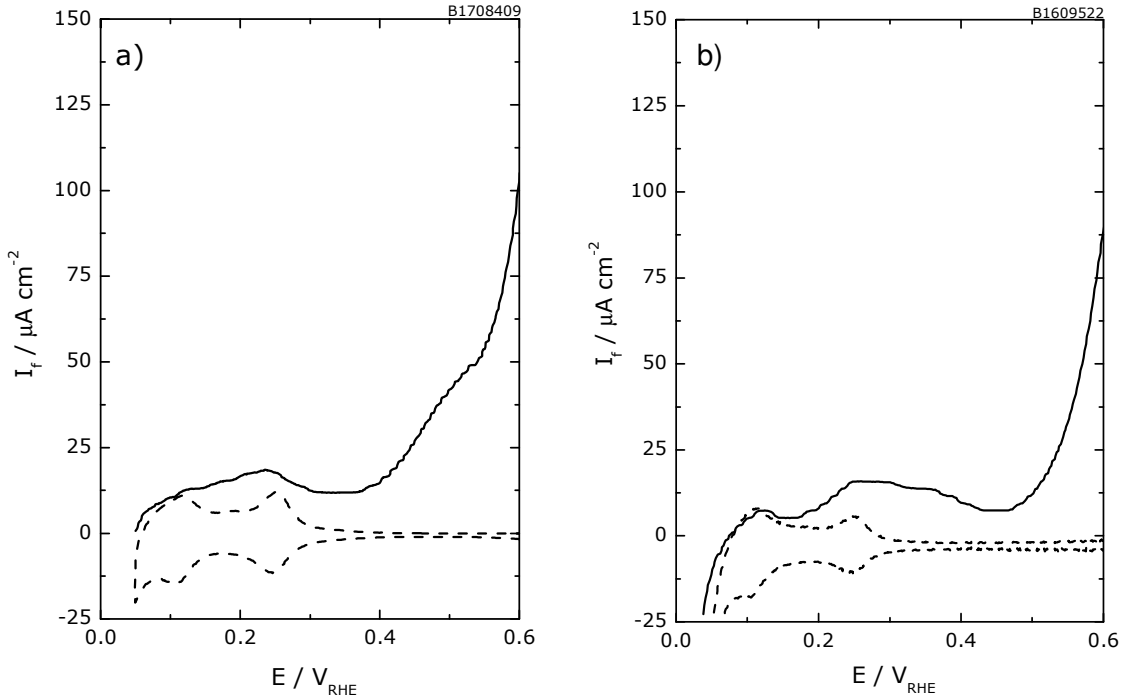

Figure 6-1 Positive-going sweep of potentiodynamic oxidation of methanol over (a) pure and (b) $Ru_{0.2}$-modified Pt(pc) in 0.1 M CH_3OH + 0.5 M H_2SO_4. Scan rate: 10 mV s^{-1}. Electrolyte flow rate: 5 µL s^{-1}. Dashed line: The current in the basic electrolyte. The current is referred to $A_{sur,CO}$.

In order to exclude large changes in the surface composition during the cycling, the second sweeps are used for the evaluation of the current and the current efficiencies in this chapter.

6.1.1. Polycrystalline Pt

In Figure 6-2, the bulk methanol oxidation is compared to the oxidative desorption of the adsorbate at (a) Ru-free and (b) $Ru_{0.2}$-modified Pt(pc) electrode. The faradaic current for the methanol oxidation at both electrodes greatly exceeds that for the adsorbate oxidation. However, in the case of the Pt(pc) electrode (Figure 6-2a), the mass spectrometric ion currents for CO_2 formation (*m/z*=44) from the adsorbate oxidation and the methanol oxidation overlap in the onset part. The formation rate of CO_2 from methanol is obviously determined by the oxidation rate of the adsorbate, thus indicating a reaction pathway *via* adsorbed CO. The much higher faradaic current for bulk methanol oxidation, as compared to the adsorbate oxidation is due to the formation of other oxidation products besides CO_2, i.e., formaldehyde, formic acid and methylformate, which are formed in a separate parallel reaction pathway.

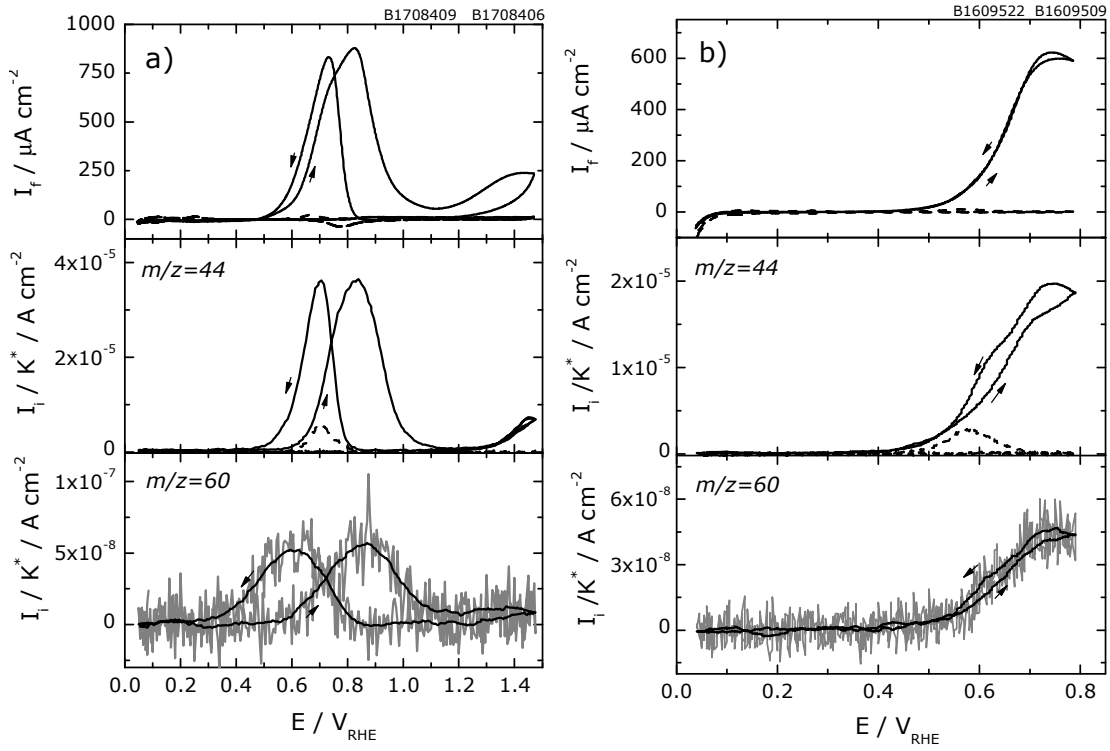

Figure 6-2 Simultaneously recorded faradaic and corresponding ion currents of CO_2, m/z=44, and methylformate, m/z=60, during bulk oxidation of methanol on (a) pure and (b) $Ru_{0.2}$ modified Pt(pc) in 0.1 M CH_3OH + 0.5 M H_2SO_4. Scan rate: 10 mV s^{-1}. Electrolyte flow rate: 5 µL s^{-1}. Dotted line: oxidation of methanol adsorbate. the currents are referred to $A_{sur,CO}$.

The formation of CO_2 on $Ru_{0.2}$-modified smooth polycrystalline platinum starts at 350 mV, i.e. about 150 mV more negatively than that on pure Pt(pc). At potentials above 700 mV, the slope of ion current of CO_2 changes, while the faradaic current

and ion intensity for methylformate increase with the same slope until 750 mV, then decrease. The change in the slope of m/z=44 points to some change in the reaction mechanism. The formation of methylformate starts at 500 mV, which is the same as in the case of polycrystalline platinum, but increases more steeply at the potential above 500 mV.

In fuel cell applications the stability of the catalyst under the reaction conditions is important. Generally, potentiostatic step experiments give more reliable correlation of I_f and I_i for calculations of the current efficiency and are more practice oriented than data observed during the bulk methanol oxidation. The faradaic current and corresponding ion currents for the formation of CO_2 (m/z=44) and methylformate (m/z=60) were recorded during the methanol adsorption experiments (see Chapter 4.1.2).

The potentiostatic experiments at the pure and $Ru_{0.2}$-modified smooth polycrystalline Pt during adsorption time of 2 minutes are shown in Figure 6-3. On pure polycrystalline platinum (Figure 6-3a) the current decreases with time and the effect of adsorption potential is clearly seen; with the increase of the adsorption potential, faradaic and ion currents increase strongly.

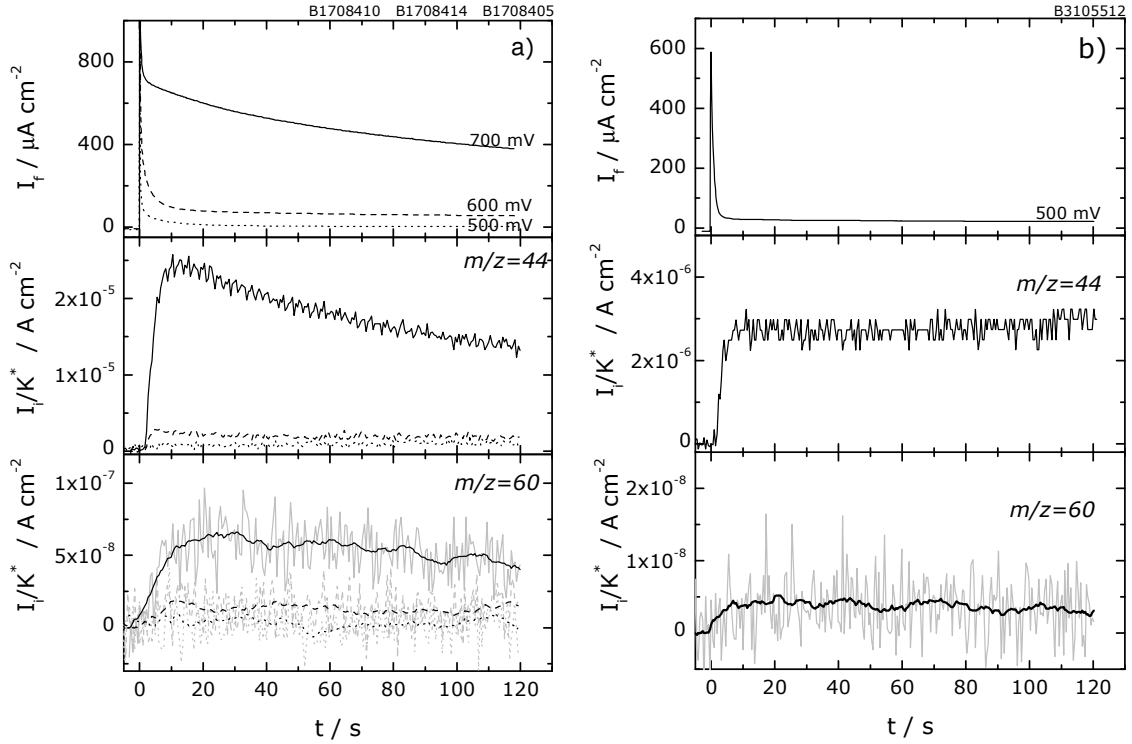

Figure 6-3 Simultaneously recorded transients of faradaic and ion current of CO_2, m/z=44, and methylformate, m/z=60, during methanol adsorption on (a) pure and (b) $Ru_{0.2}$ modified Pt(pc) in 0.1 M CH_3OH + 0.5 M H_2SO_4. Scan rate: 10 mV s^{-1}. Electrolyte flow rate: 5 µL s^{-1}. Note: Oscillations in the ion current for CO_2 are caused by peristaltic pump and mass transport limitation of CO_2 to the electrolyte gas interface at porous Teflon membrane. The currents are referred to $A_{sur,CO}$.

The potential step experiment on $Ru_{0.2}$-modified polycrystalline Pt is shown in Figure 6-3b and resembles to those found for Ru modified Pt(110) [274]. The current efficiency of CO_2 at 2 minutes after step of potential from 50 mV to 500 mV reaches 56% and the faradaic current and the ion currents for CO_2 and methylformate increase compared to the polycrystalline Pt where a current efficiency of 18% is found. Although the amount of methylformate is larger than on Pt(pc), its relative amount of about 2% with respect to CO_2 is much smaller than on pure Pt(pc) (10%).

Figure 6-4 shows the effect of potential on faradaic currents and calculated current efficiencies for CO_2 during the potentiodynamic methanol oxidation as well as at 2 minutes after potential step. On pure polycrystalline Pt the faradaic currents increase strongly with the increase of potentials, while current efficiencies increase weakly. On $Ru_{0.2}$-modified polycrystalline platinum, the higher current efficiency for CO_2 is observed at low potentials, however, at high potentials it decreases and is same as that on Pt(pc) at 700 mV, although the faradaic current still increases.

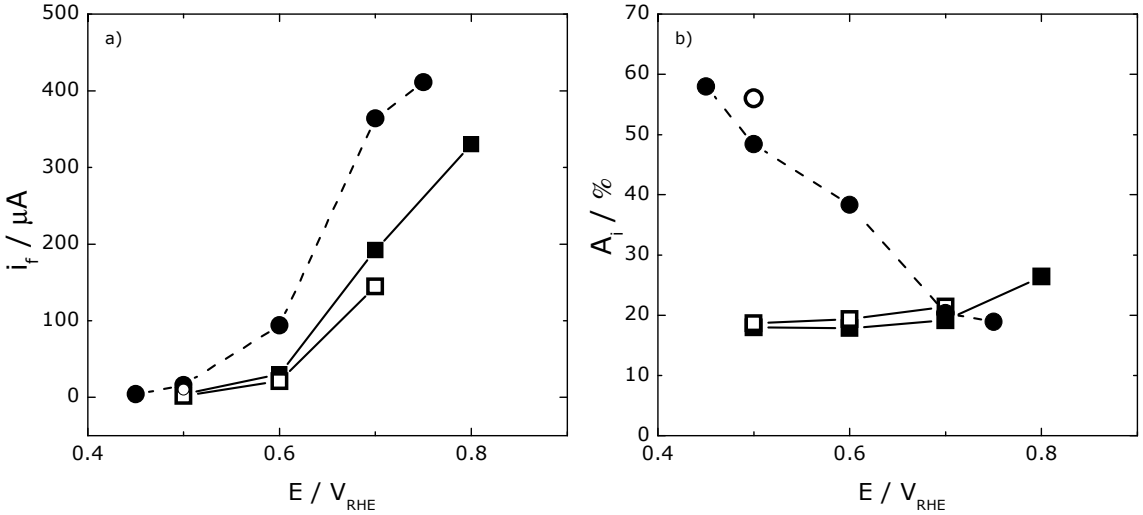

Figure 6-4 The dependence of (a) faradaic currents and (b) current efficiencies of CO_2 on the potentials during potentiodynamic (filled) and potentiostatic (open) methanol oxidation on polycrystalline platinum (squares) and $Ru_{0.2}$-modified Pt(pc) (circles) in 0.1 M CH_3OH + 0.5 M H_2SO_4 solution. Where, $A_{exp}(Pt(pc))=0.38$ cm^2 and $A_{exp}(Pt(pc)/Ru_{0.2})=0.64$ cm^2

On polycrystalline Pt the current efficiency is lower and the relative contribution of methylformate is higher at low potentials (cf. Figure 6-2a). Methylformate is probably formed in a subsequent reaction from formic acid and methanol. At low potentials, at which CO_{ad} is not oxidized, the methanol adsorption leads to quick formation of CO_{ad}. This adsorbate then hinders the further adsorption and decomposition of methanol. At the potentials higher than the onset potential of adsorbate oxidation, these two parallel oxidation paths take place simultaneously.

The methanol oxidation on $Ru_{0.2}$-modified polycrystalline Pt at low potentials exhibits a higher current efficiency of CO_2, which demonstrates that adsorbed Ru promotes the methanol oxidation *via* adsorbed CO. At low potentials the formation rate of CO_2 during the methanol bulk oxidation is higher than that for the oxidation of methanol adsorbate. This demonstrates that methanol adsorption is the rate determining step for the methanol oxidation to CO_2 on $Ru_{0.2}$-modified Pt and not the oxidation of the adsorbate. However, at the low potentials only a part of methanol adsorbate, which has low adsorption energy and is formed only at the high coverage of methanol adsorbate, can be oxidized. The rest of methanol adsorbate remains on the electrode surface and is not oxidized.

A possible reason for the decrease of the current efficiency at higher potentials could be too strong adsorption of OH species on Ru, which makes the surface inactive for the reaction path *via* adsorbed methanol.

6.1.2. Pt(665)

Similar experiments at room temperature were performed at Pt(665) (Figure 6-5a) and $Ru_{0.2}$-decorated Pt(665) (Figure 6-5b).

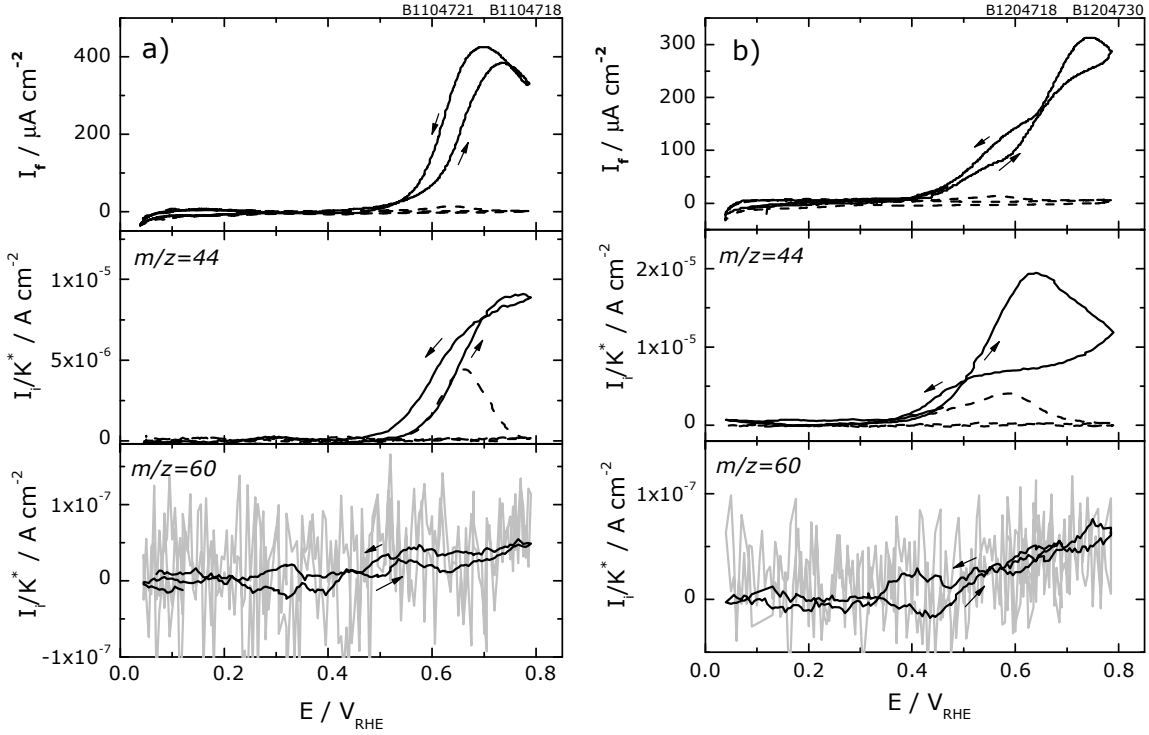

Figure 6-5 Simultaneously recorded faradaic and corresponding ion currents of CO_2, m/z=44, and methylformate, m/z=60, during bulk oxidation of methanol on (a) pure and (b) $Ru_{0.2}$ decorated Pt(665) in 0.1 M methanol + 0.5 M H_2SO_4 solution. Scan rate: 10 mV s^{-1}. Electrolyte flow rate: 5 µL s^{-1}. Dashed line: oxidation of methanol adsorbate. The currents are referred to $A_{sur,CO}$.

For the Pt(665), the formation rate of CO_2 for methanol bulk oxidation starts at ca. 500 mV and is almost the same as that for the oxidation of the methanol

adsorbate. This demonstrates that during the methanol oxidation the formation of CO_2 occurs *via* the oxidation of the methanol adsorbate, i.e., CO_{ad}. Simultaneously, a large amount of dissolved intermediates is formed, leading to a much higher faradaic current than required for the formation of CO_2. For $Ru_{0.2}$-decorated Pt(665), the oxidation starts about 150 mV more negative and the ion currents for CO_2 do not overlap at all. At lower potentials, the formation rate of CO_2 is higher for the oxidation of bulk methanol, than for the oxidation of methanol adsorbate.

Figure 6-6 shows the faradaic current and corresponding ion currents for the formation of CO_2 (m/z=44) at the pure and $Ru_{0.2}$-decorated Pt(665) during the adsorption time of 2 minutes.

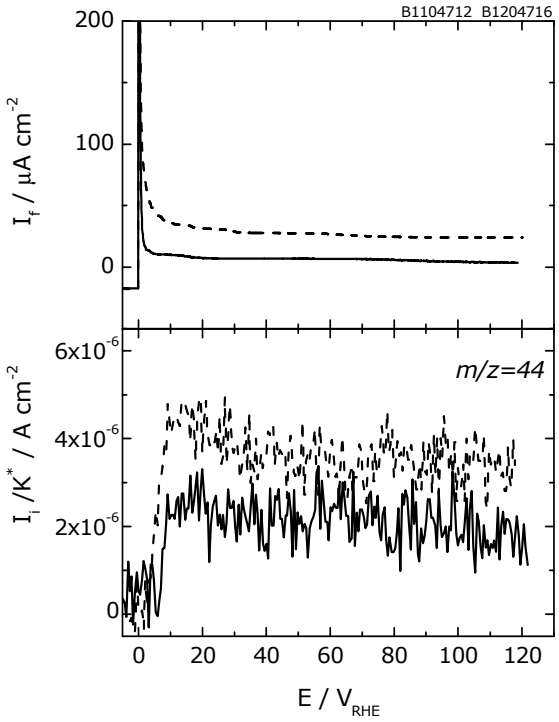

Figure 6-6 Simultaneously recorded current transients of faradaic current and ion current of CO_2, m/z=44, and methylformate, m/z=60, during potential step from 50 mV to 470 mV on pure (solid line) and $Ru_{0.2}$-decorated Pt(665) (dashed line) in 0.1 M CH_3OH + 0.5 M H_2SO_4 solution. Scan rate: 10 mV s^{-1}. Electrolyte flow rate: 5 µL s^{-1}. The currents are referred to $A_{sur,CO}$.

In these measurements, the ion currents for the formation of methyl formate (m/z=60) are very low and cannot be distinguished from the signal noise. On $Ru_{0.2}$-decorated Pt(665) the faradaic current and the ion current for CO_2 reach higher values than that at pure Pt(665). Both, the faradaic and the ion current, reach constant values within 2 minutes after the potential step. Similarly to the Pt(pc), the current efficiency of CO_2 at 2 minutes after step of potential from 50 mV to 470 mV reaches only 15% on pure Pt(665) which is lower compared to $Ru_{0.2}$-decorated Pt(665) where current efficiency of 53% is found. Also here the total

amount of methyl formate of about 8% with respect to CO_2 is larger on Pt(665) than on the $Ru_{0.2}$-decorated surface (3%).

The effect of potential on the faradaic current (Figure 6-7a) and calculated current efficiency for CO_2 (Figure 6-7b) during the potentiodynamic and potentiostatic methanol oxidation on pure and $Ru_{0.2}$-decorated Pt(665) resemble those found for polycrystalline surfaces. More precisely, in the case of $Ru_{0.2}$-decorated Pt(665) the higher current efficiency for CO_2 is observed at low potentials which decreases with increasing the potential, whereas the current efficiencies increase weakly on pure Pt(665). However, the increase of the faradaic current with the increase of potentials is less pronounced than on polycrystalline platinum. (In the measured range of potential no intersection of current efficiencies was found at higher potential.)

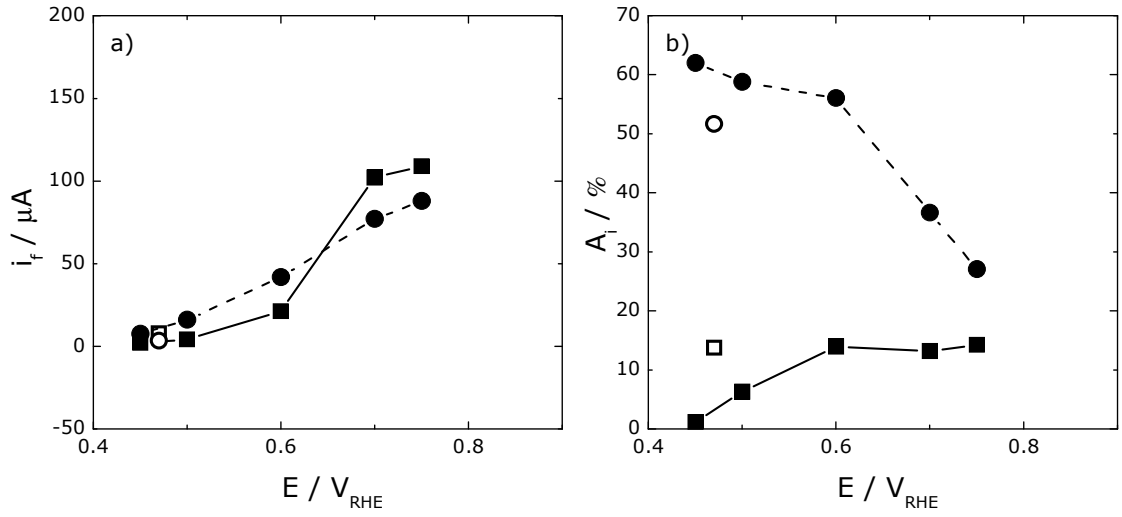

Figure 6-7 The dependence of (a) faradaic currents and (b) current efficiencies of CO_2 on the potentials during potentiodynamic (filled) and potentiostatic (open) methanol oxidation on Pt(665) (squares) and $Ru_{0.2}$ decorated Pt(665) (circles) in 0.1 M methanol + 0.5 M H_2SO_4 solution. Where, A_{exp}(Pt(665))=0.29 cm^2 and A_{exp}(Pt(665)/$Ru_{0.2}$)=0.31 cm^2

Figure 6-4 and 6-7 clearly show that the faradaic current and the calculated current efficiencies obtained from the potential step procedure are consistent with those received during the methanol oxidation from solution within an error in measurement.

It was shown by H. Wang [214] that the faradaic current and the amount of CO_2 formed during methanol oxidation increase with an increase in the step density of platinum surface. Using the similar experimental setup, the maximum current observed on Pt(111) and on Pt(332) was 27 μA and 160 μA, respectively. The peak current of ca 100 μA is found during the methanol oxidation on Pt(665), this is higher than that observed at Pt(111) but clearly lower than that observed at Pt(332)

surface, with higher step density than Pt(665). These findings obviously suggest that steps are the active sites for methanol oxidation. He also showed that Ru ad-atoms not only promote the methanol oxidation on Pt(111) and Pt(332) at low potentials but also induce the shift of the methanol oxidation from the reaction path *via* soluble intermediates to that *via* adsorbed CO, leading to higher current efficiency of formed CO_2. This is also true for our measurements on $Ru_{0.2}$-modified Pt(665), but a direct comparison of the data is not possible due to the different Ru coverage.

6.2. SUPPORTED METAL CATALYST SURFACES

In this section the potentiodynamic and potentiostatic oxidation of methanol at commercial nanoparticles on the one hand and surfaces of nanoparticles obtained from MPI Mülheim on the other hand is studied.

6.2.1. Commercial noble metal catalysts from E-Tek Inc.

The bulk methanol oxidation in contrast to the oxidative desorption of the adsorbate at PtO_x^E/C nanoparticulate catalyst is shown in Figure 6-8.

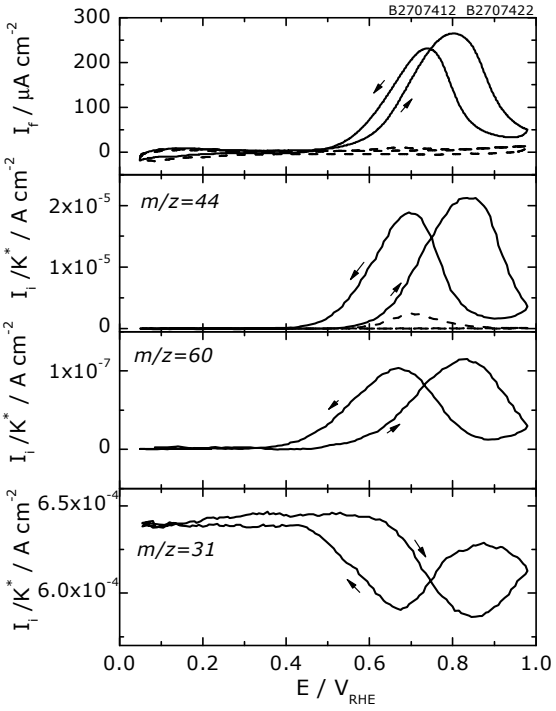

Figure 6-8 Simultaneously recorded faradaic and corresponding ion currents of CO_2, m/z=44, methylformate, m/z=60, and methanol, m/z=31, during bulk oxidation of methanol on PtO_x^E/C nanoparticle electrode in 0.1 M methanol + 0.5 M H_2SO_4 solution. Scan rate: 10 mV s^{-1}. Electrolyte flow rate: 5 µL s^{-1}. Dashed line: oxidation of the methanol adsorbate. Catalyst loading: 10 μg_{Pt} cm^{-2}. The currents are referred to $A_{sur,CO}$.

Also here, the faradaic current for methanol oxidation greatly exceeds that for the adsorbate oxidation. However, contrary to polycrystalline platinum and Pt(665), the mass spectrometric ion currents for CO_2 formation (*m*/*z*=44) from the adsorbate

oxidation and the methanol oxidation do not overlap at all. Indeed, in the low potential range is the formation rate of CO_2 for the bulk methanol oxidation higher than for the oxidation of methanol adsorbate, but not as significant as in the case of $Ru_{0.2}$-decorated Pt(665). Nevertheless also on the PtO_x^E/C nanoparticulate systems the formation of methyl formate starts at about 100 mV below the formation of CO_2.

Additionally to the ion current of CO2 (m/z=44) and methylformate (m/z=60) also the ion current of methanol (m/z=31) is shown. It is clearly seen, that during the bulk oxidation of methanol the consumption of methanol from the solution could be detected by DEMS. From the amount of methanol consumption, $\Delta\dot{n}_{CH_3OH}$, the amount of produced CO_2, $\dot{n}_{CO_2}$, and the faradaic current, If, the amount of formaldehyde, $\dot{n}_{CH_2O}$, and formic acid, $\dot{n}_{HCOOH}$, can be calculated:

$$\frac{I_f}{F} = 6 \cdot \dot{n}_{CO_2} + 2 \cdot \dot{n}_{CH_2O} + 4 \cdot \dot{n}_{HCOOH} \qquad \text{(Equation 6-1)}$$

$$\Delta\dot{n}_{CH_3OH} = \dot{n}_{CO_2} + \dot{n}_{CH_2O} + \dot{n}_{HCOOH} \qquad \text{(Equation 6-2)}$$

Where F is Faradaic constant (96500 C mol^{-1}).

For the conditions of the measurements in Figure 6-8, the yields of formaldehyde, formic acid and CO_2 are thus 68%, 5% and 27% at 600 mV. It should be noted that in these calculations a complete mixing of the electrolyte leaving the electrochemical compartment is assumed. Such complete mixing, however, is only obtained at flow values of 1 μl s^{-1} and below; therefore these values are approximations.

As already noticed in previous parts, it is possible to improve the electroactivity towards methanol oxidation using small amounts of Ru incorporated into the Pt catalyst. The voltammograms during the bulk methanol oxidation at $PtRu^E$/C alloyed catalyst and $Ru_{0.2}$-modified PtO_x^E/C are shown in Figure 6-9.

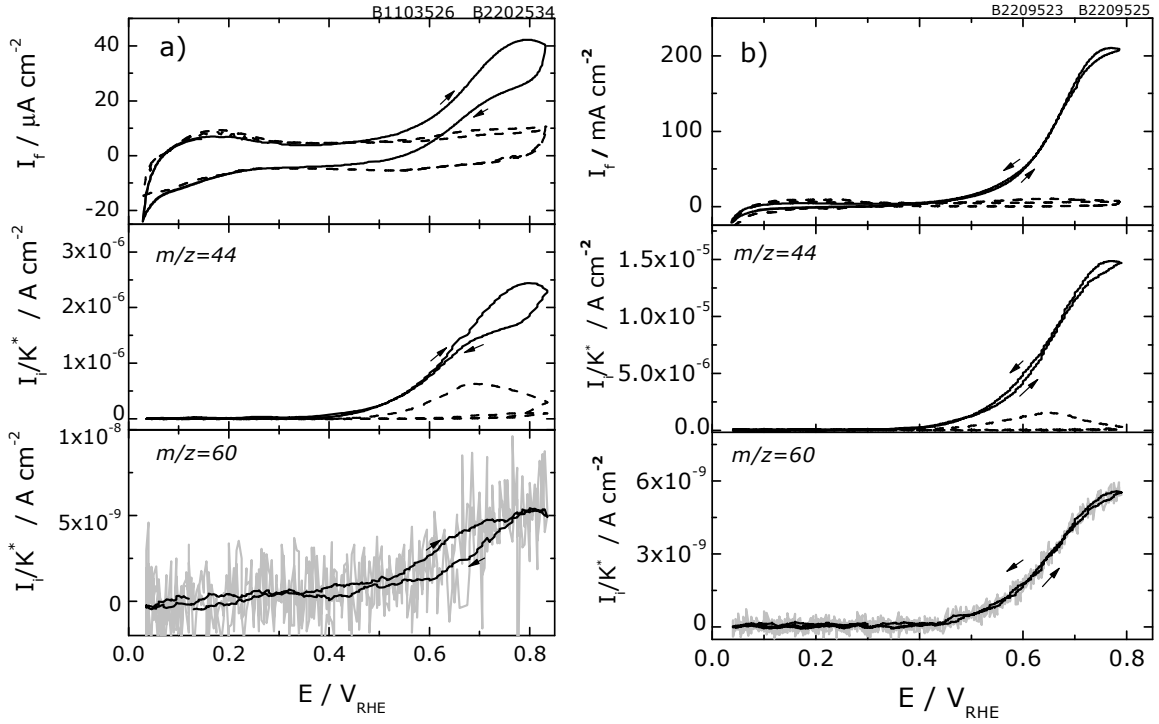

Figure 6-9 Simultaneously recorded faradaic and corresponding ion currents of CO_2, m/z=44, and methylformate, m/z=60, during bulk oxidation of methanol on (a) $PtRu^E/C$ alloy and (b) $Ru_{0.2}$ modified PtO_x^E/C electrode in 0.1 M methanol + 0.5 M H_2SO_4. Scan rate: 10 mV s^{-1}. Electrolyte flow rate: 5 µL s^{-1}. Dashed line: oxidation of methanol adsorbate. Catalyst loading: 10 μg_{Pt} cm^{-2}. Currents are referred to $A_{sur,CO}$.

The formation of CO_2 on both electrodes starts already at 400 mV, i.e. about 100 mV more negatively than that on pure platinum catalyst, which is consistent with findings for the massive electrodes (see Figure 6-2 and 6-5). Interestingly, the current densities obtained at the $Ru_{0.2}$-modified PtO_x^E/C surface exceed by far those observed at $PtRu^E/C$ alloys. Contrary to pure platinum nanocatalysts, the oxidation of methanol adsorbate on Ru modified PtO_x^E/C and $PtRu^E/C$ at the low potentials is dependent on the coverage of the methanol adsorbate. With the increase of the methanol adsorbate coverage, the onset potential of CO_2 formation shifts negatively, and the formation rate of CO_2 increases. Also the formation rate of CO_2 for the methanol bulk oxidation at low potentials is considerably higher than that for the oxidation of the methanol adsorbate. This supports the idea that methanol adsorption could be the rate determining step for the methanol oxidation to CO_2 on $Ru_{0.2}$-modified PtO_x^E/C.

Typical potential step experiments on PtO_x^E/C, $PtRu^E/C$ and $Ru_{0.2}$-modified PtO_x^E/C nanoparticulate electrodes are shown in Figure 6-10. The influence of the adsorption potential on current density is in very good agreement with the behaviour observed for above studied surfaces, i.e., with the increase of adsorption potential, faradaic and ion currents are visibly increased. In the measurements in Figure 6-10c, the ion

currents for the formation of methyl formate (*m*/*z*=60) are not shown due to their very low signal which is indistinguishable from the noise.

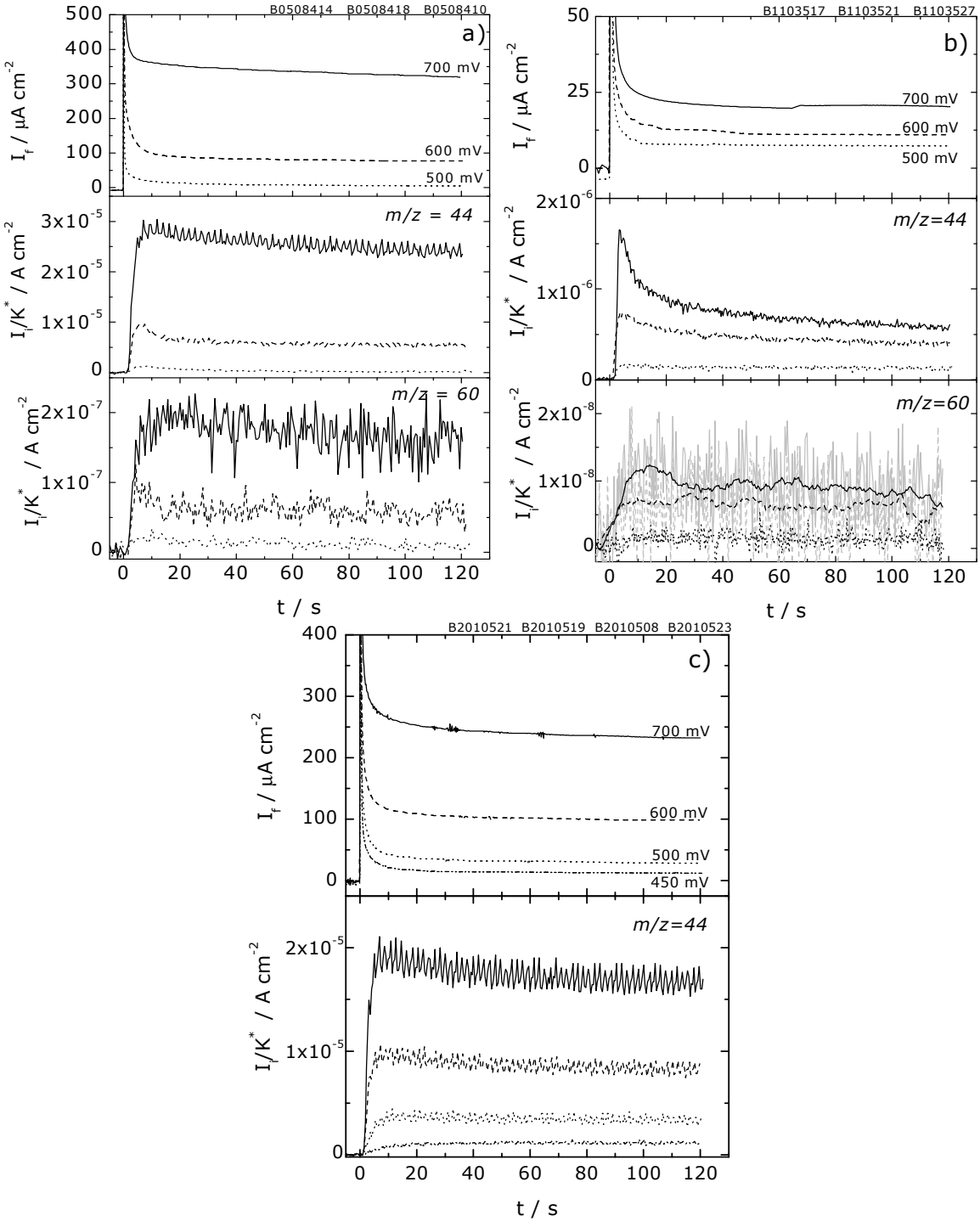

Figure 6-10 Simultaneously recorded transients of faradaic current and ion current of CO_2, m/z=44, and methylformate, m/z=60, during methanol adsorption on (a) PtO_x^E/C, (b) $PtRu^E$/C alloy and (c) $Ru_{0.2}$-modified PtO_x^E/C electrode in 0.1 M methanol + 0.5M H_2SO_4 solution. Scan rate: 10 mV s^{-1}. Electrolyte flow rate: 5 µL s^{-1}. Catalyst loading: 10 μg_{Pt} cm^{-2}. The currents are referred to $A_{sur,CO}$.

As a result, the effect of adsorption potential on the faradaic current and the current efficiency during the methanol oxidation at different commercial catalysts is shown in Figure 6-11.

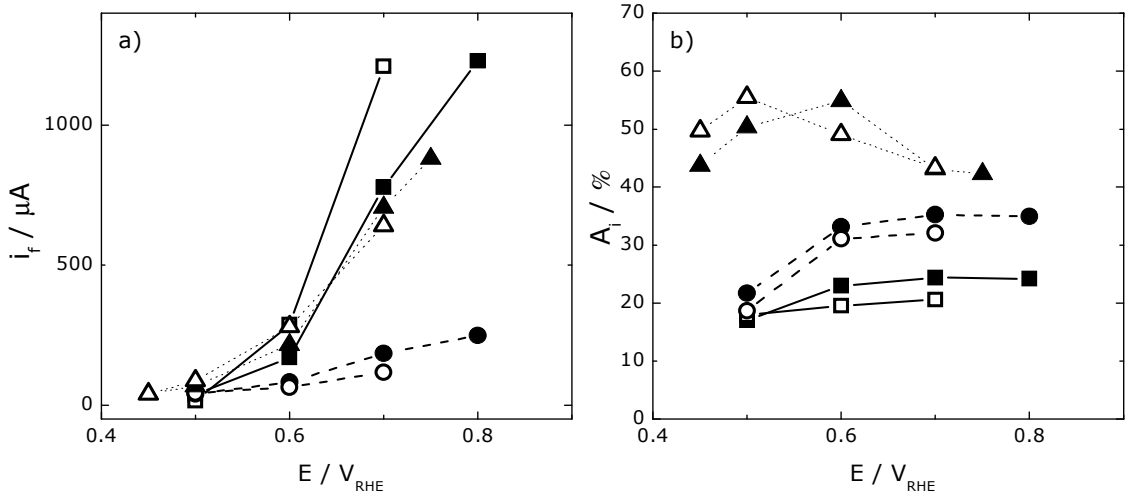

Figure 6-11 The dependence of (a) faradaic currents and (b) current efficiencies of CO_2 on the potentials during potentiodynamic (filled) and potentiostatic (open) methanol oxidation on PtO_x^E/C (squares), $PtRu^E$/C (circles) and $Ru_{0.2}$-modified PtO_x^E/C (triangles) in 0.1 M methanol + 0.5 M H_2SO_4 solution. Where, $A_{exp}(PtO_x^E/C)$=4.4 cm^2, $A_{exp}(PtRu^E/C)$=6.1 cm^2 $A_{exp}(PtO_x^E/C/Ru^{0.2})$=4.64 cm^2.

Please note, the faradaic currents presented in this Figure and similar illustrations are given as raw data in μA. The real surface areas are given in the figure captions.

On pure PtO_x^E/C catalyst, the faradaic currents increase strongly from ca 170 μA to 1230 μA as the potential increases from 600 mV to 800 mV, while the current efficiency of CO_2 stays more or less constant (23-24%) in this potential region. Astonishingly, the current efficiency on $PtRu^E$/C alloy exhibit very low current efficiencies for CO_2 in whole potential range. It is important to mention, that in the whole potential range also the current density increases only slightly, compared to the other surfaces. The situation is very different in the case of methanol oxidation at $Ru_{0.2}$-modified PtO_x^E/C catalyst. Quite a high current efficiency for CO_2 formation is observed, which is rising at low potentials. However, at high potential it decreases and is close to that on PtO_x^E/C at 800 mV.

6.2.2. Non-commercial noble metal catalysts from MPI Mülheim

Also the non-commercial PtO_x^M/C electrodes show a good electrocatalytic activity for methanol oxidation in 0.1 M CH_3OH + 0.5 M H_2SO_4, which begins at around 450 mV and reaches a maximum current density of 180 μA cm^{-2} at 760 mV (Figure 6-12a). The oxidation starts 50 mV negatively, but the maximum current density is only about 70% of that obtained at PtO_x^E/C catalyst.

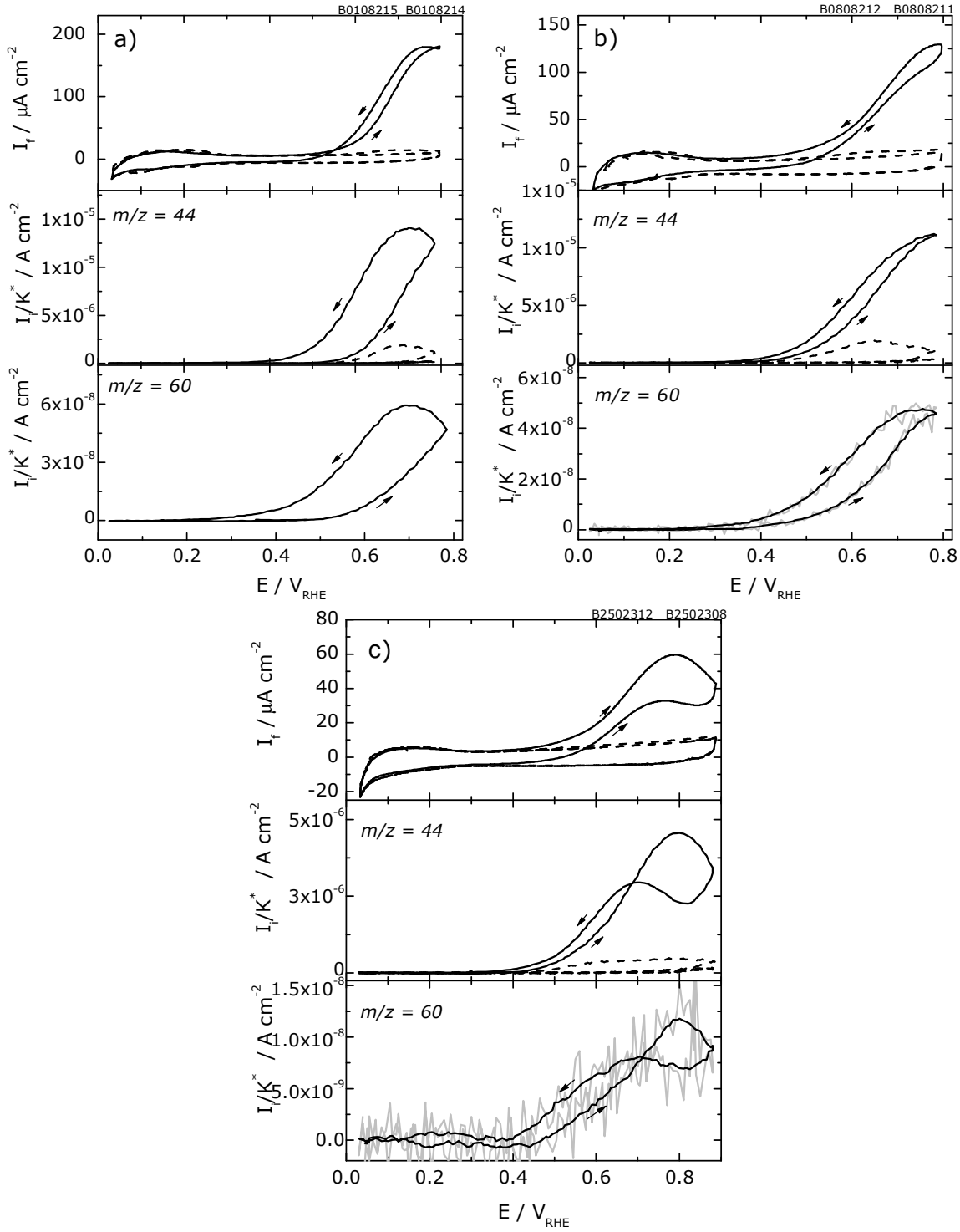

Figure 6-12 Simultaneously recorded faradaic and corresponding ion currents of CO_2, m/z=44, and methylformate, m/z=60, during bulk oxidation of methanol on (a) PtO_x^M/C, (b) $PtRuO_x^M$/C and (c) $PtRuOsIrO_x^M$/C nanoparticle electrodes in 0.1 M methanol + 0.5 M H_2SO_4 solution. Scan rate: 10 mV s^{-1}. Electrolyte flow rate: 5 µL s^{-1}. Dashed line: oxidation of the methanol adsorbate. Catalyst loading: 10 μg_{Pt} cm^{-2}. The currents are referred to $A_{sur,CO}$.

The $PtRuO_x^M$/C catalyst obtained from MPI Mülheim shows considerably better electrocatalytic behaviour in the methanol bulk oxidation in contrast to the commercial one (Figure 6-12b). The onset of the methanol bulk oxidation starts at the same potential, but the measured current density at maximum is higher by

factor of 3 than that observed for the $PtRu^{E}/C$ catalyst. In this series of experiments, the lowest current density is obtained at the $PtRuOsIrO_x^{M}/C$ catalyst (Figure 6-12c), which does not exceed 60 μA cm^{-2}.

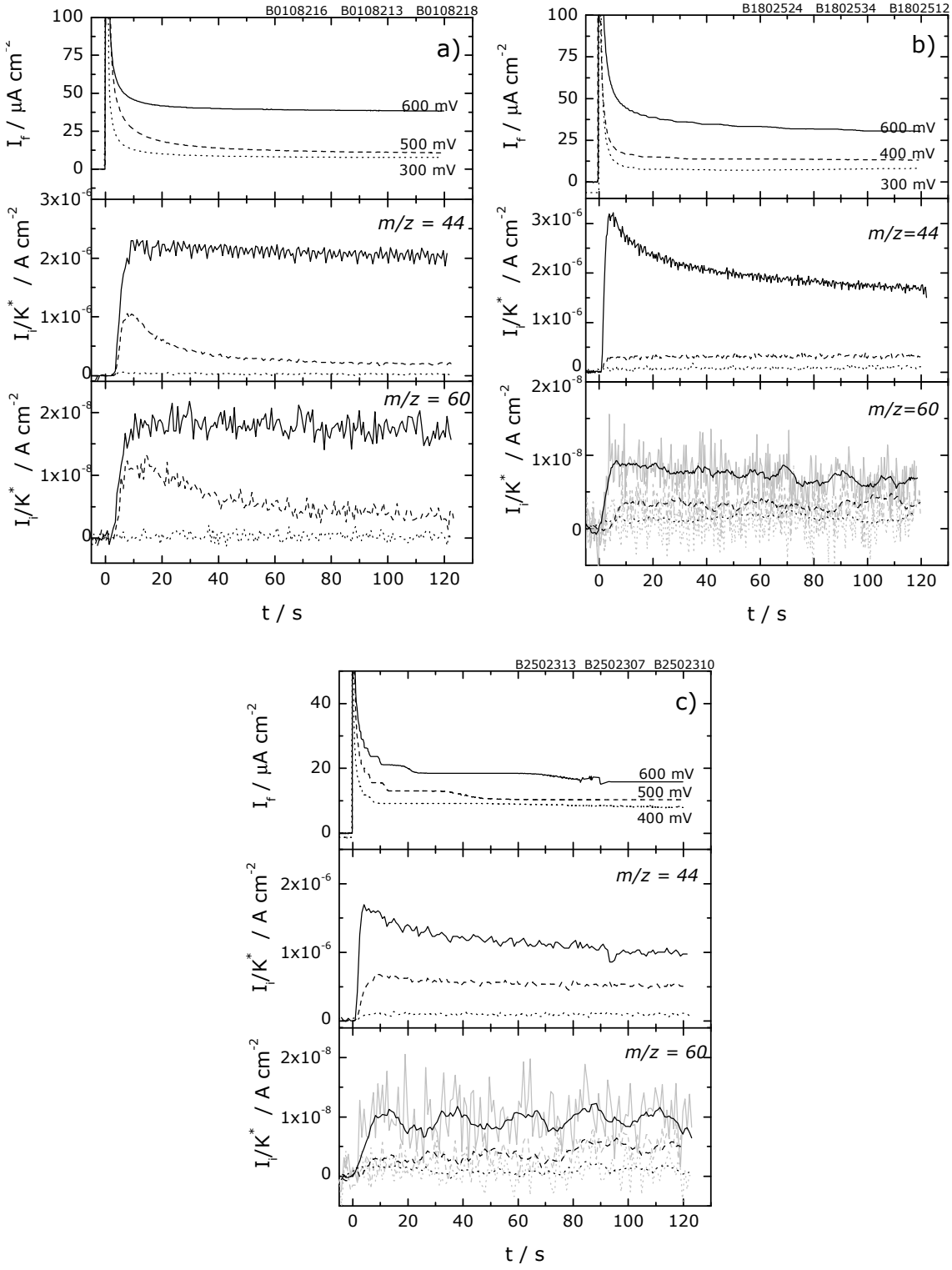

Figure 6-13 Simultaneously recorded current transients of faradaic current and ion current of CO_2, m/z=44, and methylformate, m/z=60, during methanol adsorption on (a) PtO_x^{M}/C, (b) $PtRuO_x^{M}/C$ and (c) $PtRuOsIrO_x^{M}/C$ nanoparticle electrodes in 0.1 M methanol + 0.5 M H_2SO_4 solution. Scan rate: 10 mV s^{-1}. Electrolyte flow rate: 5 μL s^{-1}. Catalyst loading: 10 μg_{Pt} cm^{-2}. The currents are referred to $A_{sur,CO}$.

Similarly to the previous experiments, the effect of potentials on the faradaic current and the current efficiencies is studied also by means of potential step experiments. The faradaic current and corresponding ion currents for the formation of CO_2 (m/z=44) and methyl formate (m/z=60) are shown in Figure 6-13. The influence of the adsorption potential on faradaic and ion currents offer the same behaviour as already found for the substrates mentioned above; i.e. the currents increase with increase in the adsorption potential.

Faradaic currents at 120 seconds after the potential step and the calculated current efficiencies are shown in Figure 6-14. At PtO_x^M/C as well as at $PtRuO_x^M$/C, the faradaic current increases slightly at potentials up to 600 mV, but above this potential the increase becomes much steeper.

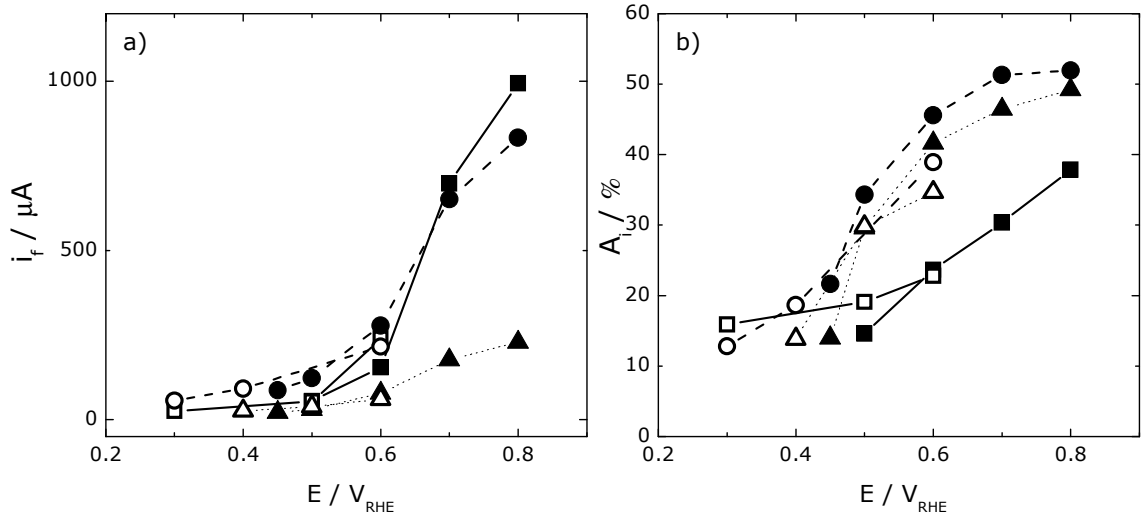

Figure 6-14 The dependence of (a) faradaic currents and (b) current efficiencies of CO_2 on the potentials during potentiodynamic (filled) and potentiostatic (open) methanol oxidation on PtO_x^M/C (squares) and $PtRuO_x^M$/C (circles) and $PtRuOsIrO_x^M$/C (triangles) in 0.1 M methanol + 0.5 M H_2SO_4 solution. Where, $A_{exp}(PtO_x^M/C)$=5.47 cm^2, $A_{exp}(PtRuO_x^M)$=7.14 cm^2 $A_{exp}(PtRuOsIrO_x^M/C)$=3.75 cm^2.

At $PtRuOsIrO_x^M$/C, there is only slight increase of the current in the whole potential range.

Interestingly, also the current efficiency, that is increasing up to ca. 50% (at 800 mV), behaves similarly on PtO_x^M/C and $PtRuO_x^M$/C. This is different from the E-TEK catalysts, where a significant difference in the current efficiency for the different surfaces is found. The current efficiency at $PtRuOsIrO_x^M$/C increases a bit steeply at higher potentials as that at PtO_x^M/C or $PtRuO_x^M$/C, nevertheless reaches only 40% at 800 mV.

6.3. DISCUSSION

In the case of the pure polycrystalline Pt, at low oxidation potentials in 0.1 M methanol solution, a current efficiency of about 21% is found for CO_2. Methyl formate was also detected and a quantitative analysis showed that it exists in amounts up to 10% of the CO_2 formed. Both the values of the current efficiency and the relative amount of methyl formate are very close to the previous findings for polycrystalline Pt [173, 175]. The low current efficiency of methanol oxidation is due to the formation of formic acid and formaldehyde, which are transported away from the electrode under the convection conditions. The current efficiency is independent of flow rate and gives the contribution of the reaction path *via* adsorbed CO to the total oxidation current. On porous electrodes with a high Pt loading, this current efficiency increases to more than 90%, because the intermediates have a higher chance of being further oxidized before leaving the electrode surface [173, 199]. The low current efficiency observed here, as well as the contribution of methyl formate formed (ca 13% of the CO_2 formed), shows that the nanoparticle electrodes with their low loading behave in a similar manner as a smooth surface in the range which is relevant for convection and diffusion [275].

A common characteristic of polycrystalline Pt and Pt(665), as compared to Pt nanoparticles, is that the adsorption sites for CO are relatively homogeneous and identical, in relation to the adsorption energy and oxidation potentials. Since the rate of CO_2 formation is the same for the oxidation of bulk methanol and the oxidation of the methanol adsorbate, it follows, as mentioned above, that the CO_2 formation from bulk methanol occurs *via* the oxidation of a methanol adsorbate. This is further confirmation that this adsorbate is the stable CO adsorbate. This adsorbed intermediate is not in a transient state, which would be oxidized faster than a "relaxed" adsorbed CO. Interestingly, the other by-products, which do not lead to CO_2, are already formed at potentials where adsorbed CO is hardly oxidized.

In this context, the fact that the maximum CO coverage formed from methanol on polycrystalline Pt is only 56% of the maximum coverage from CO dissolved in the electrolyte needs to be taken into account, i.e. there are free sites, which would be available for the adsorption of CO, but are not active for the formation of CO from methanol. Since formaldehyde and formic acid are still formed on these sites, it is obvious, that for their formation, the requirement of neighbouring sites is much less severe than for the formation and adsorption of CO from methanol.

The nanoparticle electrode offers adsorption sites which differ in adsorption enthalpies, similarly to Pt(332) [266]. Both the adsorption of methanol and the oxidation of CO occur more easily at the step sites on Pt(332). Therefore,

a continuous adsorption and oxidation of CO (from methanol) may start before an appreciable amount of previously adsorbed CO is oxidized. The same is true for the nanoparticle electrode, where some particles may be more reactive than average. The oxidation of bulk methanol is also different on polycrystalline Pt and at a nanoparticle electrode. Under continuous convection, where intermediates are quickly transported away from the electrode, the rate *via* the oxidation path involving adsorbed CO formed from methanol is limited by the rate of oxidation of CO_{ad}, both on polycrystalline Pt and on Pt(665). In contrast, on both nanoparticle electrodes the PtO_x^E/C and the PtO_x^M/C, the rate of CO_2 formation during bulk oxidation exceeds the rate of oxidation of the pre-adsorbed species. This may be due to the heterogeneity of these surfaces; and a high turnover number at active sites (steps at Pt(332) in [266]) or at active particles, leading to a continuous oxidation *via* adsorbed CO at potentials where most Pt sites are still blocked by CO_{ad}.

It is well known that the methanol adsorption does not occur on pure Ru surface [206, 210], but already small amount of Ru enhances the methanol adsorption at low potentials. The bifunctional mechanism of Pt-Ru electrode has been generally accepted, however, these experimental findings cannot be explained only by this mechanism. The experiments in this and previous chapter show that the peak potential of the methanol oxidation and the potential of the maximum saturated coverage of adsorbed methanol almost simultaneously shift to lower potentials. This might be explained by an electronic effect or a combination of both.

In addition, it also seems that the optimal catalytic activity varies with different preparation of Pt-Ru electrodes, i.e. co-deposition, ad-atom, alloy and carbon supported Pt-Ru colloid. Ru distribution and segregation to the surface appears to play a role on the optimal catalytic activity of the surface. Also, at the high potentials above 650 mV the current efficiency of CO_2 during methanol oxidation on Pt-Ru decreases and is same as that on Pt. This demonstrates that Ru looses the catalytical activity at the high potential, perhaps due to the transformation of Ru active hydrous oxide to an inactive anhydrous oxide at high potentials [176].

Chapter 7 The effect of temperature

In this chapter the influence of temperature on CO- and methanol oxidation on diverse Pt surfaces is examined.

7.1. OXIDATION OF ADSORBED CARBON MONOXIDE

To exclude possible changes of the substrate during tempering of the system, the effect of temperature on CO oxidation is studied besides that on methanol oxidation.

The CO stripping voltammograms at 25° and 50°C on various nanoparticle catalysts are shown in Figure 7-1. It is clearly seen that pure PtO_x^M/C nanoparticles show a good electrocatalytic activity for CO oxidation, which begins at around 550 mV with a maximum current density at 790 mV at 25°C (Figure 7-1a). Both the onset and the maximum current density shift about 70 mV more negative at 50°C, that is in very good agreement with the data observed earlier by Kawaguchi et. al [232].

In the case of the $PtRuO_x^M$/C nanoparticle catalysts (Fig 7-1b), at room temperature the oxidation of pre-adsorbed CO starts at 400 mV instead of 550 mV found for PtO_x^M/C catalysts. By increasing the operating temperature, a negative shift of the onset (50 mV) and also of the maximum of the oxidation (140 mV) to lower potentials are found. Seiler et al. [233] showed that the shape of the stripping peak on Pt-Ru nanoparticle electrodes is first narrowing down with increasing temperature, then broadening and above 70°C splitting into two peaks. The shift of the peak maximum was observed in the whole temperature range, contrary to T. Kawaguchi et al. [232] who found that the peak potential on similar electrodes decreases at a linear slope initially with the temperature and then remained nearly constant. The charge of CO oxidation was decreased at higher temperature and also the oxidation shoulder was found above 40°C temperature. This decrease in the charge under the oxidation peak and the constant peak potential found is simply due to a use of very high adsorption potential (300 mV vs. RHE in [232]), since at higher temperatures the electrooxidation of adsorbed CO starts already at even lower potentials [226, 233] and so the carbon monoxide is partly oxidized during the adsorption. the $PtRuOsIrO_x^M$/C nanoparticle catalyst (Figure 7-1c) of the previously discussed "pre-peak" shifts by 100 mV to lower potentials together with the position of the maximum current density.

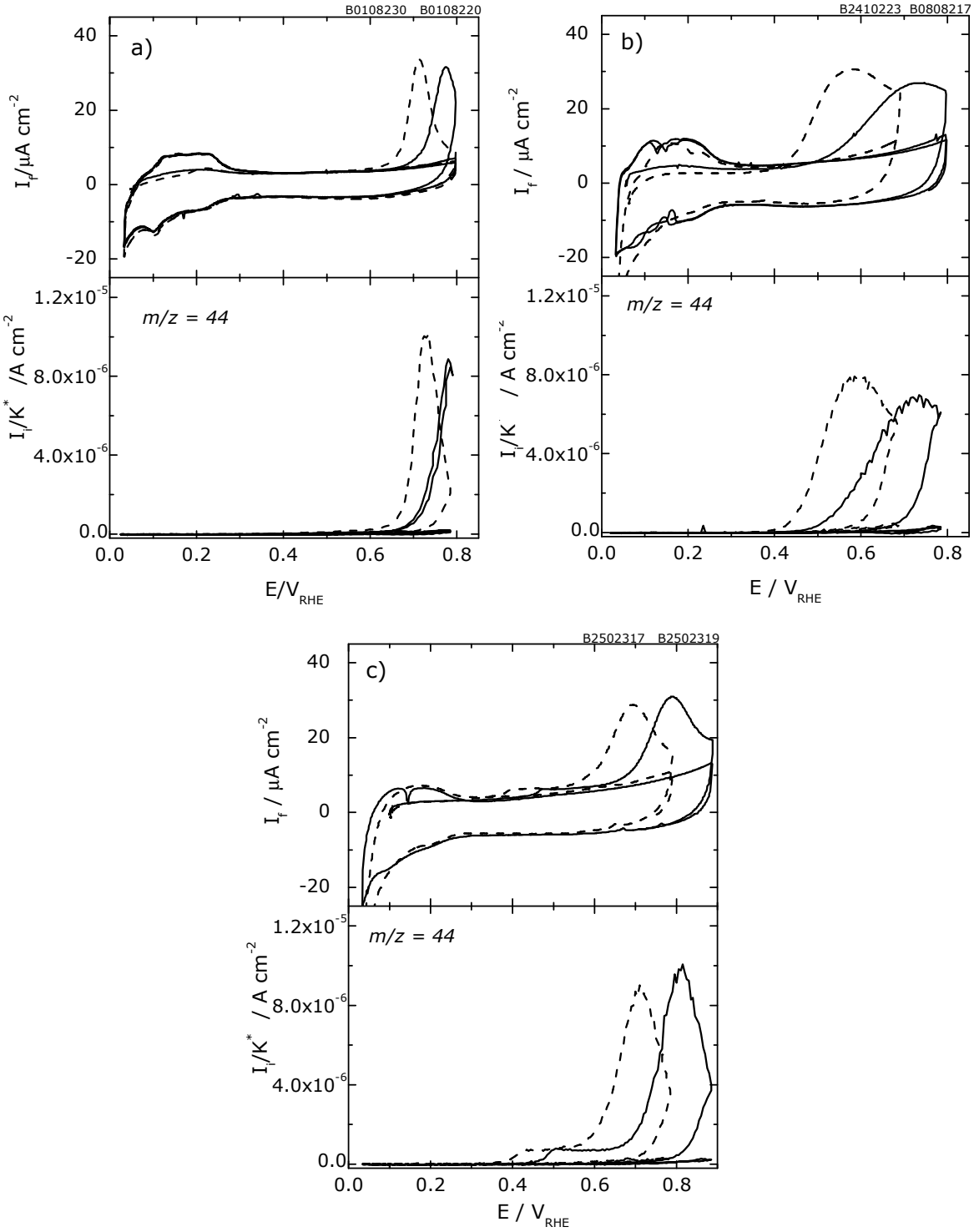

Figure 7-1 Simultaneously recorded faradaic and corresponding ion currents of CO_2, m/z=44, during oxidation of CO adsorbed on (a) PtO_x^M/C, (b) $PtRuO_x^M$/C and (c) $PtRuOsIrO_x^M$/C nanoparticles in 0.5 M H_2SO_4 at 25°C (solid line) and 50°C (dashed line). Scan rate: 10 mV s^{-1}. Electrolyte flow rate: 5 µL s^{-1}. Catalyst loading: 10 µg$_{Pt}$ cm^{-2}. The currents are referred to $A_{sur,CO}$.

The charge under the CO-oxidation peak (≈ CO coverage) and therefore also the apparent roughness factor, which is determined from the amount of CO_2 formed, is not influenced by the temperature at these three nanoparticulate surfaces (see

Table 7-1), which is in agreement with data published in literature [232, 233]. The roughness factor of the surface is calculated as the ratio of the experimental surface area, A_{exp}, and the geometric surface area of the support, A_{geom}, (0.283 cm^2).

$$RF_{exp} = \frac{A_{exp}}{A_{geom}} \qquad \text{(Equation 7-1)}$$

Table 7-1 Influence of temperature on roughness factor and faradaic charge under CO-oxidation peak.

Surface	RF_{exp}			Q_f^{max} / µA		
	0°C	25°C	50°C	0°C	25°C	50°C
PtO_x^M/C	-	20	21	-	1619	1663
$PtRuO_x^M$/C	-	28	27	-	2296	2215
$PtRuOsIrO_x^M$/C	-	14	15	-	1200	1111
Pt(pc)	1.8	1.9	1.8	138	136	142

RF_{exp}, roughness factor; Q_f^{max}, true faradaic charge

For the CO electrooxidation on polycrystalline platinum (Figure 7-2) the only effect of the increase in the temperature from 0, over 25, to 50°C is the shift of the CO stripping towards more negative potentials.

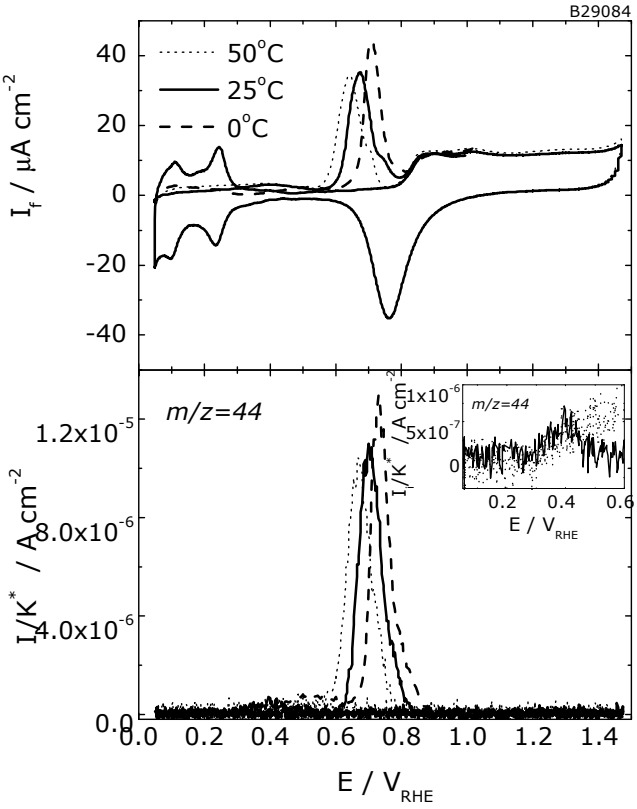

Figure 7-2 Simultaneously measured faradaic currents and corresponding ion currents of CO_2, m/z=44, during oxidation of CO adsorbed on polycrystalline platinum in 0.5 M H_2SO_4 at 0°C (dashed line), 25°C (solid line) and 50°C (dotted line). Scan rate: 10 mV s^{-1}. Electrolyte flow rate: 5 µl s^{-1}. Inset: Ion current of CO_2, m/z=44, during oxidation of pre-peak. The currents are referred to $A_{sur,CO}$.

The well known pre-peak of the CO oxidation on massive polycrystalline platinum is always found and its onset does not change with temperature (see inset of Figure 7-2). The charge found under the CO oxidation peak is also constant. A similar effect was found for Pt(111) [230] and recently for polycrystalline Pt [116]. In other references the CO oxidation at polycrystalline Pt showed a decrease of the CO coverage with increasing temperature when the higher adsorption potentials were used [116, 276]. It is obvious that at higher temperatures some electrooxidation of adsorbed CO already takes place, if the CO is adsorbed at higher potentials.

7.2. ELECTROOXIDATION OF ADSORBED METHANOL

The influence of elevated temperature on the oxidation of methanol adsorbate at three different electrochemically reduced nanoparticle catalysts is depicted in Figure 7-3. It is obvious that as the temperature of the system is increased the onset of oxidation is observed at more negative potentials. Also the maximum of oxidation current at PtO_x^M/C catalyst electrode shifts 50 mV more negative as the temperature increases from 25 to 50°C (Figure 7-3a), which corresponds to -2.0 mV K^{-1}. The same effect is found also for both alloyed catalysts; at $PtRuO_x^M$/C (Figure 7-3b) clear shift of the maximum by -2.4 mV K^{-1} observed, whereas the broad maximum found at room temperature at $PtRuOsIrO_x^M$/C (Figure 7-3c) diminishes to only one peak at 50°C. Furthermore, this peak occurs on the very spot of the negatively positioned peak at 25°C. Also the onset shifts by 30 mV to lower potentials as the temperature is increased. Interestingly, the amount of CO_2 produced during the oxidation of the methanol adsorbate on $PtRuOsIrO_x^M$/C is close to that observed during oxidation of weakly adsorbed CO ("pre-peak in Figure 7-1c).

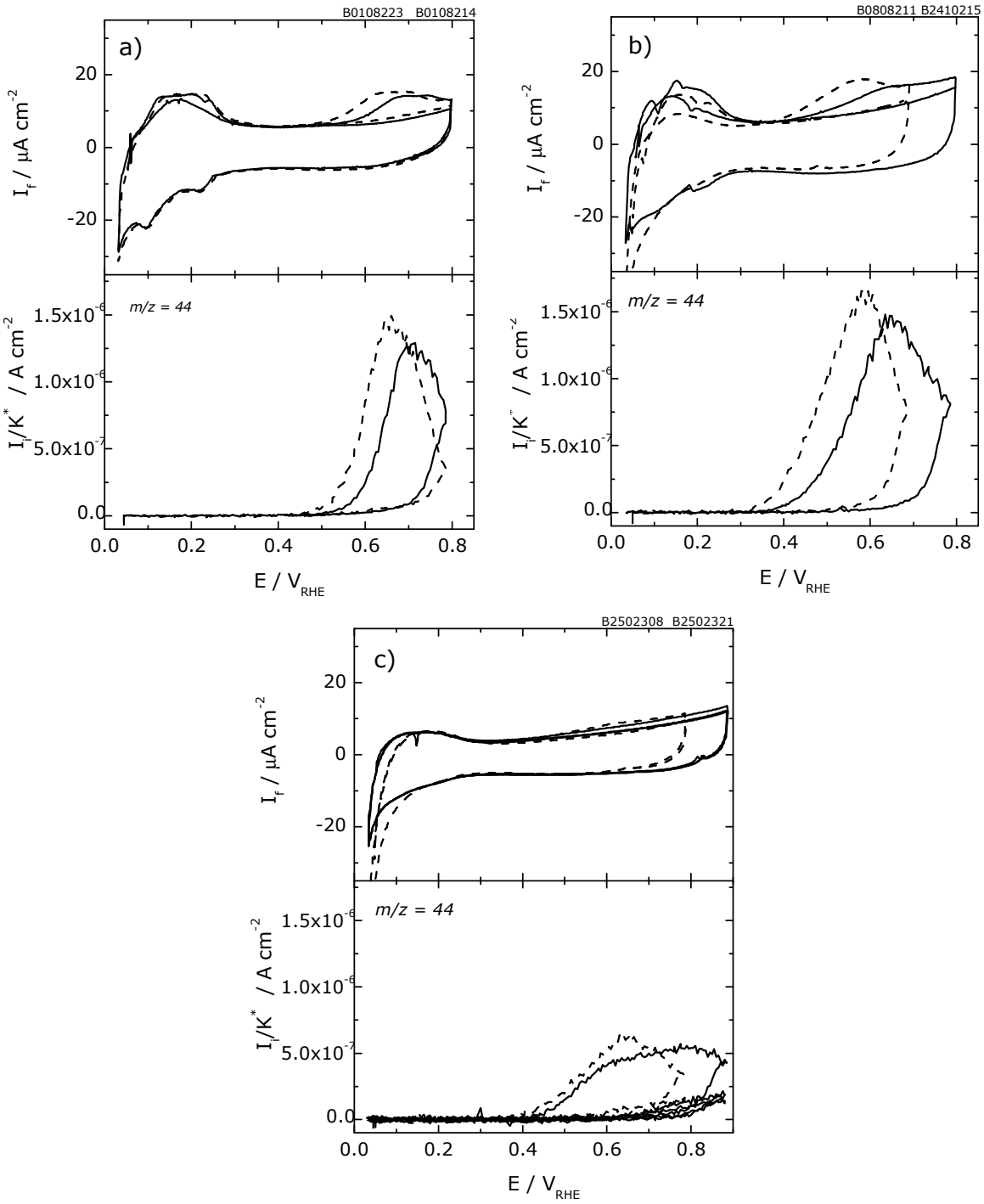

Figure 7-3 Simultaneously recorded faradaic and ion currents of CO_2, m/z=44, during oxidation of methanol adsorbed on (a) PtO_x^M/C, (b) $PtRuO_x^M$/C and (c) $PtRuOsIrO_x^M$/C in 0.5 M H_2SO_4 at 25°C (solid line) and 50°C (dashed line). Scan rate: 10 mV s^{-1}. Electrolyte flow rate: 5 µL s^{-1}. Methanol adsorption: 500 mV for 2 min. Catalyst loading: 10 μg_{Pt} cm^{-2}. The currents are referred to $A_{sur,CO}$.

For comparison, the oxidation of the methanol adsorbate (adsorbed at 500 mV for 2 minutes) on Pt(pc) at 0, 25 and 50°C is displayed in Figure 7-4. The methanol adsorption and oxidation on this surface are affected by temperature in the same

way as on nanoparticle catalysts. The peak shift of -1.6 mV K^{-1} is consistent with data found for 0.5 M CH_3OH in 0.1 M H_2SO_4 [277].

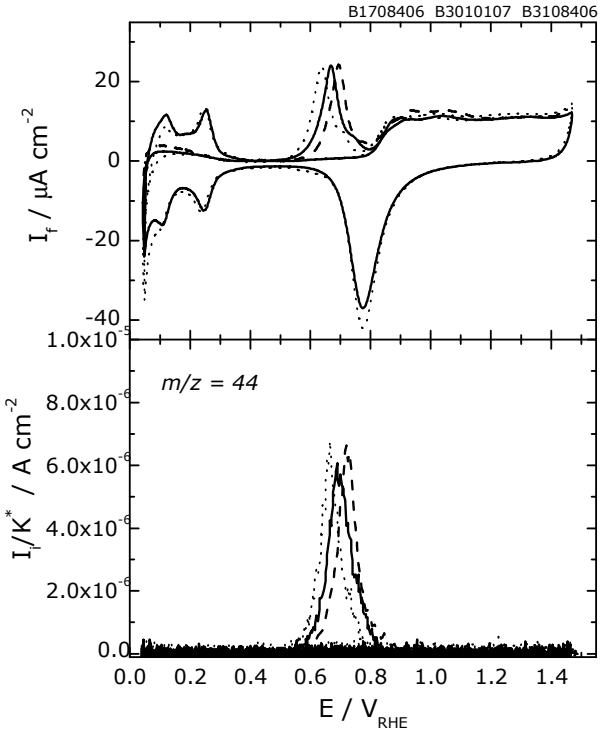

Figure 7-4 Simultaneously recorded faradaic currents and ion currents of CO_2, m/z=44, during oxidation of methanol adsorbed on Pt(pc) in 0.5 M H_2SO_4 at 0°C (dashed line), 25°C (solid line) and 50°C (dotted line). Scan rate: 10 mV s^{-1}. Electrolyte flow rate: 5 µL s^{-1}. Methanol adsorption: 500 mV for 2 min. The currents are referred to $A_{sur,CO}$.

The potential dependence of the maximum CO coverage formed from methanol on polycrystalline Pt, PtO_x^M/C, $PtRuO_x^M$/C and $PtRuOsIrO_x^M$/C at different temperatures is depicted in Figures 7-5a and 7-6a.

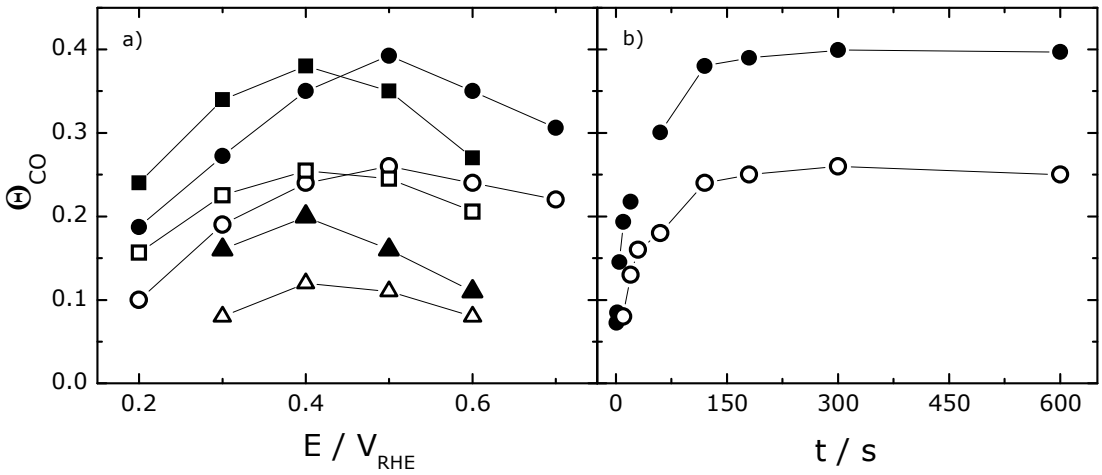

Figure 7-5 Influence of temperature on the relative coverages of methanol (Equation 2-5), Θ_{CO}, for (a) different adsorption potentials after 2 minutes and (b) different adsorption times at 500 mV on PtO_x^M/C (circles), on $PtRuO_x^M$/C (squares) and on $PtRuOsIrO_x^M$/C (triangles) at 25°C (open symbols) and 50°C (solid symbols). The adsorption of methanol was carried out in 0.1 M CH_3OH + 0.5 M H_2SO_4 solution.

At low potentials the saturation coverage of the methanol adsorbate increases with increasing adsorption potentials, and at high potentials (above 500 mV at pure PtOx/C and 400 mV at modified Pt) it decreases again, due to the oxidation of methanol adsorbate. This behavior is not influenced by temperature. On the other hand the relative coverage increases with an increase in temperature. This increase is less significant above potentials where the maximum coverage is observed. Since the position of the maximum is the same for both temperatures, the adsorption rate and the desorption rate are probably influenced in the same way.

Interestingly, the maximum saturation coverage of 56% found at room temperature for polycrystalline Pt is not significantly influenced by temperature, whereas on PtO_x^M/C nanoparticles the saturation coverage of ca. 27% at room temperature is increased to 38% as the temperature increases to 50°C. This was also confirmed in control experiments with different adsorption times. Here it was checked that after 2 minutes the saturation is achieved indeed (Figure 7-5b and 7-6b).

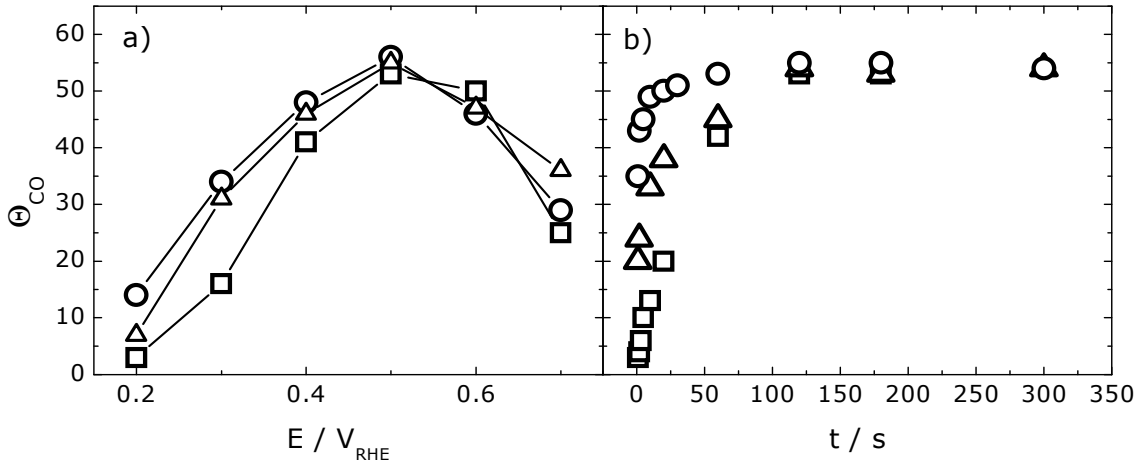

Figure 7-6 Influence of temperature on relative coverages of methanol, Θ, at (a) different adsorption potentials after 2 minutes and (b) different adsorption times at 500 mV on Pt(pc) at 0°C (open squares), 25°C (open triangles) 50°C (open circles).. The adsorption of methanol was carried out in 0.1 M CH_3OH + 0.5 M H_2SO_4 solution.

Appropriate rates of methanol adsorption were calculated from coverages achieved after very short adsorption times (1, 2 and 5 s) and the results are collected in Table 7-2. The methanol adsorption rate increases with the temperature on all measured surfaces, whereas it is faster at polycrystalline Pt than at platinum colloidal nanoparticles.

Table 7-2 Rates of methanol adsorption at Pt(pc) and PtO_x^M/C for different temperatures.

Temperature / °C	Methanol adsorption rate / ML s^{-1}	
	PtO_x^M/C	Pt(pc)
0	--	0.018
25[4]	0.021	0.047
50	0.030	0.081

ML, monolayer of adsorbate

7.3. ELECTROOXIDATION OF BULK METHANOL

Under atmospheric pressure conditions, the boiling point of methanol (64.7°C) permits measurements at elevated temperature up to 50°C without markedly variation in the concentration of the methanol solution.

Figure 7-7 shows cyclic and mass spectrometric voltammograms recorded for various nanoparticles in Ar-purged 0.5 M H_2SO_4 containing 0.1 M methanol at 25 and 50°C.

In each case, the electrode was held at 50 mV in the sulfuric acid solution as methanol solution was flushed into the cell and the electrode was left exposed to methanol at 50 mV for a total of 5 min prior to the start of the sweeps.

It is clearly seen that at 50°C the current in the forward scan arises much earlier and also falls at much lower potentials than at 25 °C. Similar temperature-dependent enhancements have been observed for methanol oxidation and ascribed to improved reaction kinetics at the higher temperatures [209, 215].

Alloying of platinum nanocatalysts by other metallic components leads to an improvement of the electroactivity in comparison to that of pure PtO_x^M/C and by increasing the operating temperature, the the co-catalytic effect is considerably increased: (The activity of the different catalysts at ambient temperature is already discussed in the previous Chapter.) At 50°C the Faradaic current densities measured at 600 mV in the positive-going scan at the PtO_x^M/C, $PtRuO_x^M/C$ and $PtRuOsIrO_x^M/C$ are 1.6, 2.8 and 3.0 times as high as at room temperature, respectively. However, the calculated average current efficiency of CO_2 in one cycle of potential scan and also the average ratio of CO_2 to methyl formate at 50°C is comparable, within error of measurement, to that at 25°C at all three measured catalysts (see Table 7-3). This allows the suggestion that at elevated temperature, at least up to 50°C, the formation of CO_2 and intermediates (formaldehyde and formic acid) is simultaneously enhanced. The ratio of the intermediates (formaldehyde and formic acid) could be changed a little, as could be indicated by the variation of current efficiency for methyl formate. Please note that the values of the average current efficiencies for $PtRuO_x^M/C$ and $PtRuOsIrO_x^M/C$ could be falsified due to the different potential range of the CV´s.

[4] The measurements at 25°C are presented in Figure 5-10.

The current efficiencies calculated using the current transients during methanol adsorption at a constant potential presented later (Figure 7-9) should give more reliable data.

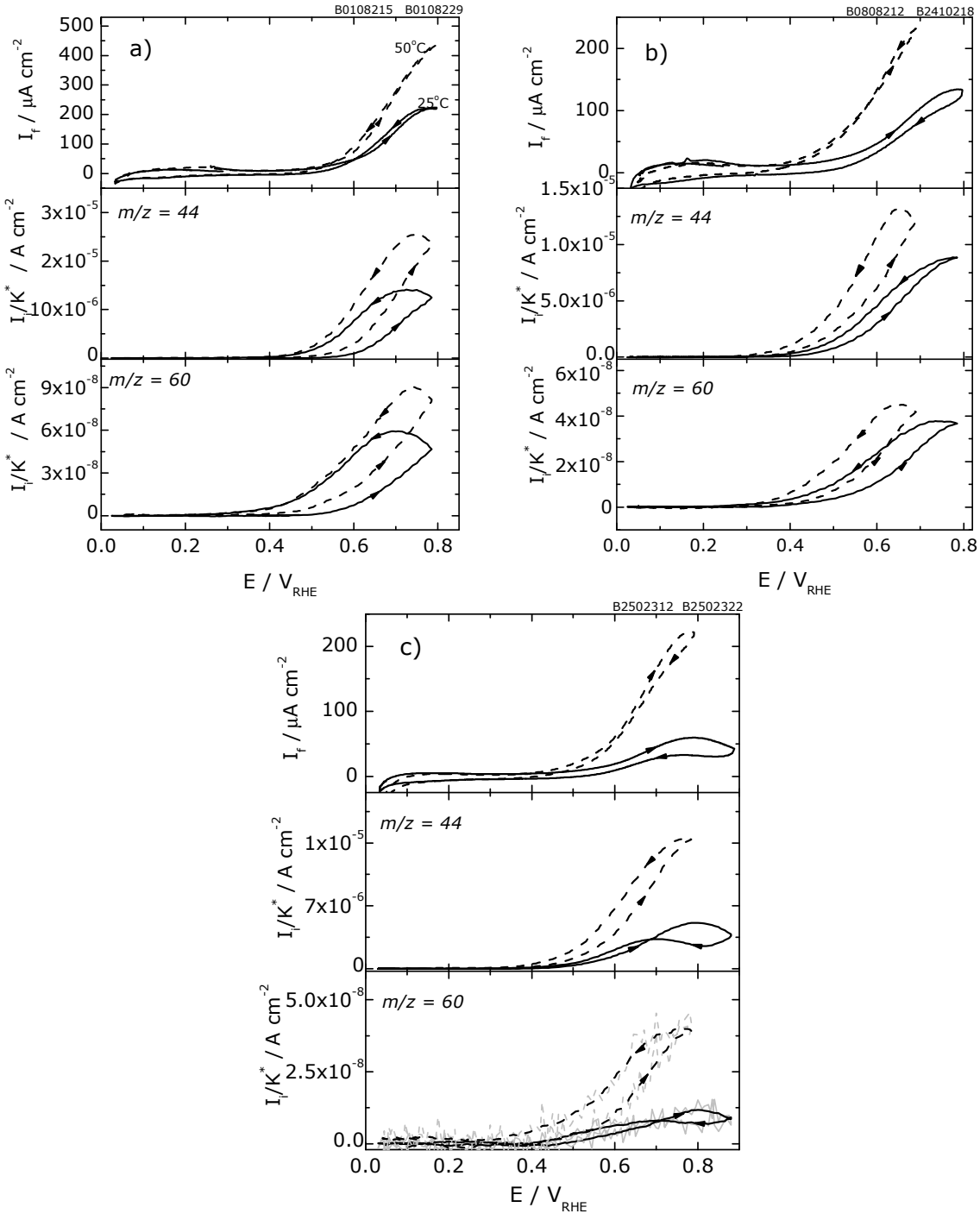

Figure 7-7 Simultaneously recorded faradaic and corresponding ion currents of CO_2, m/z=44, and methylformate, m/z=60 during oxidation of CO_{ad} on (a) PtO_x^M/C, (b) $PtRuO_x^M$/C and (c) $PtRuOsIrO_x^M$/C surface in 0.1 M CH_3OH + 0.5 M H_2SO_4 at 25°C (solid line) and 50°C (dashed line). Scan rate: 10 mV s^{-1}. Electrolyte flow rate: 5 µL s^{-1}. Catalyst loading: 10 μg_{Pt} cm^{-2}. The currents are referred to $A_{sur,CO}$.

Table 7-3 Average current efficiencies and average ratios of CO_2 to methyl formate obtained during potentiodynamic oxidation of methanol on different surfaces at 25 and 50°C.

Surface	A_q / %		n_{44}/n_{60}	
	25°C	50°C	25°C	50°C
PtO_x^M/C	40	38	33	37
$PtRuO_x^M/C$	49	45	39	42
$PtRuOsIrO_x^M/C$	51	48	54	52
Pt(pc)	25	27	44	41

A_q, average current efficiency of CO_2
n_{44}/n_{60}, average ratio of CO_2 to methyl formate

The temperature dependence of methanol bulk oxidation on polycrystalline Pt was also determined (Figure 7-8). The voltammograms presented in Figure 7-8 display a hysteresis characteristic for methanol oxidation at platinum in aqueous acid solutions [183, 191, 278]. On the forward scan, methanol oxidation is rapid between 400 and 800 mV and the decline in current above 800 mV reflects the inhibition of methanol oxidation by surface oxides. The anodic peak in the reverse scan at 50°C reaches a higher current density compared to the wave on the forward scan. The broader potential range and higher current for methanol oxidation at 50°C, compared to the measurements at ambient temperature, point out that the dissociative chemisorption of water is thermally activated. The faster rate of reactive oxide production at the higher temperature is expected to reduce the steady-state coverage of adsorbed CO and other methanol intermediates, and thereby expose more surface sites for methanol adsorption and dissociation. As the temperature increases from room temperature to 50°C, the onset of the methanol oxidation wave slightly shifts to negative potentials by ca 20 mV. These shifts demonstrate the improvement in reaction kinetics that occurs at above ambient temperatures and potentials associated with water activation.

At 50°C the faradaic currents densities at maxima in anodic sweep is 3.1 and in cathodic sweep almost 4.5 times higher than that at 25°C. This current increase reconfirmed findings in the literature [214], where an increase of 3.5 and 4.6 in the positive and negative-going sweep was reported for polycrystalline Pt. Similarly to the nanoparticulate electrode surfaces, here the average current efficiency of CO_2 in one potential scan as well as the average ratio of CO_2 to methyl formate is found to be independent on temperature at our conditions (see Table 6-2).

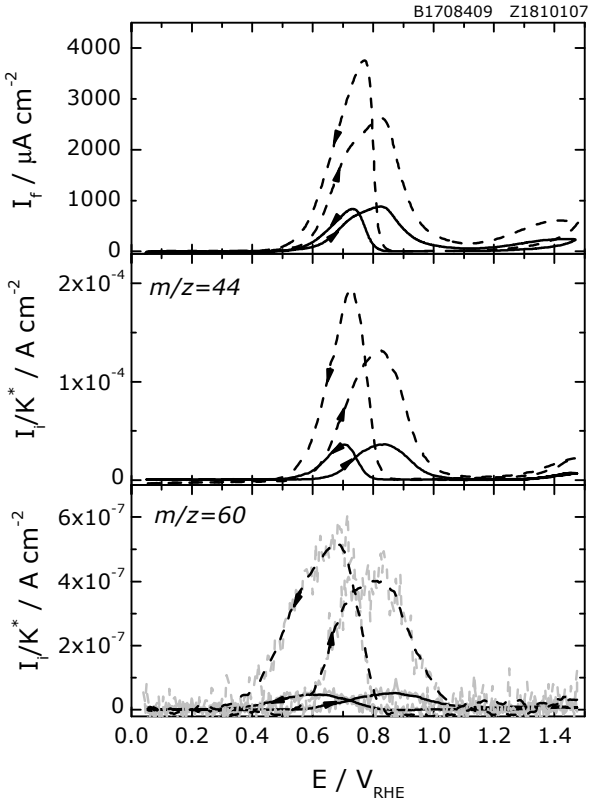

Figure 7-8 Simultaneously measured faradaic currents and corresponding ion currents of CO_2, m/z=44, and methylformate, m/z=60 during oxidation of CO adsorbed on polycrystalline Pt in 0.1 M CH_3OH + 0.5 M H_2SO_4 at 25°C (solid line) and 50°C (dashed line). Scan rate: 10 mV s^{-1}. Electrolyte flow rate: 5 µL s^{-1}. The currents are referred to $A_{sur,CO}$.

From cyclic voltammetry only the average current efficiency of CO_2 in a potential cycle can be calculated. In order to obtain more detailed information on the potential dependence of the methanol oxidation on temperature under stationary conditions, a series of chronoamperometric experiments at different potentials are also carried out at these surfaces.

The typical "steady-state" current transients at nanoparticulate surfaces and polycrystalline platinum during methanol adsorption at constant potential (600 mV) in 0.1 M CH_3OH + 0.5 M H_2SO_4 are shown in Figure 7-9.

At 50°C both, the measured faradaic and mass spectrometric currents are higher than those at 25°C on each surface, as expected from the bulk methanol oxidation. The faradaic current on smooth Pt(pc) at 0°C is considerably lower. Also here, the small oscillations in the ion currents are due to the pulsation of the peristaltic pump.

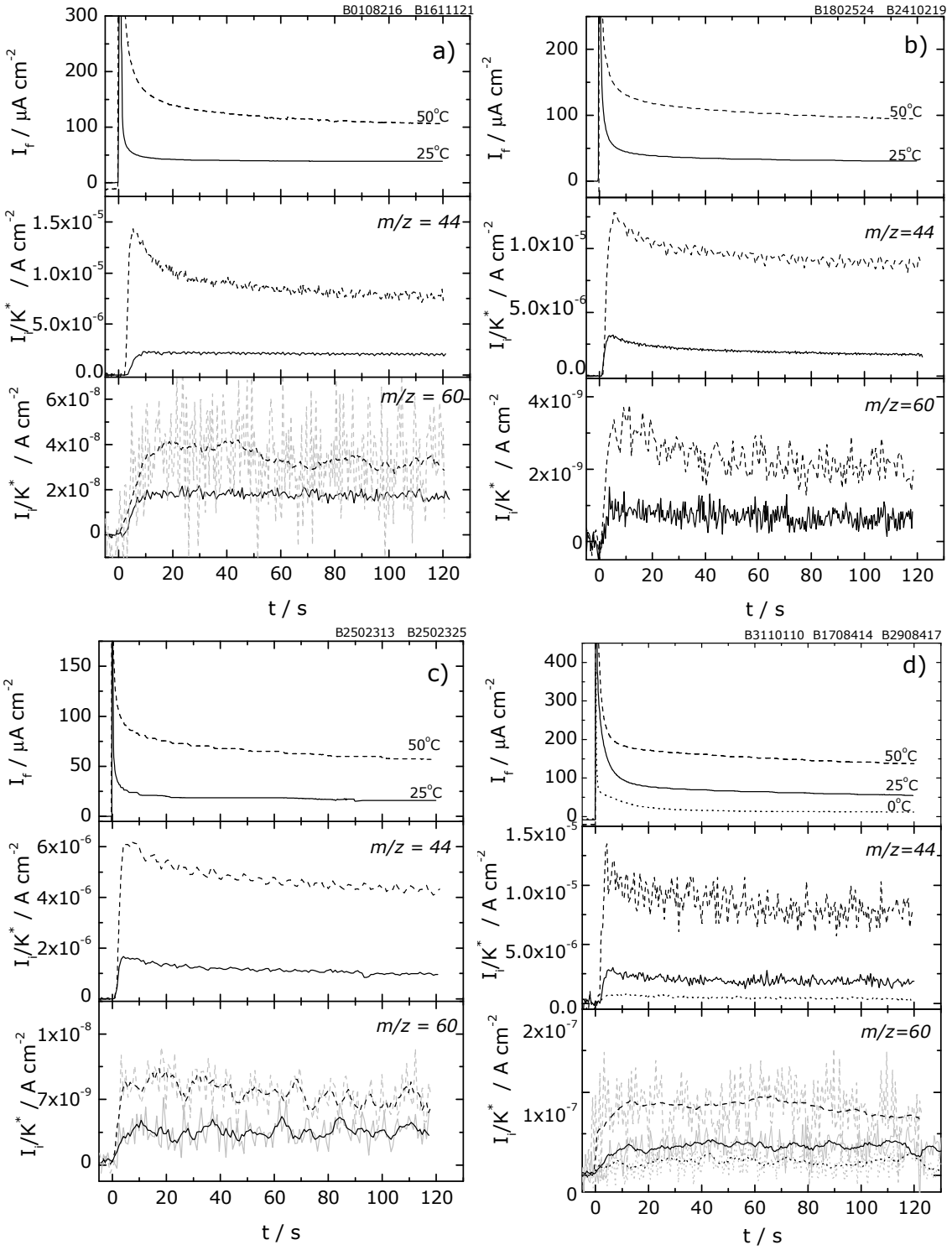

Figure 7-9 Simultaneously recorded transients of faradaic and ion current of CO_2, m/z=44, and methylformate, m/z=60 during methanol adsorption at 600 mV on (a) PtO_x^M/C, (b) $PtRuO_x^M$/C, (c) $PtRuOsIrO_x^M$/C and (d) Pt(pc) in 0.1 M CH_3OH + 0.5 M H_2SO_4 at different temperatures. Scan rate: 10 mV s^{-1}. Electrolyte flow rate: 5 µL s^{-1}. Catalyst loading: 10 μg_{Pt} cm^{-2}. The currents are referred to $A_{sur,CO}$.

Contrary to the temperature-independent average current efficiencies obtained from cyclic voltammetry, the current efficiency of CO_2 calculated from the potential step experiments at 600 mV are found to be strongly dependent on temperature, see

Table 7-4. For example, the current efficiency on a smooth polycrystalline Pt at 50°C reaches app 40%, at 25°C reaches app 20%, however at 0°C is only about 10%. As already shown, the current efficiency is dependent on potential (Figures 6-4b, 6-11b and 6-12b). Then this effect can be probably caused by the shift of the onset potential with temperature.

Table 7-4 Current efficiencies and average ratios of CO_2 to methyl formate obtained during potentiostatic oxidation of methanol at 600 mV on different surfaces at 0, 25 and 50°C.

Surface	$A_i^{0.6V}$ / %			n_{44}/n_{60}		
	0°C	25°C	50°C	0°C	25°C	50°C
PtO_x^M/C	—	23	45	—	18	34
$PtRuO_x^M/C$	—	31	57	—	52	70
$PtRuOsIrO_x^M/C$	—	35	46	—	23	63
Pt(pc)	11	19	38	6	14	29

$A_i^{0.6V}$, current efficiency of CO_2 at 600 mV

n_{44}/n_{60}, average ratio of CO_2 to methyl formate (at 600 mV)

Although a quantification of the amount of methylformate was not performed, the data in Table 7-4 show a pronounced effect of temperature at nearly steady-state conditions. The ratio of the average ion current of CO_2 to methylformate increases, the amount of the side product decreases, as the temperature is increased.

Utilizing the potential step experiments at various temperatures, it is possible to estimate the apparent activation energy, E_a, for the methanol oxidation reaction. At polycrystalline platinum the faradaic currents measured after 120 s are used to construct the Arrhenius plots of Figure 7-10. The linear fits and the potential at which the specific data points were obtained are displayed on graph.

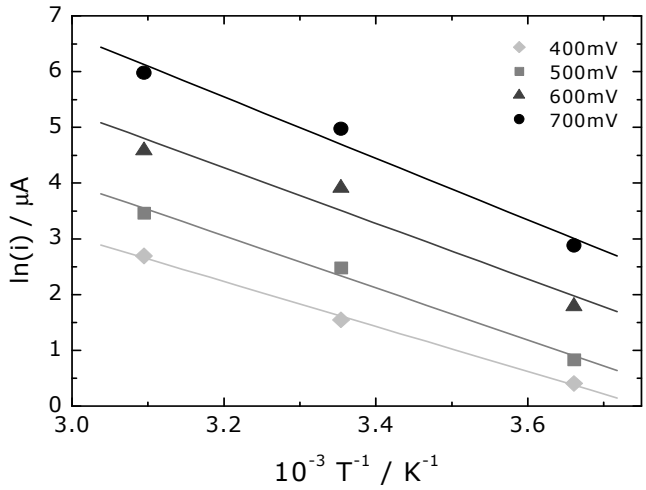

Figure 7-10 Arrhenius plot of methanol oxidation at polycrystalline Pt in 0.1 M CH_3OH + 0.5 M H_2SO_4 at different potentials. Faradaic currents are measured after 2 minutes.

Linear relationships between ln(i) and 1/T are seen for all potentials indicating that the reaction mechanism at each potential does not change with temperature, at least in the measured temperature range.

Such apparent activation energy, estimated from faradaic current, gives a mean value for both reaction paths. From the mass spectrometric ion current of CO_2 the activation energy for the indirect oxidation pathway (*via* adsorbed CO) can be determined ($E_a(I_{44})$). Figure 7-11 shows a construction of the Arrhenius plot using the ion current of CO_2. Also here the linear fits of the specific data points are presented. Due to a low signal and a high noise in the mass spectrometric transients at 400 mV, it is not possible to determine the E_a at this and lower potential.

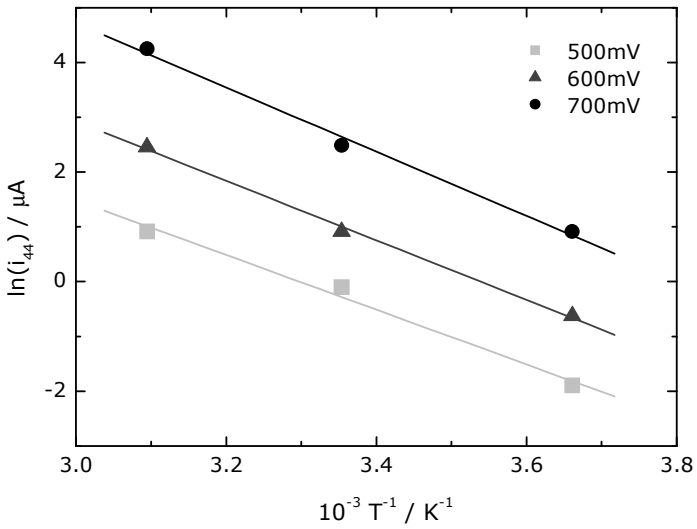

Figure 7-11 Arrhenius plot of methanol oxidation at polycrystalline Pt in 0.1 M CH_3OH + 0.5 M H_2SO_4 at different potentials. Ion currents of CO_2 m/z=44 are measured after 2 minutes.

Table 7-5 provides the apparent E_a values at different potentials for all tested electrodes. A large range of E_a values is observed for each electrode. At the most positive potentials, as the current increases abruptly, governed by the commencement of oxide reduction/consumption, the highest apparent activation energy values are determined. It can be seen, that on pure Pt surfaces the $E_a(I_{44})$ is higher than that observed for the overall reaction. This effect is more pronounced on PtO_x^M/ nanoparticles, where the $E_a(I_{44})$ is nearly two times higher than the E_a, whereas at Pt(pc) the $E_a(I_{44})$ is higher by only ca 10%. Interestingly, the difference between the E_a`s is getting smaller at higher potentials. Contrariwise, other situation is found at $PtRuO_x^M$/C and $PtRuOsIrO_x^M$/C nanoparticles, where the $E_a(I_{44})$ is somehow smaller than that observed for the overall oxidation reaction. Such lower values indicate that Ru-enriched Pt surfaces have a positive effect on the catalytic activity of towards methanol oxidation.

Table 7-5 Calculated apparent activation energies obtained from faradaic current and mass spectrometric current of m/z=44 during potentiostatic oxidation of methanol at different potentials.

E / mV	E_a / kJ mol^{-1}				E_a (I_{44}) / kJ mol^{-1}			
	Pt(pc)	PtO_x^M/C	$PtRuO_x^M/C$	$PtRuOsIrO_x^M/C$	Pt(pc)	PtO_x^M/C	$PtRuO_x^M/C$	$PtRuOsIrO_x^M/C$
400	34	12	18	29	-	-	-	-
500	37	17	36	45	42	30	32	30
600	42	23	44	50	45	32	39	33
700	46	27	-	-	48	34	-	-

The importance of the potential at which the E_a (and/or $E_a(I_{44})$) is calculated dramatically affects the values obtained and thus limits the comparisons that can be made between different experiments, as well as between different catalyst materials from literature and will be discussed below.

7.4. DISCUSSION AND REMARKS

The difference in the CO- and methanol oxidation behaviour as a function of the operating temperature was systematically studied on various electrocatalysts. Although the CO_{ad} oxidation potential maxima observed in CV and MSCV decreases with the increase in temperature, the CO coverage is not influenced by the temperature at PtO_x^M/C, $PtRuO_x^M/C$ and $PtRuOsIrO_x^M/C$ (see Table 7-6), which is in agreement with data published earlier for nanoparticle surfaces [232, 233].

Table 7-6 Influence of the temperature on CO-oxidation.

surface		R_{exp}			E^{max} / mV		
	Ø / nm	0°C	25°C	50°C	0°C	25°C	50°C
PtO_x^M/C	1.9	—	19	20	—	800	730
$PtRuO_x^M/C$	1.8	—	25	26	—	730	590
$PtRuOsIrO_x^M/C$	1.6	—	13	15	—	810	710
Pt(pc)	-	1.4	1.5	1.5	720	710	660

$\varnothing$, particle size ; RF_{exp}, roughness factor of colloid; E_{max}^{ox}, potential of maximum faradaic current

The negative shift of the peak potential with increasing temperature of -1.20 mV K^{-1} found for polycrystalline Pt is somewhat lower than that of -1.79 mV K^{-1} observed for Pt(111) [230]. In general, the slopes of the relation between the peak potential and

temperature found for nanoparticle electrodes are higher than that observed on polycrystalline Pt. A careful look on the slopes of -2.8 mV K^{-1} for PtO_x^M/C, -5.6 mV K^{-1} for $PtRuO_x^M$/C and -4.0 mV K^{-1} in the case of $PtRuOsIrO_x^M$/C clearly shows that the major effect of the temperature is observed for $PtRuO_x^M$/C electrode.

The activities for the methanol oxidation reaction are markedly enhanced by elevating temperature as indicated by the negative shift of the onset potential and the increase of the current densities and also of the current efficiency at all studied electrodes. As already shown in the previous chapters, it is possible to obtain platinum electrodes with a large active area by dispersion of small platinum nanoparticles onto the surface. However, on pure platinum, the problem of poisoning remains critical, even if it is weaker at higher temperatures and the potentials, at which methanol is oxidized, remain too high, and thus not convenient for fuel cells applications. The onset of the oxidation is at around 500 mV, and needs to be shifted 200 to 300 mV negatively to be useful in direct methanol fuel cells. Such potential shifts cannot be obtained with pure platinum, even with highly dispersed catalysts. The only way is to use plurimetalic platinum based catalysts.

With co-deposits of Pt and Ru the electrocatalytic activity is improved in comparison to pure Pt. By increasing the operating temperature, the current densities obtained at 600 mV, with the Pt-Ru deposit electrodes, increases greatly. It is seen that ruthenium presents a good promotion effect for the electrooxidation of methanol. Generally, the relative CO coverage is increased by a higher temperature at low potentials, whereas at high potentials it is not much influenced. It was also found that an increase of temperature leads to the increase of the apparent current efficiency, nevertheless the average current efficiency is not influenced.

The co-catalytical effects of Ru is more pronounced at 50°C, where the onset of the methanol oxidation at $PtRuO_x^M$/C is shifted by ca 100 mV to lower potential compared to pure PtO_x^M/C (E_{onset}(Pt)-E_{onset}(PtRu)). At room temperature, this shift is only half of this value (ca 50 mV).

E_a values determined from chronoamperometry show that the apparent activation energy is strongly dependent on oxidation potential, presumably because a number of different surface processes and adsorption processes that affect the magnitude of the current are potential dependent and also time dependent. On PtO_x^M/C, the apparent E_a of about 27 kJ mol^{-1} (at 700 mV) is equal to that obtained for thin Pt film by Wakabayashi and co-workers [235], but only half of that obtained for Pt(pc). Comparison of the apparent activation energy values obtained with $PtRuO_x^M$/C alloy with that of PtO_x^M/C catalyst demonstrates the interest in increasing the operating temperature with the bimetallic electrodes. Albeit many references have reported E_a

values ranging from 22 to 95 kJ mol^{-1} for a number of Pt, and Pt-alloy surfaces in methanol solution [69, 209, 238, 279], these values have been correlated to rate determining steps that range from activation-adsorption controlled, surface diffusion processes, to strictly adsorption controlled, depending on potential. It is difficult to compare the E_a from the fact that many of these numbers are given without stating the potential at which they were determined.

For example, the activation energy is ca 60 kJ mol^{-1} for well-defined Pt-Ru alloys with Ru surface concentration of ≈33 at.% and 46 at.%, but only half as large for 7 at.% Ru at 400 mV in 0.5 M methanol solution [209]. The higher activation energy found for Ru "rich" surfaces reflects the activation of the dissociative adsorption of methanol. The lower activation energy at 7 at.% Ru surface composition was hypothesized to be a measure of the rate limiting elementary step of surface migration of adsorbed CO on Pt-rich surfaces.

Using mass spectrometry, the apparent activation energy ($E_a(I_{44})$) for the indirect oxidation pathway *via* adsorbed CO can be determined using the mass spectrometric ion current of CO_2. The fact that at PtRu alloys, the $E_a(I_{44})$ is smaller than that observed for the overall activation energy may indicate that, at potentials bellow 600 mV, the adsorption energy of the reactive intermediates may play an important role in the kinetics of methanol adsorption.

Many of references point out that the values of the activation energy are influenced by surface coverage and many other factors; they do not follow up on how they influence the evaluations of E_a.

As mentioned in Ref. [277], differences in E_a values can be attributed to the extent of anion adsorption, the behaviour of surface oxide processes, and the formation/adsorption of poisonous intermediates during the oxidation of MeOH (i.e. CO). These processes are potential dependent, which reflects the fact that the E_a values obtained are a function of the potential at which they are calculated. These potential dependent processes also explain the directionality of the apparent E_a data. It was shown [277] shown that not only the potential at which these values were obtained is important, but also how one got to that potential (i.e. sweep rate, sweep direction, etc.). This can have a large impact on the magnitude of the Ea values obtained.

The processes that affect the adsorption of methanol, compounded with the complexity of the methanol oxidation pathways, make the assignment of E_a values to specific steps in the methanol oxidation process quite challenging.

Chapter 8 Summary and Outlook

In the present thesis, the CO and methanol oxidation kinetics at different Pt-based surfaces are studied using Differential Electrochemical Mass Spectrometry. Special emphasis is given to the comparison of bulk metals and carbon supported nanoparticulate catalysts as well as the comparison of PtRu alloy surfaces and Pt surfaces decorated with Ru. The influence of the foreign metals (especially ruthenium), potential and temperature is analyzed. It is obvious that the activity of such bimetallic surfaces depends on the preparation method, at least in view of the oxidation of methanol. Based on electrochemical data, the kinetic parameters of the methanol oxidation reaction, such as methanol adsorption and oxidation rate, current efficiency and reaction activation energy are calculated. Here, the validity of the parallel path mechanism according to the scheme below has to be taken into account:

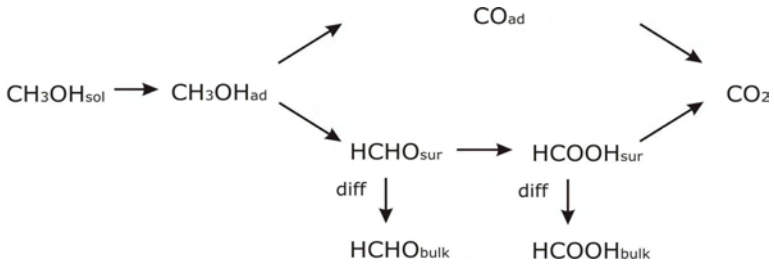

It is of fundamental importance to determine the rates and activation energies of the single reaction steps as well as the influence of the catalyst composition and structure. Thereupon, the ion current of the CO_2 was measured in parallel to the faradaic current during the adsorption of methanol, the oxidation of the methanol adsorbate and the bulk methanol oxidation.

A further important aspect of the catalyst activity is the real surface area, which is determined using the CO adsorption method (Chapter 3). It is shown that the real surface area estimated by this method is in good agreement with that calculated from a simple geometric ball model. This shows that most of the particles are accessible to CO. In preliminary experiments the underpotential deposition of Cu is also introduced as a method for the determination of the surface area. Furthermore, it is shown that the addition of Se ad-atoms to the PtO_x^E/C and $Ru_{0.2}$-modified PtO_x^M/C surface not only changes the distribution of the CO population, but also hinders the adsorption of CO on these sites.

The mechanism of the CO ad-layer oxidation on polycrystalline Pt and Pt nanoparticles is studied using potentiostatic and galvanostatic experiments. The form of the transients deviates from that which would be expected according to a "simple" Langmuir-Hinshelwood

mechanism. Thus, to fully describe the rate of the CO oxidation, rate-limiting surface diffusion and repulsive terms needs to be incorporated in the reaction equations.

In Chapter 4, the specific adsorption sites on polycrystalline Pt, Pt(665) and platinum nanoparticle electrodes modified by 0.2 monolayer of ruthenium are probed by methanol and different isotopes of CO using the differential electrochemical mass spectroscopy (DEMS) for the detection of the anodic oxidation product CO_2. It is shown, that $Ru_{0.2}$-modified Pt surfaces offer energetically different sites for the adsorption and the oxidative desorption, which can be selectively populated by CO species; either *via* the direct adsorption of CO dissolved in the electrolyte or *via* the adsorption and decomposition reaction of methanol. ^{12}CO adsorbed in the vicinity of Ru (having a less negative adsorption enthalpy) can be selectively oxidized and subsequently replaced by ^{13}CO, while the ^{12}CO further away from Ru is more strongly adsorbed and is only slowly exchanged. The low rate of the exchange between ^{13}CO and adsorbed residual ^{12}CO can be influenced by the concentration of the ^{13}CO in the solution. The result of the isotopic exchange of ^{12}C-methanol adsorbates with bulk ^{13}CO indicates that only a fraction of the methanol adsorbate (ca. 20%; depending on the surface) is weakly adsorbed CO (in the vicinity of Ru) and is exchanged by ^{13}CO.

The experimental results presented in Chapter 5 and 6 show that the oxidation of the methanol adsorbate and bulk methanol oxidation is a surface sensitive process. The adsorbate composition and the respective desorption profiles are defined by the structure of the used electrodes.

In methanol adsorption experiments on Pt surfaces it was shown that not only the relative coverage of the methanol adsorbate, but also its adsorption rate is dependent on the potential of the adsorption. On polycrystalline Pt and Pt nanoparticle electrodes, the maximum saturation coverage of adsorbed methanol is achieved at about 500 mV. It is found to be higher for polycrystalline Pt, where coverage of 0.56 ML is found in contrast to 0.28 ML for Pt nanoparticles, with respect to a full monolayer formed from dissolved CO. The fact that the maximum CO coverage formed from methanol is much lower than that obtained from CO dissolved in the electrolyte shows that there are free sites, which would be available for the adsorption of CO, but these are not active for the formation of CO from methanol. Since intermediates (i.e., formaldehyde and formic acid) are still formed on these sites, it is quite obvious, that for their formation, the necessity of neighbouring sites is much less severe than for the formation and adsorption of CO from methanol.

Further, it is shown that on Pt nanoparticle electrodes, the reactivity with respect to the different reaction steps of the methanol oxidation is quite different from that on polycrystalline Pt. On Pt nanoparticles, the rate of the adsorption of methanol is considerably lower, but a clear decrease in the oxidation rate of the methanol adsorbate is not observed. During oxidation the reaction order with respect to the adsorbate is found to be nearly zero at polycrystalline Pt and close to one at the nanoparticle electrode.

In comparison to pure Pt, the oxidation of methanol adsorbate at Ru containing Pt surfaces exhibits a shift of the peak potential to lower potentials. The methanol oxidation evokes a quick formation of CO_{ad} at very low potentials, where CO_{ad} is not yet oxidized, and so hinders the further adsorption and decomposition of methanol. At potentials above the onset potential of the adsorbate oxidation, both parallel oxidation paths are taking place simultaneously. At a low potential, higher current efficiencies for CO_2 are observed on Ru-modified electrodes than on pure Pt surfaces. This suggests that the Ru ad-atoms promote the reaction path *via* CO_{ad} in the low potential region. At higher potentials, the same current efficiency for CO_2 as on pure Pt indicates that the Ru loses its co-catalytic activity towards methanol oxidation. This loss of the activity is possibly caused by the formation of inactive anhydrous Ru oxide at higher potentials.

In Chapter 7, the temperature dependence of the adsorption and oxidation of methanol is investigated. For all surfaces, the adsorption rate increases markedly with temperature. At all potentials, the final coverage of CO adsorbed from a CO saturated solution does not depend on temperature. In contrast, at adsorption potentials below 500 mV the coverage of adsorbed CO formed *via* dehydrogenation of methanol increases with temperature at all surfaces studied. As this reaction requires at least three adjacent adsorption sites to proceed, the final CO coverage from methanol is always lower than that directly formed from dissolved CO. Above 600 mV, at polycrystalline platinum, the CO coverage from methanol decreases, whereas at nanoparticle surfaces it still increases with increasing temperature. These results are related to the relative rates of the formation and oxidation of the adsorbate. On polycrystalline platinum, below 500 mV, the formation of the adsorbate is accelerated more than the oxidation by increasing temperature. Above 600 mV, this trend is inversed.

Also the overall methanol oxidation reaction for bulk methanol is found to be markedly enhanced by the elevating temperature. This is indicated not only by the negative shift of the onset potential but also by the increase of the current densities. For all the surfaces,

during potential cycles, the average current efficiency for CO_2 does not depend on temperature. However, at a constant potential of 600 mV it increases clearly with temperature. But the increase in temperature still doesn't solve the problem of the anode poisoning. The overall apparent activation energies for the methanol oxidation increase monotonically with potential (between 400 mV and 600 mV; for Pt(pc) and PtO_x^M/C up to 700 mV). At 400 mV the sequence of the apparent activation energies for the different surfaces is $PtO_x^M/C < PtRuO_x^M/C < PtRuOsIrO_x^M/C <$ Pt(pc), while the sequence is changed to $PtO_x^M/C < PtRuO_x^M/C <$ Pt(pc) $< PtRuOsIrO_x^M/C$ at 500 mV and to $PtO_x^M/C <$ Pt(pc) $< PtRuO_x^M/C < PtRuOsIrO_x^M/C$ at 600 mV. The apparent activation energies for the indirect oxidation pathway *via* adsorbed CO ($E_a(I_{44})$), determined from the ion current of CO_2, are higher on pure Pt surfaces than that observed for the overall reaction, whereas the $E_a(I_{44})$ is smaller than the overall activation energies found for the PtRu alloy. This indicates that the Ru containing Pt surfaces have a positive effect on the catalytic activity of towards methanol oxidation.

The current transients for the potentiostatic oxidation of CO from methanol or the potential transients in galvanostatic experiments deviate from the theoretical trends for the Langmuir-Hinshelwood and the Eley-Rideal mechanism. Thus neither of the mechanisms completely describes the reaction.

The understanding of the methanol oxidation reaction is not yet completed. Similar to the present experiments on pure Pt surfaces, it will be interesting to study the reaction kinetics of CO and methanol using chronoamperometry and chronopotentiometry also on Ru modified platinum surfaces. Especially the potentiostatic experiments should be extended systematically to different step potentials. The simple mathematical models for the CO stripping and the methanol oxidation should be refined to get a better understanding of the electrode processes.

In this study it was shown that the CO and methanol oxidation on Ru modified Pt nanoparticles differ from that on Pt-Ru alloys. Hence, it will be interesting to study the behaviour on Pt nanoparticles modified with Ruthenium, Osmium and Iridium in comparison to the PtRuOsIr alloys. For these Pt catalysts modified with multiple components the question arises whether the deposition order of the foreign metals plays a role in the co-catalytic effect.

Due to time constraints, the rate of the methanol adsorption in dependence on the adsorption potential was measured only for pure Pt surfaces. It would be also interesting to

measure the reaction rate of the methanol adsorption on Ru modified Pt surfaces as well as on PtRu alloys. It is quite conceivable that the adsorption of methanol will vary depending on the surface structure as well as the amount of the Ru deposit.

Our ^{13}C exchange experiments are a first approach to studying the behaviour of Pt surfaces decorated with Ru in a systematic way. With the aid of isotopic labelling of CO and/or methanol one can get a better picture of the reactivity of these surfaces against the methanol oxidation, and how this reactivity is influenced by the amount of Ru present.

The non volatile intermediates produced during the methanol oxidation cannot be determined by DEMS. It would be of particular interest to determine these intermediates for example using an electrochemical flow-cell connected to an electrospray mass spectrometer (ESI-MS). In ESI-MS the samples are introduced in the mass spectrometer in solution and ionised at atmospheric pressure, therefore it is possible to identify as well as to quantify the oxidation and reduction products of different electrochemical reactions (and hence to study electrochemical reactions in general).

Abbreviations and symbols

Abbreviations	
AES	Auger Electron Spectroscopy
CV	Cyclic Voltammogram
DEMS	Differential Electrochemical Mass Spectrometry
DMFC	Direct Methanol Fuel Cell
EI	Electron Ionisation
EMS	Electrochemical Mass Spectroscopy
ESDIAD	Electron Stimulated Desorption Ion Angular Distribution
FTIR	Fourier Transformations Infra Red Spectroscopy
GC	Glassy Carbon
LEED	Low Energy Electron Diffraction
LEIS	Low Energy Ion Spectroscopy
L-H	Langmuir-Hinshelwood
ML	Monolayer
MOR	Methanol Oxidation Reaction
MSCV	Mass Spectrometrical Cyclic Voltammogram
NMR	Nuclear Magnetic Resonance
PEMFC	Proton Exchange Membrane Fuel Cell
PTFE	Polytetrafluorethylen (Teflon)
RHE	Reversible Hydrogen Electrode
SEM	Secondary Electron Multiplier
STM	Scanning Tunneling Microscopy
TOF	Turnover Frequencies
TPD	Temperature Programmed Desorption
UHV	Ultra-High Vacuum
UPD	Underpotential Deposition
XPS	X-ray Photoelectron Spectroscopy

Symbols	
τ	time dwell / s
Θ	relative coverage
Δ	voltammetric feature
ϑ	coverage
Γ_{CO}	surface coverage of CO
"*"	"free site"
"$_{ads}$"	"adsorbed"
A_i	current efficiency of CO_2 / %
A_{sur}	electrochemically active surface area / cm^2
dn_i/dt	flow rate of species / mol s^{-1}
E_a	activation energy / kJ mol^{-1}
E_{ads}	adsorption potential / mV
F	faraday constant; 96485 C mol^{-1}
I_f^*	faradaic current corresponding to CO_2 formation Eq. (2-9) / A
I_i	ion current / A
K^o, K^*	mass spectrometrical calibration constants
N	transfer efficiency
N_A	Avogadro's number; 6.022 141 79 · 10^{23} mol^{-1}
n_f	total amount of species produced electrochemically / mol
n_i	amount of the mass spectrometrically detected species / mol
N_{Pt}	number of Pt sites per cm^2
q	electrolysis charge involved by the electrolysis / C
$Q(Cu_{upd})^{exp}$	experimental charge for Cu UPD desorption peak / C
$Q(H_{ad})^{exp}$	experimental total charge in the hydrogen adsorption region / C
$Q(H_{ad})^{theo}$	theoretical charge in hydrogen adsorption region / C
Q_f	faradaic charge (integrated faradaic current) / C
Q_i	ionic charge (integrated ion current of corresponding masses) / C
z	number of electrons

Literature

1. W. Vielstich, *Fuel Cells. Modern Processes for the Electrochemical Production of Energy*, p. 501, Wiley-Interscience, London, New York, Sydney, Toronto (1965).

2. EG&G Services Parsons Inc. and S. A. I. Corporation, *Fuel Cell Handbook*, U.S. Department of Energy, Office of Fossil Energy, National Energy Technology Laboratory (2000).

3. L. Carrette, K. A. Friedrich and U. Stimming, *ChemPhysChem*, **1**, 162 (2000).

4. V. S. Bagotzky, N. V. Osetrova and A. M. Skundin, *Russ. J. Electrochem.*, **39**, 919 (2003).

5. M. Watanabe and S. Motoo, *J. Electroanal. Chem.*, **60**, 267 (1975).

6. M. Watanabe, S. Saegusa and P. Stonehart, *J. Electroanal. Chem.*, **271**, 213 (1989).

7. S. Mukerjee, *J. Appl. Electrochem.*, **20**, 537 (1990).

8. T. Frelink, W. Visscher and J. A. R. van Veen, *J. Electroanal. Chem.*, **382**, 65 (1995).

9. F. Maillard, M. Eikerling, O. V. Cherstiouk, S. Schreier, E. Savinova and U. Stimming, *Faraday Discuss.*, **125**, 357 (2004).

10. K. J. J. Mayrhofer, M. Arenz, B. B. Blizanac, V. Stamenkovic, P. N. Ross and N. M. Markovic, *Electrochim. Acta*, **50**, 5144 (2005).

11. K. J. J. Mayrhofer, B. B. Blizanac, M. Arenz, V. R. Stamenkovic, P. N. Ross and N. M. Markovic, *J. Phys. Chem. B*, **109**, 14433 (2005).

12. K. Bergamaski, A. L. N. Pinheiro, E. Teixeira-Neto and F. C. Nart, *J. Phys*. *Chem. B*, **110**, 19271 (2006).

13. F. Maillard, E. R. Savinova and U. Stimming, *J. Electroanal. Chem.*, **599**, 221 (2007).

14. B. Speiser, *Chem. unserer Zeit*, **15**, 21 (1981).

15. J. Heinze, *Angew. Chem.*, **96**, 823 (1984).

16. D. H. Evans, K. M. Oconnell, R. A. Petersen and M. J. Kelly, *J. Chem. Educ.*, **60**, 290 (1983).

17. J. Heitbaum and Vielstic.W, *Angewandte Chemie-International Edition*, **13**, 683 (1974).

18. B. Speiser, *Chem. unserer Zeit*, **15**, 62 (1981).

19. R. R. Bruckenstein and J. Gadde, *J. Am. Chem. Soc.*, **93**, 793 (1971).

20. O. Wolter and J. Heitbaum, *Ber. Bunsenges. Phys. Chem.*, **88**, 2 (1984).

21. T. Löffler, Der Einfluß monoatomarer Stufen und der Temperatur auf die Adsorption und Hydrierung ungesättigter organischer Verbindungen, in *Mathematisch Naturwissenschaftliche Fakultät*, Rheinische-Friedrich-Wilhelms-Universität, Bonn (2003).

22. Z. Jusys, H. Massong and H. Baltruschat, *J. Electrochem. Soc.*, **146**, 1093 (1999).

23. T. Löffler, Charakterisierung und Anwendung einer neuen Dünnschichtzelle für die elektrochemische Massenspektrometrie, in *Institut für Physikalische und Theoretische Chemie*, p. 93, Universität Bonn, Bonn (1997).

24. H. Baltruschat and U. Schmiemann, *Ber. Bunsenges. Phys. Chem.*, **97**, 452 (1993).

25. J. Willsau and J. Heitbaum, *Electrochim. Acta*, **31**, 943 (1986).

26. J. Clavilier, R. Albalat, R. Gómez, J. M. Orts, J. M. Feliu and A. Aldaz, *J. Electroanal. Chem.*, **330**, 489 (1992).

27. H. Baltruschat, *J. Am. Soc. Mass. Spectrom.*, **15**, 1693 (2004).

28. B. Lang, R. W. Joyner and G. A. Somorjai, *Surf. Sci.*, **30**, 440 (1972).

29. N. Furuya and S. Koide, *Surf. Sci.*, **220**, 18 (1989).

30. G. Somorjai, *Chemistry in Two Dimensions: Surfaces*, Cornell University Press, Ltd., London, Ithaca and London (1981).

31. F. T. Wagner and P. N. Ross, *J. Electroanal. Chem.*, **150**, 141 (1983).

32. J. Clavilier, R. Faure, G. Guinet and R. Durand, *J. Electroanal. Chem.*, **107**, 205 (1980).

33. J. Clavilier, *J. Electroanal. Chem.*, **107**, 211 (1980).

34. Y. Uchida and G. Lehmpfuhl, *Surf. Sci.*, **243**, 193 (1991).

35. S. Motoo and N. Furuya, *J. Electroanal. Chem.*, **172**, 339 (1984).

36. L. Palaikis, D. Zurawski, M. Hourani and A. Wieckowski, *Surf. Sci.*, **199**, 183 (1988).

37. J. Clavilier, K. E. Achi and A. Rodes, *J. Electroanal. Chem.*, **272**, 253 (1989).

38. J. Clavilier, K. El Achi and A. Rodes, *Chem. Phys.*, **141**, 1 (1990).

39. A. Rodes, K. El Achi, M. A. Zamakchardi and J. Clavilier, *J. Electroanal. Chem.*, **284**, 245 (1990).

40. K. Sashikata, N. Furuya and K. Itaya, *J. Vac. Sci. Technol.*, **B 9**, 457 (1991).

41. H. Graoui, S. Giorgio and C. R. Henry, *Surf. Sci.*, **417**, 350 (1998).

42. K. Kinoshita, *J. Electrochem. Soc.*, **137**, 845 (1990).

43. C. R. Henry, *Prog. Surf. Sci.*, **80**, 92 (2005).

44. A. Wieckowski, E. R. Savinova and C. G. Vayenas, *Catalysis and Electrocatalysis at Nanoparticle Surfaces*, p. 970, Marcel Dekker Inc, New York (2003).

45. P. Müller and R. Kern, *Appl. Surf. Sci.*, **164**, 68 (2000).

46. P. Müller and R. Kern, *Appl. Surf. Sci.*, **162**, 133 (2000).

47. P. Müller and R. Kern, *Surf. Sci.*, **457**, 229 (2000).

48. C. R. Henry, *Surf. Sci. Rep.*, **31**, 235 (1998).

49. Y. Takeuchi, T. Ida and K. Kimura, *J. Phys. Chem. B*, **101**, 1322 (1997).

50. N. Satoh, H. Hasegawa, K. Tsujii and K. Kimura, *J. Phys. Chem.*, **98**, 2143 (1994).

51. S. T. Lin, M. T. Franklin and K. J. Klabunde, *Langmuir*, **2**, 259 (1986).

52. G. C. Papavassiliou, *Journal of Physics F-Metal Physics*, **6**, L103 (1976).

53. M. S. Yeh, Y. S. Yang, Y. P. Lee, H. F. Lee, Y. H. Yeh and C. S. Yeh, *J. Phys. Chem. B*, **103**, 6851 (1999).

54. A. M. Morales and C. M. Lieber, *Science*, **279**, 208 (1998).

55. M. S. Sibbald, G. Chumanov and T. M. Cotton, *J. Phys. Chem.*, **100**, 4672 (1996).

56. M. Reetz and W. Helbig, *J.Am.Chem.Soc.*, **116**, 7401 (1994).

57. J. A. Becker, R. Schafer, R. Festag, W. Ruland, J. H. Wendorff, J. Pebler, S. A. Quaiser, W. Helbig and M. T. Reetz, *J. Chem. Phys.*, **103**, 2520 (1995).

58. M. T. Reetz and S. A. Quaiser, *Angewandte Chemie-International Edition*, **34**, 2240 (1995).

59. U. Nickel, A. Z. Castell, K. Poppl and S. Schneider, *Langmuir*, **16**, 9087 (2000).

60. M. T. Reetz and M. Maase, *Adv. Mater.*, **11**, 773 (1999).

61. K. Meguro, M. Torizuka and K. Esumi, *Bull. Chem. Soc. Jpn.*, **61**, 341 (1988).

62. K. L. Tsai and J. L. Dye, *Chem. Mater.*, **5**, 540 (1993).

63. M. T. Reetz, M. Lopez, W. Grunert, W. Vogel and F. Mahlendorf, *J. Phys. Chem B*, **107**, 7414 (2003).

64. M. T. Reetz and M. G. Koch, *J. Am. Chem. Soc.*, **121**, 7933 (1999).

65. F. Maillard, F. Gloaguen and J. M. Leger, *J. Appl. Electrochem.*, **33**, 1 (2003).

66. E. Herrero, J. M. Feliu and A. Wieckowski, *Langmuir*, **15**, 4944 (1999).

67. W. Chrzanowski and A. Wieckowski, *Langmuir*, **13**, 5974 (1997).

68. W. Chrzanowski, H. Kim and A. Wieckowski, *Catal. Lett.*, **50**, 69 (1998).

69. G. Tremiliosi-Filho, H. Kim, W. Chrzanowski, A. Wieckowski, B. Grzybowska and P. J. Kulesza, *J. Electroanal. Chem.*, **467**, 143 (1999).

70. A. Crown, I. R. Moraes and A. Wieckowski, *J. Electroanal. Chem.*, **500**, 333 (2001).

71. A. Crown and A. Wieckowski, *PCCP*, **3**, 3290 (2001).

72. H. Kim, I. R. d. Moraes, G. Tremiliosi-Filho, R. Haasch and A. Wieckowski, *Surf. Sci.*, **474**, L203 (2001).

73. P. Waszczuk, J. Solla-Gullon, H. S. Kim, Y. Y. Tong, V. Montiel, A. Aldaz and A. Wieckowski, *J. Catal.*, **203**, 1 (2001).

74. A. Crown, C. Johnston and A. Wieckowski, *Surf. Sci.*, **506**, L268 (2002).

75. G. Q. Lu, P. Waszczuk and A. Wieckowski, *J. Electroanal. Chem.*, **532**, 49 (2002).

76. S. Park, A. Wieckowski and M. J. Weaver, *J. Am. Chem. Soc.*, **125**, 2282 (2003).

77. P. A. Christensen, J. M. Jin, W. F. Lin and A. Hamnett, *J. Phys. Chem. B*, **108**, 3391 (2004).

78. S. Cramm, K. A. Friedrich, K. P. Geyzers, U. Stimming and R. Vogel, *Fresenius J. Anal. Chem.*, **358**, 189 (1997).

79. K. A. Friedrich, K.-P. Geyzers, U. Linke, U. Stimming and J. Stumper, *J. Electroanal. Chem.*, **402**, 123 (1996).

80. K. A. Friedrich, K. P. Geyzers, A. Marmann, U. Stimming and R. Vogel, *Zeitschrift Fur Physikalische Chemie*, **208**, 137 (1999).

81. K. A. Friedrich, K. P. Geyzers, A. J. Dickinson and U. Stimming, *J. Electroanal. Chem.*, **524**, 261 (2002).

82. T. Iwasita, H. Hoster, A. John-Anacker, W. F. Lin and W. Vielstich, *Langmuir*, **16**, 522 (2000).

83. J. C. Davies, B. E. Hayden, D. J. Pegg and M. E. Rendall, *Surf. Sci.*, **496**, 110 (2002).

84. J. C. Davies, B. E. Hayden and D. J. Pegg, *Surf. Sci.*, **467**, 118 (2000).

85. J. C. Davies, B. E. Hayden and D. J. Pegg, *Electrochim. Acta*, **44**, 1181 (1998).

86. W. Chrzanowski and A. Wieckowski, *Langmuir*, **14**, 1967 (1998).

87. G. Samjeské, X.-Y. Xiao and H. Baltruschat, *Langmuir*, **18**, 4659 (2002).

88. G. Samjeske, Metallische Submonolagen auf Platin-Einkristall- Elektroden und ihr Einfluß auf die CO-Oxidation: UHV- und elektrochemische Untersuchungen, in *Mathematisch Naturwissenschaftliche Fakultät*, Rheinische-Friedrich-Wilhelms-Universität, Bonn (2003).

89. F. Vigier, F. Gloaguen, J. M. Leger and C. Lamy, *Electrochim. Acta*, **46**, 4331 (2001).

90. Z. D. Wei, L. L. Li, Y. H. Luo, C. Yan, C. X. Sun, G. Z. Yin and P. K. Shen, *J. Phys. Chem. B*, **110**, 26055 (2006).

91. J. A. Shropshire, *J. Electrochem. Soc.*, **112**, 465 (1965).

92. W. S. Li, L. P. Tian, Q. M. Huang, H. Li, H. Y. Chen and X. P. Lian, *J. Power Sources*, **104**, 281 (2002).

93. H. Kita, H. Nakajima and K. Shimazu, *J. Electroanal. Chem.*, **248**, 181 (1988).

94. J. Wang, H. Nakajima and H. Kita, *J. Electroanal. Chem.*, **250**, 213 (1988).

95. H. Nakajima and H. Kita, *Electrochim. Acta*, **35**, 849 (1990).

96. G. Samjeské, H. Wang, T. Löffler and H. Baltruschat, *Electrochim. Acta*, **47**, 3681 (2002).

97. M. Shibata, O. Takahashi and S. Motoo, *J. Electroanal. Chem.*, **249**, 253 (1988).

98. R. N. Bhattacharya, A. M. Fernandez, M. A. Contreras, J. Keane, A. L. Tennant, K. Ramanathan, J. R. Tuttle, R. N. Noufi and A. M. Hermann, *J. Electrochem. Soc.*, **143**, 854 (1996).

99. D. Lippkow and H. H. Strehblow, *Electrochim. Acta*, **43**, 2131 (1998).

100. A. Steponavicius and D. Simkunaite, *Russ. J. Electrochem.*, **38**, 488 (2002).

101. M. J. Llorca, E. Herrero, J. M. Feliu and A. Aldaz, *J. Electroanal. Chem.*, **373**, 217 (1994).

102. E. Herrero, A. Rodes, J. M. Pérez, J. M. Feliu and A. Aldaz, *J. Electroanal. Chem.*, **412**, 165 (1996).

103. J. M. Feliu, R. Gomez, M. J. Llorca and A. Aldaz, *Surf. Sci.*, **289**, 152 (1993).

104. M. P. Kiskinova, A. Szabo and J. T. Yates, *Surf. Sci.*, **226**, 237 (1990).

105. T. Matsushima, *Bull. Chem. Soc. Jpn.*, **51**, 1956 (1978).

106. O. Wolter and J. Heitbaum, *Ber. Bunsenges. Phys. Chem.*, **88**, 6 (1984).

107. M. W. Breiter, *J. Phys. Chem.*, **72**, 1305 (1968).

108. L. Grambow and S. Bruckenstein, *Electrochim. Acta*, **22**, 377 (1977).

109. A. M. d. Becdelièvre, J. d. Becdelièvre and J. Clavilier, *J. Electroanal. Chem.*, **294**, 97 (1990).

110. C. McCallum and D. Pletcher, *J. Electroanal. Chem.*, **70**, 277 (1976).

111. R. Dalbeck, H. W. Buschmann and W. Vielstich, *J. Electroanal. Chem.*, **372**, 251 (1994).

112. A. Couto, M. C. Pérez, A. Rincón and C. Gutiérrez, *J. Phys. Chem.*, **100**, 19538 (1996).

113. S. A. Bilmes and A. J. Arvia, *J. Electroanal. Chem.*, **361**, 159 (1993).

114. R. Ianniello, V. M. Schmidt, U. Stimming, J. Stumper and A. Wallau, *Electrochim. Acta*, **39**, 1863 (1994).

115. M. Watanabe and S. Motoo, *J. Electroanal. Chem.*, **206**, 197 (1986).

116. A. Rincon, M. C. Perez, A. Cuesta and C. Gutierrez, *Electrochem. Commun.*, **7**, 1027 (2005).

117. I. Fromondi and D. A. Scherson, *J. Phys. Chem. B*, **110**, 20749 (2006).

118. A. Cuesta, A. Couto, A. Rincon, M. C. Perez, A. Lopez-Cudero and C. Gutierrez, *J. Electroanal. Chem.*, **586**, 184 (2006).

119. A. Lopez-Cudero, A. Cuesta and C. Gutierrez, *J. Electroanal. Chem.*, **586**, 204 (2006).

120. A. Lopez-Cudero, A. Cuesta and C. Gutierrez, *J. Electroanal. Chem.*, **579**, 1 (2005).

121. I. Villegas and M. J. Weaver, *J. Chem. Phys.*, **101**, 1648 (1994).

122. N. M. Markovic and P. N. Ross, *Surf. Sci. Rep.*, **45**, 117 (2002).

123. A. Cuesta, M. d. C. Pérez, A. Rincón and C. Gutiérrez, *ChemPhysChem*, **7**, 2346 (2006).

124. J. M. Feliu, J. M. Orts, A. Fernandez-Vega, A. Aldaz and J. Clavilier, *J. Electroanal. Chem.*, **296**, 191 (1990).

125. A. Wieckowski, M. Rubel and C. Gutiérrez, *J. Electroanal. Chem.*, **382**, 97 (1995).

126. H. Kita, H. Naohara, T. Nakato, S. Taguchi and A. Aramata, *J. Electroanal. Chem.*, **386**, 197 (1995).

127. H. Kita and K. Shimazu, *J. Electroanal. Chem.*, **241**, 163 (1988).

128. H. Kita, H. Narumi, S. Ye and H. Naohara, *J. Appl. Electrochem.*, **23**, 589 (1993).

129. W. Akemann, K. A. Friedrich and U. Stimming, *J. Chem. Phys.*, **113**, 6864 (2000).

130. B. N. Grgur, N. M. Markovic, C. A. Lucas and P. N. Ross, *J. Serb. Chem. Soc.*, **66**, 785 (2001).

131. A. Rodes, R. Gomez, J. M. Feliu and M. J. Weaver, *Langmuir*, **16**, 811 (2000).

132. D. Curulla, A. Clotet, J. M. Ricart and F. Illas, *J. Phys. Chem. B*, **103**, 5246 (1999).

133. I. N. Yakovkin and N. V. Petrova, *Surf. Sci.*, **600**, 2600 (2006).

134. A. V. Petukhov, W. Akemann, K. A. Friedrich and U. Stimming, *Surf. Sci.*, **402-404**, 182 (1998).

135. N. M. Markovic, C. A. Lucas, B. N. Grgur and P. N. Ross, *J. Phys. Chem. B*, **103**, 9616 (1999).

136. B. Beden, C. Lamy, N. R. d. Tacconi and A. J. Arvia, *Electrochim. Acta*, **35**, 691 (1990).

137. N. P. Lebedeva, M. T. M. Koper, J. M. Feliu and R. A. van Santen, *J. Electroanal. Chem.*, **524**, 242 (2002).

138. N. P. Lebedeva, M. T. M. Koper, E. Herrero, J. M. Feliu and R. A. van Santen, *J. Electroanal. Chem.*, **487**, 37 (2000).

139. N. P. Lebedeva, M. T. M. Koper, J. M. Feliu and R. A. van Santen, *J. Phys. Chem. B*, **106**, 12938 (2002).

140. F. Maillard, S. Schreier, M. Hanzlik, E. R. Savinova, S. Weinkauf and U. Stimming, *PCCP*, **7**, 385 (2005).

141. O. V. Cherstiouk, P. A. Simonov, V. I. Zaikovskii and E. R. Savinova, *J. Electroanal. Chem.*, **554-555**, 241 (2003).

142. O. V. Cherstiouk, P. A. Simonov and E. R. Savinova, *Electrochim. Acta*, **48**, 3851 (2003).

143. F. Maillard, E. R. Savinova, P. A. Simonov, V. I. Zaikovskii and U. Stimming, *J. Phys. Chem. B*, **108**, 17893 (2004).

144. M. Arenz, K. J. J. Mayrhofer, V. Stamenkovic, B. B. Blizanac, T. Tomoyuki, P. N. Ross and N. M. Markovic, *J. Am. Chem. Soc.*, **127**, 6819 (2005).

145. B. M. Rush, J. A. Reimer and E. J. Cairns, *J. Electrochem. Soc.*, **148**, A137 (2001).

146. M. Watanabe and S. Motoo, *J. Electroanal. Chem.*, **60**, 275 (1975).

147. P. Liu, A. Logadottir and J. K. Norskov, *Electrochim. Acta*, **48**, 3731 (2003).

148. P. Waszczuk, A. Wieckowski, P. Zelenay, S. Gottesfeld, C. Coutanceau, J. M. Leger and C. Lamy, *J. Electroanal. Chem.*, **511**, 55 (2001).

149. S. Wasmus and A. Küver, *J. Electroanal. Chem.*, **461**, 14 (1999).

150. T. Frelink, W. Visscher and J. A. R. Vanveen, *Surf. Sci.*, **335**, 353 (1995).

151. T. Yajima, H. Uchida and M. Watanabe, *J. Phys. Chem. B*, **108**, 2654 (2004).

152. J. R. Kitchin, J. K. Norskov, M. A. Barteau and J. G. Chen, *Phys. Rev. Lett.*, **93**, 156801 (2004).

153. P. Liu and J. K. Norskov, *PCCP*, **3**, 3814 (2001).

154. H. Massong, H. S. Wang, G. Samjeske and H. Baltruschat, *Electrochim. Acta*, **46**, 701 (2000).

155. G. Q. Lu, J. O. White and A. Wieckowski, *Surf. Sci.*, **564**, 131 (2004).

156. D. X. Cao and S. H. Bergens, *Electrochim. Acta*, **48**, 4021 (2003).

157. C. E. Lee and S. H. Bergens, *J. Phys. Chem. B*, **102**, 193 (1998).

158. P. Waszczuk, G. Q. Lu, A. Wieckowski, C. Lu, C. Rice and R. I. Masel, *Electrochim. Acta*, **47**, 3637 (2002).

159. Y. Y. Tong, H. S. Kim, P. K. Babu, P. Waszczuk, A. Wieckowski and E. Oldfield, *J. Am. Chem. Soc.*, **124**, 468 (2002).

160. E. M. Crabb, M. K. Ravikumar, D. Thompsett, M. Hurford, A. Rosec and A. E. Russell, *PCCP*, **6**, 1792 (2004).

161. W. F. Lin, T. Iwasita and W. Vielstich, *J. Phys. Chem. B*, **103**, 3250 (1999).

162. S. Z. Zou, I. Villegas, C. Stuhlmann and M. J. Weaver, *Electrochim. Acta*, **43**, 2811 (1998).

163. C. M. Johnston, S. Strbac, A. Lewera, E. Sibert and A. Wieckowski, *Langmuir*, **22**, 8229 (2006).

164. R. Parsons and T. VanderNoot, *J. Electroanal. Chem.*, **257**, 9 (1988).

165. J.-M. Leger and C. Lamy, *Ber. Bunsenges. Phys. Chem.*, **94**, 1021 (1990).

166. M. P. Hogarth and G. A. Hards, *Platinum Met. Rev.*, **4**, 150 (1996).

167. M. W. Breiter, *Electrochim. Acta*, **12**, 1213 (1967).

168. K.-I. Ota, Y. Nakagawa and M. Takahashi, *J. Electroanal. Chem.*, **179**, 179 (1984).

169. T. Iwasita and W. Vielstich, *J. Electroanal. Chem.*, **201**, 403 (1986).

170. W. Vielstich and X. H. Xia, *J. Phys. Chem.*, **99**, 10421 (1995).

171. C. Korzeniewski and C. L. Childers, *J. Phys. Chem.*, **102**, L489 (1998).

172. V. S. Bagotzky and Y. B. Vassilyev, *Electrochim. Acta*, **12**, 1323 (1967).

173. H. S. Wang, C. Wingender, H. Baltruschat, M. Lopez and M. T. Reetz, *J. Electroanal. Chem.*, **509**, 163 (2001).

174. S. Wasmus, J. T. Wang and R. F. Savinell, *J. Electrochem. Soc.*, **142**, 3825 (1995).

175. H. Wang, T. Löffler and H. Baltruschat, *J. Appl. Electrochem.*, **31**, 759 (2001).

176. A. Hamnett, *Catal. Today*, **38**, 445 (1997).

177. G. T. Burstein, C. J. Barnett, A. R. Kucernak and K. R. Williams, *Catal. Today*, **38**, 425 (1997).

178. B. Beden, A Bewick, M. Razaq and J. Weber, *J. Electroanal. Chem.,* **139**, 203 (1982).

179. T. D. Jarvi and E. M. Stuve, in *Electrocatalysis*, J. Lipkowski and P. N. Ross, 75, Wiley-VCH, New York (1998).

180. E. M. Belgsir, E. Huser, J. M. Leger and C. Lamy, *J. Electroanal. Chem.*, **225**, 281 (1987).

181. E. A. Batista, G. R. P. Malpass, A. J. Motheo and T. Iwasita, *J. Electroanal. Chem.*, **571**, 273 (2004).

182. H. Kita, Y. Gao, T. Nakato and H. Hattori, *J. Electroanal. Chem.*, **373**, 177 (1994).

183. E. Herrero, K. Franaszczuk and A. Wieckowski, *J. Phys. Chem.*, **98**, 5074 (1994).

184. S. G. Sun and J. Clavilier, *J. Electroanal. Chem.*, **236**, 95 (1987).

185. T. Iwasita, *Electrochim. Acta*, **47**, 3663 (2002).

186. E. Herrero, W. Chrzanowski and M. J. Weaver, *J. Phys. Chem.*, **99**, 10423 (1995).

187. J. Greeley and M. Mavrikakis, *J. Am. Chem. Soc.*, **126**, 3910 (2004).

188. T. D. Jarvi, S. Sriramulu and E. M. Stuve, *Colloids and Surfaces - Physicochemical and Engineering Aspects*, **134**, 145 (1998).

189. D. Cao, G. Q. Lu, A. Wieckowski, S. A. Wasileski and M. Neurock, *J. Phys. Chem. B*, **109**, 11622 (2005).

190. T. H. M. Housmans, A. H. Wonders and M. T. M. Koper, *J. Phys. Chem. B*, **110**, 10021 (2006).

191. K. Franaszczuk, E. Herrero, P. Zelenay, A. Wieckowski, J. Wang and R. I. Masel, *J. Phys. Chem.*, **96**, 8509 (1992).

192. B. Bittins-Cattaneo, E. Santos, W. Vielstich and U. Linke, *Electrochim. Acta*, **33**, 1499 (1988).

193. S. Juanto, B. Beden, F. Hahn, C. Lamy and J. M. Leger, *J. Electroanal. Chem.*, **237**, 119 (1987).

194. B. Beden, S. Juanto, J. M. Leger and C. Lamy, *J. Electroanal. Chem.*, **238**, 323 (1987).

195. X. H. Xia, T. Iwasita, F. Ge and W. Vielstich, *Electrochim. Acta*, **41**, 711 (1996).

196. T. H. M. Housmans and M. T. M. Koper, *J. Phys. Chem. B*, **107**, 8557 (2003).

197. A. V. Tripkovic and K. D. Popovic, *Electrochim. Acta*, **41**, 2385 (1996).

198. A. V. Tripkovic, S. L. Gojkovic, K. D. Popovic and J. D. Lovic, *J. Serb. Chem. Soc.*, **71**, 1333 (2006).

199. Z. Jusys, J. Kaiser and R. J. Behm, *Langmuir*, **19**, 6759 (2003).

200. A. Kabbabi, F. Gloaguen, F. Andolfatto and R. Durand, *J. Electroanal. Chem.*, **373**, 251 (1994).

201. K. Yahikozawa, Y. Fujii, Y. Matsuda, K. Nishimura and Y. Takasu, *Electrochim. Acta*, **36**, 973 (1991).

202. R. Lampitt, L. Carrette, M. Hogarth and A. Russell, *J.Electroanal.Chem.*, **460**, 80 (1999).

203. S. Park, Y. Xie and M. J. Weaver, *Langmuir*, **18**, 5792 (2002).

204. Y. Takasu, Y. Fujii and Y. Matsuda, *Bull. Chem. Soc. Jpn.*, **59**, 3973 (1986).

205. T. Iwasita, F. C. Nart and W. Vielstich, *Ber. Bunsenges. Phys. Chem.*, **94**, 1030 (1990).

206. M. Krausa and W. Vielstich, *J. Electroanal. Chem.*, **379**, 307 (1994).

207. H. Hoster, T. Iwasita, H. Baumgartner and W. Vielstich, *J. Electrochem. Soc.*, **148**, A496 (2001).

208. Z. D. Wei and S. H. Chan, *J. Electroanal. Chem.*, **569** (2004).

209. H. A. Gasteiger, N. Markovic, J. Philip N. Ross and E. J. Cairns, *J. Electrochem. Soc.*, **141**, 1795 (1994).

210. N. M. Markovic, H. A. Gasteiger, P. N. Ross, X. D. Jiang, I. Villegas and M. J. Weaver, *Electrochim. Acta*, **40**, 91 (1995).

211. H. Hoster, T. Iwasita, H. Baumgartner and W. Vielstich, *PCCP*, **3**, 337 (2001).

212. D. Kardash, C. Korzeniewski and N. Markovic, *J. Electroanal. Chem.*, **500**, 518 (2001).

213. A. Kabbabi, R. Faure, R. Durand, B. Beden, F. Hahn, J.-M. Leger and C. Lamy, *J. Electroanal. Chem.*, **444**, 41 (1998).

214. H. Wang and H. Baltruschat, *J. Phys. Chem. C*, **111**, 7038 (2007).

215. H. A. Gasteiger, N. Markovic, P. N. Ross and E. J. Cairns, *J. Phys. Chem.*, **97**, 12020 (1993).

216. A. Lima, C. Coutanceau, J. M. Leger and C. Lamy, *J. Appl. Electrochem.*, **31**, 379 (2001).

217. Z. Jusys, T. J. Schmidt, L. Dubau, K. Lasch, L. Jorissen, J. Garche and R. J. Behm, *J. Power Sources*, **105**, 297 (2002).

218. C. J. Song, M. Khanfar and P. G. Pickup, *J. Appl. Electrochem.*, **36**, 339 (2006).

219. K. L. Ley, R. Liu, C. Segre and E. S. Smotkin, *J. Electrochem. Soc.*, **144**, 1543 (1997).

220. B. Gurau, R. Viswanathan, R. Liu, T. Lafrenz, K. Ley, E. Smotkin, E. Reddington, A. Sapienza, B. Chan and T. Mallouk, *J.Phys.Chem B*, **102**, 9997 (1998).

221. L. Liu, R. Viswanathan, R. Liu and E. Smotkin, *Electrochemical and solid-state-letters*, **1**, 123 (1998).

222. H. W. Lei, S. Suh, B. Gurau, B. Workie, R. X. Liu and E. S. Smotkin, *Electrochim. Acta*, **47**, 2913 (2002).

223. E. Reddington, A. Sapienza, B. Gurau, R. Viswanathan, S. Sarangapani, E. S. Smotkin and T. E. Mallouk, *Science*, **280**, 1735 (1998).

224. K. Jambunathan, S. Jayaraman and A. C. Hillier, *Langmuir*, **20**, 1856 (2004).

225. A. S. Arico, P. L. Antonucci, E. Modica, V. Baglio, H. Kim and V. Antonucci, *Electrochim. Acta*, **47**, 3723 (2002).

226. H. N. Dinh, X. M. Ren, F. H. Garzon, P. Zelenay and S. Gottesfeld, *J. Electroanal. Chem.*, **491**, 222 (2000).

227. A. S. Aricò, P. Creti, H. Kim, R. Mantegna, N. Giordano and V. Antonucci, *J. Electrochem. Soc.*, **143**, 3950 (1996).

228. T. J. Schmidt, H. A. Gasteiger and R. J. Behm, *Electrochem. Commun.*, **1**, 1 (1999).

229. G. Meli, J. M. Leger, C. Lamy and R. Durand, *J. Appl. Electrochem.*, **23**, 197 (1993).

230. E. Herrero, J. M. Feliu, S. Blais, Z. Radovic-Hrapovic and G. Jerkiewicz, *Langmuir*, **16**, 4779 (2000).

231. H. Nonaka and Y. Matsumura, *J. Electroanal. Chem.*, **520**, 101 (2002).

232. T. Kawaguchi, W. Sugimoto, Y. Murakami and Y. Takasu, *Electrochem. Commun.*, **6**, 480 (2004).

233. T. Seiler, E. R. Savinova, K. A. Friedrich and U. Stimming, *Electrochim. Acta*, **49**, 3927 (2004).

234. R. J. Bellows, E. P. MarucchiSoos and D. T. Buckley, *Industrial & Engineering Chemistry Research*, **35**, 1235 (1996).

235. N. Wakabayashi, H. Uchida and M. Watanabe, *Electrochemical and Solid State Letters*, **5**, E62 (2002).

236. A. Aramata, T. Kodera and M. Masuda, *J. Appl. Electrochem.*, **18**, 577 (1988).

237. S. L. Gojkovic, T. R. Vidakovic and D. R. Durovic, *Electrochim. Acta*, **48**, 3607 (2003).

238. D. Chu and S. Gilman, *J. Electrochem. Soc.*, **143**, 1685 (1996).

239. T. Iwasita and U. Vogel, *Electrochim. Acta*, **33**, 557 (1988).

240. M. S. McGovern, P. Waszczuk and A. Wieckowski, *Electrochim. Acta*, **51**, 1194 (2006).

241. M. Heinen, Y.-X. Chen, Z. Jusys and R. J. Behm, *ChemPhysChem*, **8**, 2484 (2007).

242. T. J. Schmidt, H. A. Gasteiger, G. D. Stäb, P. M. Urban, D. M. Kolb and R. J. Behm, *J. Electrochem. Soc.*, **145**, 2354 (1998).

243. T. Biegler, D. A. J. Rand and R. Woods, *J. Electroanal. Chem.*, **29**, 269 (1971).

244. V. Climent, R. Gómez and M. Feliu, *Electrochim. Acta*, **45**, 629 (1999).

245. C. L. Green and A. Kucernak, *J. Phys. Chem. B*, **106**, 1036 (2002).

246. N. Bogolowski, T. Nagel, B. Lanova, S. Ernst, H. Baltruschat, K. Nagabhushana and H. Boennemann, *J. Appl. Electrochem.*, **37**, 1485 (2007).

247. T. Nagel, N. Bogolowski and H. Baltruschat, *Journal of applied Elektrochemistry*, **36**, 1297 (2006).

248. W. Chen, Y. X. Jiang and S. G. Sun, *Chin. Sci. Bull.*, **48**, 135 (2003).

249. K.-P. Geyzers, Untersuchung der CO-Elektrooxidation an mit Ruthenium modifizierten Platin-Elektroden, in *Institut für Physikalische und Theoretische Chemie*, Universität Bonn, Bonn (1997).

250. H. A. Gasteiger, N. A. Markovic, J. Philip. N. Ross and E. J. Cairns, *J. Phys. Chem.*, **98**, 617 (1994).

251. C. L. Green and A. Kucernak, *J. Phys. Chem. B*, **106**, 11446 (2002).

252. P. Carbonnelle and L. Lamberts, *J. Electroanal. Chem.*, **340**, 53 (1992).

253. M. Gustavsson, H. Fredriksson, B. Kasemo, Z. Jusys, J. Kaiser, C. Jun and R. J.Behm, *J. Electroanal. Chem.*, **568**, 1 (2004).

254. M. T. M. Koper, A. P. J. Jansen, R. A. v. Santen, J. J. Lukien and P. A. J. Hilbers, *J. Chem. Phys.*, **109**, 6051 (1998).

255. M. T. M. Koper, A. P. J. Jansen and J. J. Lukkien, *Electrochim. Acta*, **45**, 645 (1999).

256. H. Massong, S. Tillmann, T. Langkau, E. A. Abd El Meguid and H. Baltruschat, *Electrochim. Acta*, **44**, 1379 (1998).

257. T. Frelink, W. Visscher, A. P. Cox and J. A. R. v. Veen, *Ber. Bunsenges. Phys. Chem.*, **100**, 599 (1996).

258. H. A. Gasteiger, N. A. Markovic and J. Philip. N. Ross, *J. Phys. Chem.*, **99**, 16757 (1995).

259. T. Frelink, W. Visscher and J. A. R. v. Veen, *Langmuir*, **12**, 3702 (1996).

260. Z. Jusys, J. Kaiser and R. J. Behm, *Electrochim. Acta*, **47**, 3693 (2002).

261. C. Korzeniewski and D. Kardash, *J. Phys. Chem. B*, **105**, 8663 (2001).

262. B. Love and J. Lipkowski, in *ACS Symp. Ser.*, M. Soriaga Editor, Molecular Phenomena at Electrode Surfaces (1988).

263. E. Herrero, J. M. Orts, A. Aldaz and J. M. Feliu, *Surf. Sci.*, **440**, 259 (1999).

264. D. Lide, *CRC Handbook of Chemistry and Physics*, CRC Press, Boca Raton (1999).

265. E. P. M. Leiva, E. Santos and T. Iwasita, *J. Electroanal. Chem.*, **215**, 357 (1986).

266. B. Lanova, H. Wang and H. Baltruschat, *Fuel Cells*, **6**, 214 (2006).

267. L. Gans, G. Q. Lu, E. Oldfield and A. Wieckowski, in *38th Heyrovsky Discussion on Electrocatalysis in Nanoscale*, Trest, Czech Republic (2005).

268. H. Wang, Electrocatalytic oxidation of adsorbed CO and methanol on Mo, Ru and Sn modified polycrystalline and monocrystalline platinum electrodes: A quantitative DEMS study, in, normal university, Bejin (2001).

269. H. Wang, in *Mathematisch-Naturwissenschaftliche Fakultät*, Rheinische-Friedrich-Wilhelms-Universität Bonn, Bonn (2001).

270. H. A. Gasteiger, N. Markovic, P. N. Ross and E. J. Cairns, *Electrochim. Acta*, **39**, 1825 (1994).

271. P. Berenz, S. Tillmann, H. Massong and H. Baltruschat, *Electrochim. Acta*, **43**, 3035 (1998).

272. K. A. Friedrich, F. Henglein, U. Stimming and W. Unkauf, *Electrochim. Acta*, **45**, 3283 (2000).

273. W. Vielstich and X. H. Xia, *J. Phys. Chem.*, **99**, 10421 (1995).

274. E. Herrero, K. Franaszczuk and A. Wieckowski, *J. Electroanal. Chem.*, **361**, 269 (1993).

275. T. J. Schmidt, H. A. Gasteiger, G. D. Stab, P. M. Urban, D. M. Kolb and R. J.Behm, *J. Electrochem. Soc.*, **145**, 2354 (1998).

276. D. Kardash, J. M. Huang and C. Korzeniewski, *Langmuir*, **16**, 2019 (2000).

277. J. L. Cohen, D. J. Volpe and H. D. Abruna, *PCCP*, **9**, 49 (2007).

278. T. D. Jarvin and E. M. Stuve, in *Electrocatalysis*, J. Lipkowski and P. N. Ross Editors, New York u.a. (1998).

279. P. S. Kauranen, E. Skou and J. Munk, *J. Electroanal. Chem.*, **404**, 1 (1996).

Acknowledgements

This thesis is the result of projects realised at the University of Bonn. I learned many things, not only scientifically but also nonscientifically, during my years as a Ph.D student and I am grateful for the experience I had during this time. This work could not have been generaterd without the help and support of many people, in particular:

First and foremost, my hearty gratitude goes to my supervisor, Prof. Dr. Helmut Baltruschat, for giving me the opportunity to accomplish this work in the Department of Electrochemistry at the University of Bonn, as well as for his guidance and help during these years. His enthusiastic support, his input, his tolerance and kindness encouraged to me to finish this dissertation.

I would like to thank Prof. Dr. Moritz Sokolowski, Prof. Dr. Werner Mader, and Prof. Dr. Karl Maier for agreeing to be members of my Ph.D. committee.

My hearty and special thanks go to my friends, colleagues and students, who assisted, advised and supported my research and writing efforts over the past years. Especially, I need to express my gratitude and deep appreciation to Nicky Bogolowski, Michael und Christine Nielinger whose friendship, hospitality, knowledge and wisdom have supported, enlightened and entertained me over the years of our friendship. They have consistently helped me keep perspective on what is important in life and shown me how to deal with reality.

Thanks are also given to the members of fine mechanics, electronics and glass blowing workshops, namely Mr Backhausen, Mr Böhmer, Mr Königshoven, Mr Langen as well as Mr Paulig, for their friendly and professional support during the maintance and repair of our measurement devices and in planning and constructing of new elements.

Děkuji také své rodině za cennou podporu během celé doby mého studia, především mé matce Heleně Pololáníkové a bratru Jakubovi Pololáníkovi.

PUBLICATIONS

"Methanol Oxidation on Carbon Supported Pt and Ru - Modified Pt Nanoparticles: a Comparison with Single Crystal and Polycrystalline Electrodes"; B. Lanova, H. Wang, H. Baltruschat, Fuel Cells, Vol. 6, Iss. 3-4, Pages 214 – 224

"Activity of selenium modified ruthenium-electrodes and determination of the real surface area"; N. Bogolowski, T. Nagel, B. Lanova, S. Ernst, H. Baltruschat, K. S. Nagabhushana and H. Boennemann, Journal of Applied Electrochemistry, Vol. 37, Iss. 12 (2007) 1485-1494

"DEMS Study of the Acetic Acid Oxidation on Boron-Doped Diamond Electrode"; A. Kapalka, B. Lanova, H. Baltruschat, G. Foti, and Ch. Comninellis, J. Electrochem. Soc., Vol. 155 (2008) E96-E100

"Electrochemically induced mineralization of organics by molecular oxygen on boron-doped diamond electrode"; A. Kapałka, B. Lanova, H. Baltruschat, G. Fóti and Ch. Comninellis Electrochemistry Communications, Vol. 10, Iss. 9 (2008) 1215-1218

"Effect of Temperature on CO and Methanol Oxidation on Polycrystalline Pt and Pt Colloid Catalysts"; B. Lanova, H. Baltruschat, in preparation

"Consecutive adsorption of methanol and CO on platinum and platinum based electrodes"; B. Lanova, H. Baltruschat, in preparation

POSTER CONTRIBUTIONS

"A DEMS Study of Methanol Oxidation on Colloid Catalysts for DMFC", E. Ezerskis, B. Lánová, H. Baltruschat, 53rd ISE Meeting, October 15th-20th 2002, Düsseldorf, Germany

"Ideal and real catalysts for methanol oxidation: a quantitative product analysis using differential electrochemical mass spectrometer"; H. Wang, B. Lanova, T. Löffler, H. Baltruschat, 3rd International Conference A.B.A., June 16th-20th 2002, Brno, Czech Republic

"Methanol and CO Oxidation on Pt and Pt-colloid Catalysts for DMFC"; B. Lanova and H. Baltruschat, 4th International Conference A.B.A, June 15th-19th 2003, Brno, Czech Republic

"Characterization of specific adsorption sites on bimetallic catalysts for methanol oxidation by isotopic labeling"; B. Lanova, H. Baltruschat, GDCh Wissenschaftsforum Chemie, September 16th-19th 2007, Ulm Germany

---

LECTURES

"Methanol and CO Oxidation on Pt and Pt-colloid Catalysts for DMFC"; B.Lanova and H. Baltruschat, 5th International Conference A.B.A, June 13th-16th 2004, Brno, Czech Republic

"Methanol and CO Oxidation on Pt and Pt-colloid Catalysts for DMFC"; B.Lanova and H. Baltruschat, AGEF - Euregio Workshop on "Modern Trends in Interfacial Electrochemistry – Theory meets Experiment" May 06th-07th 2004, Rolduc Abbey, the Netherlands